February 2013

Impact of CO_2 Impurities on Storage Performance and Assurance

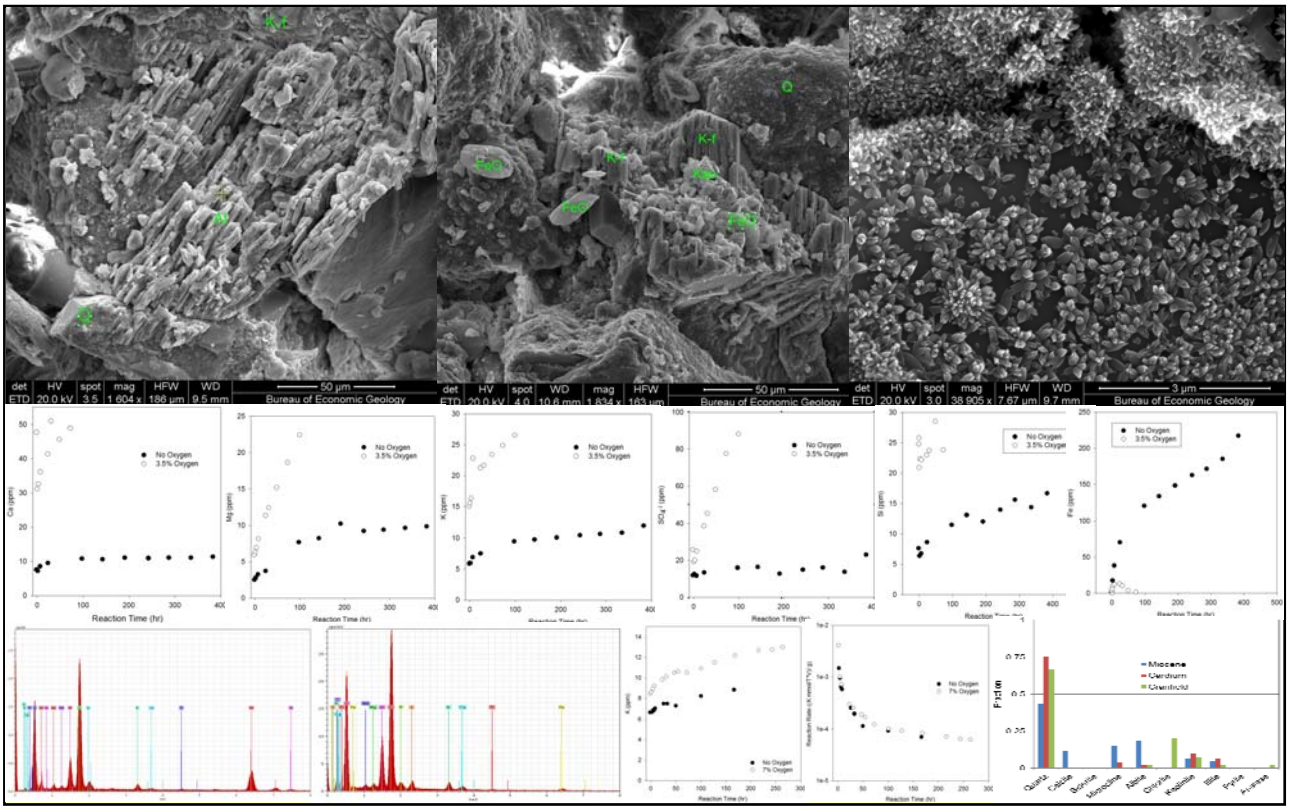

Report on Tasks 3 and 4 (Geochemistry) Prepared for:
CO_2 Capture Project (Phase III)

by
Jean-Philippe Nicot, Jiemin Lu, Patrick Mickler, Changbing Yang, Katherine Romanak, and Tongwei Zhang

Bureau of Economic Geology
John A. and Katherine G. Jackson School of Geosciences
The University of Texas at Austin
Austin, Texas 78713-8924

Impact of CO_2 Impurities on Storage Performance and Assurance

Tasks 3 and 4: Geochemistry

Jean-Philippe Nicot, Jiemin Lu, Patrick Mickler, Changbing Yang, Katherine Romanak, and Tongwei Zhang

Bureau of Economic Geology
John A. and Katherine G. Jackson School of Geosciences
The University of Texas at Austin
Austin, Texas 78713-8924

Executive Summary

This document presents results of Tasks 3 and 4 out of 5 tasks focusing on the geochemical impacts of impurities in the CO_2 stream. Tasks 1 and 2 were concerned with impacts on flow behavior. Impurities consist mostly of N_2, O_2, and Ar to which several minor reactive species can be added (CO, H_2, SOx, and other trace gases). The problem is approached through laboratory autoclave experiments coupled with geochemical numerical modeling. The autoclave consists of a 250-ml reactor able to sustain temperatures as high as 150°C and pressures as high as 400 bars, that is, conditions seen in reservoirs up to a depth of 12,000 ft. A computer automatically regulates pressure and temperature and the system also allows for water sampling during the experiments. Typically 10 to 15 samples of the solution were taken during the 5-to-10 day course of each of the 19 experiments. Rock samples were exposed to a supercritical mixture of CO_2 and O_2 (in general 3.5% molar) or to pure supercritical CO_2 that filled about half of the reactor cell. The other half consisted in a single core fragment or a few large fragments (~8g total) submerged into ~140 ml of synthetic brine (~1.88 mol NaCl corresponding to a TDS of 100,000-110,000 mg/L). The study analyzed three clastic rock samples: (1) a "dirty sandstone" of Miocene age from a deep well in the shallow offshore off the Texas coast; (2) a relatively clean sandstone from the Cardium Formation of Cretaceous age from Alberta; (3) a chlorite-rich sandstone from the Tuscaloosa Formation in Mississippi originating from the Cranfield site that BEG has been thoroughly studying for several years. Composition of the samples is presented in Table ES1.

Table ES1. Summary of sample mineralogical composition

	Offshore Miocene, TX Well OCS-G-3733 Depth 9205 ft	Cardium Sands, AB Well unknown Depth unknown	Cranfield, MS Tuscaloosa Formation Well CFU31F-3 Depth 10,476.6 ft
Quartz	43.5%	75.5%	66.9%
Calcite	11.8%		
Siderite		1%	
Microcline	15.2%	4.2%	
Albite	18.4%	2.5%	1.8%
Chlorite			20.2%
Kaolinite	6.2%	10.4%	7.3%
Illite	5.0%	6.5%	2.0%
Pyrite	Trace++	Trace+++	Trace
Anatase			1.8%
Total	100.1%	100.1%	100%

Note: this table is identical to Table 15

In addition to quartz, the Miocene sample is dominated by calcite (11.8%) and feldspars (31.6%), the Cardium sample is dominated by clays (16.9%) with some feldspar (6.7%) and siderite (~1%), and the Cranfield sample is dominated by chlorite (20.2%) with some clays (9.3%). Both the Miocene and Cardium samples show evidence of not uncommon pyrite. The "dirty sandstone" Miocene sample allows for investigating carbonate behavior with and without O_2 whereas the relatively clean and non-reactive Cardium sample is a good candidate to investigate feldspar behavior without the overprint of carbonates. The Cranfield sample with abundant clay minerals dominated by chlorite is even less reactive vis-à-vis CO_2. Minerals sensitive to the presence of O_2 are pyrite (present in the Miocene and Cardium samples), siderite (present in the

Cardium sample), and chlorite (abundant in the Cranfield sample). They all contain ferrous iron-bearing minerals.

We performed 19 experiments varying various parameters but only 10 are thoroughly described. They are displayed in the matrix of Table ES2.

Table ES2. Summary of runs.

		70°C	100°C	130°C
Offshore Miocene	CO_2	√	√	√
	$CO_2 + O_2$	√	√	
Cardium Sands	CO_2	√	√	
	$CO_2 + O_2$	√		
Cranfield	CO_2	√		
	$CO_2 + O_2$	√		

Note: this table is identical to Table 6

The offshore Miocene samples showed dissolution of carbonate (Ca and Mg increase) as well as of feldspars (Ca and K increase, Na concentrations are irrelevant because experiments are done with a NaCl brine). Feldspar dissolution is more intense when O_2 is present. Kaolinite is presumed to form in both cases. The Cardium samples displayed deep attack of carbonates and of some feldspars with kaolinite formation and maybe very minor authigenic illite. Pyrite and siderite are degraded when O_2 is added and FeOx precipitate. The Cranfield samples have limited reactivity when exposed to pure CO_2. They contain little carbonates. When O_2 is added, some chlorite is degraded and FeOx deposits can be observed as well as some authigenic clay. Those qualitative observations were confirmed by geochemical modeling which was able to reproduce them.

In terms of release rates, results confirmed well-known results and delivered new observations. In pure-CO_2 cases carbonates were observed to dissolve quickly with a sharp increase in Ca, Mg, and other elements typically present in calcite. Calcite solubility was also observed to decrease with increasing temperature. As expected, feldspars showed an increase in solubility with increasing temperature whereas clays, including chlorite, stayed unreacted. Adding O_2, however, brought in interesting observations, pyrite framboids were clearly degraded, adding H+ ions to the system and increasing carbonate dissolution. The siderite (Cardium sample) is another source of ferrous iron. Both pyrite and siderite attack led to deposition of FeOx on mineral surfaces. Chlorite could also be an important source of ferrous iron but it is mostly stable unless pH drops very low. Such a case could happen if pyrite is present at a few percent level and lack of pH-buffering capacity through carbonates. Some chlorite alteration was seen in the Cranfield sample. Early in the study it was believed that O_2 had a catalytic effect on dissolution of other minerals. It turns out that, correctly for CO_2 fugacity, the O_2 effect disappears when considering carbonate dissolution. Feldspar dissolution is enhanced in the presence of O_2 but in an indirect way, though pyrite oxidation and drop in pH. Overall the additional impact of a few percent O_2 when comparing samples reacted with pure CO_2 and with a CO_2+ O_2 mixture is limited. The observation is also true for trace elements added to the brine following mineral dissolution; concentration in some cases increased several-fold but aqueous concentrations of several elements (V, Mo, As) drop when O_2 is added because they form oxyanions that sorb to precipitating FeOx and clays. We also looked at other reactive species contained in the gas

stream from a modeling standpoint and in particular the concentrations at which they would have an impact on the pH of the solution. They would start having an impact on pH (and therefore on carbonates and feldspar dissolution) at concentrations ranging from 100 to 1000 ppm depending on depth and reservoir conditions.

Although this needs to be confirmed by coreflood experiments, the reactive transport modeling suggests that porosity changes due to mineral reactions in siliciclastic material is minor and that permeability decrease following mineral precipitation does not impact flow. Overall, it does not seem that a few percent O_2 in the CO_2 stream has much impact beyond the impact due to CO_2 only.

Table of Contents

List of Figures

List of Tables

Acknowledgments

The authors would like to thank the CO_2 Capture Project Phase 3 (CCP3) for funding this project and, in particular, the project manager, Scott Imbus, and ECRB for providing the Cardium samples. We are also grateful to the DOE-sponsored SECARB project for providing the Cranfield samples, to the DOE- and State of Texas-sponsored Mega-Transect Carbon Repository project for providing the Miocene samples, and to the Jackson School of Geosciences at The University of Texas at Austin for the financial help in setting up the high-pressure and -temperature laboratory.

Acronyms

ACPP	Alberta CO_2 Purity Project
BEG	Bureau of Economic Geology
CCP3	CO_2 Capture Project Phase III
DI water	Deionized water
DOE	Department of Energy
EDS	Energy dispersive X-ray spectroscopy
EPA	Environmental Protection Agency
FeOx	Iron oxyhydroxides
GC	Gas chromatograph
ICP-M	Inductively-coupled-plasma-mass-spectrometer
IC	Ion chromatography
MCL	Maximum contaminant level
PVT	Pressure, volume, temperature
RTM	Reactive transport model
SEM	Scanning electron microscope
TDS	Total dissolved solids
XRD	X-ray diffraction
ZPC	Zero point charge

I. Introduction

This work is funded by Phase III of the CO_2 Capture Project (http://www.co2captureproject.org/) (CCP3). CCP3 is a partnership of seven major energy companies interested in advancing the technologies that will support the deployment of industrial-scale CO_2 capture and storage. CCP3 requested a proposal from the Bureau of Economic Geology at the University of Texas at Austin (BEG) to address some of the issues related to non-pure CO_2 stream. Geologic sequestration of carbon dioxide (CO_2) is poised to become an important technology for addressing high CO_2 atmospheric concentrations and global warming. The impurities of interest consist of N_2, O_2, H_2, CO, Ar, and SOx to which CH_4, often present in the subsurface, can be added. However, little work has been done to explain the impact of impurities on subsurface behavior of the CO_2-dominated injection stream. In particular, this report investigates the impact of impurities on geochemical changes in the injection formation and their consequences on flow and ultimate capacity. Concerns about capture economics provided the incentive to investigate those issues. In general, the purer the desired CO_2 stream, the more expensive the capture process. Leaving some of the impurities in the injection stream could save both capital and operational costs possibly without consequences to the storage part of the project. For example, pipelines and compressors could be re-engineered to handle impurities. In this context, the work attempts to understand the impact of impurities on the behavior of the system. It does not address legal and regulatory issues such as the permissible level of impurities before which an injection scheme would become a waste disposal operation rather than a CO_2 injection operation. The submitted proposal intended to evaluate and understand the impact of CO_2 capture stream impurities on plume dynamics and trapping and fluid-rock interactions. The contract between CCP3 and BEG was executed in December 2009 with an end date of March 31, 2011. It was subsequently extended to September 30, 2012 with additional tasks, in particular related to the Alberta CO_2 Purity Project (ACPP). The technical tasks consisted of:

1. Accessing the PVT data through literature search and experimental work
2. Conducting a parametric study on impact of impurities on plume dynamics and rate and extent of trapping mechanisms in saline aquifers. This task is mostly a desktop numerical study performed with synthetic simplified cases and on actual field models.
3. Conducting rock-fluid interaction studies. This task has a large laboratory component
4. Conducting reactive transport numerical modeling
5. Integrating the results to qualitatively assess the impact of gas impurities on (1) plume shape and evolution, (2) CO_2 permanence, (3) CO_2 storage capacity, (4) well injectivity, (5) storage reservoir integrity, and (6) trace elements released/absorbed during dissolution / precipitation caused by addition of impurities.

Overall, the objectives of the project are (1) to understand plume dynamics as it impacts Area of Review and permanence / containment / leakage (including impacts on trapping mechanisms); (2) to assess impact on capacity; and (3) to assess impact on injectivity. This report documents full results of Tasks 3 and 4. An earlier report documents results of Tasks 1 and 2 (Nicot and Solano, 2012). The following paragraph is an excerpt of its executive summary that summarizes the conclusions of Tasks 1 and 2:

Impurities impact density and viscosity of the CO_2-rich mixture. A lower density impacts CO_2 capacity not only because of the smaller fraction injected and space needed for storing

impurities but also because of the generally lower density of the impurities at the same conditions. An approximate proxy for capacity change owing to impurities is given by the density ratio. The loss in capacity can be as high as >50% at very shallow depths (~3000 ft, CO_2 and 15% molar N_2) but the difference quickly decreases with depth. Similarly, mass injectivity, that can be represented by the proxy metric of density over viscosity ratio, also shows a decreased value at very shallow depths that quickly recovers with increasing depth. In terms of plume shape and extent, the impact of impurities is again more marked at shallow depth where the contrast in density and viscosity with neat CO_2 is the largest. It decreases with depth. For example, about 4% mole fraction in a binary system suffices to increase plume length in "shallow" low-dip sloping layers by 25% whereas 9 to 15%, depending on the component, are needed in a "deep" system. In all cases, plume extent is greater with impurities however residual trapping occurs faster. This relationship mostly holds for all systems whatever the level of heterogeneity and complexity. The contrast is most extreme in very simple systems and heterogeneity assuming adequate operational choices seems to dampen impacts of impurities. This presumably occurs because heterogeneity creates multiple tongues blunting the impact of impurities. It also suggests a trade-off between plume extent (area of review with risk of CO_2 leakage) and decreased risk owing to faster trapping. A larger plume translates into a larger area to inspect for leakage pathways such as faults and abandoned wells but a faster trapping translates into a shorter period of time to monitor the site.

The geochemical tasks consisted of laboratory autoclave experiments combined with numerical modeling. The scope of work called for the following (paraphrased). While conducting Task 3 (rock-fluid interaction studies), the following subtasks were performed: (a) ***identify core samples*** with specific features (interbedded clean sand and shale-rich layers; clean sand with extensive authigenic phases such as clays and carbonate cements; marine shale) and consistent with major formations likely to be chosen for CO_2 injection in the US and Europe; (b) ***conduct time-temperature batch autoclave experiments*** on core segments with pre- and post- reaction rock and fluid analyses (petrographic, petrophysical, geomechanical and formation damage analyses; rock quantitative analyses –XRD, XRF, microprobe, BET sorptometer; fluid geochemistry –pH, TDS, anions, cations, water and DIC stable isotopes; and mineral dissolution kinetics analyses; (c) ***compile published data*** for relevant mineral precipitation/dissolution rates, reaction constants, molar volume changes, redox reaction/microbial activity rates, and other parameters as needed. Literature search and bibliographic summary of previous work on reactivity of the selected gases in saline aquifers. The search will be complemented as needed by a compilation of similar studies in shallow aquifers.

Task 4 (reactive transport in saline aquifers) included the following subtasks: (a) ***develop simple batch geochemical models*** using the USGS-developed and -supported PHREEQC; (b) ***develop a 2D reactive transport model*** (RTM) reproducing observations made during the autoclave experiments, most likely using the LBNL-developed and -supported TOUGHREACT; and (c) graphically ***document likely mineralogical changes*** (dissolution / precipitation) over time in the near well-bore and distal reservoir.

We present the main results of the study in the body of the report and placed additional material in several appendices. Appendix A covers the experimental setup. Appendix B contains a literature review of peer-reviewed papers documenting numerical modeling and laboratory experiments of behavior of a mixed-stream of CO_2 as well as selected impurities in the subsurface. Appendix C present s a more detailed description of core samples when available.

Appendix D describes the acid species analysis performed on behalf of ACPP. Appendix E documents example input files for the RTM model described in the main body of this document. Appendix F displays all chemical analysis results and Appendix G documents some of the modeling done to assess experimental results.

Work presented in this report is a collaborative effort by several BEG researchers: Dr. C. Yang did the literature search and modeling, Drs. P. Mickler and J. Lu performed the experiments, Dr. J. Lu did the petrographic analyses, Dr. K. Romanak supervised the laboratory, and Dr. J.-P. Nicot directed the work.

II. Approach

II-1. What are the Gases of Interest?

The report on Tasks 1 and 2 (Nicot and Solano, 2012) collected information of the gas impurities likely to be present in an oxygas waste stream. Unlike these two tasks, Tasks 3 and 4 reported in this document were mostly accomplished after collaboration with the ACPP team started. Table 1 presents typical projections from recent ACPP work whereas Table 2 presents projected compositions from earlier documents. In addition to CO_2, two no-reactive gas make the bulk of impurities N_2 and Ar. O_2 is the reactive gas the most commonly cited with molar concentration ranging from <1% to >5%. Other reactive gases possibly present in the flue stream include CO, H_2 and NO and SO_2 (more generally NOx and SOx). H_2S is not mentioned but can be present in the formation as suggested in Table 3. The most likely source of CH_4 is also from the injection formation itself. H_2O is sometimes cited as an impurity but clearly its presence is relevant only to pipelines and other surface facilities. As soon as the mixed stream will encounter the water-saturated porous media, water will partition into the previously dry stream. The transition zone, that is, the entire wellbore and engineered material, from the wellhead to the perforated section, should also be expected to be exposed to aqueous environments.

Table 1. ACPP December 2012 purity scenarios

	"Pure" Case	Low Purity	Mid Purity		High Purity	
Fuel	Gas	Heavy	Heavy	Heavy	Gas	Both
Process	SMR*	Oxy	IGCC	Oxy	Sour	Post Comb.
	(mol%)	(mol%)	(mol%)	(mol%)	(mol%)	(mol%)
CO_2	99.4	91.7	95.0	96.0	97.4	99.8
N_2	0.3	2.5	-	1.6	0.2	0.2
O_2	-	5.8	-	2.4	-	-
Ar	-	-	-	-	-	-
CO	-	-	0.5	-	-	-
H_2	0.3	-	4.0	-	-	-
CH_4	-	-	0.5	-	2.4	-
Total	100.0	100.0	100.0	100.0	100.0	100.0

Table 2. Compilation of stream compositions from oxy-fuel combustion (molar compositions).

	Wet Recycle[(1)] (pure O_2)	Dry Recycle[(1)] (pure O_2)	95% Oxygen purity[(2)]	98% Oxygen purity[(2)]	99.5% Oxygen purity[(2)]	Wilkinson, 2003[(3)]	Wilkinson, 2001[(4)]
Ar	-	-	5.761	3.570	0.950	1.1	1.35
CO	-	-	0.030	0.030	0.030	-	-
CO_2	92.745	93.278	86.469	91.879	94.679	96.2	95.67
H_2	-	-	-	-	-	-	-
H_2S	-	-	-	-	-	-	-
N_2	4.488	4.508	3.580	0.500	0.330	1.9	1.65
NO	-	-	0.160	0.020	0.010	-	-
O_2	2.767	2.194	4.000	4.000	4.000	0.7	0.57
SO_2	-	-	-	-	-	0.1	0.76
Total	**100.0**	**100.0**	**100.0**	**100.0**	**100.0**	**100.0**	**100.0**

(1) Zanganeh et al. (2004); (2) Aimard et al. (2008); (3) Wilkinson et al. (2003); (4) Wilkinson et al. (2001)

Table 3. CO_2 stream composition recommended limits

Component	Unit (Max unless Otherwise noted)	Carbon Steel Pipeline		Enhanced Oil Recovery		Saline Reservoir Sequestration		Saline Reservoir CO_2 & H_2S Co-sequestration		Venting Concerns (See Section 3.0)
		Conceptual Design	Range in Literature	Conceptual Design	Range in Literature	Conceptual Design	Range in Literature	Conceptual Design	Range in Literature	
CO_2	vol% (Min)	95	90-99.8	95	90-99.8	95	90-99.8	95	20 – 99.8	Yes-IDLH 40,000 ppmv
H_2O	ppm_{wt}	300	20 - 650	300	20 - 650	300	20 - 650	300	20 - 650	
N_2	vol%	4	0.01 - 7	1	0.01 - 2	4	0.01 - 7	4	0.01 – 7	
O_2	vol%	4	0.01 – 4	0.01	0.001 – 1.3	4	0.01 – 4	4	0.01 – 4	
Ar	vol%	4	0.01 – 4	1	0.01 – 1	4	0.01 – 4	4	0.01 – 4	
CH_4	vol%	4	0.01 – 4	1	0.01 – 2	4	0.01 – 4	4	0.01 – 4	Yes-Asphyxiate, Explosive
H_2	vol%	4	0.01 - 4	1	0.01 – 1	4	0.01 – 4	4	0.02 – 4	Yes-Asphyxiate, Explosive
CO	ppm_v	35	10 - 5000	35	10 - 5000	35	10 - 5000	35	10 - 5000	Yes-IDLH 1,200 ppmv
H_2S	vol%	0.01	0.002 – 1.3	0.01	0.002 – 1.3	0.01	0.002 – 1.3	75	10 - 77	Yes-IDLH 100 ppmv
SO_2	ppm_v	100	10 - 50000	100	10 - 50000	100	10 - 50000	100	10 - 50000	Yes-IDLH 100 ppmv
NO_X	ppm_v	100	20 - 2500	100	20 - 2500	100	20 - 2500	100	20 - 2500	Yes-IDLH NO-100 ppmv, NO_2 - 200 ppmv
NH_3	ppm_v	50	0 - 50	50	0 - 50	50	0 - 50	50	0 - 50	Yes-IDLH 300 ppmv
COS	ppm_v	trace	trace	5	0 - 5	trace	trace	trace	trace	Lethal @ High Concentrations (>1,000 ppmv)
C_2H_6	vol%	1	0 - 1	1	0 - 1	1	0 - 1	1	0 - 1	Yes-Asphyxiant, Explosive
C_3+	vol%	<1	0 - 1	<1	0 - 1	<1	0 - 1	<1	0 - 1	
Part.	ppm_v	1	0 - 1	1	0 - 1	1	0 - 1	1	0 - 1	
HCl	ppm_v	N.I.*	N.I.*	N.I.*	N.I.*	N.I.*	N.I.*	N.I.*	N.I.*	Yes-IDLH 50 ppmv
HF	ppm_v	N.I.*	N.I.*	N.I.*	N.I.*	N.I.*	N.I.*	N.I.*	N.I.*	Yes-IDLH 30 ppmv
HCN	ppm_v	trace	trace	trace	trace	trace	trace	trace	trace	Yes-IDLH 50 ppmv
Hg	ppm_v	N.I.*	N.I.*	N.I.*	N.I.*	N.I.*	N.I.*	N.I.*	N.I.*	Yes-IDLH 2 mg/m^3 (organo)
Glycol	ppb_v	46	0 - 174	46	0 - 174	46	0 - 174	46	0 - 174	
MEA	ppm_v	N.I.*	N.I.*	N.I.*	N.I.*	N.I.*	N.I.*	N.I.*	N.I.*	MSDS Exp. Limits 3 ppm_v, 6 mg/m^3
Selexol	ppm_v	N.I.*	N.I.*	N.I.*	N.I.*	N.I.*	N.I.*	N.I.*	N.I.*	

Source: USDOE (2012), Exhibit 2-1
Note: * not enough information available to determine the maximum allowable amount

US DOE / NETL (USDOE, 2012) prepared a document by performing a literature search and meant mostly for transportation pipeline (as noted by their inclusion of water concentration limits for subsurface injection). Still, Table 3 is in good agreement with Table 1 and Table 2 and adds a list of minor and trace species possibly present in the injection stream. Some of those gases, in addition of being reactive, are also toxic (RHS column of Table 3), sometimes at low concentrations (CO, H_2S are the most likely to be found at high concentrations).

Given the likely waste stream composition, the autoclave ***experiments were performed only with a CO_2+O_2 mixture***. To our knowledge there is no documented similar experiments in the peer-reviewed literature although the interest of the CCS community at large have increased in the past few years, see for example the IEAGHG (2011) desktop study (IEAGHG, 2011; Wang et al., 2011) on effects of impurities on CCS. Appendix B documents other, mostly modeling, bibliographic references to the impact of impurities. However, there is at least one documented case of field injection of a mixed stream of CO_2 and O_2 at Rousse, France, a depleted gas reservoir investigated by Total (Monne and Prinet, 2012). With a starting date of January 8th, 2010, ~50,000 tons of the mixed stream (CO_2=92%, O_2=4%, Ar=3-7%, N_2=0-4%) have been injected into a low-porosity (3%), low-permeability (1 mD) dolomite at a depth of ~4500m. Mineral phases are : dolomite (93.5%), Calcite (0.5%), quartz (2.5%), apatite (0.2%), pyrite (0.4%), (magnesian) chlorite (0.3%), illite and smectite (2.5%) and insoluble organic matter (0.1%) (Girard et al., 2012). Observations suggest that reservoir rocks are mostly unreactive. The company performed general geochemical modeling and experiments and modeling with impurities (Renard et al., 2011; Corvisier et al., 2012). Renard et al. (2011) reported that experiments were conducted in batch reactors with a 2 cm^3–cell in the presence of rock fragments, saline water (25 g/l NaCl) and gas (82% CO_2, 4% SO_2, 4% O_2, 4% N_2 and 6% Ar) at 100 bar and 150°C for one month. The presence of SO_2 in the experiments, which totally reacted with the rock while ~40% of O_2 remained, deviates from the actually injected stream (as far as I can tell) and from our own experiments and obscures the contribution of each reactive species. Renard et al. (2011) proposed that SO_2 reacted with O_2 to produce sulfuric acid that went on and dissolved carbonates (calcite then dolomite). Remaining O_2 oxidized some of the pyrite. Anhydrite and barite (cations from carbonate dissolution and sulfate mostly from SO_2) precipitated as small crystals. Corvisier et al. (2012) were able to numerically reproduce the experimental observations.

Interest on the impact of O_2 in the subsurface is not recent. It was investigated in the context of EOR and direct flue gas injection by Argonne National Laboratory several decades ago (Taber, 1985). Taber (1985) examined several projects in which O_2 is injected either on purpose or as a co-injectant: flue gas injection / exhaust fumes; fire-flooding; steam injection; air injection. In the latter case, Taber noted that O_2 was consumed relatively quickly with no detrimental impact to the reservoirs besides material corrosion issues. Taber's work, however, underlines the risk of, perhaps violent, reaction with hydrocarbon if O_2 is injected with CO_2. This aspect is not considered in this document that focuses on saline aquifers.

II-2. Samples for Experiments

The samples used in this project have various geological as well as operational sources. The samples will be referred to as *Offshore Miocene* (samples provided by the DOE- and State of Texas-sponsored Mega-Transect Carbon Repository project headed by Dr. T. Meckel), *Cranfield* (samples provided by the DOE-sponsored SECARB project headed by Dr. S. Hovorka), and

Cardium (samples provided by the Alberta Energy Resources Conservation Board –ERCB- core repository through Mr. W. Sawchuk from ARC Resources ltd). The former two are available from the BEG core repository (http://www.beg.utexas.edu/facilities.php). As described below, the three samples are siliciclastic with various amount of carbonates and feldspars. The proposal called for using a sample from the Frio formation as the most reactive sample. For convenience, we used Offshore Miocene samples instead. Geologically Frio and Offshore Miocene samples are separated by a single marine episode interval (Anahuac Shale) but represent similar type of sediments. In this round of experiments we did not used carbonate rocks (Redwater Leduc carbonates from Alberta)..

The samples were analyzed using a variety of tools, first on a fresh sample, then on multiple reacted samples: X-ray diffraction (XRD), scanning electron microscope (SEM) and energy dispersive X-ray spectroscopy (EDS) analyses. No particular precaution was taken when handling the cores and rock fragments. XRD projects the crystal structure of a mineral and provides the amount of the most abundant ones (quartz, feldspars, carbonates, clays) but not necessarily of minerals in minute amount (<1%) such as pyrite or maybe anhydrite. SEM produces sharp images showing the topography of a microscopic surface allowing the visual determination of minerals and of their spatial relationships. EDS gives the elemental composition of the surface of a sample and allows to create maps of, for example, Fe or Ca distribution.

Samples for XRD analyses were prepared the following way. Bulk powders of the original and reacted rock samples were prepared by means of wet grinding and spray drying. The samples were first disintegrated using a TEMA ball mill before further grinding in a McCrone Micronizing Mill. The samples were ground for 16 minutes in 0.5% (wt./vol) aqueous solution of polyvinyl alcohol to reduce particle size sufficiently to less than 10 µm. The resulted slurry samples were sprayed from top of a spray drier and dry samples were collected at the bottom. X-ray diffraction analysis was conducted on a Bruker AXS D8 diffractometer at the University of Texas at Austin. Bruker's Eva software was used to identify mineral phases. Quantitative analysis was conducted using Topas 3, a personal computer software based on the Rietveld method (Bish, 1994). Quantitative phase analysis results from this method are accurate to within 2% absolute error (Hiller, 1999).

II-2-1 Offshore Miocene

The samples used originated from an Early Miocene core sample from well OCS-G-3733 (A-6, 9205 ft) part of a 200-ft cored section south of Matagorda County in Texas (Figure 1a). The section, located above the *Amphistegina B.* interval, contains mainly fine-grained sandstone of delta fringe alternating with muddy siltstone of pro-delta deposits (http://www.beg.utexas.edu/gccc/miocene/stratigraphic_containment.php). The sandstones are usually moderately to poorly sorted and poorly rounded. Major framework grains include quartz (average 38%), plagioclase (17%) and K-feldspar (13%). Calcite with an average of 22% exists as detrital grains, fossils and cements. Clay minerals are mostly illite (6%) and kaolinite (3%) as pore-filling and mineral replacing habits. Metamorphic and volcanic rock fragments are up to 5% and are usually deformed and altered. More petrographic and mineralogical details on the formation are provided in Appendix C. Samples were provided through an ongoing project funded by the Texas General Land Office and by the U.S. DOE / NETL and managed by the BEG.

Resident brine composition has not been sampled but a look at the USGS produced water database (Breit, 2002) suggests that the brine is mostly a NaCl brine in the 50-100,000 mg/L TDS range.

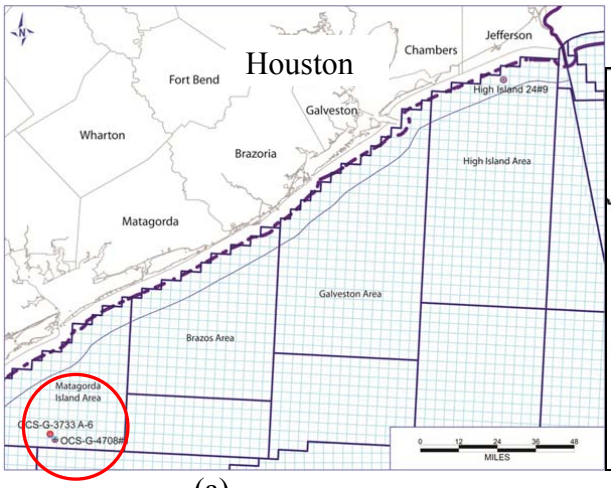

(a)

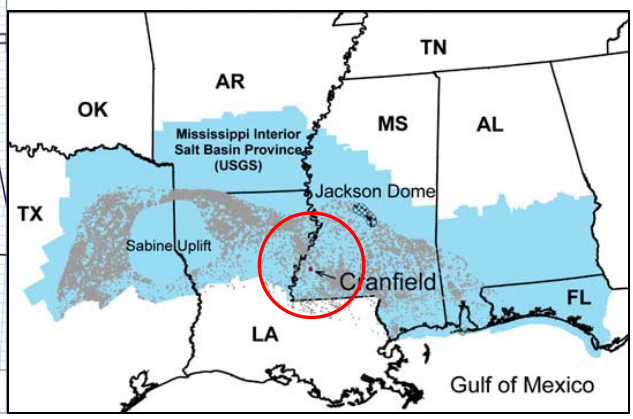

(b)

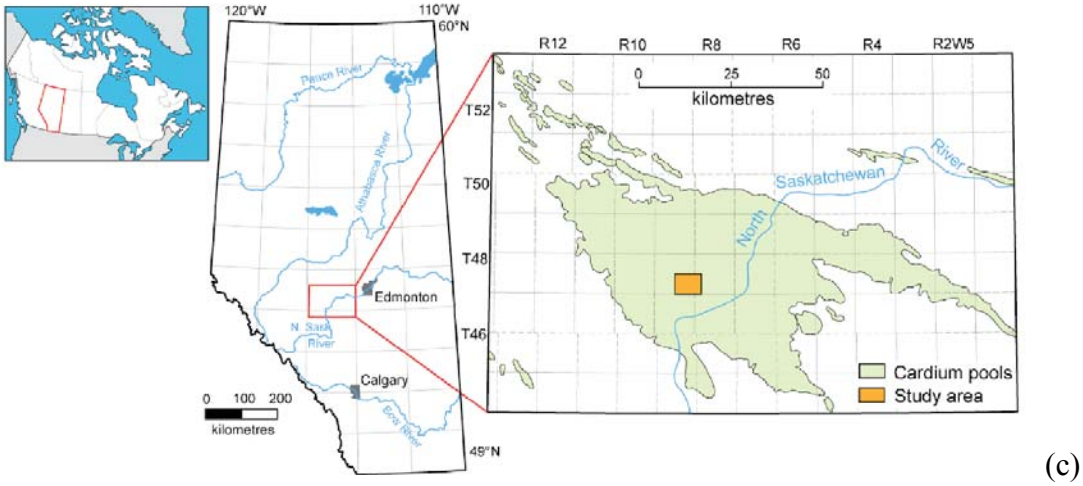

(c)

Note: (c) from Dashtgard et al. (2008)

Figure 1. Sample locations (a) Offshore Miocene off the Texas Gulf Coast; (b) Cranfield, Mississippi; and (c) approximate location of the Pembina field in the Cardium Fm. in Alberta

II-2-2 Cranfield

The Cranfield reservoir is a basal fluvial sandstone of the lower Tuscaloosa Cretaceous Formation in western Mississippi (Figure 1b). It is made up of mostly quartz with a porosity varying from 15% to 25%. Permeability varies from hundreds of md in cleaner coarser intervals to <10 md when authigenic chlorite cement is abundant with some carbonate cement The seal is composed of a marine mudstone (mostly illite with some kaolinite) with silty-sandy intervals totally occluded by carbonate cement. The mudstone intervals have also some carbonate (those were planned but not performed autoclave experiments). Reservoir temperature is ~125°C, and reservoir pressure was initially 32 MPa at a depth of 3,040 m. The reservoir rock, which is composed mainly of minerals with low reactivity (average quartz 79.4%, chlorite 11.8%, kaolinite 3.1%, illite 1.3%, concretionary calcite and dolomite 1.5%, and feldspar 0.2%), is

relatively unreactive to CO_2. A more thorough description of the Cranfield samples used in the autoclave experiments is given in Section VIII and in a paper by Lu et al. (2012). Samples were provided through the U.S. DOE-funded SECARB Early Test project managed by the BEG.

The brine composition at Cranfield has been described in several papers (Lu et al., 2012). The Lower Tuscaloosa reservoir brine is an Na–Ca–Cl-type water with relatively uniform salinity (~150,000 mg/L TDS). The brine contains relatively high concentrations of Ca (7600–14,000 mg/L), Mg (890–1180 mg/L) and Sr (480–760 mg/L) but low values of SO_4 (25–55 mg/L).

II-2-3 Cardium Sands (Alberta)

The Cardium Sands located in the Pembina Area in Alberta, Canada (Figure 1c) were associated with a shoreline depositional environment. The samples used in the experiments come from a clean sandstone lithofacies that were the primary exploration targets based on their higher permeability. They come from a core fragment we called ARC-PC-3 ARC-PC-4b from the so-called parasequences 3 an4, respectively, chosen because (1) it contains no or very little calcite and (2) it is the largest fragment. See Dashtgard et al. (2008), Krause et al. (1987) for more details. We based our reactive transport model on this formation and more information is provided in Sections II-7 and III-3.

The chemical composition of the resident brine is given, for example, in Melrose et al.(1976). Resident water is releatively fresh at ~10,000 ppm and dominated by Na, Cl, and bicarbonate ions. It is somewhat lower that the synthetic brine used in the autoclave experiments.

II-3. Autoclave Reactor

The autoclave reactor and related equipment represent a state-of-the-art apparatus that was recently installed and tested at the BEG (see Appendix A). The stainless-steel reactor cell volume is approximately 250 ml and we performed batch not column experiments. Experiments were usually conducted at 70°C, 100°C, or 130°C and 200 atm (corresponding to a depth of ~6,000 ft) with1.88 molal NaCl synthetic solution (~110,000 ppm or a ionic strength just above 1 mol/L). CO_2 or the binary CO_2-O_2 mixtures are supercritical at those conditions. The temperature range was not chosen to try to reproduce reservoir conditions but rather to assess kinetics. Temperature has typically a much larger impact on reactions than pressure so we focused on temperature but with a realistic reservoir pressure. Similarly, we chose to work with a synthetic brine to mimic the ionic strength of a typical brine. Although some Cranfield brine was available for the experiments, we thought results would be more informative using a brine with little complexity and a very simple chemical composition allowing for an understanding of the behavior of trace elements. We decided to use a more realistic brine make sure that pH stays within the expected field range and that reaction mechanisms stay the same as they would be at field conditions. Dissolution amounts have been described in Appendix A of Tasks1&2 report (Nicot and Solano, 2012).

II-3-1 Procedure

Approximately 8 g of core fragments of relatively large size (that is, one or several big fragments) are loaded into the reactor. The rock chips were not disintegrated in order to keep mineral surface area relatively unchanged and to minimize the risk of plugging the lines of the sampling system. The synthetic brine is then added, approximately a volume of 100-150 ml. It is

prepared by dissolving a precise amount of pure NaCl (see blank results) into DI water. A brine volume of 150 ml and around 5-10g rock chips in the reactor initially gives a brine/rock ratio in volume about 70. To remove air from the system, He is pumped into the reactor and bubbled through the prepared solution and allowed to flow out for approximately 10 minutes.

The reactor is loaded and allowed to equilibrate at experimental pressures and temperatures without supercritical CO_2 for approximately two days. The reactor is then sealed and pumped to 200 atm with He and heated to ~100°C. Temperature and pressure are automatically controlled by regulators. The reaction temperature was maintained by a computer controlled heater with a thermocouple positioned in the reaction chamber. An impeller stirs the solution to facilitate gas and rock dissolution. The magnetic stirrer homogenizes the system and speeds reactions by removing slow diffusion-based controls; this is an apparatus which is not commonly implemented in autoclave reactors. It gives us confidence that the solution is well-mixed and that aqueous samples are representative of the rock-water interactions. Once the temperature is reached, a liquid sample (~3-4 mL) is taken through a dip tube in the reactor. A sample is then taken once per day for 2 days. After this baseline data is collected, the reactor heater is turned off and purged by releasing He slowly to reduce the amount of water loss. Once atmospheric pressure is obtained, the heater is restarted and a supercritical CO_2 pump is used to a load CO_2 into the reactor to a pressure of 200 atm. For the experiment containing O_2, 100 to 200 psi of O_2 is added to the reactor just before CO_2 addition. In CO_2 only experiments, the reaction vessel was sealed and a super critical CO_2 pump was used to increase the pressure in the reaction vessel to 200 bar resulting in a water-rock-supercritical CO_2 system inside the cell. When 200 bar of pressure was reacted, the time was noted as the start of the reaction, approximately 15 minutes after the introduction of CO_2. In reactions involving O_2 as an impurity the reaction vessel was purged with O_2 gas for 5 minutes to remove the He atmosphere. The vessel was then sealed and pressurized to 100 psi (6.9 bar) or 200 psi for the R-series experiment. The supercritical CO_2 pump was then used to increase the reaction vessel pressure to 200 bar resulting in a water-rock-O_2-supercritical CO_2 system inside the cell. After reactor reaches 100°C and 200 atm, a liquid sample is taken through the dip tube. A sample is then taken every 2 hours for the first 6-8 hours, then once daily for approximately 14 days until the analyzed species concentrations remain constant. No additional brine is added during the experiment. As little water as possible (~8 ml/sample for alkalinity measurement, chemical analyses, and purging the lines) is taken from the solution. The solution volume cannot be assumed constant and we correct for this in the release rate calculation. No correction for evaporation was needed. We used Br as a tracer to assess evaporation and other leaks that turned out to be very limited (see opposite figure). We also used blanks as control (see Table 5). Blank experiments without CO_2 injection (i.e., ultrapure de-ionized) were used as controls. We tentatively increased the reactor to 150°C in several instances but were unable to achieve good sealing and the experiments were aborted.

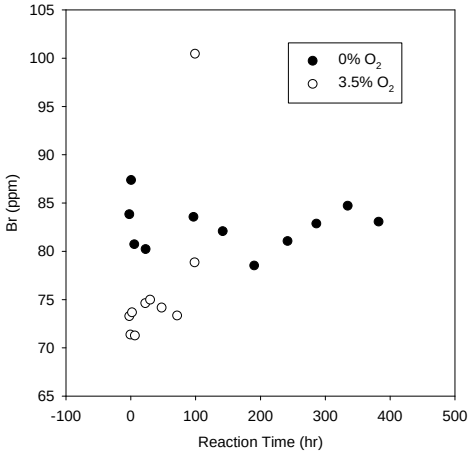

A major concern during the experiments was avoiding corrosion of the reactor, especially when O_2 is introduced. The introduction of O_2 initially caused severe corrosion of some fittings. The quartz liner, provided by the vendor, could not be installed to protect the reactor walls from

corrosion because it required a modification of the stirring propeller and relocating the liquid sampling port. After a failed attempt to fit the inner surface of the reactor with an additional protective Teflon-like membrane, the so-called *blue armor*, we eventually used a relatively low tech but ingenious solution inserting an appropriately-shaped open top polyethylene sample bottle into the reactor eliminating any contact between solution and solids and the reactor itself. In addition, the liquid sampling port was modified by adding a plastic dip tube that extended into the sample-brine container. Separating the brine from contact with the reaction vessel walls significantly limited observed corrosion. Any corrosion of the reactor steel does not impact the solution since the solution is confined in a non-corrosive plastic container not in direct contact with any metal reactor pieces.

The vessel body is made of 17-4PH stainless steel whereas the vessel cap is made of Nitronic 60 (literature from the vendor "Thar"). In addition to iron, the stainless steel reactor components are composed of Cr and Ni to which Mn, Mo, and Cu can be added (Table 4). Those are the components that mostly reacted with O_2 in the failed C series experiment.

Table 4. Typical composition of autoclave vessel components

17-4PH Stainless Steel (main vessel body)		**Nitronic 60 Stainless Steel (vessel cap)**	
Element	**Composition (weight %)**	**Element**	**Composition (%)**
Iron	>75%	Iron	~60%
Chromium	15.5	Chromium	16-17
Nickel	4.5	Nickel	8-8.5
Manganese	0.40	Manganese	7.5-8.5
Silicon	0.50	Silicon	3.7-4.2
		Molybdenum	0.75
Copper	3.50	Copper	0.75
		Vanadium	0.20
		Tungsten	0.15
		Nitrogen	0.1-0.18
Columbium + Tantalum	0.30	Columbium	0.10
	0.04	Carbon	0.06-0.08
		Titanium	0.050
		Tin	0.050
Phosphorus	0.020	Phosphorus	0.040
Sulfur	0.005	Sulfur	0.030
		Aluminum	0.020
		Boron	0.0015

Source: vendor information

In order to test the impact of leaching of reactor walls and the elements potential added by the NaCl used to make the synthetic brine, we ran two blank experiments with very similar results (Table 5). They were run at 100°C, 200 bars with CO_2 and no O_2 and synthetic brine (but with no samples) for 4 days. The solution was in direct contact with the reactor walls. There is evidence

of some minor leaching, Fe, Ni, and Mn are relatively high compared to the other trace elements with 436.4 ppb, 409.5 ppb, and 130.7 ppb, respectively, abundance that can be related to the stainless steel composition. Si displayed a concentration of 123.9 ppb. Interestingly, Cr was not detected (it probably sorbed on steel degradation products as chromate) and Cu (31.14ppb) and especially Mo (0.35 ppb, it also likely sorbed as molybdate) are low. Co and Zn are in the 10-20 ppb range but not listed in the composition of the steel as opposed to V and Ti which show very low aqueous concentration values at 0.15 and 0.35 ppb, respectively. The NaCl salt used to make the synthetic brine does not increase the concentration of any element but Na and Cl, except maybe B (32.57 ppb) which could also come from the steel.

Table 5. trace element aqueous concentration in blank runs.

B	Mg	Al	Si	P	K	Ca	Ti	V	Cr	Mn
(ppb)	(ppb)	(ppb)	(ppb)	(ppb)	(ppb)	(ppb)	(ppb)	(ppb)	(ppb)	(ppb)
32.57	18.13	2.68	123.90	7.23	27.11	no data	0.15	0.35	0.02	130.70
Fe	**Co**	**Ni**	**Cu**	**Zn**	**As**	**Se**	**Rb**	**Sr**	**Zr**	**Mo**
(ppb)	(ppb)	(ppb)	(ppb)	(ppb)	(ppb)	(ppb)	(ppb)	(ppb)	(ppb)	(ppb)
436.40	16.73	409.50	31.14	10.21	0.02	0.00	0.02	1.31	0.01	0.35
Ag	**Cd**	**Sn**	**Sb**	**Cs**	**Ba**	**Tl**	**Pb**	**Bi**	**Th**	**U**
(ppb)	(ppb)	(ppb)	(ppb)	(ppb)	(ppb)	(ppb)	(ppb)	(ppb)	(ppb)	(ppb)
0.12	-0.01	-0.01	0.00	0.00	1.04	-0.01	0.03	1.31	-0.01	-0.01

Note: values in blue cells are below detection limits

In the first O_2 experiment (C-series with a Miocene sample), no liner was used to protect the steel of the reactor walls and various fittings against the corrosive action of O_2. The chemical analysis was contaminated with metals present in the steel, and may have impacted the overall reaction progress by quickly consuming O_2 and covering the reactive surface areas with FeOx deposits.

II-3-2 Chemical Analyses

The reaction fluid brine was incrementally sampled during the sample run by purging approximately 3 ml of fluid through a capillary tube controlled by a valve to remove fluid that was isolated from the water rock reactions in the sample tubing. The purged fluid was set aside and used for an alkalinity titration. After the purge, approximately 1 ml of brine was collected in a pre-weighed glass vial and immediately acidified with 40 µl of 16N HNO_3 for major and trace elemental analyses.

Ion chromatography is used to determine concentrations of major cations and anions (two Dionex ICS-1100 devices). Inductively-coupled plasma mass spectrometry (ICP-MS, Agilent 7500ce model) is used to determine major and minor cation concentrations, including silica and aluminum. The solution purged before sampling was analyzed for alkalinity. A gas chromatograph is used for gas samples to determine contaminant gas composition.

Initial brine concentrations were determined by mixing measured aliquots of NaCl salts, NaBr salts and deionized water. Na and Cl concentrations were largely outside analytical calibration on the IC and the ICP-MS. In many experiments Na and Cl concentrations were higher than the calibration range. It was assumed that the Na and Cl concentrations were 43,221 ppm and 66,646

ppm, respectively (all experiments but one were conducted using a 1.88 Mol/L NaCl brine solution). It follows that increases in Na concentration from dissolution of Na-rich minerals, such as albite, is not directly measurable because the potential increase in Na concentrations in the reaction fluid is lower that the analytical error associated with analysis. Wet chemical procedures were used to determine initial Na and Cl compositions and the samples diluted until the calibrated range was reached for the other elements. Each sample vial used in IC and ICP-MS analysis is weighed empty, with sample and again after acidification with nitric acid so that acid dilution can be calculated. A calibrated Orion pH meter was used to determine pH values of the brine during sampling. It was determined that rapid CO_2 degassing associated with the decrease in pressure during sampling significantly altered the pH of the reaction fluid. Geochemical modeling suggests the pH was increased by ~2 units so measured pH is of dubious value and often not measured. A Hach digital titrator using 0.1600 M H_2SO_4 cartridge and a Orion pH meter was used to measure alkalinity. Because of the small volumes of brine used, 2-3 ml of reacted brine were diluted to ~40 ml using de-ionized water and the alkalinity was determined using the inflection point method calculated on the USGS alkalinity calculator (http://or.water.usgs.gov/alk/). Headspace gas concentrations to determine O_2 levels were performed with a gas chromatograph (GC). No isotopic analyses were performed.

The reacted brine was diluted with DI water and Major cations and anions were analyzed on two Dionex ICS-1100 Ion Chromatography systems, one for anions and one for cations, equipped with an ASAP auto-sampler at the University of Texas at Austin. Samples were initially diluted with DI water so Na and Cl concentration were less than 1000 ppm but these elements remain outside calibration range. Trace elements were analyzed on an Agilent 7500ce Quadropole inductively-coupled-plasma-mass-spectrometer (ICP-MS) at the University of Texas at Austin. Samples for trace metals were diluted with 2% HNO_3 so that the Na and Cl concentrations were close to 500 ppm.

Table 6. Summary of runs.

		70°C	100°C	130°C
Offshore Miocene	CO_2	√ **D**	√ **L (B)**	√ **H**
	$CO_2 + O_2$	√ **R**	√ **S**	**4**
Cardium Sands	CO_2	√ **K**	√ **J**	
	$CO_2 + O_2$	√ **N**	**3**	
Cranfield	CO_2	√ **P**	**2**	**6**
	$CO_2 + O_2$	√ **O**	**1**	**5**
Red River (dolomite)	CO_2			
	$CO_2 + O_2$			

Note: letters represent experiment series (see Section III-1); numbers represent the order in which the additional experiments will be performed

II-4. Map of the Experimental Study

Table 6 summarizes the various CO_2 and CO_2+O_2 experiments performed and the ones to be performed in the near future in a companion project. The matrix table shows that a total of 10 experiments were performed on three types of samples: five experiments at 70°C, three at 100°C, and one experiment at 130°C. Offshore Miocene samples underwent a total of five experiments, Cardium sands a total of three experiments, and Cranfield underwent two experiments. A total of

six experiments were performed with CO_2 only whereas four experiments had a mixture of O_2 and CO_2. The amount of O_2 added was done on a pressure basis either 100 or 200 psi (6.9 or 13.8 bars) of O_2 versus 200 bars of CO_2 translating to ~3.5% or 7.0% O_2. Only Offshore Miocene samples with pure CO_2 have been treated at three different temperatures. Note that several experiments were done more than once and that parameters not shown here (salinity, pressure) were also evaluated.

II-5. Literature Search

We compiled peer-reviewed publications related to reactive transport in the deep subsurface (there are more for the shallow aquifers that are not directly applicable) and started extracting the relevant information. About 30 are related to acid gas injection (CO_2 or more frequently CO_2 and H_2S). Appendix C presents a summary of the review.

II-6. Kinetics

We performed the same experiment at three different temperatures regardless of the reservoir conditions corresponding to the sample being treated: 70°C, 100°C, or 130°C. We could have performed the same experiments at a slightly lower range (50 ºC, 75 ºC and 100 ºC) but decided against it. The higher the temperature, the faster the kinetics and even if many potential reservoirs have temperatures <100 ºC, it is not uncommon to have temperatures >100 ºC, for example at Cranfield, MS (Hosseini et al., 2013). We need the reaction rates to be fast enough (which translates into higher temperature) to be able to observe changes that can then be extrapolated to lower temperatures. However, this can be done only if we take steps to ensure that the reaction mechanisms are the same at both sets of temperatures. The key is to understand the main controlling reactions / species. Note that experiments were not designed to derive thermodynamic equilibrium data at elevated pressure and high temperature. It is true that such data is often lacking but it is a much larger endeavor that we are concerned with in this project. In addition, we are not dealing with a single reaction with one homogeneous mineral of well-constrained mineralogical composition. Consequently we used the term of *release rate* rather than *reaction rate*. We reserve the use of *reaction rate* for specific individual reactions.

Because the experiments deal with actual rock with multiple minerals, it is not possible to extract specific kinetics information although it can be pointed out that one reaction is likely to dominate the system (carbonate dissolution or pyrite dissolution). It is, however, possible to rank and compare experiments. To be able to compare experiments, we need to scale the aqueous concentrations by (1) the rock/water ratio, and (2) CO_2 partial pressure. The ratios vary within a small range and are unlikely to have a large impact on the concentrations. They need to be scaled, though, for consistency of the results. Presence of O_2 decreases CO_2 partial pressure by a non-negligible amount. The partial pressure correction is linear in agreement with the kinetics law of calcite dissolution with an exponent n=1 (Palandri and Kharaka, 2004, p.42). This approach is only approximate as different samples were used for each experiment. A necessary complement to the analysis presented in this document would be to perform three identical runs of each experiment with different samples but from the same source. It would provide an assessment of the variability between rock samples and increase confidence in the conclusions presented later. Two experiments were performed in somewhat similar conditions (L and B series, Miocene, pure CO_2, 100°C) and their results suggest that there is no large difference between samples from the same location and same core interval.

Overall release rates were calculated for the batch experiments similar to the method outlined in Matter et al. (2007). In the batch experiment, the chemical composition of the reaction fluid before the introduction of super-critical CO_2 were considered the initial elemental concentrations. The overall release rate was calculated for every time step after the start of the experiment by:

$$R=M_r/(V\times t)$$

where, R is the overall release rate or release rate (mmol/L/hr), M_r is the change in elemental concentration in the water rock experiment at time t (mmol), V is the volume of the solution (L) and t is the reaction time from start (hr). Overall release rates were then normalized to sample size rather than mineral surface area because reactive mineral surface area was unknown. Positive release rates indicate the element was added to solution by mineral dissolution, ion exchange reactions or desorption reactions. Negative release rates indicate the element was removed from solution by precipitation, ion exchange or sorption reactions. The units the release rate are expressed in mmol/L/hr/g. Ions Li^+, NH_4^+, F^-, NO_2^-, NO_3^-, PO_4^{-3} where below detection limits of the IC and were not considered in the release rate calculations. Rates were to be compared in two ways: (1) with increasing temperature, and (2) with and without O_2.

II-7. Batch and Reactive Transport Modeling

Model tools for simulating 3-D multiphase-flow transport of CO_2, O_2, and other gas components and brine in deep geological storage formations and complex interactions among rocks, brine and gases are not currently readily available in the public domain and require some code modifications (see Section VII-4 in Appendix B for list of codes and assessment). We decided to use PHREEQC for the simulations, other choices were Geochemist Workbench, Toughreact, Fast, and CMG GEM-GHT. The popular USGS-developed PHREEQC software (Parkhurst and Appelo, 1999) is based on an ion-association aqueous model and has capabilities for (1) speciation and saturation-index calculations; (2) batch-reaction and one-dimensional (1D) transport calculations involving reversible reactions, which include aqueous, mineral, gas, solid-solution, surface-complexation, and ion-exchange equilibria, and irreversible reactions, which include specified mole transfers of reactants, kinetically controlled reactions, mixing of solutions, and temperature changes; and (3) inverse modeling, which finds sets of mineral and gas mole transfers that account for differences in composition between waters, within specified compositional uncertainty limits. PHREEQC has been used to perform a wide variety of low-temperature aqueous geochemical calculations. In addition, it has been used to simulate water-rock-CO_2 interactions under high pressure and high temperature conditions (Berger et al., 2009; Heeschen et al., 2011; Jacquemet et al., 2009; Koenen et al., 2011; Soong et al., 2004; Strazisar et al., 2006; Tarkowski and Uliasz-Misiak, 2007; Xie et al., 2006) as long as an appropriate thermodynamic database is used.

In this study, batch and reactive transport models are based on the integrated LLNL thermodynamic database, ‘‘thermo.com.V8.R6.230’’ (Johnson et al., 2000). The reaction constants compiled in this database can be applied to temperatures ranging from 0°C to 300°C. However, PHREEQC simulates gas phases as ideal gases. This may lead to significant errors if total pressures of the gas phase measured in the batch experiments are directly used in PHREEQC. So in this study, we used WINPROP to calculate fugacity of CO_2 and O_2 under reservoir conditions and then fugacity was used as partial pressures of CO_2 and O_2 in

PHREEQC. WINPROP is CMG's equation of state multiphase equilibrium property package featuring fluid characterization, lumping of components, matching of laboratory data through regression, simulation of multiple contact processes, phase diagram construction, solids precipitation, and more (CMG, 2011). High salinity requires the use of the Pitzer formalism or at least of the SIT formalism. Pitzer formalism is available in PHREEQC but with a reduced set of minerals. The approach we took was to assume activity coefficients obtained through the extended Debye-Huckel formula were more or less appropriate. This formula tends to overestimate activity of ions (especially multi-charged ions) in a brine and impact the surface area computed by calibrating model with observations (see below). See Allen et al. (2005) for a discussion of these issues.

The geochemical models consider several primary and secondary minerals. Mineral dissolution and precipitation were simulated with kinetic theory and kinetics rates for individual minerals are extracted from Palandri and Kharaka (2004) (Table 7). Remember that we can model only the overall reaction progress:

$$\frac{dm}{dt} = -SA\left[\begin{array}{l} k_{acid}^{298.15K} e^{\frac{-E_{acid}}{R}\left(\frac{1}{T}-\frac{1}{298.15K}\right)} a_{H^+}^{n_1}(1-\Omega^{p_1})^{q_1} \\ +k_{neutral}^{298.15K} e^{\frac{-E_{neut}}{R}\left(\frac{1}{T}-\frac{1}{298.15K}\right)}(1-\Omega^{p_2})^{q_2} \\ +k_{base}^{298.15K} e^{\frac{-E_{base}}{R}\left(\frac{1}{T}-\frac{1}{298.15K}\right)} a_{H^+}^{n_3}(1-\Omega^{p_3})^{q_3} \end{array}\right]$$

where SA is reactive surface area, $k_{acid}^{298.15}$, $k_{neutral}^{298.15}$, $k_{base}^{298.15}$ are rate constants for acid, neutral and base conditions at temperature, 298.15 K, E_{acid}, $E_{neutral}$, E_{base} are activation energies (J mol^{-1}), T is the temperature (K), R is the gas constant, Ω is mineral saturation index, p and q are empirical and dimensionless parameters, a_{H+} is activity of H^+ in water and n is a parameter estimated from experiments. It can be seen that a mineral reaction rate is assumed to include three general mechanisms.

Table 7. Parameters for calculating kinetic rate constants of minerals

Mineral	Neutral mechanism		Acid mechanism			Base mechanism		
	k (mol/m^2/s)	E(kj/mol)	k (mol/m^2/s)	E(kj/mol)	n_1	k (mol/m^2/s)	E(kj/mol)	n_3
Primary								
Quartz	1.023×10^{-14}	87.7						
Kaolinite	6.918×10^{-14}	22.2	4.898×10^{-14}	65.9	0.777	8.913×10^{-18}	17.9	-0.472
Calcite	1.549×10^{-6}	23.5	5.012×10^{-1}	14.4	1.0			
Illite	1.660×10^{-13}	35	1.047×10^{-11}	23.6	0.34	3.020×10^{-17}	58.9	-0.4
K-feldspar	3.890×10^{-13}	38	8.710×10^{-11}	51.7	0.5	6.310×10^{-22}	94.1	-0.823
Albite	2.754×10^{-13}	69.8	6.918×10^{-11}	65.0	0.457	2.512×10^{-16}	71	-0.572
Secondary								
Magnesite	4.571×10^{-10}	23.5	4.169×10^{-7}	14.4	1.0			
Siderite	1.260×10^{-9}	62.76	1.590×10^{-4}	45.0	0.9			
Ankerite	1.260×10^{-9}	62.76	1.590×10^{-4}	45.0	0.9			
Dawnsonite	1.260×10^{-9}	62.76	1.590×10^{-4}	45.0	0.9			
Ca-smectite	1.660×10^{-13}	35	1.047×10^{-11}	23.6	0.34	3.020×10^{-17}	58.9	-0.4

Note: all rate constants are listed for dissolution

The trial and error method was used to calibrate reactive surface area of minerals for each batch experiment by fitting concentrations of major ions. The input file of PHREEQC model for the A series is given in Appendix A.

Reactive Transport Model

The reactive transport model used all the information presented earlier in this section as well as site specific information. The model is based on the Cardium Sands of Alberta, and in particular, on their characteristics in the vicinity of the Pembina oil field (from where the cores used in the autoclave experiments originated). It is an mature filed with production dating back from the 1930's and, as such, has been subject of many publications. We extracted the needed information from the following papers: Hodgson and Baker (1959), Melrose et al. (1976), Michael and Bachu (2001), and Dashtgard et al. (2008). The reservoir depth is approximately 1600m (~5230 ft) at a pressure of ~2400 psi and temperature of 60°C. Porosity of the formation is ~16%. Permeability is relatively low and in the 10-30 md range. Cardium Sands resident water is relatively fresh at ~10,000 ppm and dominated by Na, Cl, and bicarbonate ions.

III. Results

III-1. Autoclave Experiments

A total of 19 runs were performed in the autoclave, some of them unsuccessful (Table 8).

Table 8. List of autoclave runs.

Experiment	Temperature (°C)	Pressure (bars)	Fluid	Sample Origin	Sample weight (g)	Brine volume (ml)	Comments
A	100	200	DI	Miocene			0% O_2
B	100	200	1.88 mol/kg NaCl sol.	Miocene			0% O_2, maybe leakage, rerun as series L
C	100	200	1.88 mol/kg NaCl sol.	Miocene			1.4% O_2 gas added at beginning of experiment, corrosion of reactor steel
D	70	200	1.88 mol/kg NaCl sol.	Miocene	6.65	155	0% O2
E	100	300	1.88 mol/kg NaCl sol.	Miocene			0% O_2
F	150	200	1.88 mol/kg NaCl sol.	Miocene			failed after 9 samples,
G	135	200	1.88 mol/kg NaCl sol.	Miocene			failed after 3 samples
H	130	200	1.88 mol/kg NaCl sol.	Miocene	6.43	140	0% O2
I	70	200	1.88 mol/kg NaCl sol.	Cardium			problems with this run, duplicated in series K
J	100	200	1.88 mol/kg NaCl sol.	Cardium	8.45	140	0% O2
K	70	200	1.88 mol/kg NaCl sol.	Cardium	8.03	140	0% O2
L	100	200	1.88 mol/kg NaCl sol.	Miocene	7.26	140	0% O_2, re-run of series B
M	70	200	1.88 mol/kg NaCl sol.	Cardium			3.5% O_2, failed after 48 hours, duplicated in series N
N	70	200	1.88 mol/kg NaCl sol.	Cardium	10.39	110	3.5% O_2
O	70	200	1.88 mol/kg NaCl sol.	Cranfield	8.11	110	3.5% O_2
P	70	200	1.88 mol/kg NaCl sol.	Cranfield	8.44	110	0% O_2
Q	70	200	1.88 mol/kg NaCl sol.	Miocene			3.5% O_2, failed after 24 hours
R	70	200	1.88 mol/kg NaCl sol.	Miocene	8.40	110	7% O_2 (200 psi)
S	100	200	1.88 mol/kg NaCl sol.	Miocene	8.89	110	3.5% O_2 (100 psi)

Note: Shaded rows represent experiments fully discussed in the document.

The following sections present results of experiments for the three locations one at a time. For each, we follow the same outline. First, we describe the unreacted sample, in general the first sample at that location to be reacted with pure CO_2 or the mixture. Next, we describe experimental results of rock samples exposed to pure CO_2, followed by results of the exposure to the CO_2-O_2 mixture, both focused on the reacted sample. We conclude by doing an analysis of the chemical analyses time series and discussing kinetics aspects.

To understand kinetics of interaction among brine- CO_2-O_2-rocks, we need to look at major ions (Ca, K, Mg; Na results are obscured by the NaCl brine) but also at Al and Si of water samples. Ca and Mg concentration trends illuminate carbonate dissolution whereas Al and Si concentrations are important to quantify kinetics of silicate mineral reactions. K and Na cannot provide enough information to quantify the kinetics of silicate mineral dissolutions. Alkalinity and sulfate complement the analysis; Fe is also a relevant indicator of the system behavior. Trace elements have in general two origins: they are (1) contained in minute amounts in major minerals (such as Sr in calcite or Cs in K-feldspar) in which case their concentrations will trend similarly to that of the major elements or (2) mobilized from sorbing material such as FeOx grain coatings or clay mineral edges (kaolinite and illite). Addition or destruction of sorbing material can complicate the interpretation of trace element behavior. Ion exchange is unlikely to play a major role because the samples as a whole have little exchangeable capacity (a few percent illite that could be mixed-layered) or no capacity in the more common chlorite and kaolinite. A last point impacting the concentration of trace metal is their ability to be complexed by chloride (for example, $CdCl^{\circ}$) or carbonate.

III-1-1 Offshore Miocene

III-1-1.1 Description of Unreacted Sample (Miocene)

The rock samples used in the reaction experiment are from the Lower Miocene of the offshore Texas continental shelf near Matagorda Island. Mineralogy of the unreacted sample is shown in Table 9. The sample is a very fine-grained sandstone with 22% porosity. It contains ~12% calcite. Thin section examination shows that the majority of the calcite exists in the form of fossils (mostly foraminifera), and that calcite cementation is sporadic. Mineral dissolution (e.g., mostly feldspar dissolution) is evident in the unreacted sample and enhances porosity (Figure 2A). Both plagioclase (albite) and K-feldspar exhibit some dissolution (Figure 2B). Carbonate cements usually show some smooth surfaces (Figure 2C and D). Figure 3A is an SEM energy dispersive spectrometry (EDS) image of the unreacted sample and Figure 3B is the EDS spectrum of the scanned area in Figure 3A.

Table 9. Offshore Miocene core sample composition (%)

Depth (ft)	Quartz	Kaolinite	Calcite	Illite	Albite	K-feldspar	Total
9205	43.5	6.2	11.8	5.0	18.4	15.2	100.0

Note: XRD mineralogical composition of core sample chosen for the reaction experiments; well OCS-G-3733 A-6, Matagorda Island, API: 427034015800

Figure 2. Unreacted offshore Miocene sample

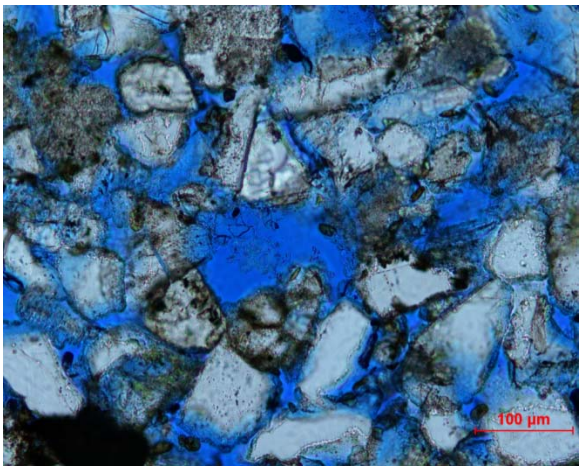

Figure 2A. Thin section image of unreacted sample. Oversized secondary pores derived from mineral dissolution. Porosity: 22.0%; permeability: 62.7 mD. 9205 ft, OCS-G-3733 A-6.

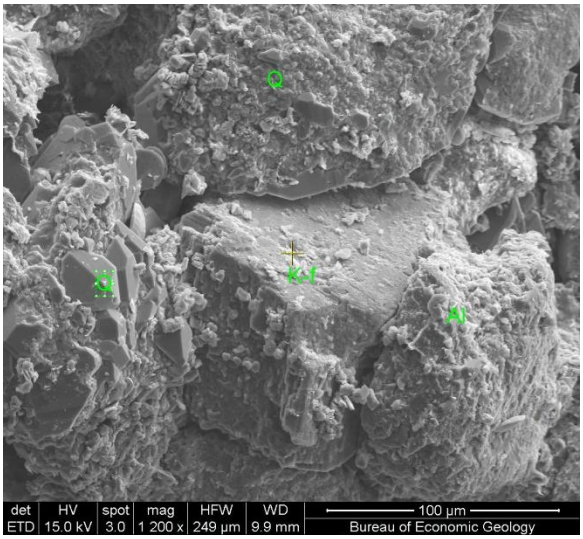

Figure 2B. SEM image of unreacted sample. Plagioclase (albite) (Al) and potassium feldspar (K-f) grains are usually blocky and sometimes show some corrosion features. 9205 ft, OCS-G-3733 A-6.

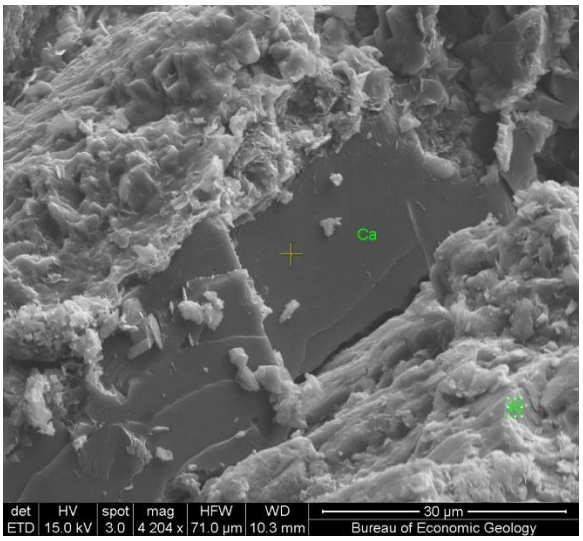

Figure 2C Unreacted sample. SEM image showing calcite cements with fresh-looking surface. 9205 ft, OCS-G-3733 A-6.

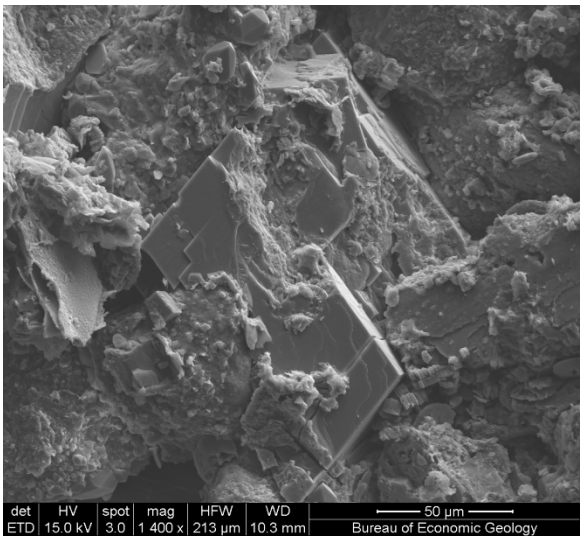

Figure 2D Unreacted sample. A rare rhombic dolomite crystal. 9205 ft, OCS-G-3733 A-6.

Figure 3. Unreacted offshore Miocene sample

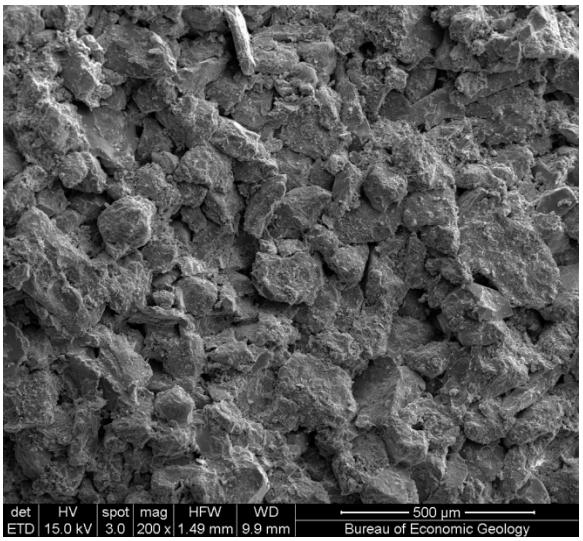

Figure 3A Full frame SEM energy dispersive spectrometry (EDS) scan area (1.48×1.28 cm) of unreacted sample. 9205 ft, OCS-G-3733 A-6.

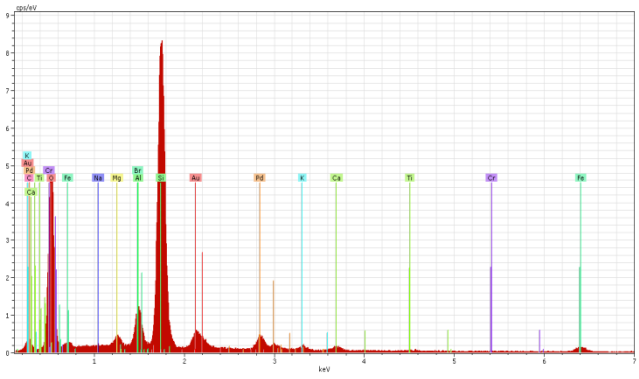

Figure 3B EDS spectrum of the scanned area in Figure 3A. Cation concentrations of the area: Ca, 5.0 %; Na, 1.4%; K, 1.3%; Mg, 0.7%; Fe, 6.3%; Ti, 0.7%.

III-1-1.2 Description of Sample Reacted with DI water and CO_2

XRD results show small differences between the original and reacted sample. The reacted sample shows decreases in calcite and K-feldspar abundances and increases in kaolinite and quartz. For all minerals except quartz, changes are less than 2%, within the range of instrument error. However, quartz abundance in the reacted sample is 5.6% higher than the unreacted sample. The reacted sample (A series) exhibits a brown-colored reaction surface approximately 1 mm thick. Beneath the brown reaction rim, the sample it is still greenish grey. At the reacted surface, K-feldspar and plagioclase (albite) grains display more dissolution features than the unreacted sample. Reacted feldspar crystals often shows fresh and sharp corrosion marks (Figure 4A and B). For example, Figure 4A shows that a K-feldspar grain was corroded from within and only a thin skin remains. Kaolinite can often be seen in the vicinity of corroded feldspar grains (Figure 4C). As Reactions 1 and 2 suggest, the kaolinite may be a reaction product of feldspar dissolution.

Reaction (1):

$2NaAlSi_3O_8$ (albite) + $2H^+$ + H_2O → $2Na^+$ + $Al_2Si_2O_5(OH)_4$ (kaolinite) + $4SiO_{2(aq)}$

Reaction (2):

$2KAlSi_3O_8$ (K-feldspar) + $2H^+$ + H_2O → $2K^+$ + $Al_2Si_2O_5(OH)_4$ (kaolinite) + $4SiO_{2(aq)}$

Figure 4. Offshore Miocene sample reacted with DI and CO_2

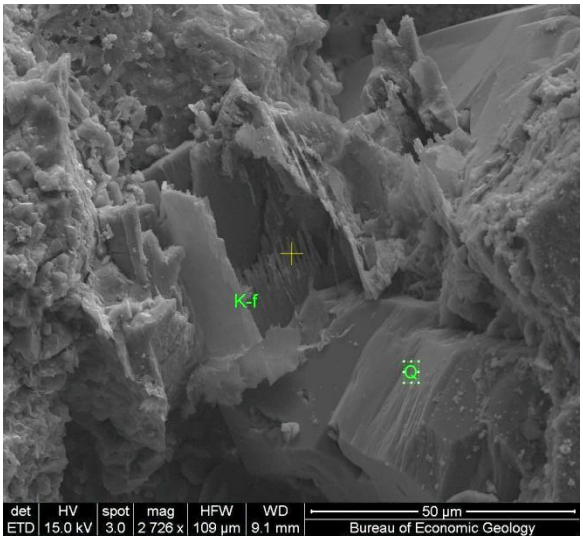

Figure 4A Sample surface reacted with DI water and CO_2. A severely corroded K-feldspar grain (K-f) . 9205 ft, OCS-G-3733 A-6.

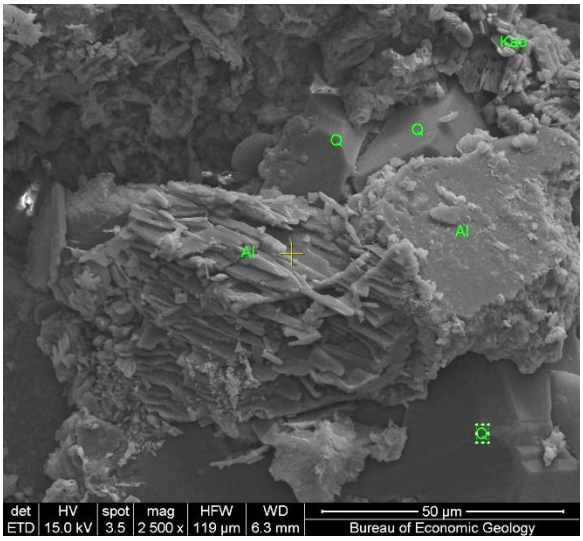

Figure 4B Sample surface reacted with DI water and CO_2. An albite grain (Al) showing severe partial dissolution possibly caused by CO_2 reactions. 9205 ft, OCS-G-3733 A-6.

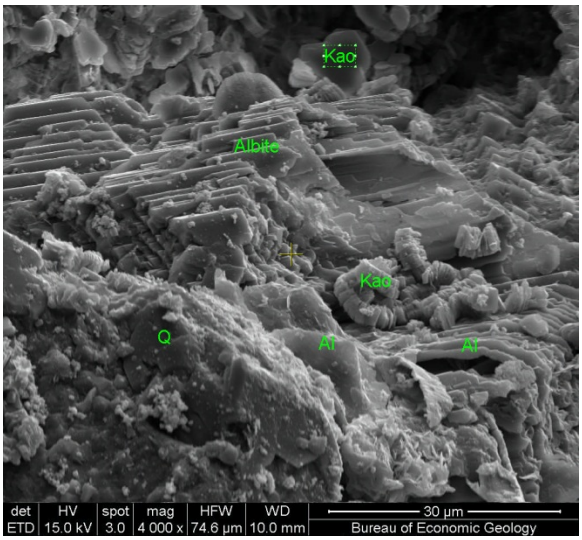

Figure 4C Sample surface reacted with DI water and CO_2 . Kaolinite booklets in the vicinity of corroded albite (Al) may be reaction products. 9205 ft, OCS-G-3733 A-6.

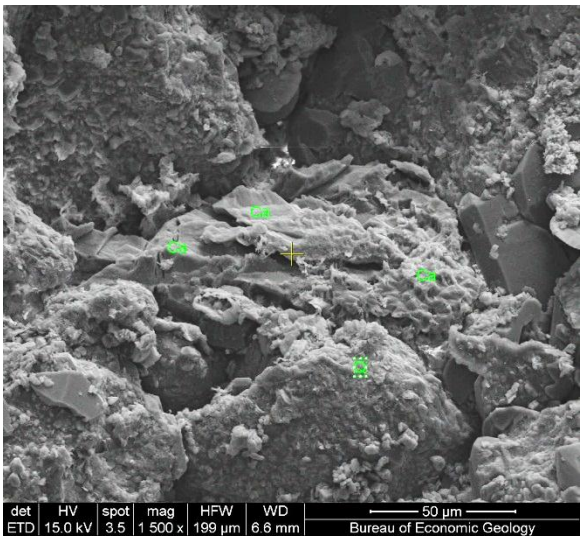

Figure 4D Sample surface reacted with DI water and CO_2 . Calcite (Ca) dissolution remaining. 9205 ft, OCS-G-3733 A-6.

Most calcite was dissolved at the reaction surface, and only a trace amount was visible (Figure 4D). Energy dispersive spectrometry (EDS) coupled with SEM was used to conduct a semi-quantitative chemical analysis on the sample surface. Areas of 1.48×1.28 cm were randomly chosen and scanned to derive average elemental concentrations. Examples are shown in Figure 3 and Figure 5. Comparisons between reacted and unreacted areas show relative changes of cation

concentrations. The Ca concentration decreased significantly from 4.7% to 1.1% (Table 10), strongly suggesting calcite dissolution. However, beneath the reacted surface, sample shows unchanged elemental concentrations with Ca content of 4.8%. Apparently, only the calcite at the sample surface was dissolved by acid solution and the solution quickly became saturated with calcite. Although calcite and CO_2 were both continuously available for reaction, the reaction stopped when the solution was saturated relative to calcite and equilibrium was attained.

Figure 5. Offshore Miocene sample reacted with DI and CO_2

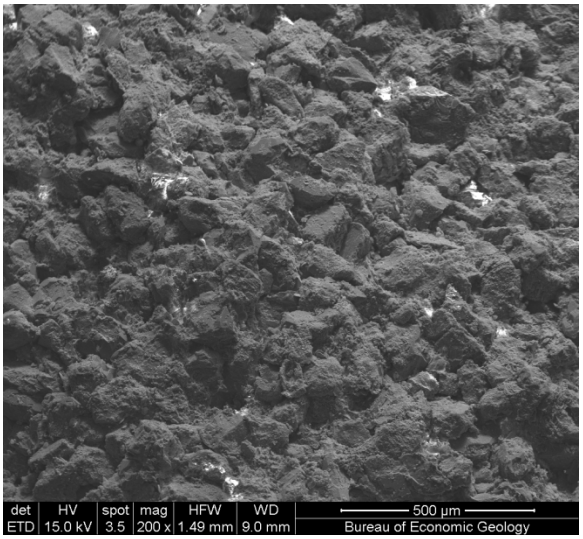

Figure 5A EDS scan area (1.48×1.28 cm) of reacted surface. 9205 ft, OCS-G-3733 A-6.

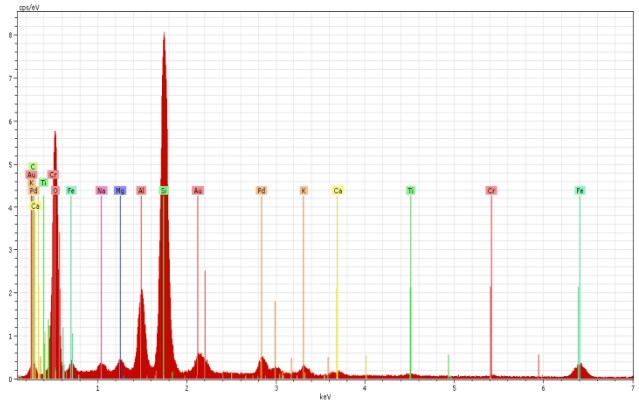

Figure 5B EDS spectrum of scan area in Figure 5A, showing lower Ca contents (Ca, 0.7%; Na, 1.0 %; K, 1.1%; Mg, 0.8%; Fe, 7.5%; Ti, 0.7), indicating dissolution of calcite.

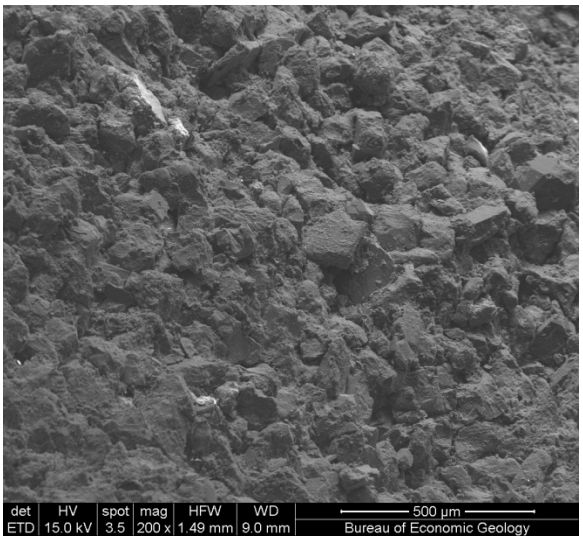

Figure 5C EDS scan (1.48×1.28 cm) inside of the reacted sample with deionized water and CO_2. 9205 ft, OCS-G-3733 A-6.

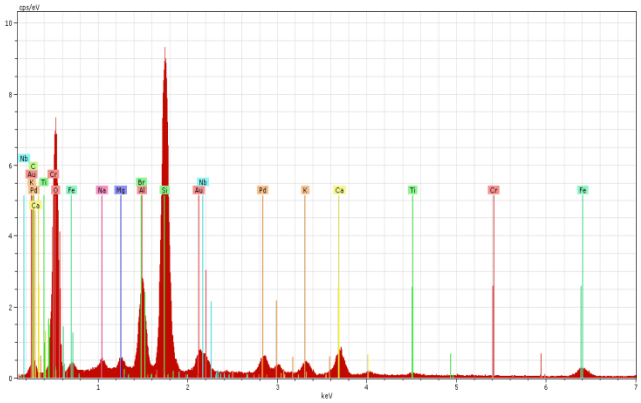

Figure 5D EDS spectrum of scan area inside of reacted sample (Figure 3C), showing similar chemical composition as unreacted sample (Fig. 2B): Ca, 4.8%; Na, 1.4%; K, 1.8%; Mg, 0.9%; Fe, 5.9%; Ti, 0.8%, indicating limited dissolution of calcite and feldspar.

Table 10. Chemical composition of Miocene (DI+CO_2, brine+CO_2/O_2) rock sample using SEM and EDS

	Ca %	Na %	K %	Mg %	Fe%	Ti %	Cr %
Unreacted sample							
1	4.2	1.2	1.7	0.6	5.8	0.7	
2	5.0	1.4	1.3	0.7	6.3	0.7	
3	4.9	1.2	1.4	0.6	6.3	0.8	
4	4.6	1.2	1.4	0.7	6.3	0.7	
Average	***4.7***	***1.2***	***1.4***	***0.7***	***6.2***	***0.7***	
Reacted with DI+CO_2							
Within sample (beneath reaction rim (DI+CO_2)							
1	4.8	1.4	1.8	0.9	5.9	0.8	
2	4.7	1.3	1.2	0.8	5.4	0.8	
Average	***4.8***	***1.4***	***1.5***	***0.8***	***5.7***	***0.8***	
Reacted surface (DI+CO_2)							
1	1.8	1.4	1.6		7.5	0.7	
2	0.8	1.0	1.3	0.8	7.1	0.7	0.8
3	0.7	1.0	1.1	0.8	7.5	0.7	0.6
Average	***1.1***	***1.1***	***1.3***	***0.8***	***7.4***	***0.7***	***0.7***
Reacted with brine+CO_2							
1	0.7	1.5	1.9	0.4	4.7		
2	0.5	1.2	1.9	0.3	5.6		
Average	***0.6***	***1.3***	***1.9***	***0.3***	***5.2***		
Reacted with brine+CO_2+O_2							
1	0.7	1.1	1.7	0.5	20.3	0.6	0.7
2	0.6	1.9	1.8	0.8	14.8	0.5	
Average	***0.7***	***1.5***	***1.7***	***0.7***	***17.5***	***0.6***	***0.7***

Note: Each result obtained from an EDS scan over an area of 1.48×1.28 cm^2

Water chemical analyses indicate that K concentration in solution increased from 2.6 to 7.5 ppm and Na from 24.3 to 44.7 ppm after CO_2 was introduced (Appendix F). Release of K and Na into solution is most likely sourced from feldspar. The observations of water chemistry match well with SEM imaging as dissolution features of feldspar minerals are pronounced in the images (Figure 4). However, the amount of dissolution is apparently below the detection of the EDS analysis because, as Table 10 shows, Na and K contents of the reacted rock surface remained at similar levels to the unreacted sample.

III-1-1.3 Description of Sample Reacted with brine and CO_2 (Miocene)

1.88 molal NaCl solution was used to replace deionized water in this experiment. Other conditions remained the same as the last experiment. Similarly to the DI sample, the reaction features are mostly apparent on the sample surface. K-feldspar and plagioclase were heavily leached and corroded (Figure 6A and B) compared to the original sample. However, it is difficult to completely separate the dissolution caused by CO_2 injection from what occurred during natural diagenesis and quantify it based only on SEM examination. Changes to water chemistry

(increases of Na and K concentration) are more sensitive and can be used to calculate the amount of dissolution.

Amount of calcite dissolution is higher in this experiment compared to the DI water case. Calcite minerals were almost consumed at the reacted surface (below the surface reaction rim calcite is still abundant). EDS scan results show that Ca content dropped from 4.7% to 0.6%. Clearly, more calcite was consumed in the brine experiment than in DI water experiment in which 1.1% Ca remained at the reacted surface. The SEM observation matches well with the water chemical analyses. Ca concentration in the brine reached 914 ppm at the end of the brine experiment compared to 544 ppm in the DI water run. Calcite solubility is higher in this brine than in the fresh water under the reaction conditions.

Figure 6. Offshore Miocene sample reacted with brine and CO_2

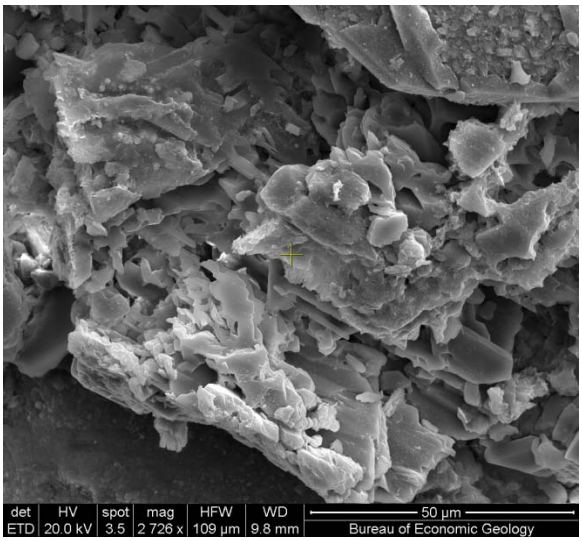

Figure 6A Sample surface reacted with brine and CO_2 . A strongly corroded plagioclase grain. 9205 ft, OCS-G-3733 A-6.

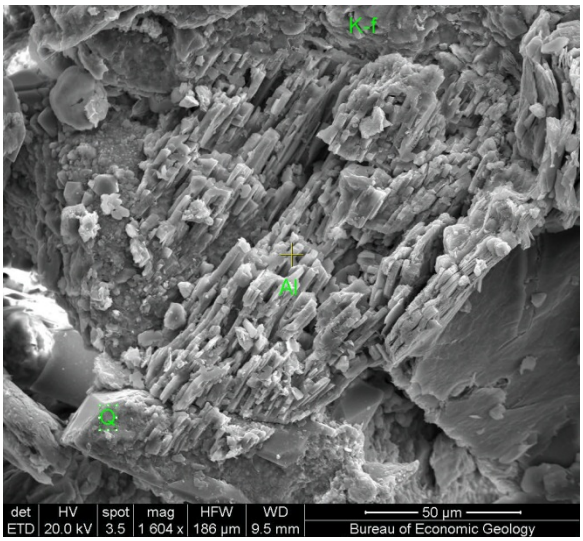

Figure 6B Reacted sample with brine and CO_2. A heavily leached albite grain with only the grain's skeleton left. 9205 ft, OCS-G-3733 A-6.

III-1-1.4 Description of Sample Reacted with Brine, CO_2 and O_2 (Miocene)

Early Tentative (failed) Experiment (Miocene)

In this experiment run, O_2 was added after helium stage into the reaction vessel for once at 2.8 bar (40 psi). Then CO_2 was pumped into the reaction vessel and pressure increased to and maintained at 200 bar to the end of the experiment. Therefore, at the beginning of the CO_2+O_2 stage, O_2 partial pressure was ~2.8 bar and O_2 content in gas phase ~1.4% (C series).

The reacted rock sample surface became dark brown at the end of reaction. SEM examination shows that dark brown color was caused by precipitation of iron oxides. Iron oxides formed at mineral surface and occur as little spheres of 500 nm (Figure 7A) and disks up to 30 micrometers (Figure 7B). They only occurred in the skin (approximately 1 mm thick) of the rock chip and were not found inside of the rock. Rare occurrence of iron oxides was also seen in the previous samples, but not nearly as much as in this sample. The high amount of iron oxides was clearly caused by the addition of O_2 to the reaction vessel. Iron was released from corrosion of steel tubes and joints of the inlets and outlets of the reaction system where most rust deposits were

formed, not the vessel itself which is made of different material and little corrosion was found on its walls (see Table 4 on reactor wall and other component composition).

Figure 7. Offshore Miocene sample reacted with brine, CO_2 and O_2

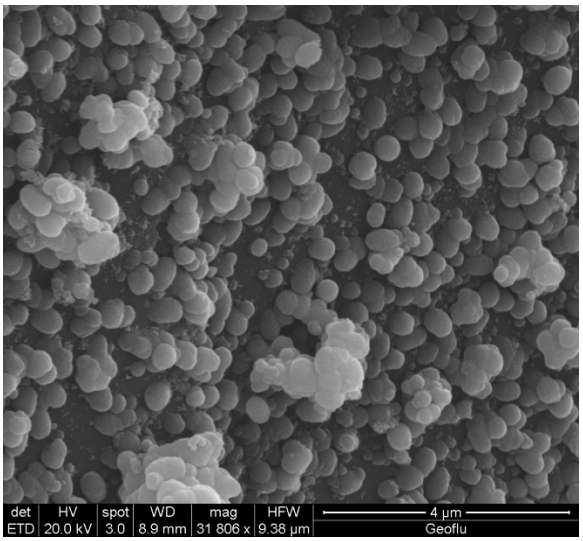

Figure 7A. Iron oxides spheres precipitated at quartz surface. Reacted sample with brine, CO_2 and O_2. 9205 ft, OCS-G-3733 A-6.

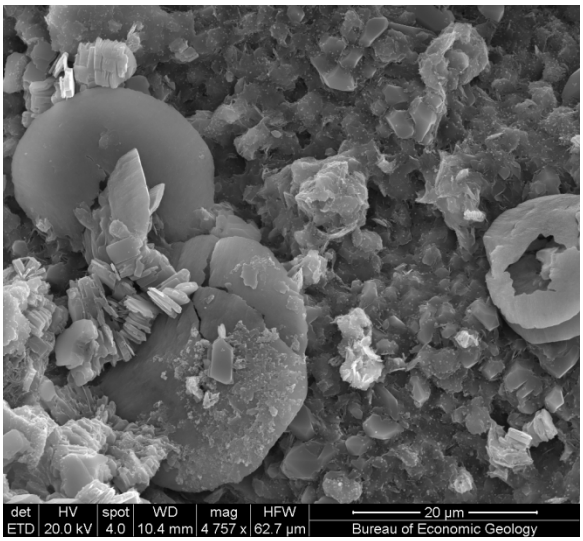

Figure 7B. Disk-like iron oxide crystals among kaolinite booklets. Reacted sample with brine, CO_2 and O_2. 9205 ft, OCS-G-3733 A-6.

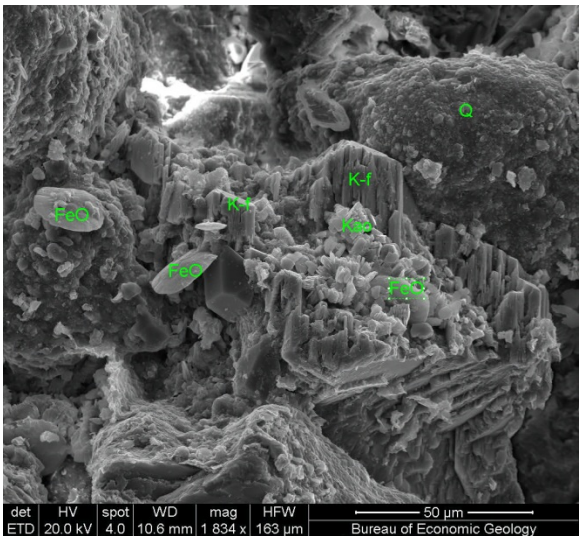

Figure 7C Potassium was strongly corroded. Kaolinite booklets often seen at the dissolution site. Iron oxide disks precipitated. Reacted sample with brine, CO_2 and O_2. 9205 ft, OCS-G-3733 A-6.

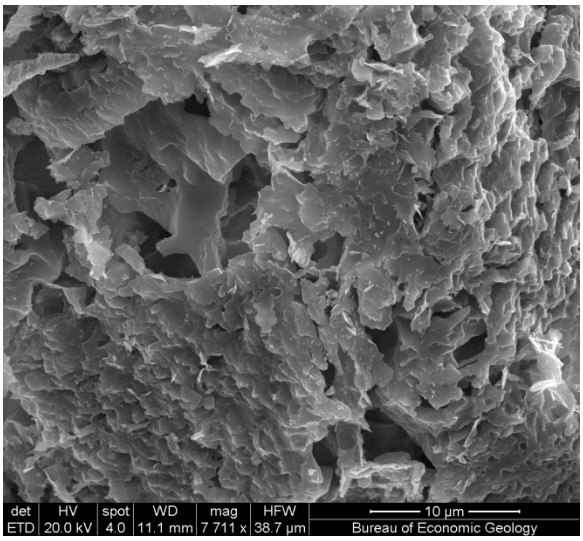

Figure 7D Rare remaining of corroded calcite showing severe leaching features. Reacted sample surface with brine, CO_2 and O_2. 9205 ft, OCS-G-3733 A-6.

Despite the corroded steel and similar to the previous reactions, feldspar and calcite minerals show strong dissolution features. Relics of K-feldspar and plagioclase are often seen at the reacted rock surface (Figure 7C). Kaolinite occurring as booklets habit can usually be seen in the vicinity of the dissolution site, suggesting the reaction of feldspar dissolution coupled with

kaolinite precipitation (Equation 1 and 2). Remaining calcite is rare and often shows leached surface littered with crystalline cavities (Figure 7D). EDS analyses show lower Ca (0.7%) and higher Fe (17.5%) contents than the unreacted sample (Ca, 4.7%; Fe, 6.2%). Compared with previous reacted samples, the presence of oxygen did not enhance reaction with the minerals. Except precipitation of iron oxides, which was mostly derived from reaction with stainless steel, no new reactions were observed on the rock sample. Water chemical results do not show significant difference from the non-O_2 runs. The lack of observed reducing minerals (such as pyrite) in this mineral assemblage is the likely reason for the muted effects from O_2 (pyrite remnants were, however, observed in a different sample).

Figure 8. Offshore Miocene sample reacted with brine, CO_2 and O_2

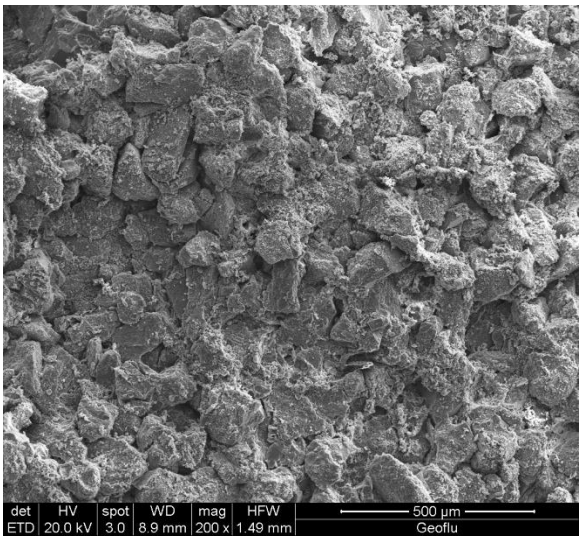

Figure 8A EDS scan (1.48×1.28 cm) inside of the reacted sample with brine, CO_2 and O_2. 9205 ft, OCS-G-3733 A-6.

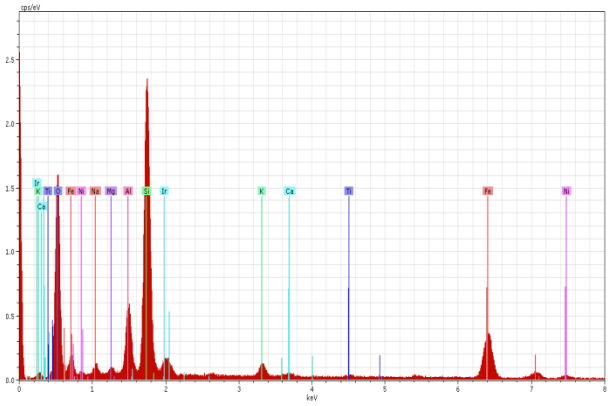

Figure 8B EDS spectrum of scan area of Figure 8A, showing low Ca and high iron contents: (Ca, 0.6%; Na, 1.9%; K, 1.8%; Mg, 0.8%; Fe, 14.8%; Ti, 0.5%).

Two-Temperature Comparison of Successful O_2 Runs (Miocene)

Two reacted rock samples from R series (70°C and 200 bar) and S series (100°C and 200 bar) experiments were examined using SEM aided with Energy Dispersive X-ray Spectroscopy. The reactions observed are not dissimilar to non-O_2 experiments, though it appears dissolution is more widespread in O_2 runs. Most common dissolution features observed are associated with K-feldspar and plagioclase (albite) grains. All K-feldspar and albite grains after reaction show severe corrosion features such as pits and steps (Figure 9A and B).

Carbonate minerals are rare in the reacted samples. The vast majority was dissolved. In fact, only one dolomite relic was observed in the two reacted samples. It shows severe destruction of the original mineral grain to a degree that it is no longer recognizable (Figure 9C).

Pyrite oxidation is the only new reaction observed in these O_2 experiments. Several rare pyrite framboids were found in the reacted samples and they appeared to be oxidized to various degrees. For example, the left pyrite framboid in Figure 10 is completely oxidized and show no signal of sulfur in the EDS element map (Figure 10B). Its original pyrite octahedral crystals were altered, though the shape of framboid remained. The center of the other pyrite framboid (to the right) was not completely oxidized and its chemical composition may remain unchanged (Figure

10B). At its edge, however, pyrite crystals appear to have been converted into iron oxides and sulfide is no longer detectable in EDS image.

Figure 9. Offshore Miocene sample reacted with brine, CO_2 and O_2

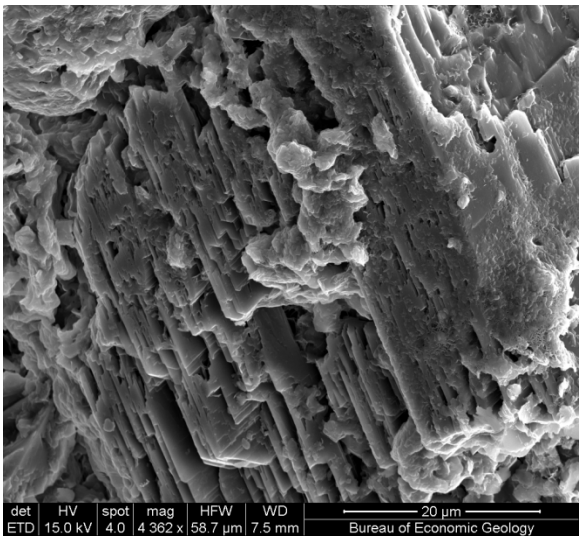

Figure 9A Reacted sample, 100ºC and 200 bar. SEM image showing a corroded K-feldspar grain.

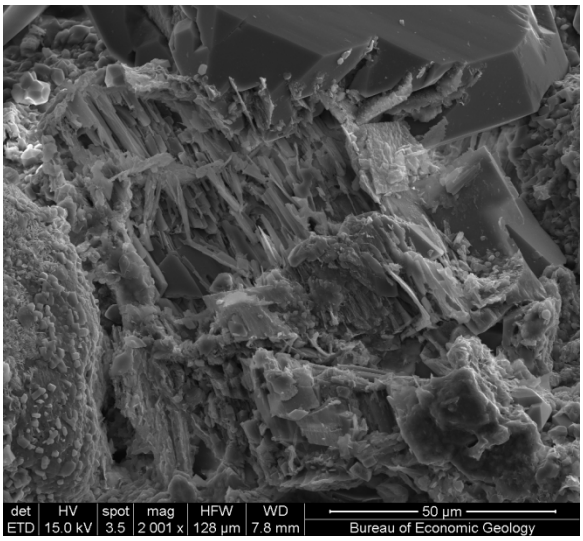

Figure 9B Reacted sample, 70ºC and 200 bar. A skeleton of albite grain from dissolution.

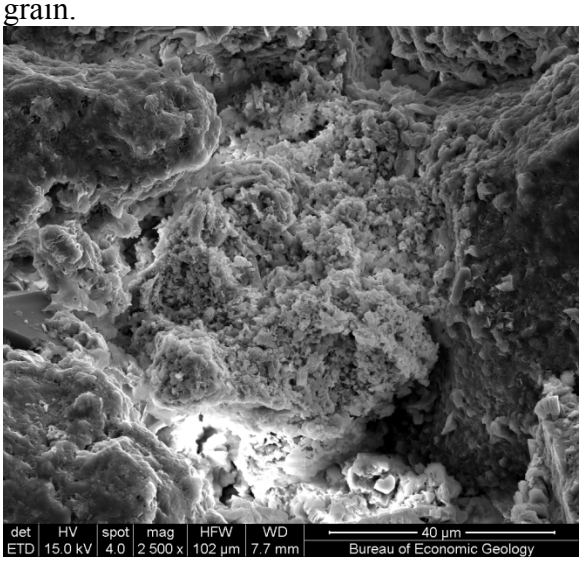

Figure 9C Reacted sample, 100ºC and 200 bar. Dissolution relic of a dolomite grain. EDS point scan shows presence of Ca and Mg.

Because very little pyrite is present in the original rock samples, the effect of pyrite oxidation is thought not to be important. Though the reacted samples show reddened surface, little iron oxides were observed on reacted mineral surfaces. Unlike the Lower Tuscaloosa sandstone at Cranfield which contains abundant iron-rich chlorite, and the Cardium ARC-PC-4B sample which contains more pyrite (both reacted samples show abundant iron oxides precipitated on mineral surface), the presence of O_2 did not significantly impact the Miocene samples. Evidence of dissolution and precipitation observed in these O_2 experiment are overall similar to the non-O_2

experiments, though it seems that dissolution of carbonate and feldspar minerals are more thorough (maybe impact of the rare pyrite?).

Figure 10. Offshore Miocene sample reacted with brine, CO_2 and O_2

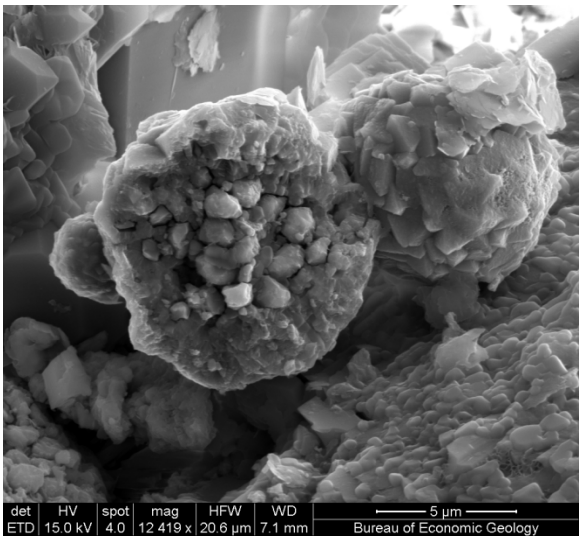

Figure 10A. Reacted sample, 100ºC and 200 bar. SEM image showing two altered pyrite framboids.

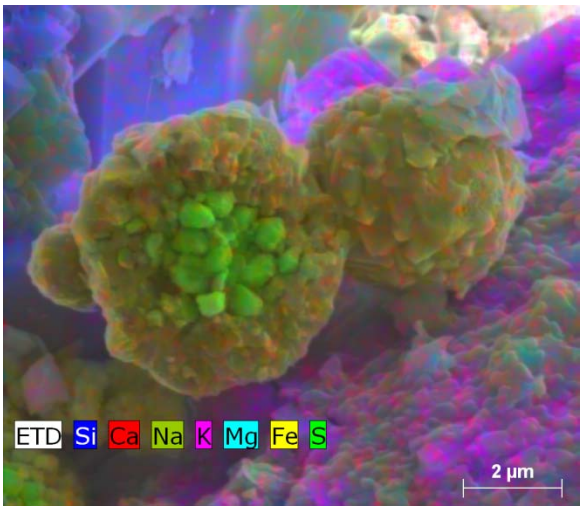

Figure 10B. Same view as Figure 10A overlain with EDS element map showing the center of the right pyrite still retains its iron sulfide composition, while the rest is converted to iron oxide.

Figure 11. Offshore Miocene sample reacted with brine, CO_2 and O_2

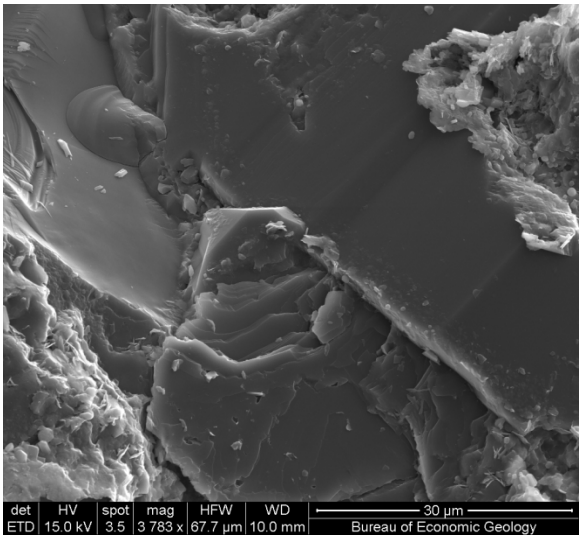

Figure 11A. Reacted sample, 70ºC and 200 bar. Quartz surface without notable iron oxide precipitates.

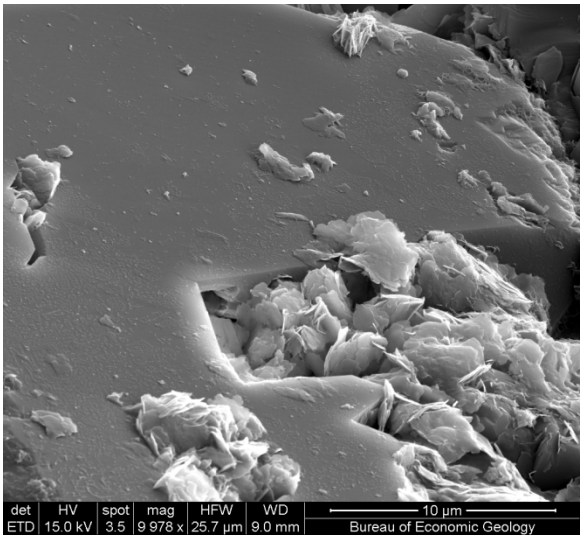

Figure 11B. Reacted sample, 100ºC and 200 bar. Quartz grain surface littered with some clay flakes, but no iron oxide was detected.

The calcite dissolution rate is dependent on temperature and partial CO_2 pressure, with more prominent control from temperature. In the temperature range of this study, calcite dissolution decreases with higher reaction temperature. The difference caused by pressure variations is much

smaller. In fact, calcite dissolution rates at 200 bar and 300 bar (L and E series runs) are similar. B series at 200 bar shows lower dissolution rates, but this experiment showed signs of leakage during the process and the results may be problematic.

Plagioclase (albite) dissolution rate is as high as K-feldspar; therefore, dissolution of plagioclase may also have occurred during the experiment as suggested by modeling results. The first reaction experiment (A series) using DI water showed that Na concentrations in water increased from 24 ppm to 54 ppm during CO_2 stage. The additional sodium indicates albite dissolution. In other experiments in which a 1.88 molar NaCl solutions was used, no notable Na increases were observed. The modest release of sodium from albite dissolution is overwhelmed by high Na background concentrations.

Kaolinite is a usual reaction product of feldspar dissolution as Equation 1 states. However, kaolinite XRD abundance in reaction sample is not higher; in fact it is lower than the original sample. XRD analysis of clay minerals usually has higher analytic errors because it is very difficult to achieve and control random orientation of clay minerals. Therefore, it is possible that small amount of kaolinite may have precipitated during the experiment, but XRD analysis is not sufficiently precise to detect its increase. Another possible explanation is that due to slow kinetic rate, kaolinite precipitation may be limited even if it is supersaturated in the solution.

III-1-1.5 Analysis of Time Series (Miocene)

III1.1.5.1 Presentation of Results (Miocene)

Pure CO_2 vs. Temperature (Miocene)

Most dissolution occurs within 24 hours, with asymptotic increase toward equilibrium over the next 10-12 days. Impact of temperature is displayed in Figure 12 to Figure 17. Part of the following discussion and most of the pure CO_2 plots are extracted from Lu et al. (2011). Element behavior is binned into three groups: (1) element/species concentrations increase with time (Figure 12); (2) no concentration trend is visible (Figure 13); and (3) element/species concentrations decrease with time (Figure 14). Carbonate dissolution controls Ca concentrations which are the highest in experiments with the lowest temperature (Figure 12A) because of higher calcite and CO_2 solubility values at lower temperatures. However the asymptotic value seems to be reached faster at 130°C suggesting faster reaction rates at higher temperatures. Mg concentrations are also likely controlled by carbonate dissolution (Figure 12B) and follow a similar pattern: lower plateau that is reached faster at higher temperature. Si and K concentrations (Figure 12C and D) are controlled by K-feldspar dissolution. The silicate dissolution reactions appear to be positively correlated with experimental temperature although K concentration timeline shows complications. Phosphate concentrations are positively correlated with reaction temperatures for most experiments but the correlation is weak and the abundances stay relatively low and constant (Figure 12E). Phosphate is likely sorbed on sorbing materials such as FeOx grain coatings and clay platelet edges; the alternative apatite corrosion is very unlikely. Mn concentrations are likely controlled by both carbonate and silicate weathering. Some source of Mn from silicates is likely because Mn shows a steady increase after Ca concentrations stabilize indicate carbonate dissolution has slowed (Figure 12F). Fe concentrations also increases with time with little difference with temperature but drop to zero at 130°C suggesting that the reactor was exposed to O_2 (Figure 12G). Ba concentrations show the same general behavior as Ca suggesting they are controlled by carbonate dissolution (Figure

12H). Contamination from drilling fluids is also a possibility albeit unlikely because rock fragments were selected from the center of the core. Sulfate concentration increase (Figure 12H2) is related to pyrite dissolution and oxidation. Rb, Sr, Co and Cs show a positive correlation with reaction time (Figure 12I, J, K, and L). Sr is likely controlled by carbonate dissolution and associated with Ca. Rb and Cs are typically sourced from K-feldspar. Co is likely associated with Fe but it does not show the quick drop at 130°C. Steady increase in elemental concentrations suggests a silicate source. Ni concentrations (Figure 12M) are positively correlated with reaction time, however it have been identified as a component of the stainless steel vessel but could also be controlled by water rock interactions as demonstrated by the L series results, an experiment performed relatively late in the project. Zn Figure 12N) increase with time and Pb increase in concentrations (Figure 12O) may be a result of water rock interactions. The source of Pb and Zn is currently unclear but likely K-feldspar. Another possibility for the release of metallic cations is the reductive dissolution of FeOx coatings triggered by the decrease in pH and bringing them further away from their thermodynamic stability region. Assuming that FeOx coatings do not dissolve, competition from carbonate for sorption sites would have the same effect of releasing the sorbed metals.

Some element concentrations show no clear trend with time and reaction progress, no correlation between reaction time and elemental abundance (Figure 13). With the exception of B (Figure 13A) these elements (Ti, U, Cu, Se, Zr, Cd, Sb, Bi, and V) generally have low concentrations that are not variable over the course of the run. U has concentrations close to the detection limit as indicated by the negative concentrations

Some elements show a negative correlation between reaction time and elemental abundance (Figure 14). Al, Cr, As and Mo all show the same general behavior. These elements are initially mobilized with the introduction of the super critical CO_2. However, these elements are not very soluble at low pH and their concentrations drop to near zero soon after the reaction starts. Al likely precipitate as clay and Cr, As, and Mo likely sorb onto Fe coatings found in the rock sample (and maybe the reaction vessel). Molybdate and arsenate/arsenite sorb more strongly to FeOx as pH decreases.

The reaction temperature had a significant effect on calcite solubility. Experiment D was run at 70^0C, B and L were run at 100^0C, and H was run at 130^0C. The experiment run at the lowest temperature shows the highest calcite solubility and possibly calcite dissolution rates. The experiment run at the highest temperature shows the lowest calcite solubility and possibly calcite dissolution rates (Figure 13a). The calcite solubility is likely controlled by CO_2 solubility which is higher at lower temperatures. The higher CO_2 solubility lowers pH which results in higher calcite solubility.

There were significant differences between the reactions with NaCl brine and DI water, which contained roughly half the Ca concentration at equilibrium. The NaCl brine reactions were very similar in terms of kinetics and equilibrium concentrations with respect to Ca. For all of the reactions, most of the dissolution was complete after 24 hours, with an asymptotic increase toward equilibrium over the next 10-12 days. The calcium concentration in the water was ~65% of that in brine, suggesting that more calcite dissolves in brine than in water.

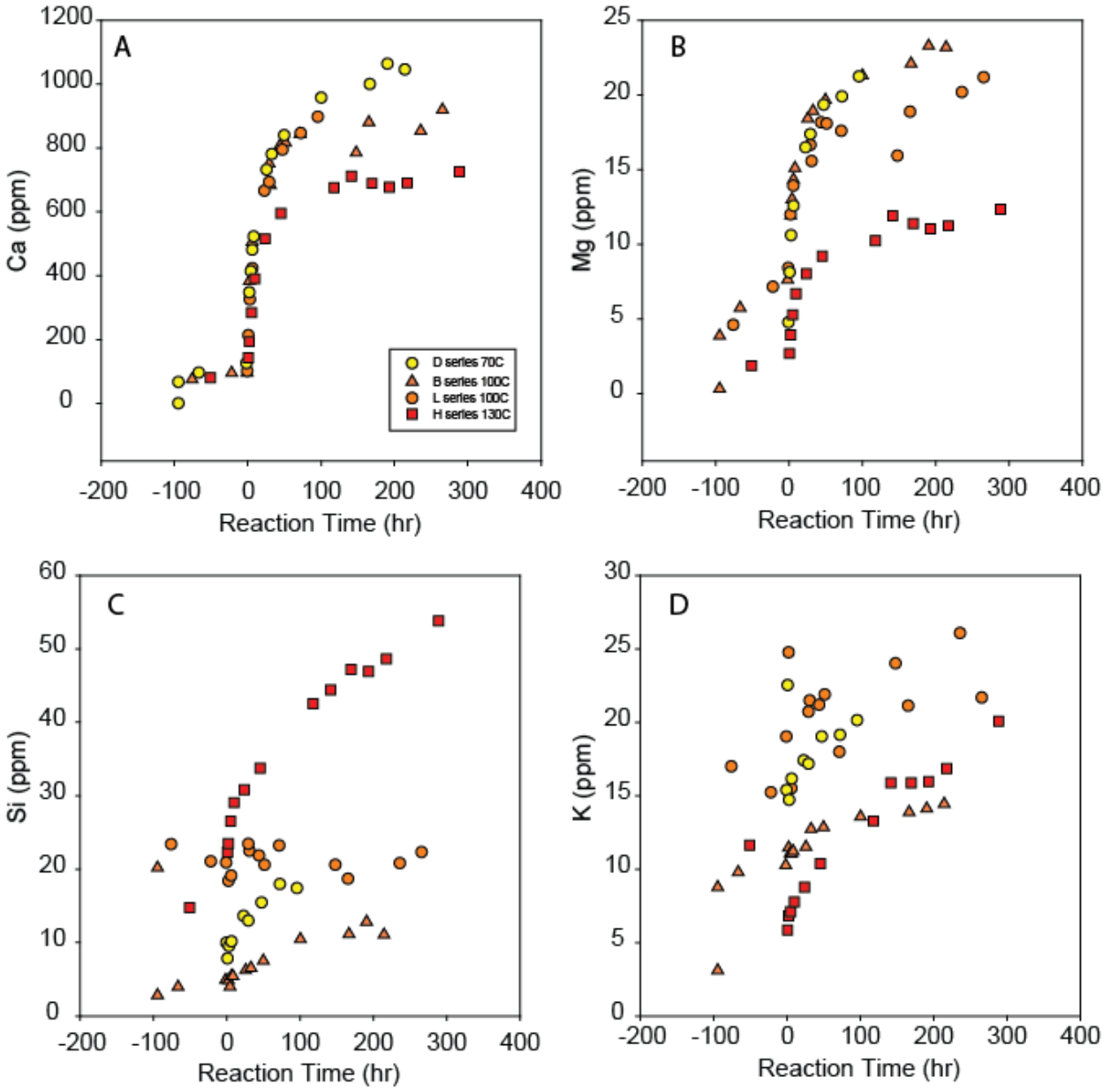

Figure 12. Impact of temperature variation on reaction progress (Miocene), D series (70°C), B and L series (100°C), and H series (130°C) (all at 200 bars with pure CO_2) – Species showing increase with time

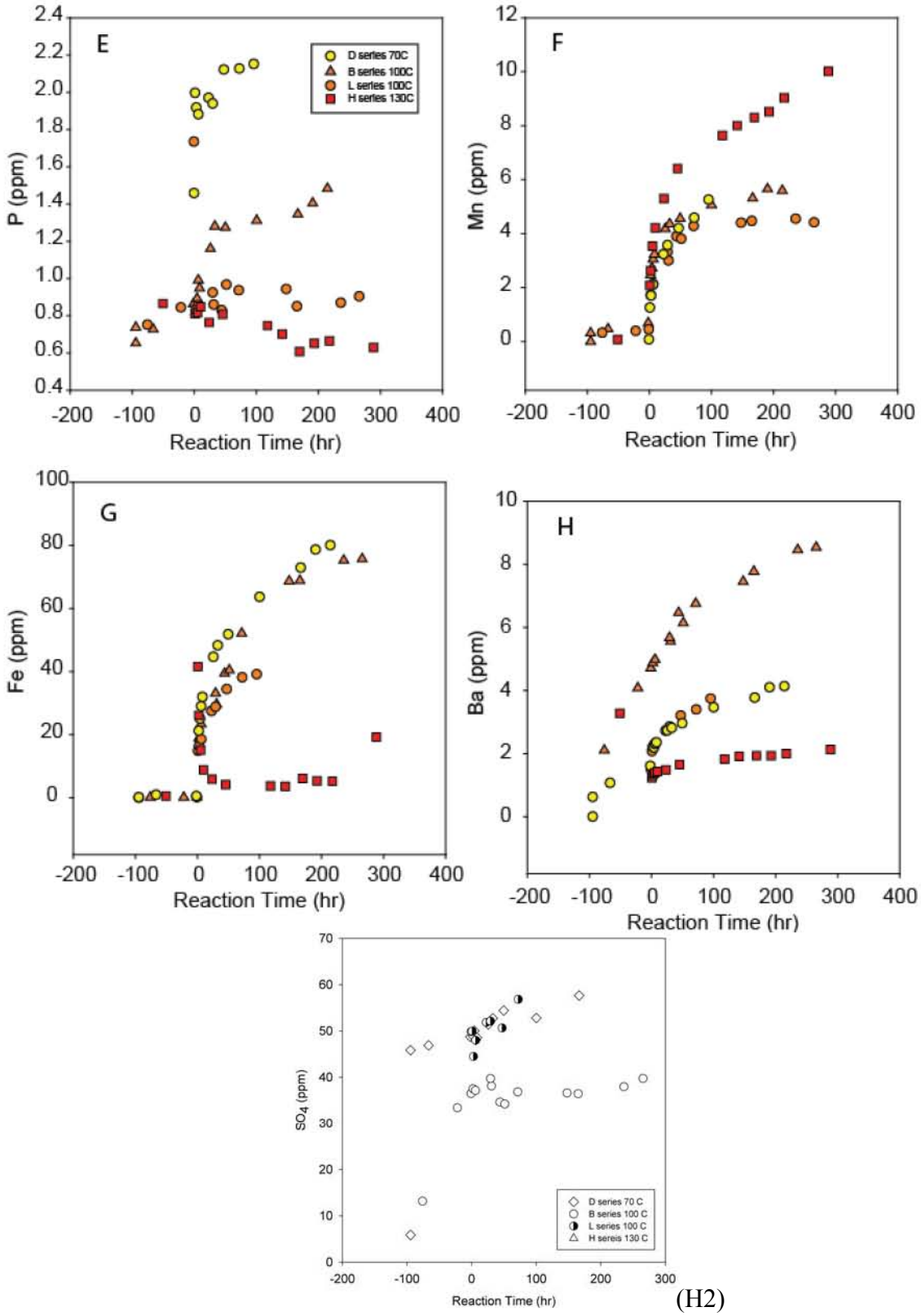

(H2)

Figure 12. Impact of temperature variation on reaction progress (Miocene), D series (70°C), B and L series (100°C), and H series (130°C) (all at 200 bars with pure CO_2) – Species showing increase with time (continued)

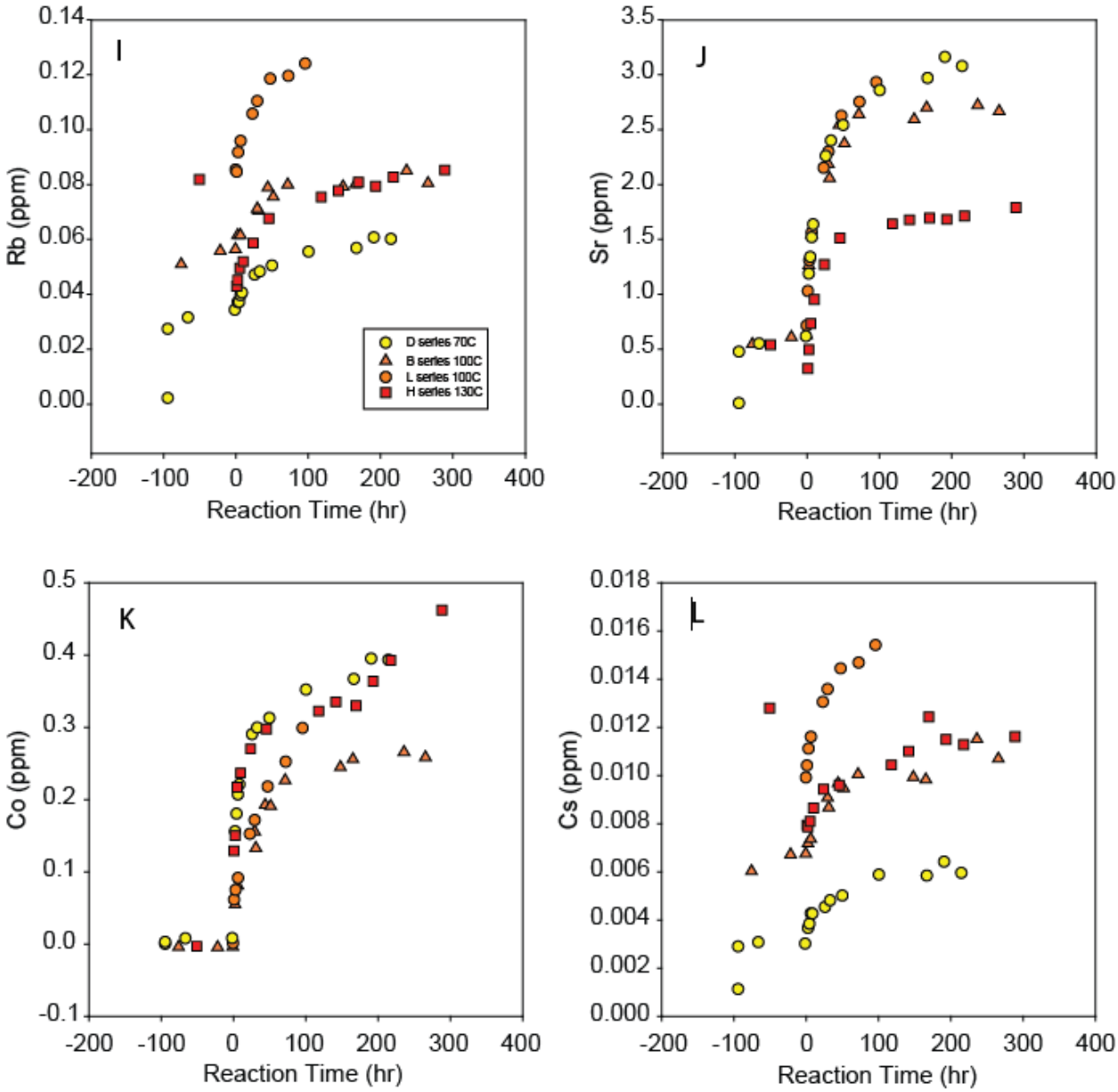

Figure 12. Impact of temperature variation on reaction progress (Miocene), D series (70°C), B and L series (100°C), and H series (130°C) (all at 200 bars with pure CO_2) – Species showing increase with time (continued)

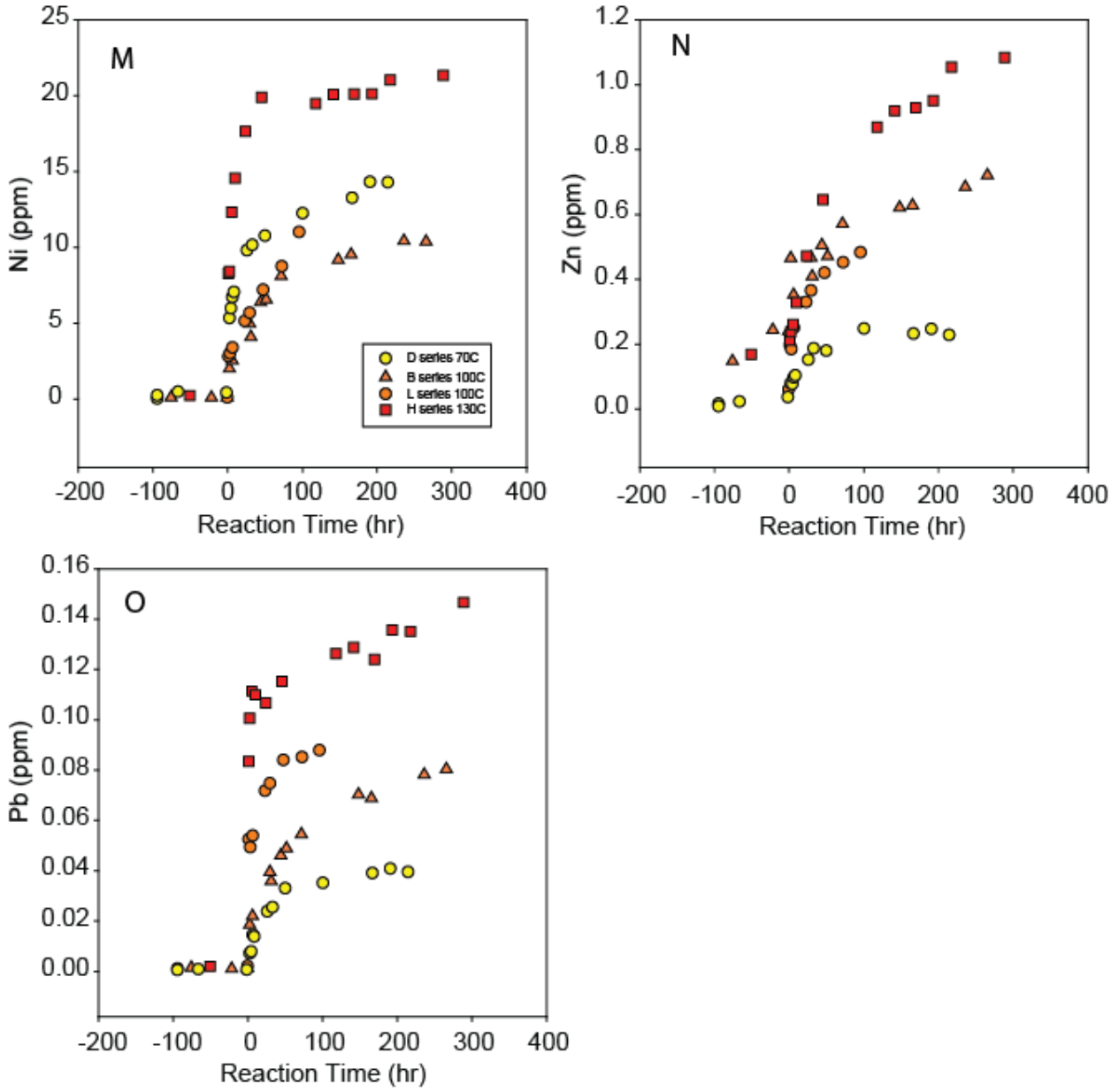

Figure 12. Impact of temperature variation on reaction progress (Miocene), D series (70°C), B and L series (100°C), and H series (130°C) (all at 200 bars with pure CO_2) – Species showing increase with time (continued)

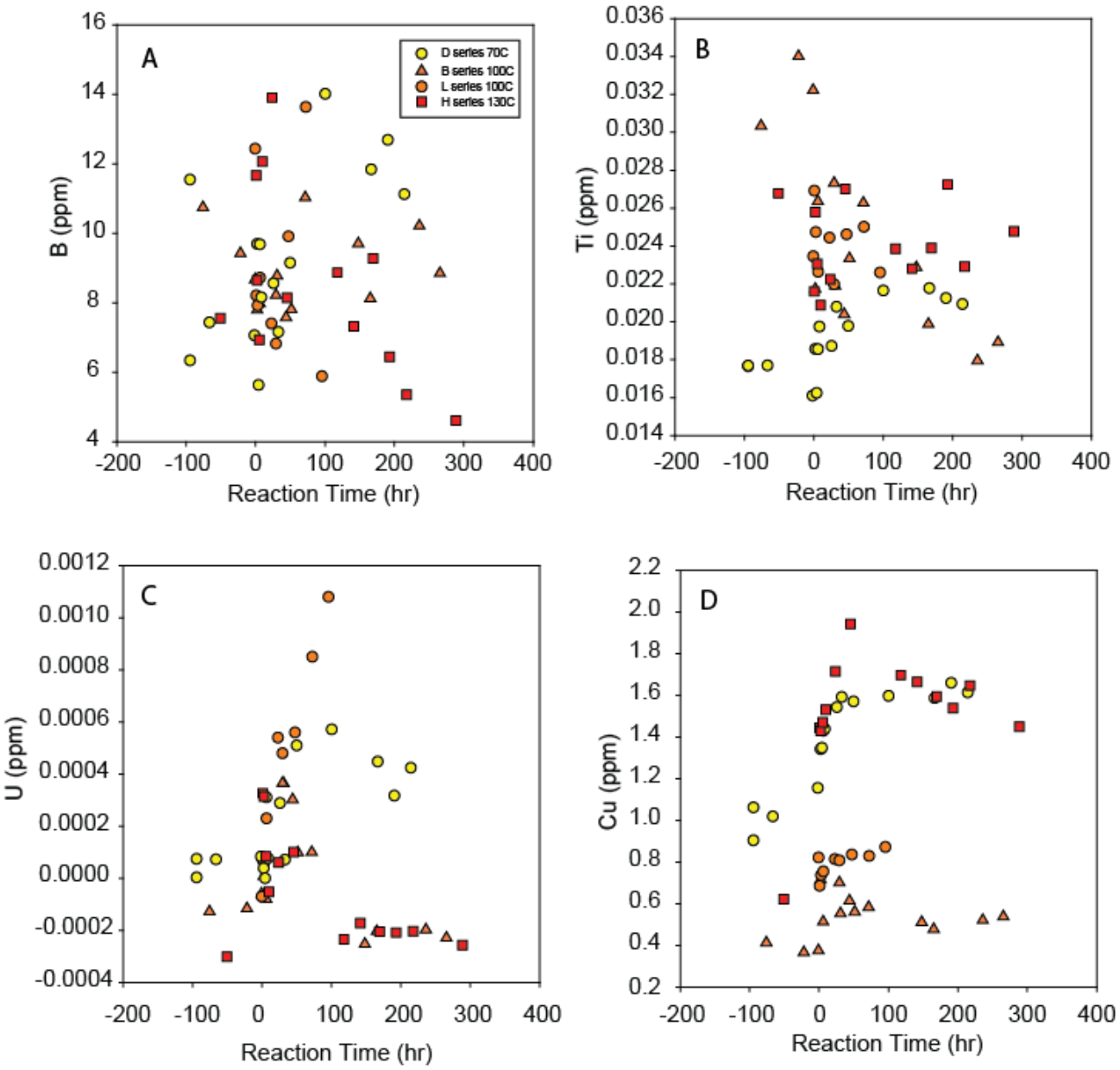

Figure 13. Impact of temperature variation on reaction progress (Miocene), D series (70°C), B and L series (100°C), and H series (130°C) (all at 200 bars with pure CO_2) – Species showing no trend with time

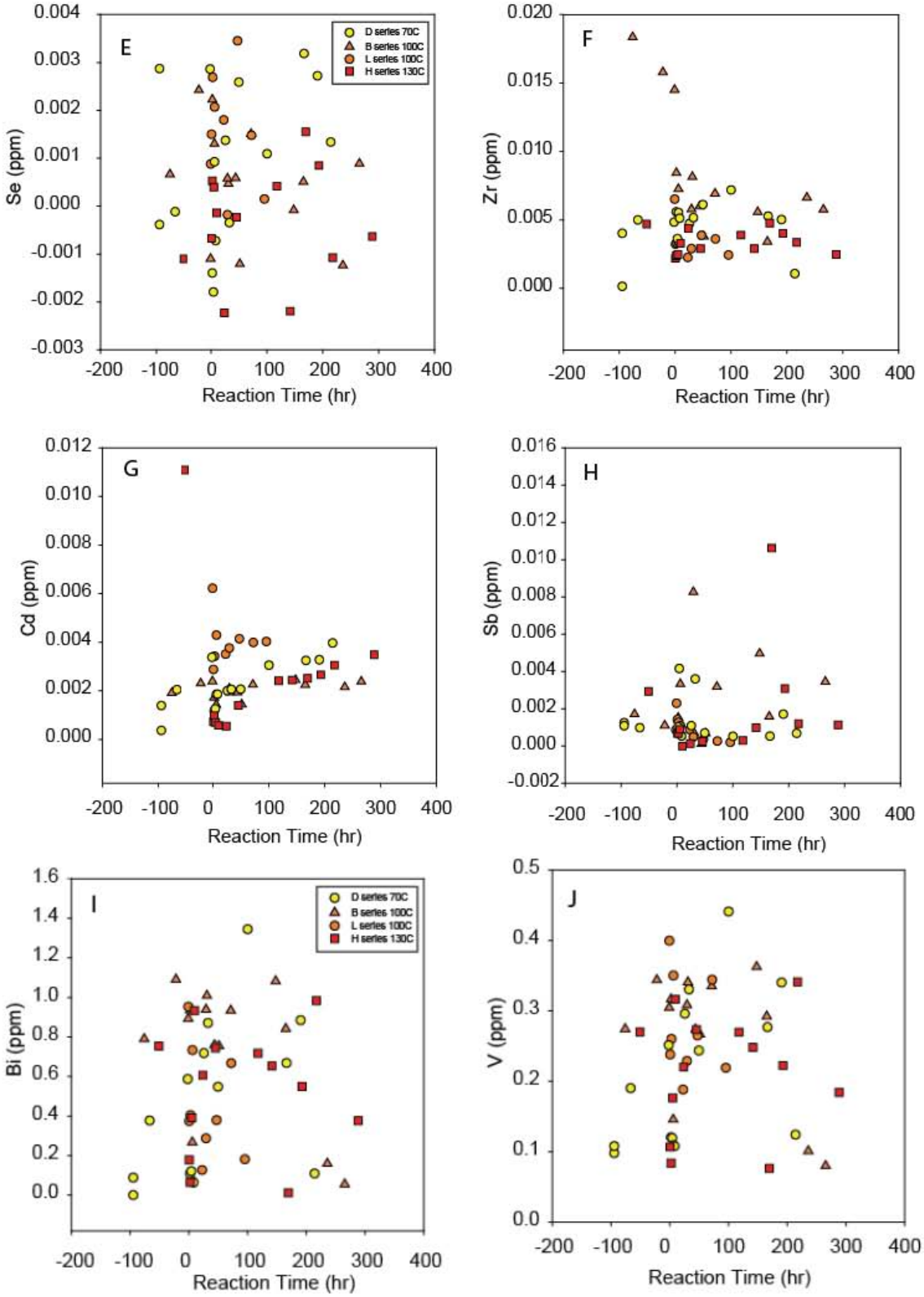

Figure 13. Impact of temperature variation on reaction progress (Miocene), D series (70°C), B and L series (100°C), and H series (130°C) (all at 200 bars with pure CO_2) – Species showing no trend with time (continued)

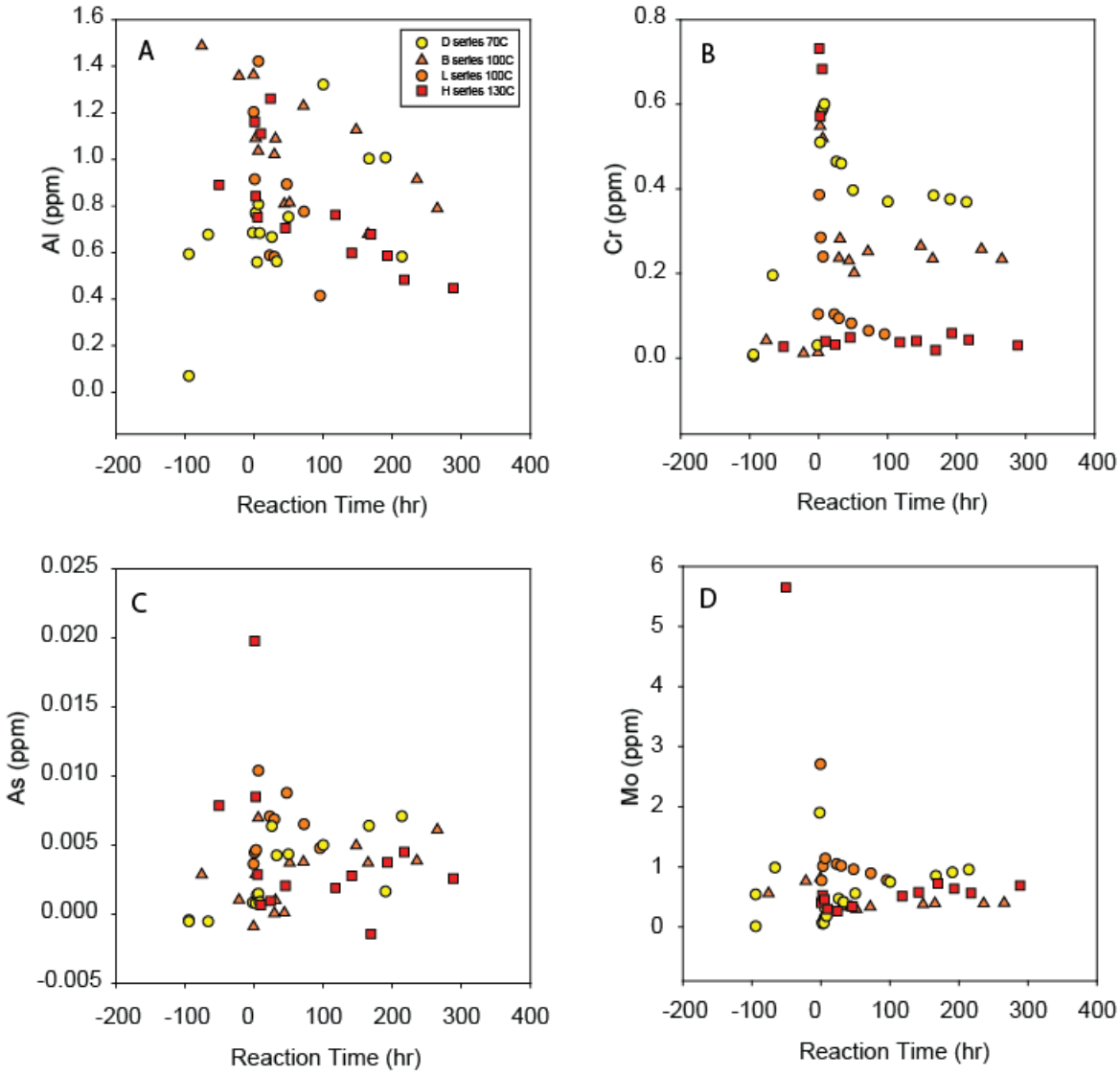

Figure 14. Impact of temperature variation on reaction progress (Miocene), D series (70°C), B and L series (100°C), and H series (130°C) (all at 200 bars with pure CO_2) – Species showing decrease with time

CO_2+O_2 mixture vs. Temperature

Comparison of reactions of the rock samples with the CO_2+O_2 mixture at different temperatures (R and S series, Figure 15) show a general behavior similar to that of the pure CO_2 case. Unfortunately, it is obscured by a difference in O_2 concentration (7% at 70°C and 3.5% at 100°C). For example, sulfate concentration is higher in the S series (100°C, 3.5% O_2) than in the R series (70°C, 7% O_2). In the pure CO_2 cases, that is, without O_2, sulfate concentration stays around 40-60 ppm in the Miocene water samples whereas with O_2 they jump to double this value, very likely due to the oxidation of pyrite. The likely decrease in pH, using sulfate concentration as proxy, higher at 100°C than at 70°C despite lower O_2 concentration (sulfate plot on Figure 15) balances the reduced solubility of calcite at higher temperatures resulting in an overlap of the Ca curves (Figure 15). Mg concentrations, although increasing through time, do not display such behavior and seem to be following the feldspar dissolution trend with higher

dissolution at higher temperatures. Sr (Figure 17) tends to follow Ca with both curves overlapping whereas Mn (Figure 17) is more similar to Mg and silicate-controlled minerals. Same observations can be made in the pure CO_2 case. Si, K, Rb concentrations increase with time and are higher at higher temperatures (Figure 16). Al concentrations show a complex pattern reflecting concomitant dissolution / precipitation mechanisms. They do not seem to be impacted by temperature. Fe and Cr concentrations stay low and similarly do not seem to be impacted by temperature (Figure 18). This is true as well of P, B, Ti, V, Cu, Zr, and Bi, all of which do not display a consistent concentration time series and whose concentration appear independent of temperature (proximity to detection limit might explain some of this). Co, Ni, Mo, Pb (Figure 18) all show individually a clear pattern but Co and Pb, similarly to Fe and Cr have a lower aqueous concentration at higher temperature whereas Ni and Mo both show the reverse behavior with higher concentrations at lower temperatures. The pure CO_2 case shows higher concentrations for Ni and Pb, lower concentrations for Cr at higher temperatures and Mo concentrations indifferent to temperature. Undoubtedly, understanding of trace elements requires more attention that can be given in this project.

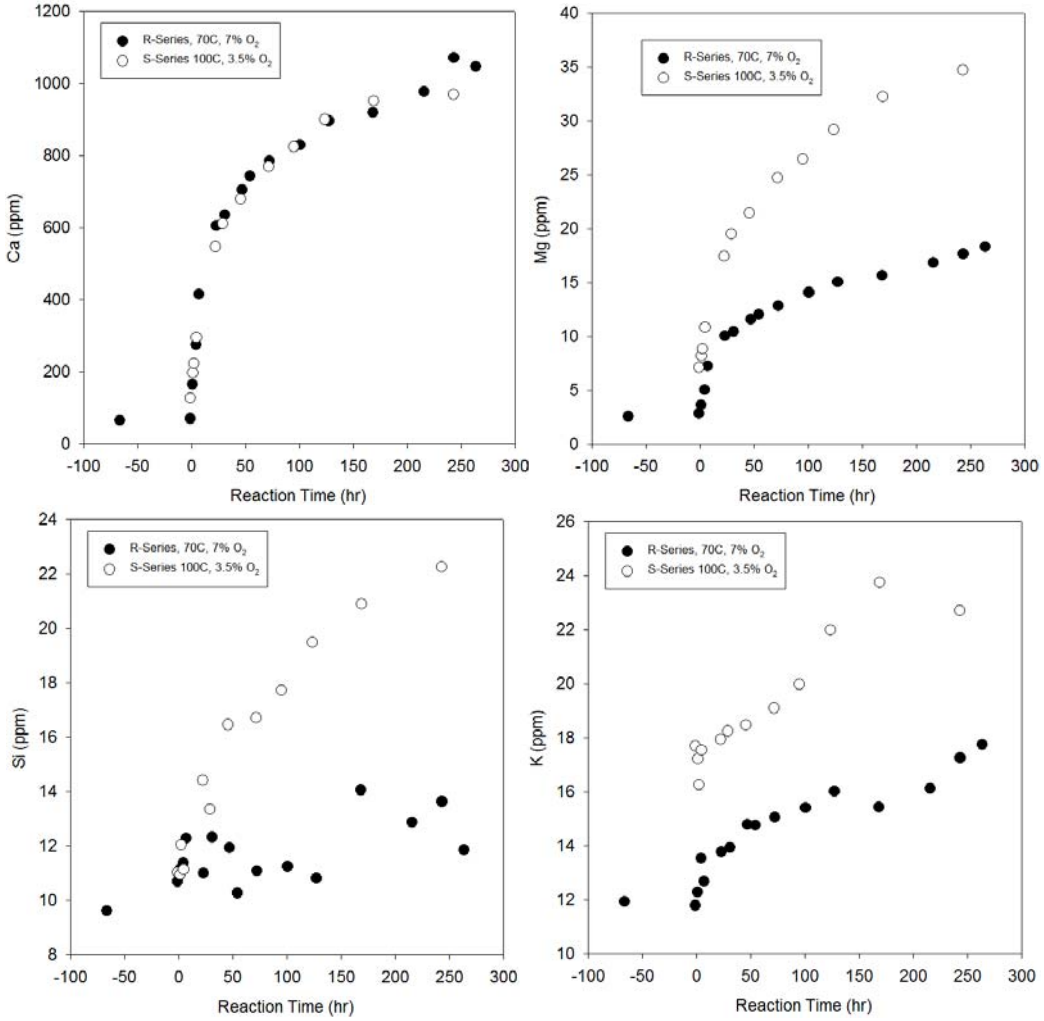

Figure 15. Impact of temperature variation on reaction progress (Miocene), R series (70°C) and S series (100°C) (at 200 bars with O_2+CO_2) – Major elements

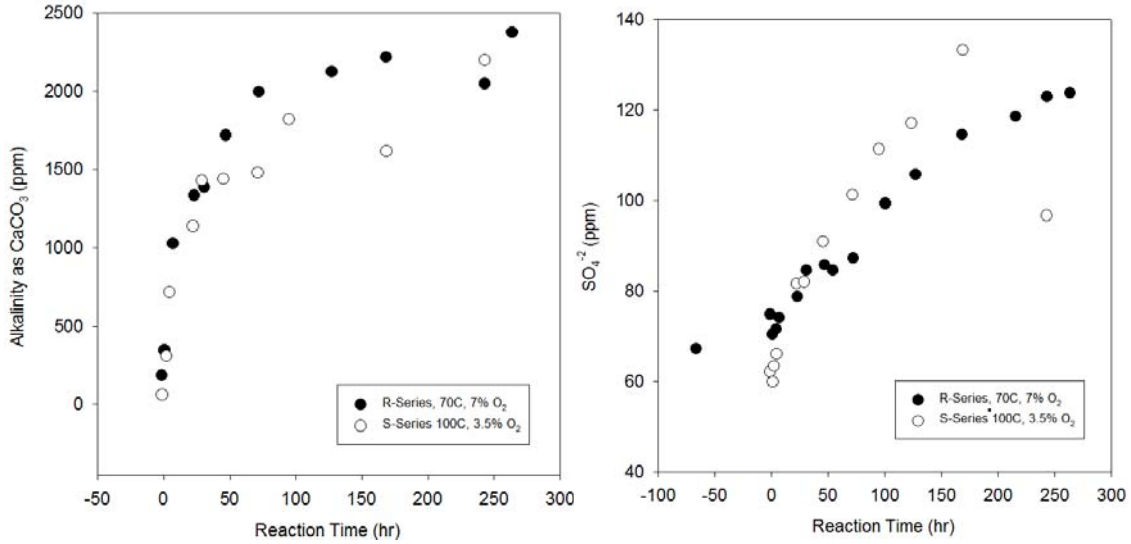

Figure 15. Impact of temperature variation on reaction progress (Miocene), R series (70°C) and S series (100°C) (at 200 bars with O_2+CO_2) – Major elements (continued)

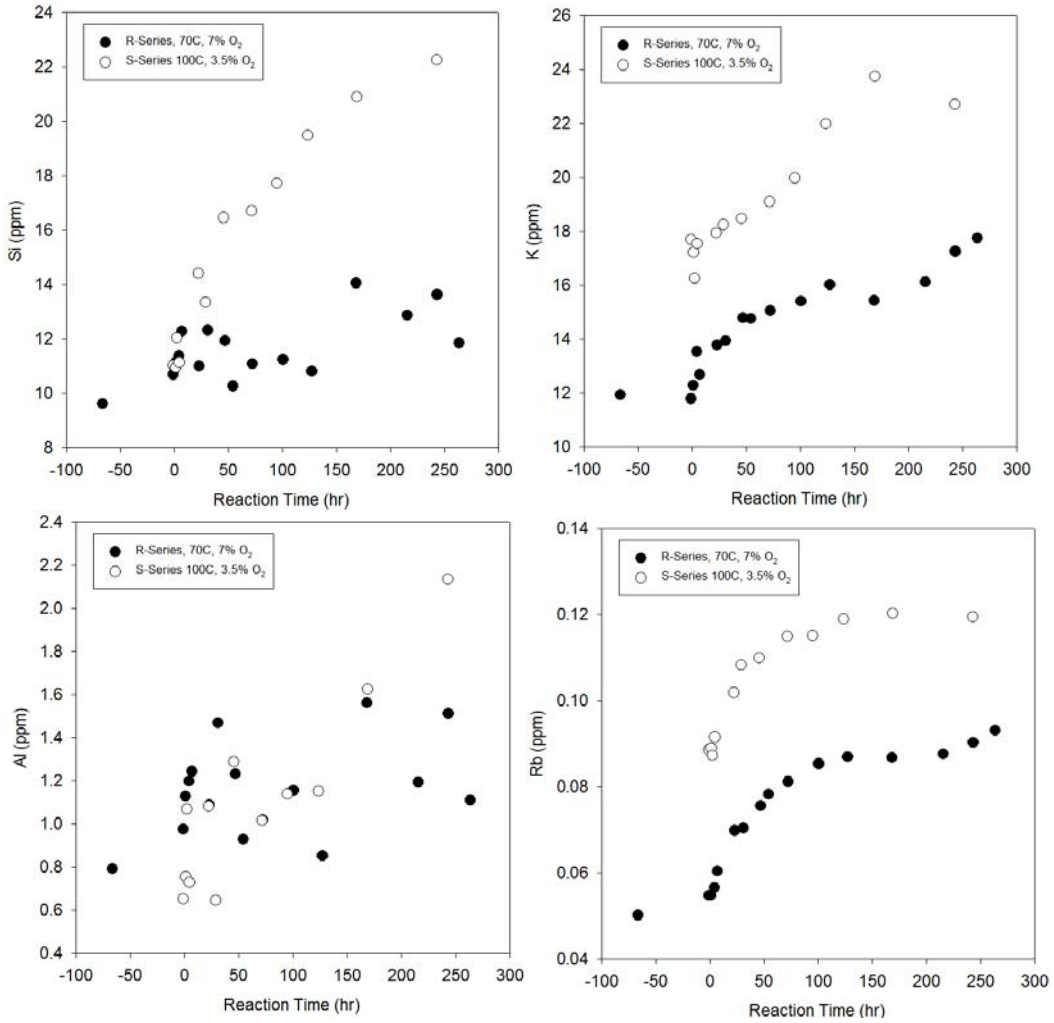

Figure 16. Impact of temperature variation on reaction progress (Miocene), R series (70°C) and S series (100°C) (at 200 bars with O_2+CO_2) – Silicate-controlled elements

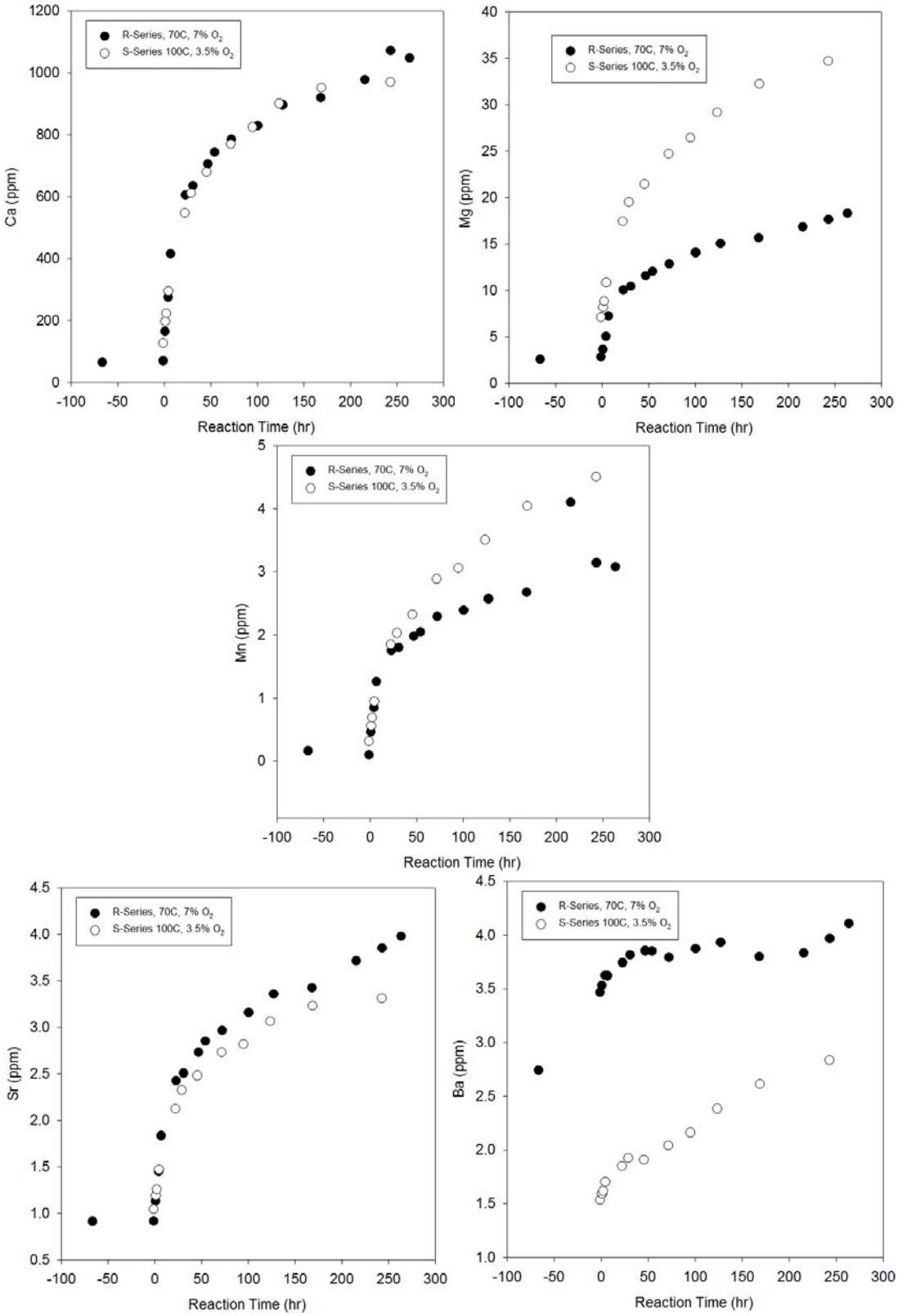

Figure 17. Impact of temperature variation on reaction progress (Miocene), R series (70°C) and S series (100°C) (at 200 bars with O_2+CO_2) – Carbonate-controlled elements

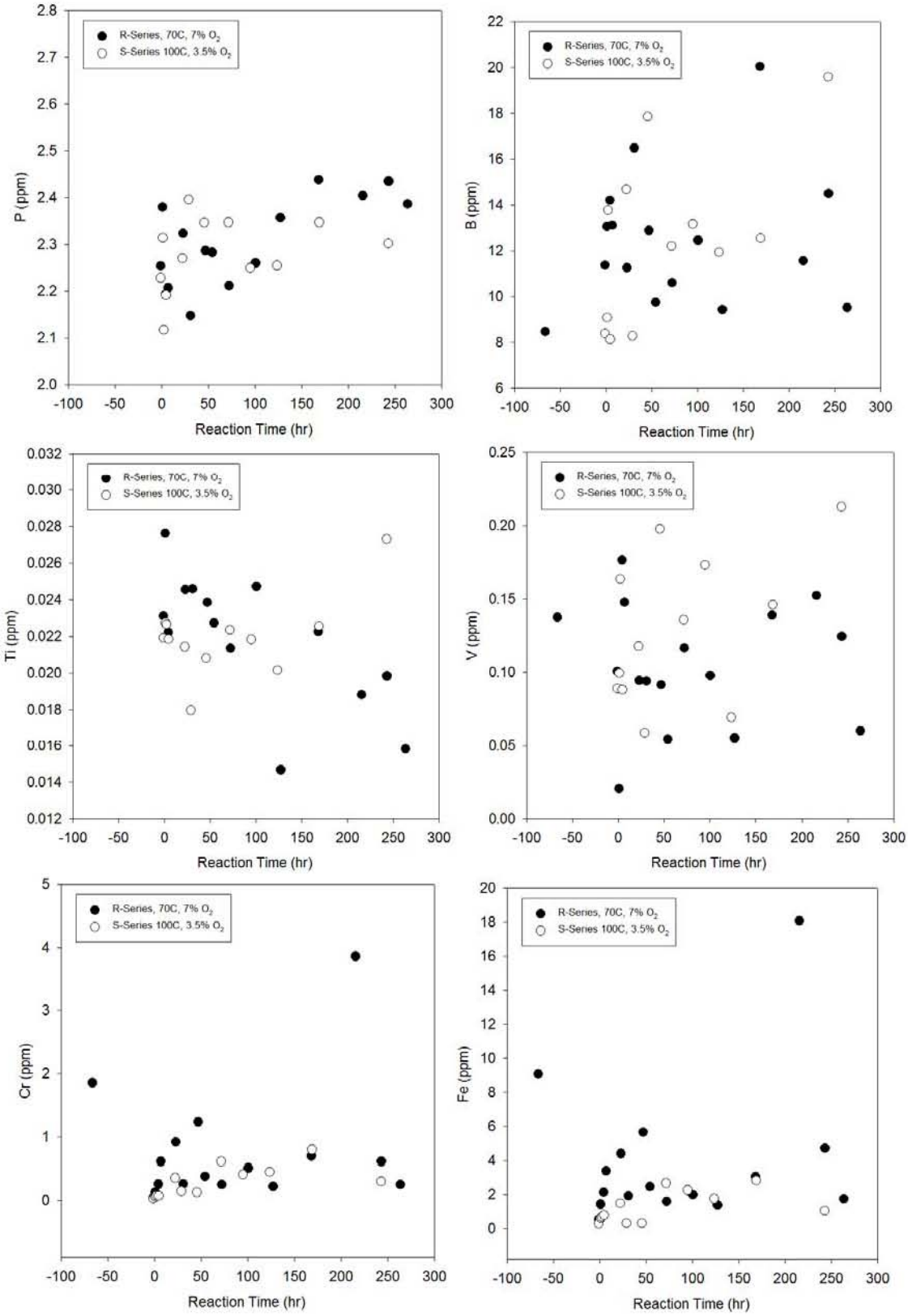

Figure 18. Impact of temperature variation on reaction progress (Miocene), R series (70°C) and S series (100°C) (at 200 bars with O_2+CO_2) – Trace elements

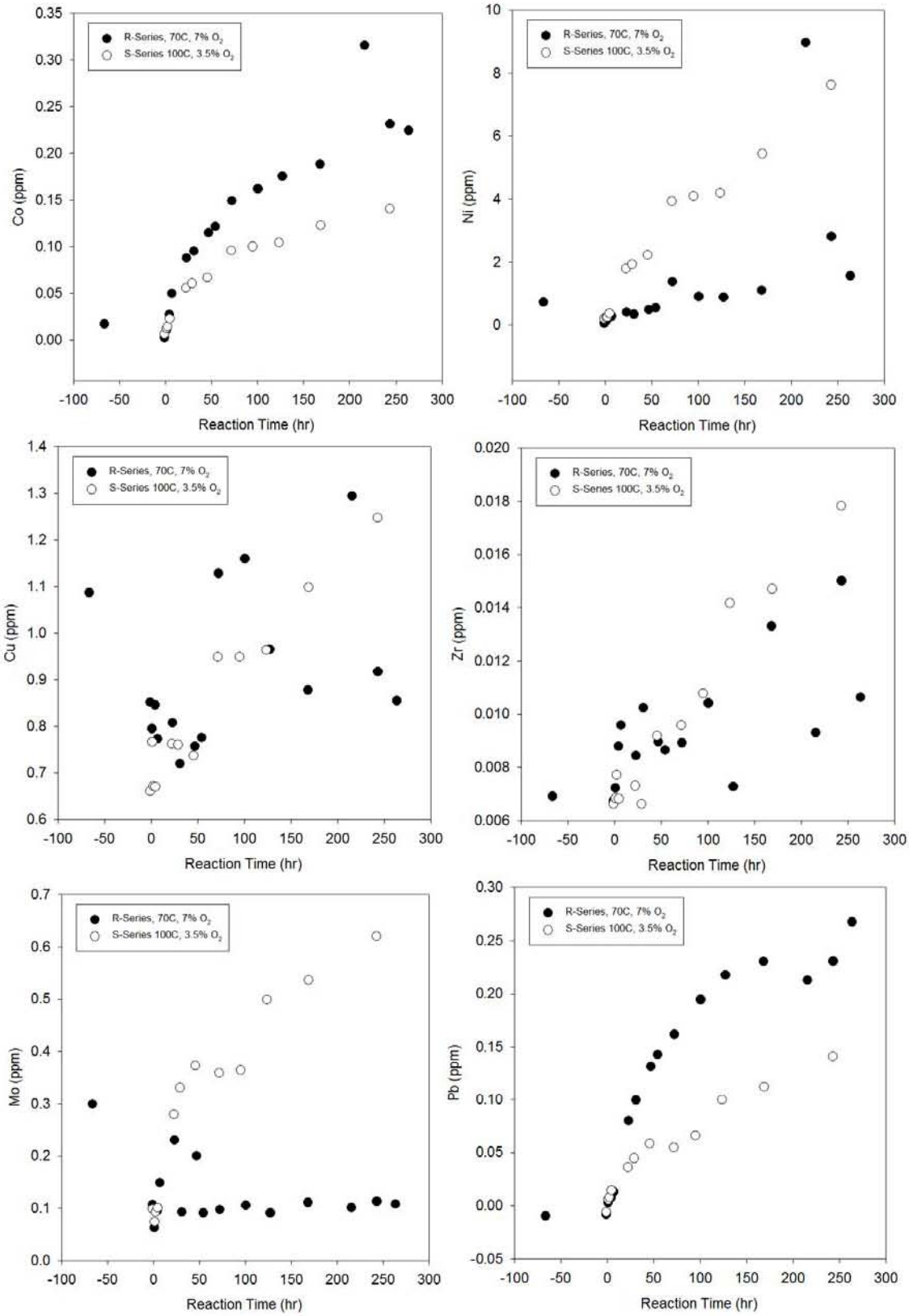

Figure 18. Impact of temperature variation on reaction progress (Miocene), R series (70°C) and S series (100°C) (at 200 bars with O_2+CO_2) – Trace elements (continued)

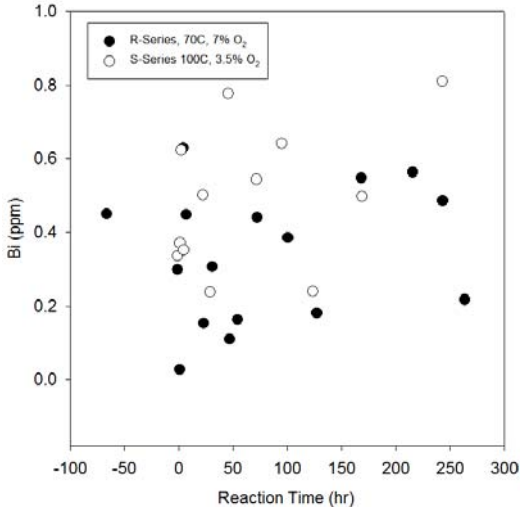

Figure 18. Impact of temperature variation on reaction progress (Miocene), R series (70°C) and S series (100°C) (at 200 bars with O_2+CO_2) – Trace elements (continued)

Pure CO_2 vs. CO_2+O_2 mixture at two temperatures

The addition of O_2 does not impact Ca values in brine, but does affect Mg, SO4 and K concentrations suggesting that feldspars and/or clays may experience enhanced reactivity in the presence of O_2 (Figure 19 and Figure 20). The clear increase in SO4 concentration in response to O_2, more dramatic at higher temperature despite the lower O_2 concentration is most likely due to the oxidation of pyrite. Gypsum has not been described in these rocks and it is unclear why it would dissolve only when O_2 is present. The D and R series (70°C) and L and S series (100°C) display exactly the same behavior: Ca concentrations are unaffected by O_2, very likely because Ca has already reached saturation next to the dissolving mineral surface even without the help of the pH drop due to pyrite oxidation. However, K shows a large increase when O_2 is added likely related to the increase in feldspar dissolution due to the drop in pH. Perplexedly, Mg behavior is inconsistent, showing higher concentrations at lower temperature (70°C) and lower concentrations at higher temperature when O_2 (70°C) is present. This behavior may be due to the variable magnesium content in the samples.

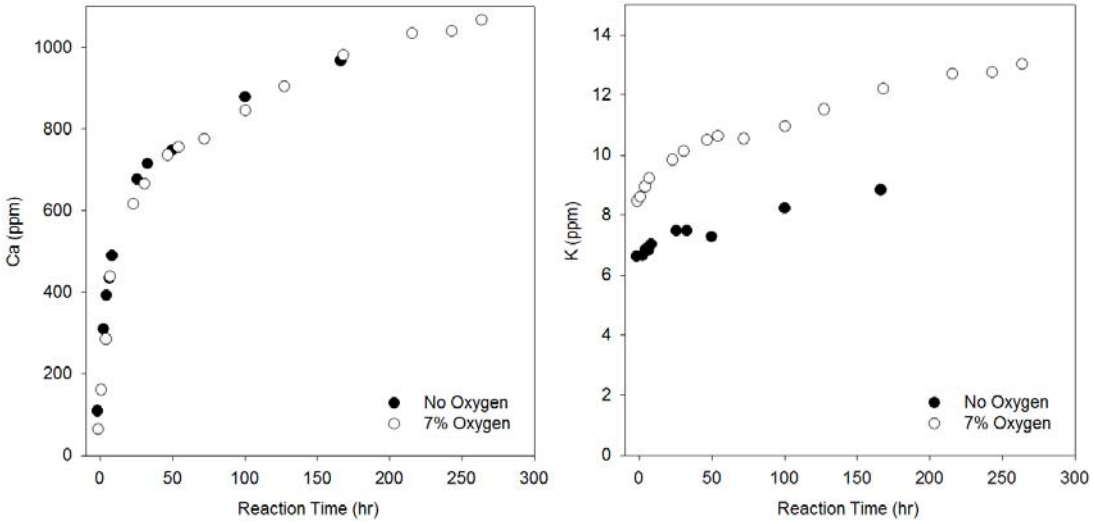

Figure 19. Miocene (70°C, 200 bars, with and without O_2) – D and R Series

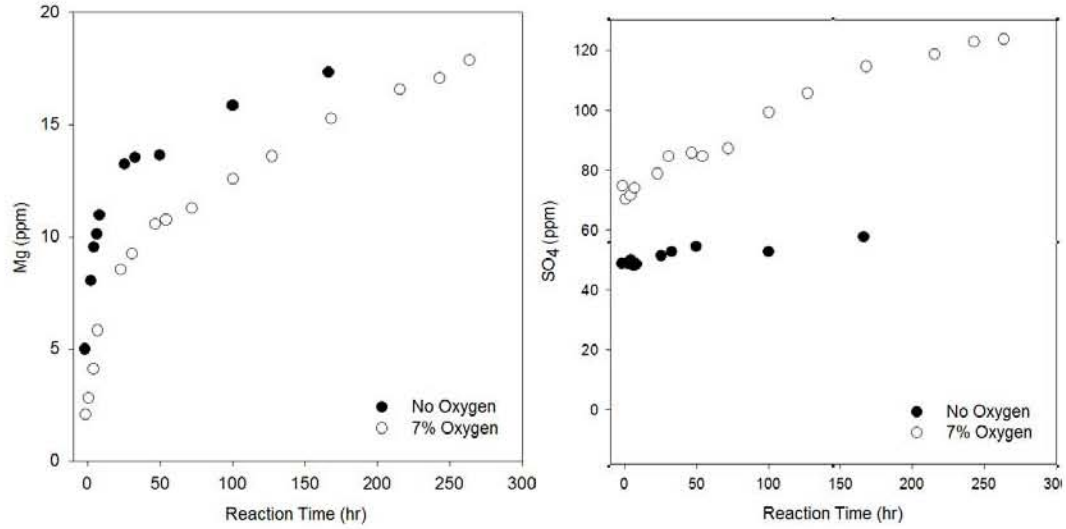

Miocene (70°C, 200 bars, with and without O_2) – D and R Series (continued)

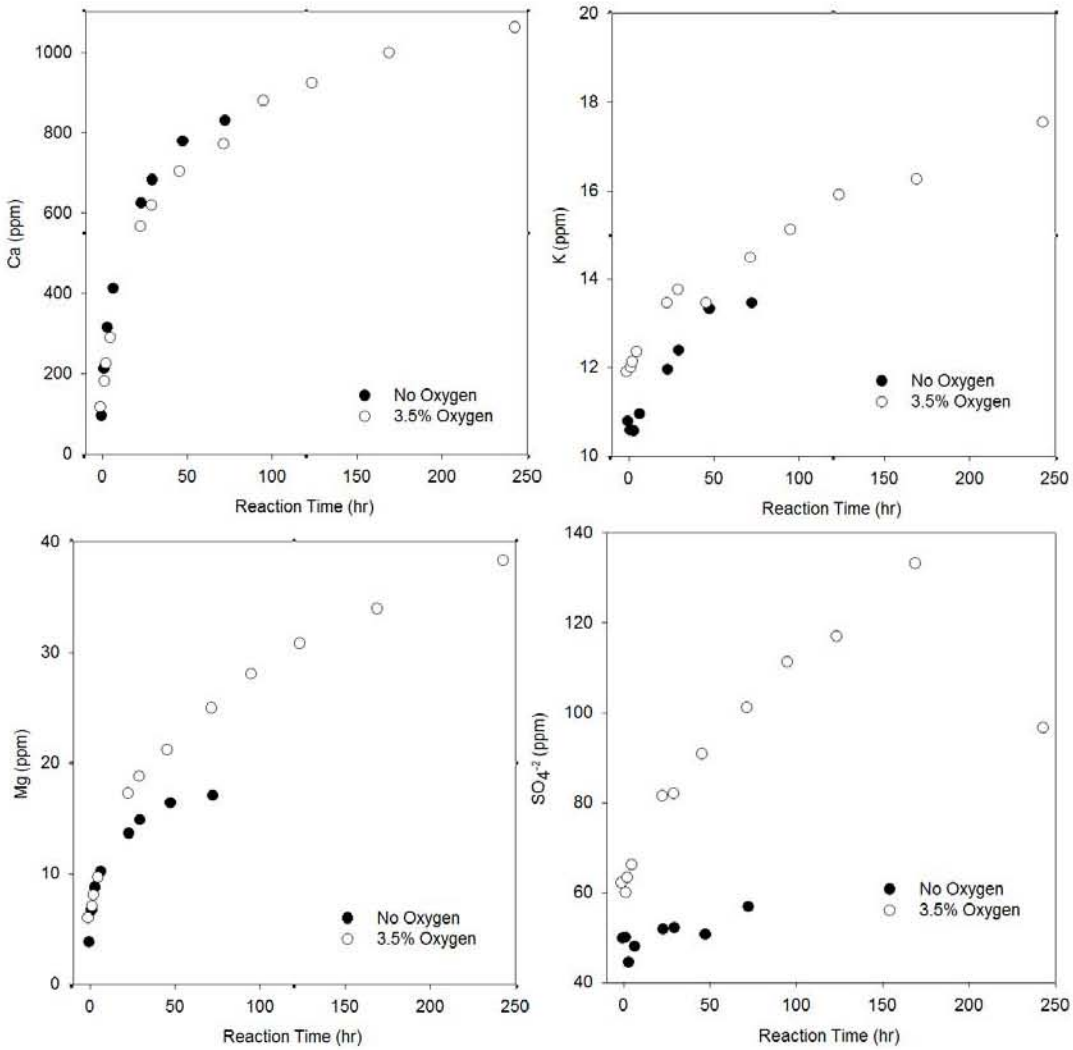

Figure 20. Miocene (100°C, 200 bars, with and without O_2) – L and S series

Sensitivity Analysis

Earlier we touched upon the difference between using DI or brine. Figure 21 assesses the effect of ionic strength on release rates. An important aspect of increased salinity is the decrease in CO_2 solubility and the change in ionic strength of the reaction fluid from DI to 1.88Mol/L NaCl had a significant effect on reactions related to carbonate dissolution as seen in Ca and Mg concentrations (Figure 21A and B). The effect is lower in elements controlled by silicate dissolution, as seen in Si and K concentrations (Figure 21C and D). Mn has high release rates and elemental concentrations controlled by higher carbonate dissolution in the NaCl brine (Figure 21E). Fe has very low concentrations in the DI water experiment likely due to the non-reactive nature of the reaction vessel. With the brine solution, the brine likely corroded the reaction vessel exposing reactive surfaces and higher Fe concentrations, along with Ni (not shown). Co concentrations remain relatively low and are likely controlled by silicate dissolution. Ca concentrations are higher in the brine solution suggesting enhanced dissolution; however Si and K concentrations do not show this increase. The amount of calcite dissolution is greater in the brine experiment compared to that of the DI water case. As previously reported, calcite minerals were almost completely consumed at the reacted surface; whereas, below the surface reaction rim calcite is still abundant. EDS scan results show that calcium content dropped significantly on the reacted sample surface. Clearly, more calcite was consumed in the brine experiment than in the DI water experiment. The SEM observation matches well with the water chemical analyses. Ca concentration in the brine reached 914 ppm at the end of the brine experiment compared to 544 ppm in the DI water run. Under the reaction conditions calcite solubility is higher in brine than in fresh water.

Next, we discussed another sensitivity parameter, the impact of pressure (Figure 22) using results from the E series that was run at 300 bars (instead of 200 bars) at 100°C (B series rerun as L series). At the same time we also touch upon the issue of intersample variability (B and L series but which operated under slightly different experimental conditions). Results indicate that variations in pressure do not significantly alter the release rates. Higher pressure allows for a higher CO_2 solubility and seems to have little impact on carbonate dissolution (Ca, Mg, and Mn in Figure 22A, B, and E) and some slight impact on silicate dissolution (Figure 22C, D, and G). However we note more variability for Mg than for Ca between B and L series.

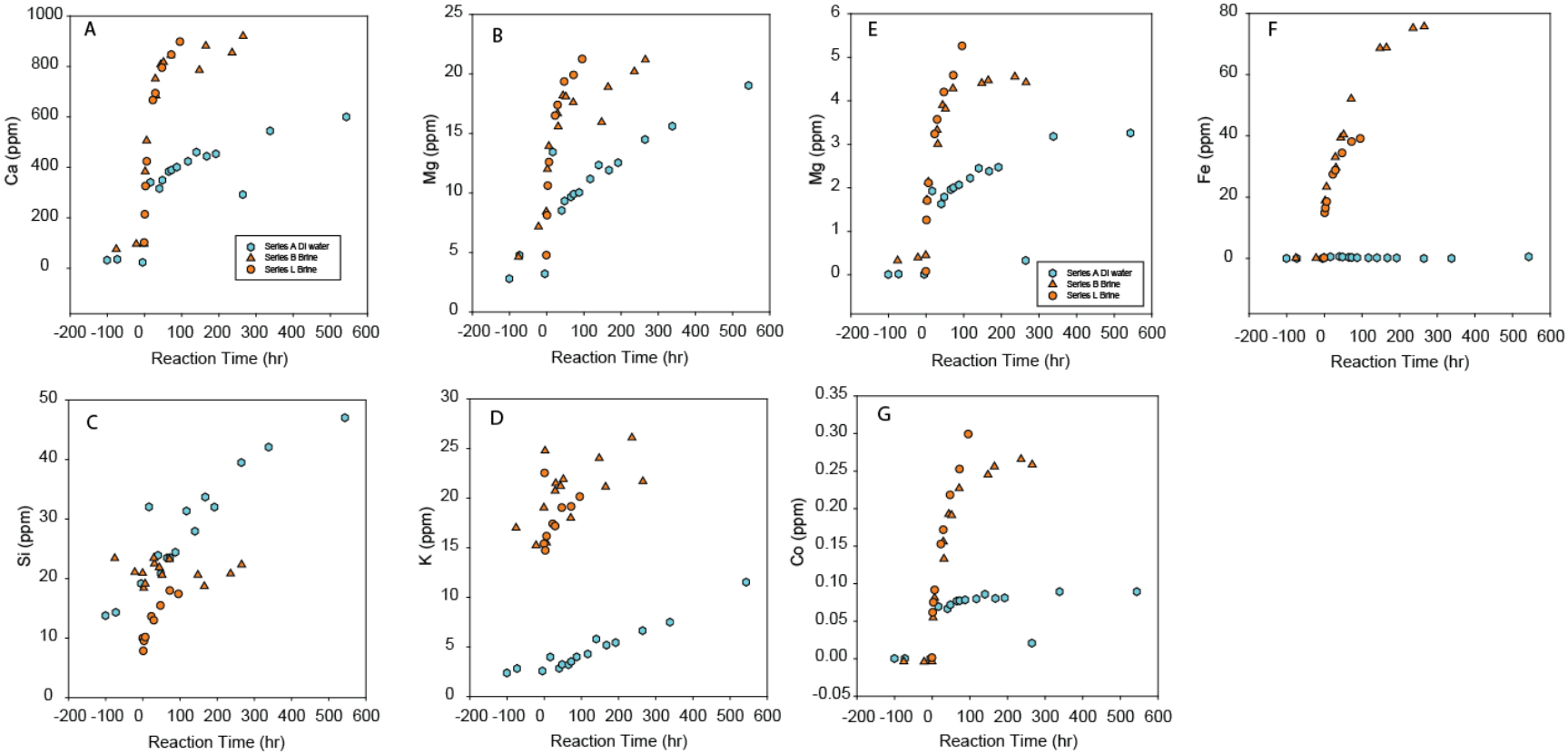

Note: A=Ca; B=Mg; C=Si; D=K; E=Mn; F=Fe; G=Co

Figure 21. Comparison DI-brine results (Miocene, 100°C, 200 bars)- A, B, and L series

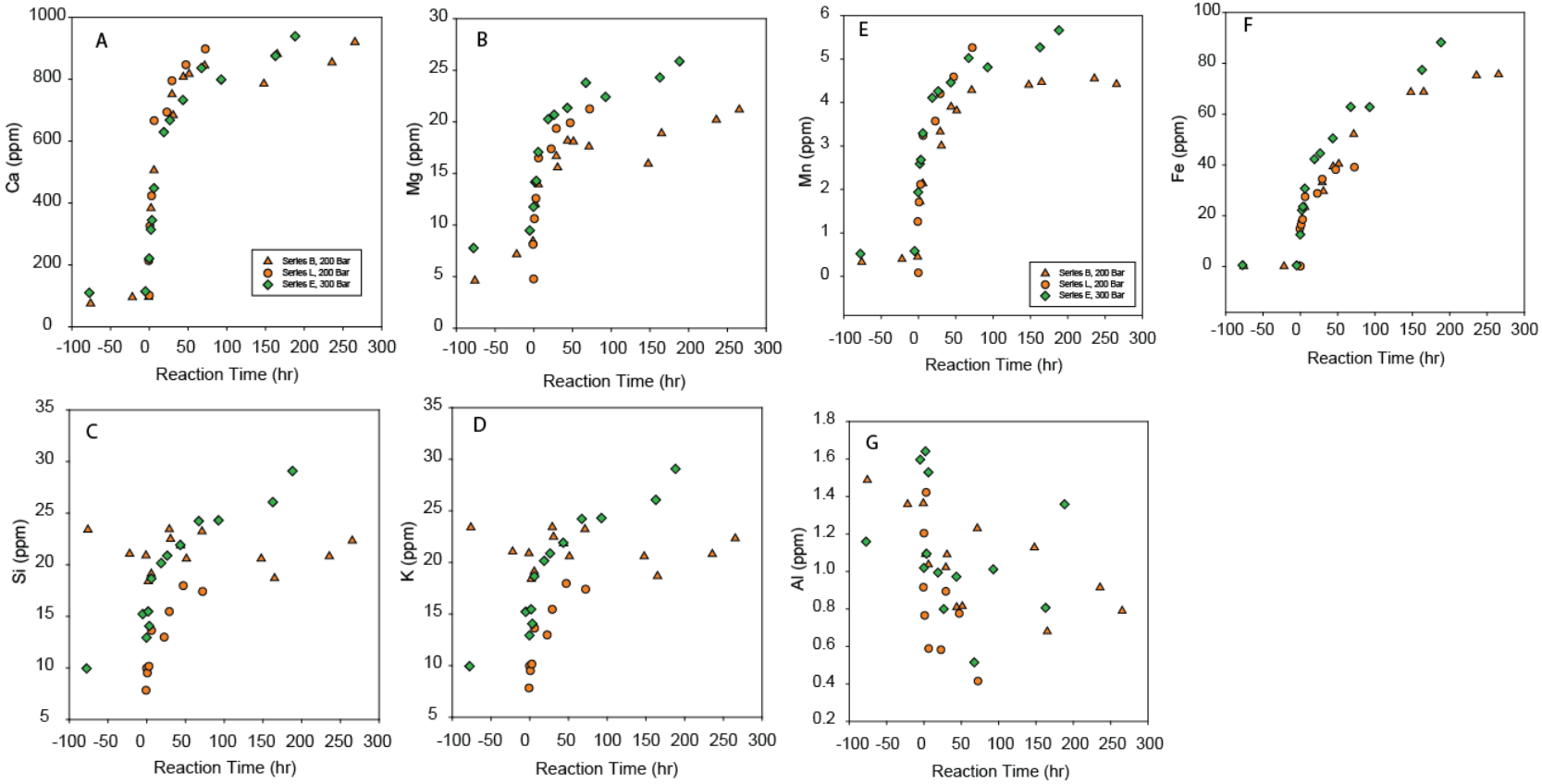

Figure 22. Impact of pressure (Miocene, 100°C, 200/300 bars) – E, B, and L series

III1.1.5.2 Modeling Results (Miocene)

In this section we show that we can fully explain the observed aqueous concentrations of various elements through time by dissolving observed minerals. We used the following composition, assumed constant for all samples: quartz (43.5%), kaolinite (6.2%), calcite (11.8%), illite (5.0%), K-feldspar (15.2%), and albite (18.4%). Water compositions of batch experiments (Table 11) measured immediately before CO_2 was introduced into the reactor were used as initial conditions in the models. Initial value of pH in the model is assumed to be 7 since the brine was made by adding NaCl to the distilled water. Modeled and observed results are matched by calibrating the reactive surface area through a trial-and-error approach (Table 12). Because secondary minerals were not initially present in the rock samples, surface areas for those minerals are assumed to be 0.01 m^2, and no calibrations were conducted for those minerals. The reactive surface area of calcite was calibrated to fit concentration measurements of Ca and Mg (Figure 23, Figure 24, Figure 25, Figure 26, and Figure 27). It should be noted that since Mg concentrations have a strong correlation with Ca concentrations in all five batches, Mg is consider as a replacement of Ca in the calcite molecular structure. Reactive surface areas of calcite in the B, D, E and H are very close, about 25 times the reactive surface area of calcite in the A-batch (likely due to activity effects as explained earlier). Surface areas of silicate minerals are calibrated to fit concentrations of Na^+, K^+, Si, and Al^{3+}. It appears that the reactive surface areas are consistent in the four brine series (B, D, E, and H) although reactive surface areas of K-feldspar and kaolinite showed some differences. The DI experiment (A series) yields different surface area values especially for calcite. The discrepancy in results between DI and brine experiments is due to the activity model used in PHREEQC which breaks down at high salinity, especially for double-charged ionic species such as Ca and Mg. In any case, the geochemical models reproduced concentration measurements of Ca and Mg well, confirming dissolution of calcite when CO_2 was injected into the reactor. The geochemical models also fit well K concentration measurements, suggesting that K came from dissolution of K-feldspar when CO_2 was injected. Modeled Na concentrations match well Na concentration measurements in the DI case indicating CO_2 injection leads to dissolution of albite (nature of the NaCl brine overwhelmed Na concentration and small variations in Na cannot be detected). The geochemical models slightly overestimate Si concentration measurements and underestimate Al concentration measurements. Si and Al are dominated by dissolution-precipitation of silicate minerals and potential secondary minerals. Proper selection of secondary minerals in the geochemical model seems very important.

Table 11. Initial water composition used in the geochemical model of 5 batch experiments

Element (mol/kg H_2O)	Series A	Series B	Series D	Series E	Series H
Al	3.01E-05	5.26E-05	2.72E-05	5.92E-05	3.18E-06
Ca	5.74E-04	2.50E-03	2.91E-03	2.87E-03	2.17E-03
Cl	2.50E-03	1.82E+00	1.77E+00	1.83E+00	1.88E+00
K	6.58E-05	5.07E-04	2.81E-04	3.72E-04	1.65E-04
Mg	1.32E-04	3.61E-04	2.81E-04	3.90E-04	8.38E-05
Na	1.06E-03	1.82E+00	1.76E+00	1.88E+00	1.88E+00
Si	6.82E-04	7.75E-04	1.86E-04	5.42E-04	2.64E-04
pH	7	7	7	7	7
Temperature (^oC)	100	100	70	100	130
Total Pressure (Bar)	200	200	200	300	200
CO_2 Fugacity (atm)	120.4	120.4	97.5	152.2	138.2
O_2 Fugacity (atm)	0	0	0	0	0
Water volume (ml)	150.0	150.0	150.0	150.0	150.0
Rock samples (g)	8.0	8.0	8.0	8.0	8.0

Note: Cl concentrations were estimated based on charge balance

Table 12. Calibrated mineral reactive surface areas (Miocene, pure CO_2 series)

		A		B		D		E		H	
Mineral	mass (g)	Surface area (m^2)	Surface area (cm^2/g)	Surface area (m^2)	Surface area (cm^2/g)	Surface area (m^2)	Surface area (cm^2/g)	Surface area (m^2)	Surface area (cm^2/g)	Surface area (m^2)	Surface area (cm^2/g)
primary											
quartz	3.48	1.0E+02	2.874E+05	1.0E+02	2.874E+05	1.0E+02	2.874E+05	1.0E+02	2.874E+05	1.0E+02	2.874E+05
kaolinite	0.496	1.0E-01	2.016E+03	1.0E-02	2.016E+02	6.0E-02	1.210E+03	2.0E-02	4.032E+02	2.0E-02	4.032E+02
Calcite	0.944	4.0E-06	4.237E-02	1.0E-04	1.059E+00	2.0E-04	2.119E+00	1.5E-04	1.589E+00	1.0E-04	1.059E+00
Illite	0.4	1.0E-01	2.500E+03	5.0E-01	1.250E+04	5.0E-01	1.250E+04	5.0E-01	1.250E+04	5.0E-01	1.250E+04
Albite	1.472	5.0E-02	3.397E+02	5.0E-02	3.397E+02	5.0E-02	3.397E+02	5.0E-02	3.397E+02	5.0E-02	3.397E+02
K-feldspar	1.216	3.5E-02	2.878E+02	1.0E-01	8.224E+02	1.5E+00	1.234E+04	1.4E+00	1.151E+04	5.0E-01	4.112E+03
Secondary											
Magnesite		0.01		0.01		0.01		0.01		0.01	
Siderite		0.01		0.01		0.01		0.01		0.01	
Ankerite		0.01		0.01		0.01		0.01		0.01	
Dawsonite		0.01		0.01		0.01		0.01		0.01	

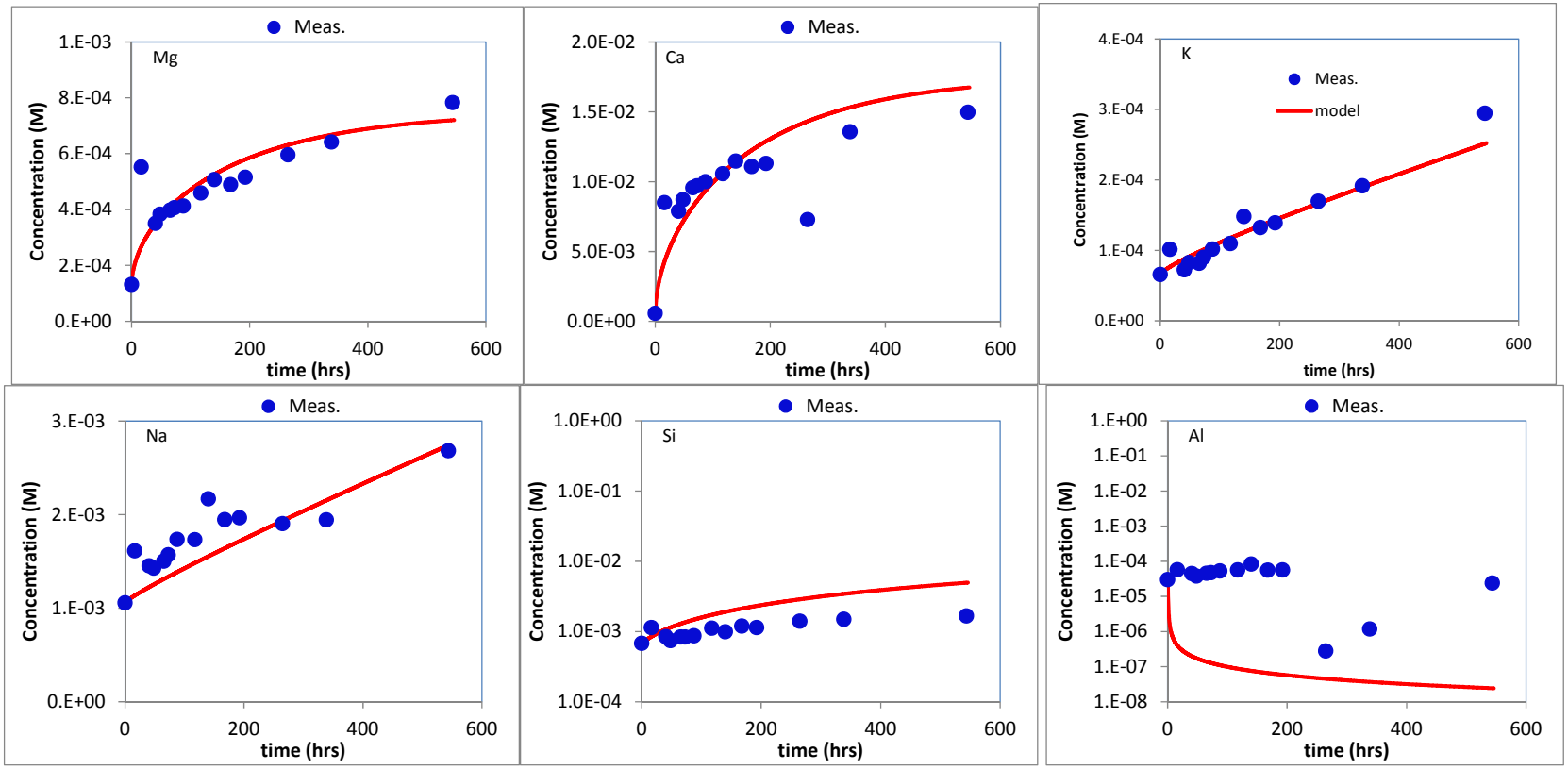

Figure 23. Comparison of measured and modeled major ion concentrations (A series; Miocene, 100°C, 200 bars, DI)

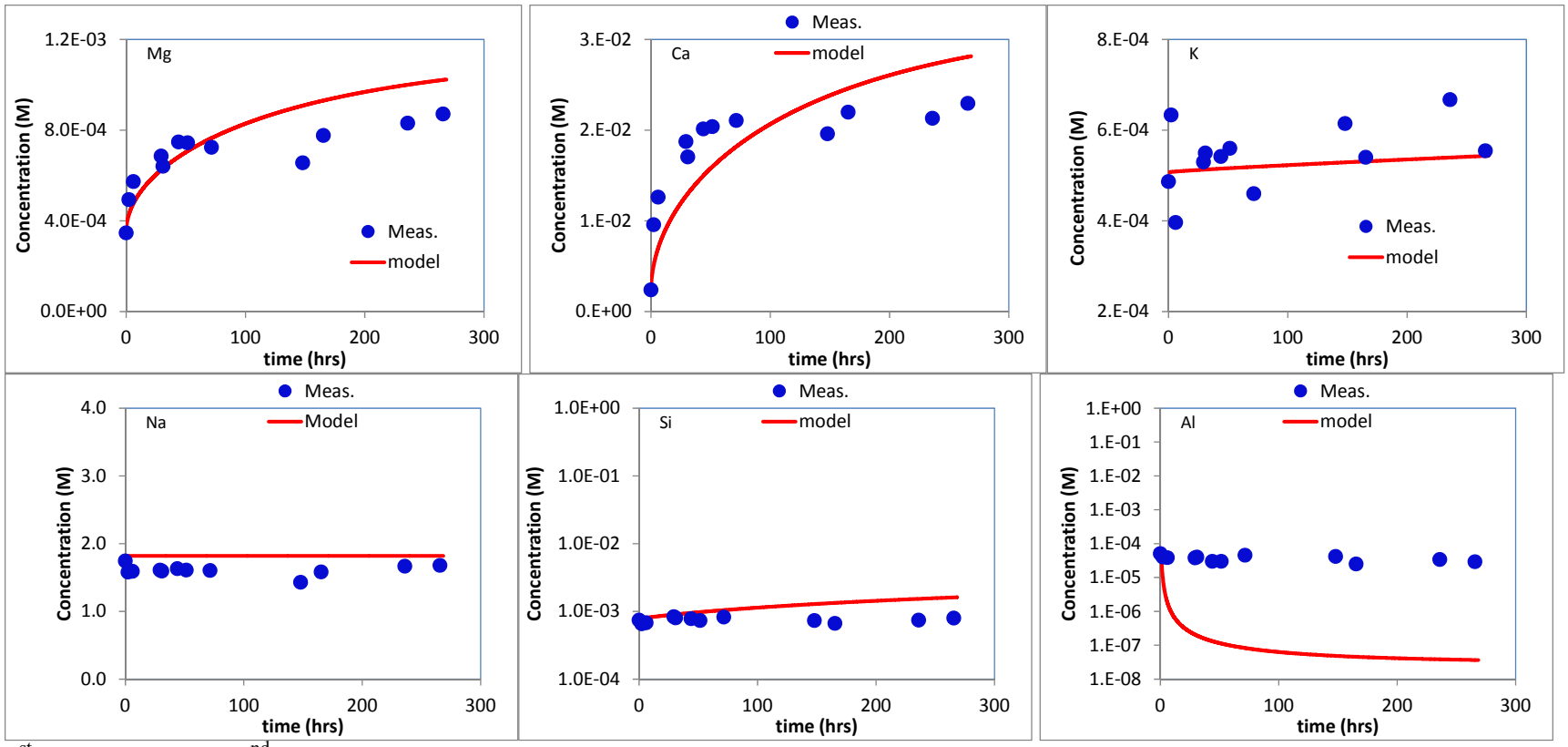

1st row: Mg, Ca, K; 2nd row: Na, Si, Al

Figure 24. Comparison of measured and modeled major ion concentrations (B series; Miocene, 100°C, 200 bars)

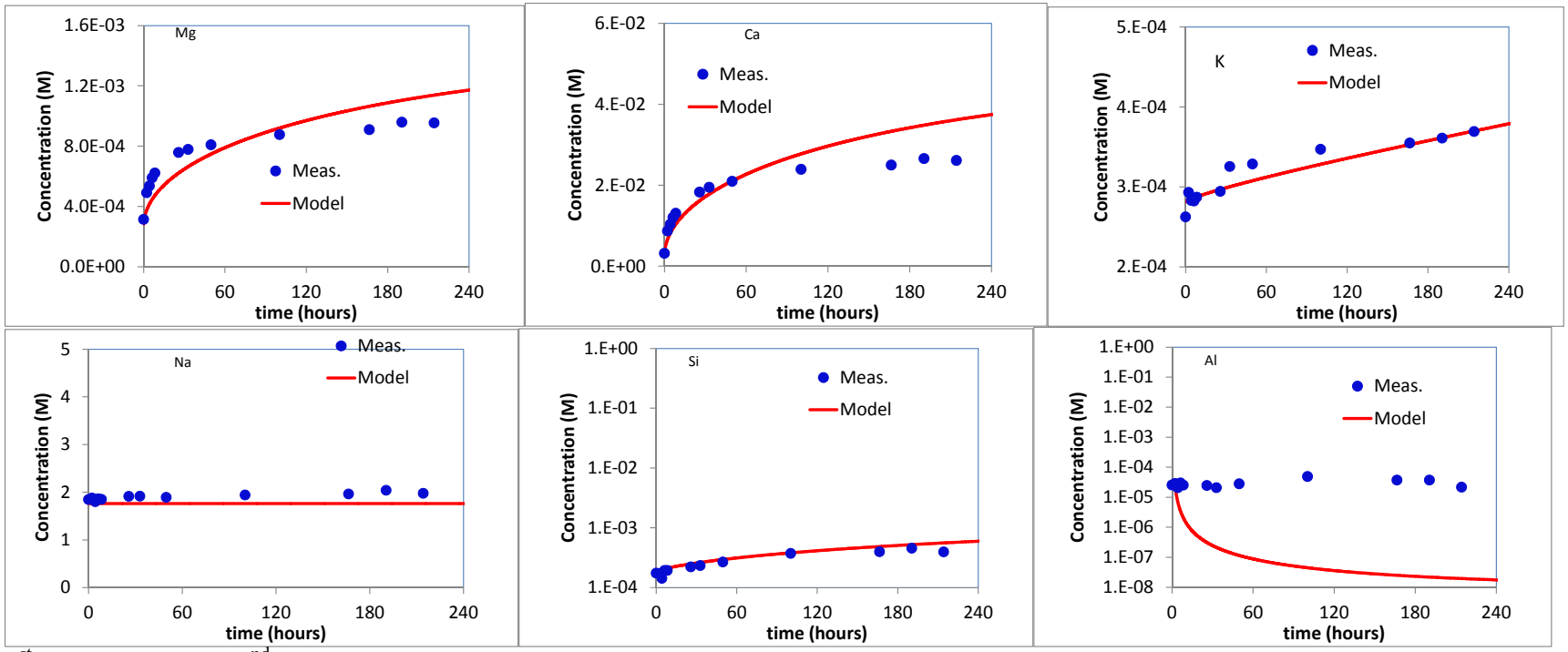

1st row: Mg, Ca, K; 2nd row: Na, Si, Al

Figure 25. Comparison of measured and modeled major ion concentrations (D series; Miocene, 70°C, 200 bars)

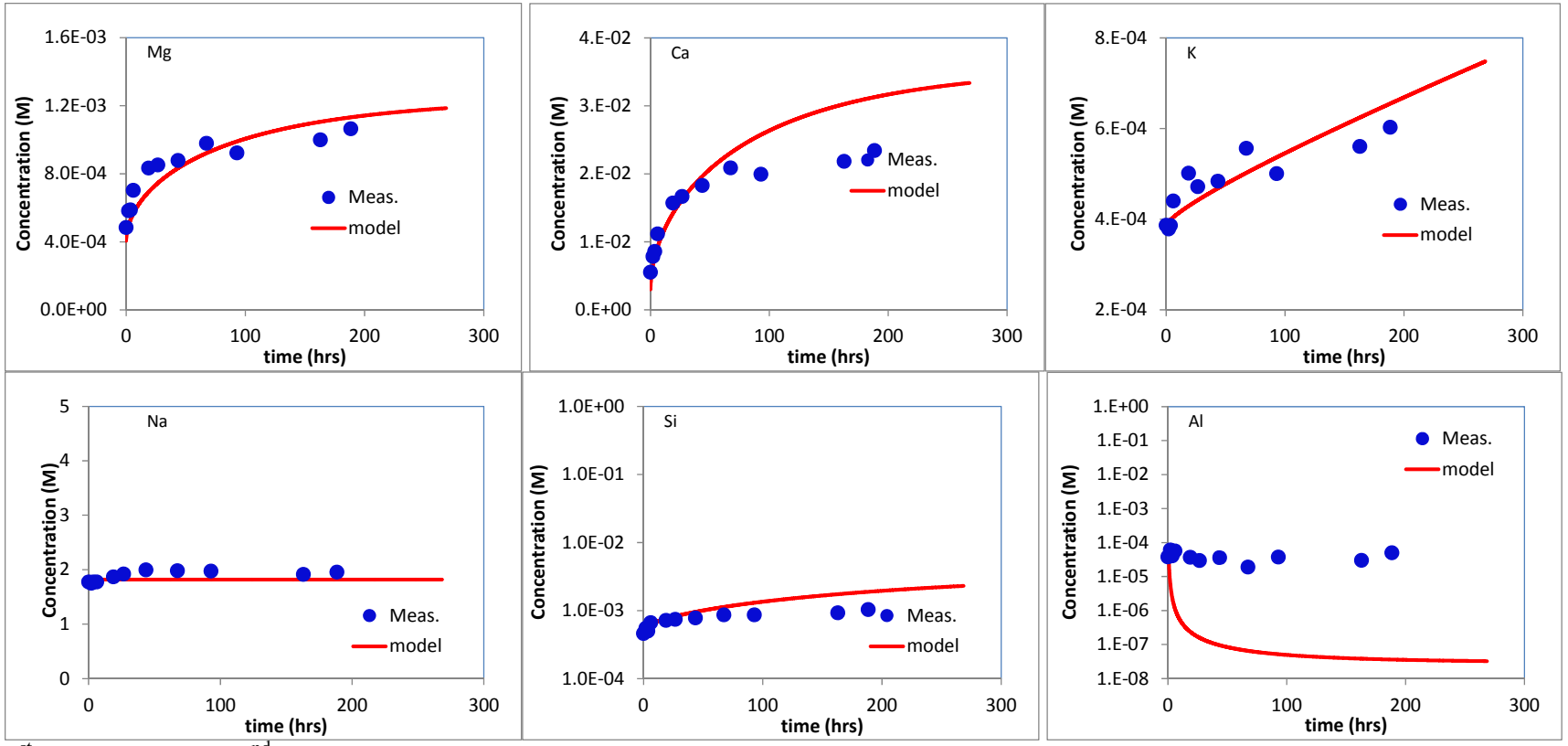

1st row: Mg, Ca, K; 2nd row: Na, Si, Al

Figure 26. Comparison of measured and modeled major ion concentrations (E series; Miocene, 100°C, 300 bars)

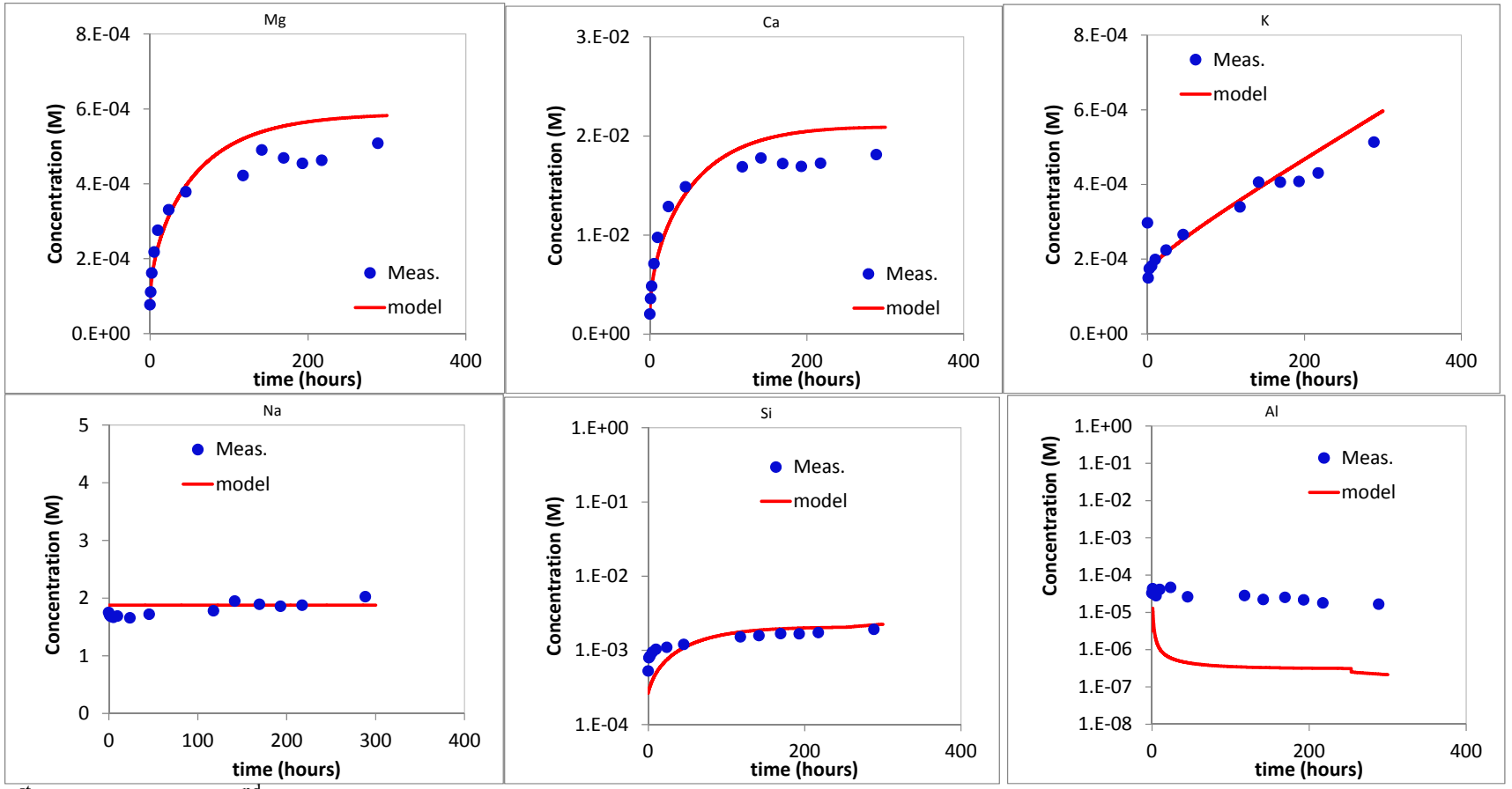

1st row: Mg, Ca, K; 2nd row: Na, Si, Al

Figure 27. Comparison of measured and modeled major ion concentrations (H series; Miocene, 130°C, 200 bars)

III-1-1.6 Kinetics Evaluation (Miocene)

Reactions are fast and happened in a matter of days. In the following figures, raw concentration data are plotted on the left-hand side whereas release rates corrected for amount of rock, water, and CO_2 partial pressure are displayed on the right-hand side (units are mmol/L/hr/g). Species analyzed are Ca, K, Mg, and sulfate. The presence of O_2 does not seem to have an impact on normalized release rates (note the log scale for the release rates).

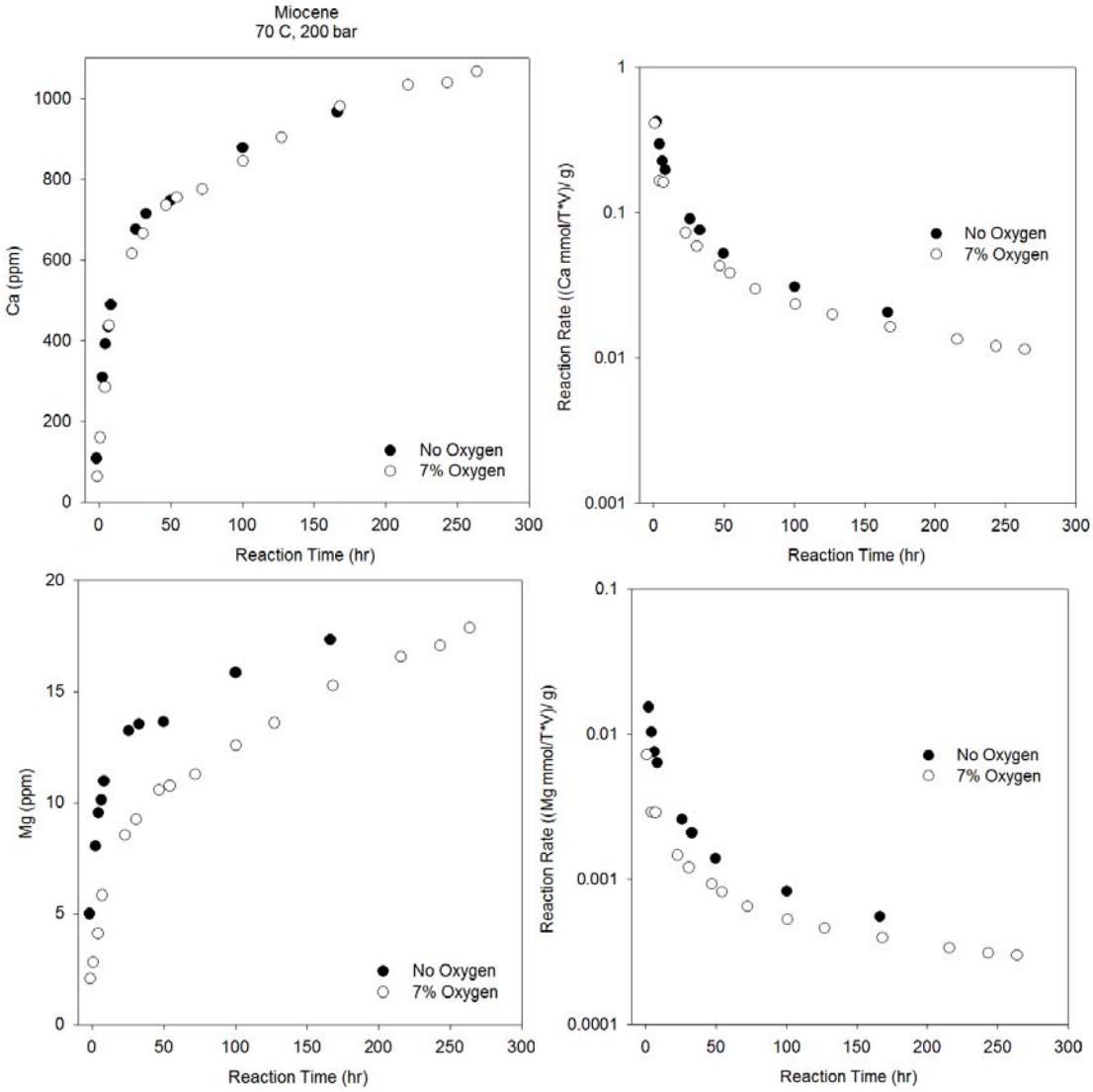

Figure 28. Miocene (70°C, 200 bars, with and without O_2) – D and L series

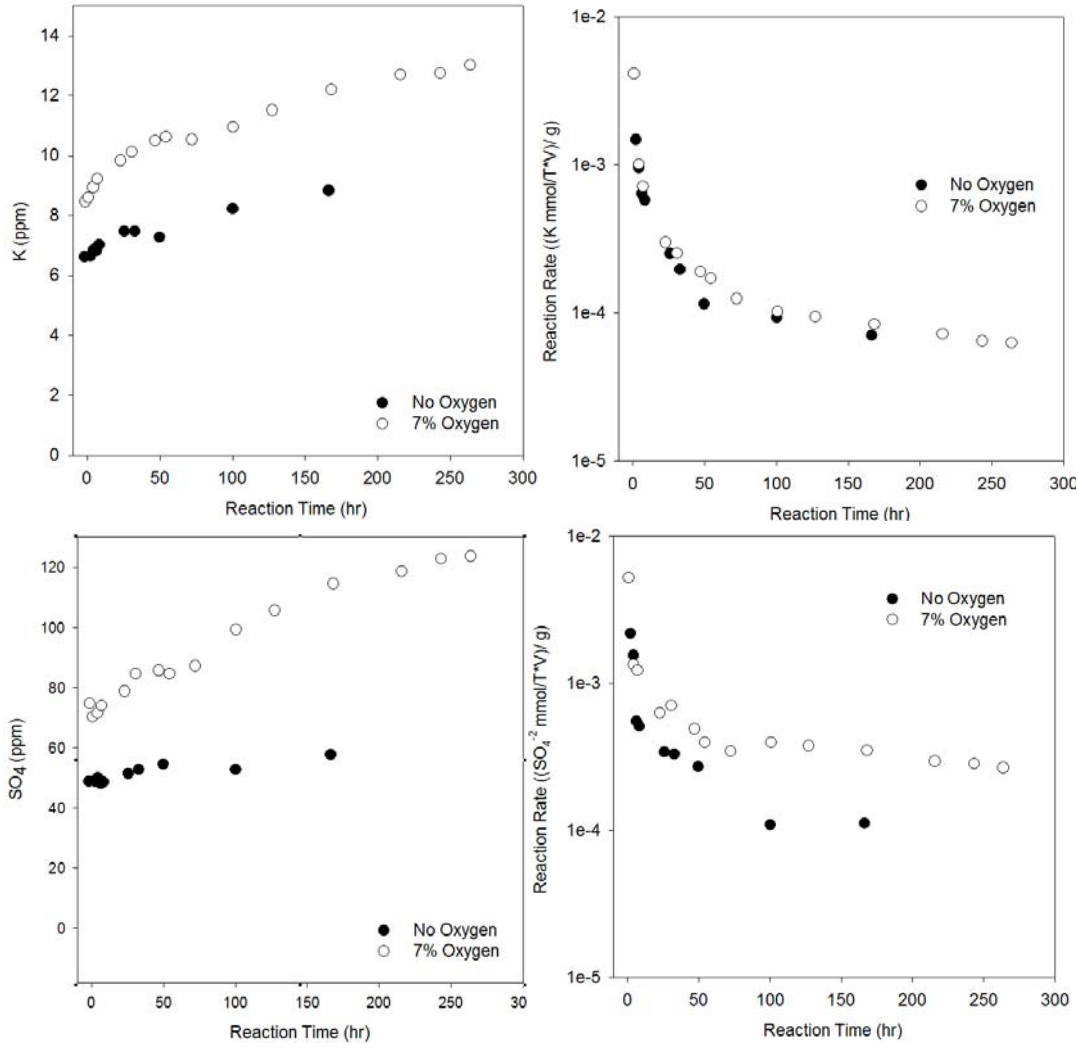

Figure 28. Miocene (70°C, 200 bars, with and without O_2) – D and L series (continued)

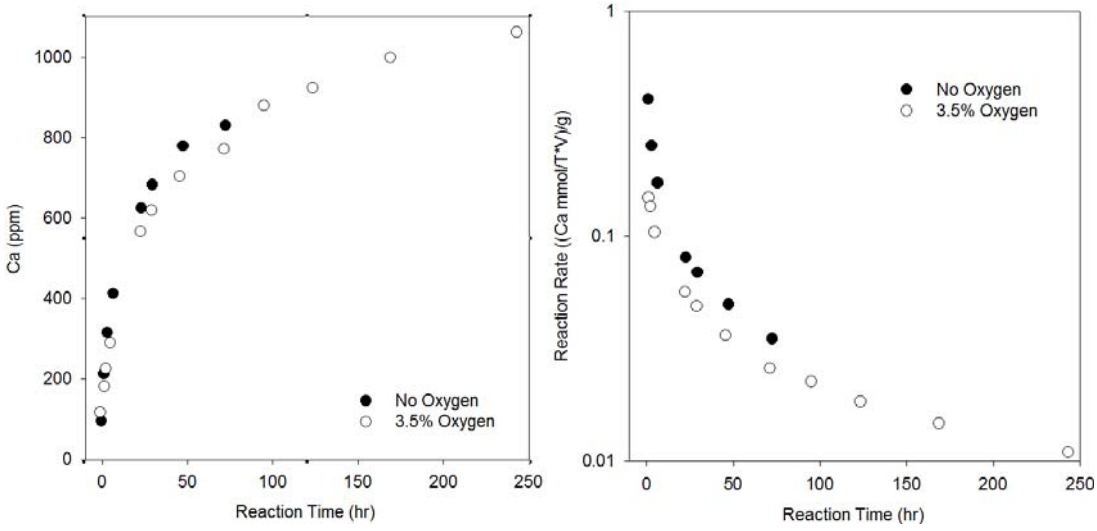

Figure 29. Miocene (100°C, 200 bars, with and without O_2) – R and S series

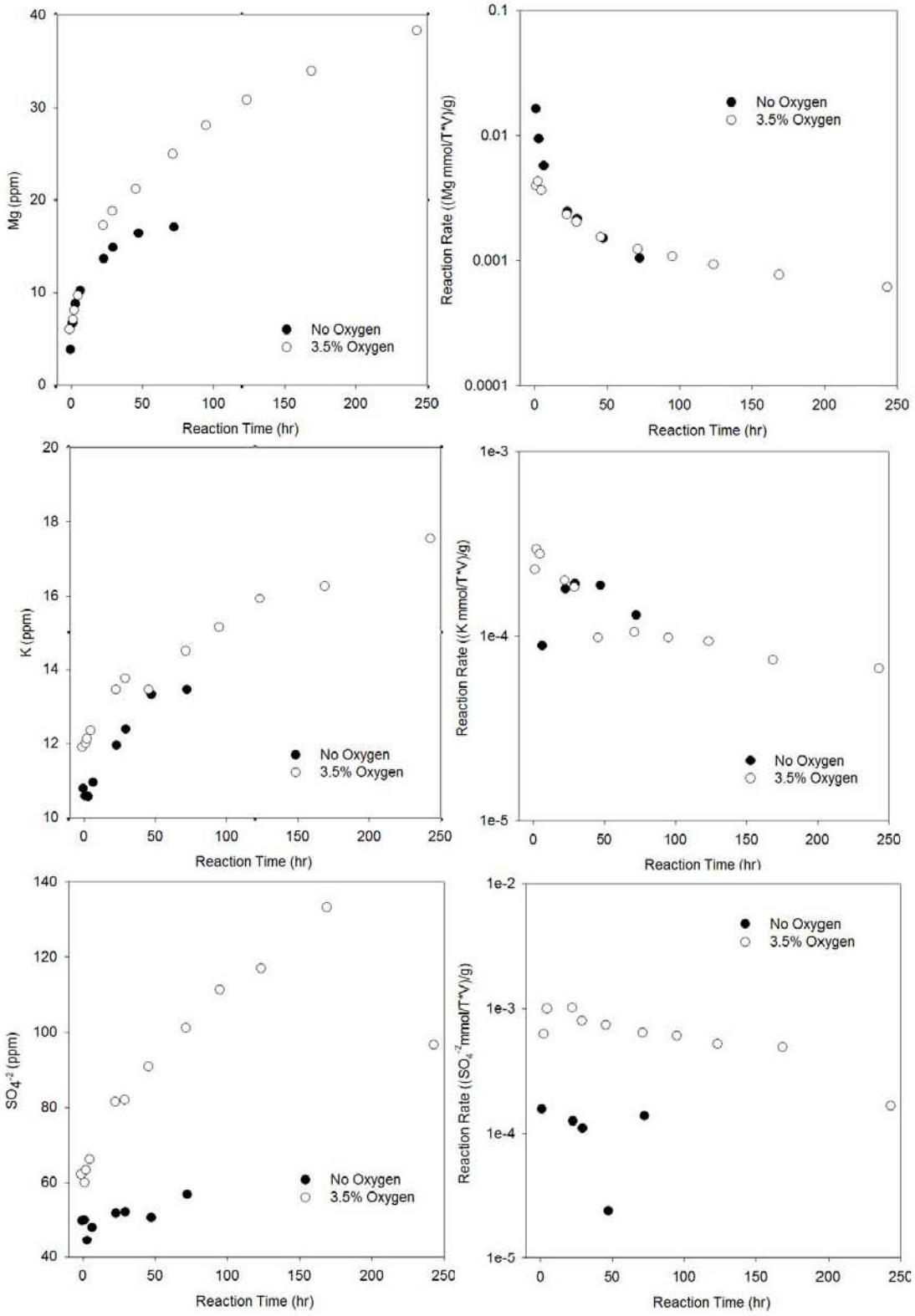

Figure 29. Miocene (100°C, 200 bars, with and without O_2) – R and S series (continued)

III-1-2 Cranfield

III-1-2.1 Description of Unreacted Sample (Cranfield)

The Cranfield sample tested in the CO_2 and CO_2+O_2 reaction experiment is a typical Tuscaloosa sandstone which mainly comprises of quartz grains and chlorite coatings. Kaolinite and some chlorite occur as pore-filling phases. There is only small amount of reactive minerals such as albite. The sample contains only trace amount of carbonate minerals. XRD mineral analysis shows that the tested sample contains quartz and chlorite as the most abundant minerals (Table 13). Combined, they consist of 87% of the rock. Kaolinite is other major mineral phase at 7%.

See Appendix C for a detailed description of Cranfield rocks.

Table 13. XRD mineral composition (%) of Cranfield core sample for reaction experiment

Sample	Quartz	Chlorite	Kaolinite	Illite	Albite	Anatase	Total
CFU31F-3 10476.6	66.89	20.25	7.31	1.96	1.76	1.82	99.99

III-1-2.2 Description of Sample Reacted with brine and CO_2 (Cranfield)

Previous studies of reservoir geochemistry during CO_2 injection (field measurements) and laboratory autoclave experiments suggest limited mineral reactions between the Tuscaloosa sandstone and CO_2 (Lu et al., 2012). In this study, the experiment with pure CO_2 at 70 ºC and 200 bar shows similar results with little reactivity. The rock sample was not altered by CO_2 saturated brine. The reacted rock sample show intact mineral surface of quartz grains and chlorite flakes (Figure 30A and B). Apart from occasional salt crystals formed from drying of remained brine, the rock sample reacted with brine and CO_2 does not show any notable difference from the original sample.

III-1-2.3 Description of Sample Reacted with Brine, CO_2 and O_2 (Cranfield)

Series O documents the impact of O_2 on the Cranfield samples that was chosen particularly chlorite-rich. Cranfield rocks have been exposed to pure CO_2 in experiments unrelated to this project (Lu et al., 2012). Reservoir minerals [quartz -79.4%, chlorite (chamosite variety) -11.8%, kaolinite -3.1%, illite -1.3%, calcite -1.1%, dolomite -0.4%), and albite -0.2%] were fairly unresponsive to CO_2. However, the rock sample reacted with CO_2 and O_2 shows notable reaction evidence. Red-brown stain appeared at sample surface after it was retrieved from the reaction cell. Under high magnification SEM, it is found that the red color is from iron oxide buds of nanometer size which precipitated on mineral surface (Figure 30C, D, and E). The iron oxide crystals occur on chlorite flakes in an orderly fashion, while they appear to be randomly littered on quartz surface. The source of iron is likely a chlorite which is a common iron-bearing member of the chlorite group called chamosite. (Ferrous) iron is the major cation in chamosite as shown in the Energy Dispersive X-ray (EDS) spectrum (Figure 30F). Apparently, iron (II) in chlorite was released by reacting with carbonic acid and oxidized by O_2 during the experiment (Equations 1 and 2). Both CO_2 and O_2 are necessary as CO_2 alone did not impact chlorite. These reactions would also release Si, Mg and Al.

$$(Fe^{2+},Mg)_5Al(AlSi_3O_{10})(OH)_8 + 16H^+ = 5(Fe^{2+}, Mg^{2+}) + 3SiO_{2(aq)} + 2\,Al^{3+} + 12H_2O \quad (1)$$

$$4Fe^{2+} + 3O_2 \rightarrow 2Fe_2O_3 \quad (2)$$

Figure 30. Cranfield sample reacted with pure CO_2 and with CO_2+O_2

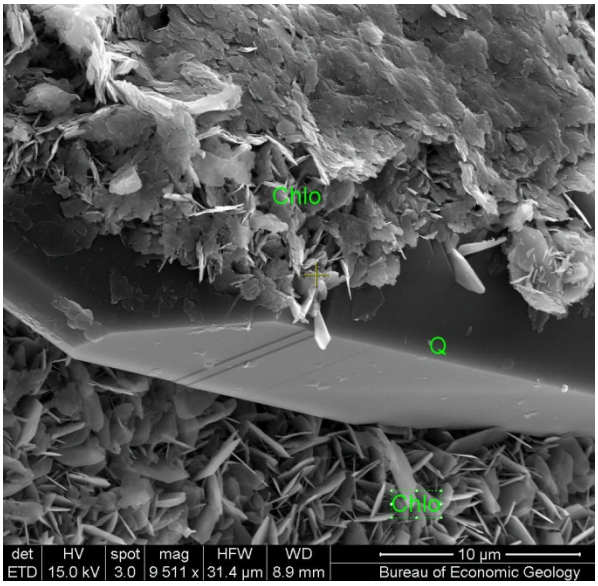

Figure 30**A.** Chlorite flakes surrounding a quartz crystal with no evidence of reaction. Reacted with CO_2.

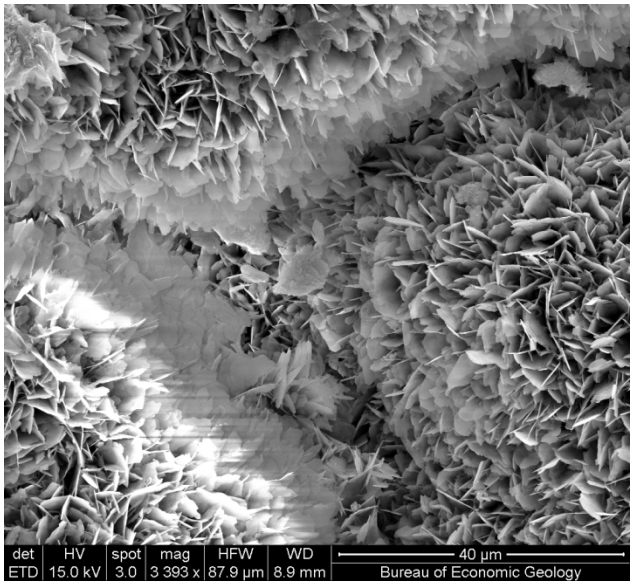

Figure 30**B.** Chlorite coats on mineral grains with intact flaky occurrence. Reacted with CO_2.

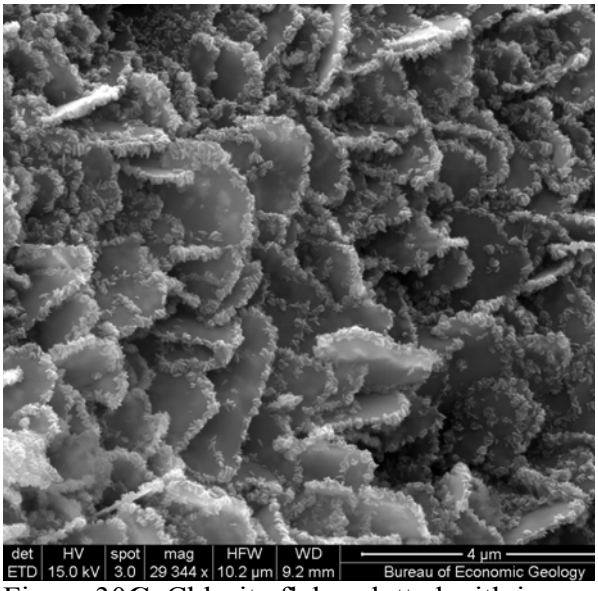

Figure 30**C.** Chlorite flakes dotted with iron oxide crystals which may be derived from oxidation of chlorite. Reacted with CO_2 and O_2.

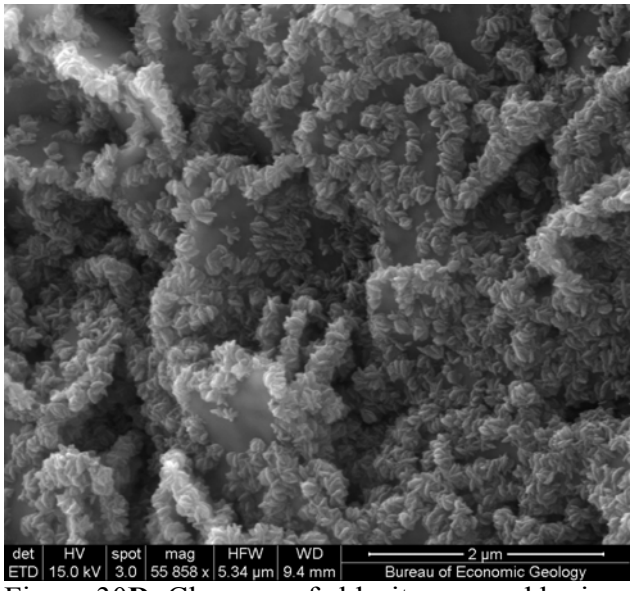

Figure 30**D.** Close-up of chlorite covered by iron oxide. Reacted with CO_2 and O_2.

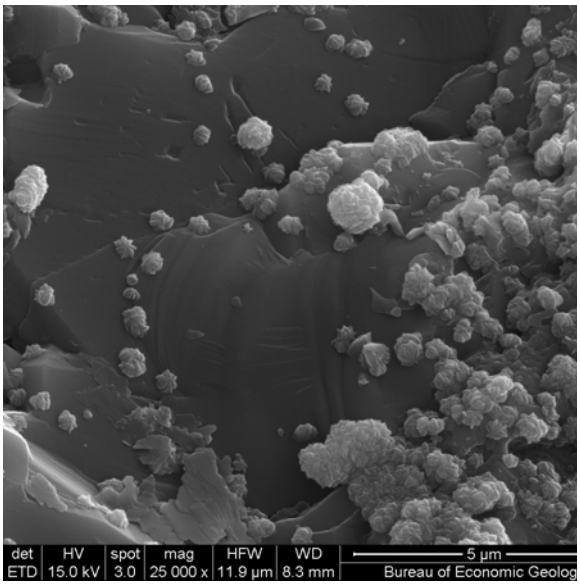

Figure 30**E.** Iron oxide buds precipitated on quartz surface. Reacted with CO_2 and O_2.

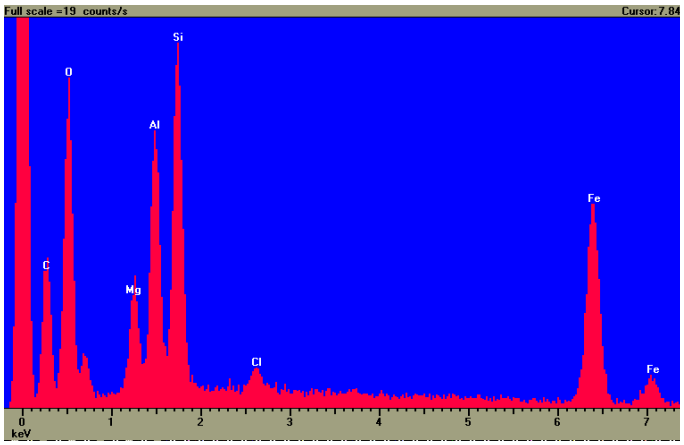

Figure 30**F** Energy Dispersive X-ray spectrum of original chlorite showing chemical composition of chamosite $(Fe^{2+},Mg)_5Al(AlSi_3O_{10})(OH)_8$

III-1-2.4 Analysis of Time Series (Cranfield)

III1.2.4.1 Presentation of Results (Cranfield)

Only two experiments were performed with Cranfield samples (O and P series at 70°C with and without O_2). No assessment of temperature-related variations is then possible. We present comparison of the two cases with and without O_2. Ca concentrations are much lower than in the Miocene owing to the lack of calcite and appear ~independent of the presence of O_2. Sulfate is also relatively independent of the presence of O_2 but still slightly higher likely denoting the presence of some undetected pyrite; sulfate concentrations stay <50 ppm as opposed to <150 ppm in the Miocene case for which some very minor pyrite has been detected. Mg (also true for Ba, Sr, Zn, and Pb but not Mn), Si, K (also true for Rb), and alkalinity are slightly higher with pure CO_2 than when O_2 is present. Al concentrations are also higher with pure CO_2 but in both cases, with and without O_2, they drop quickly suggesting precipitation of silicates probably clays. Si concentration time series also show some irregularities but not a clear drop as visible in the Al time series. O_2 seems to favor silicate precipitation maybe because some building components have been released by alteration of chlorite. Ti, Ni, Cu, and Mn increase somewhat when O_2 is added and suggest some minor steel degradation (see Table 4 for chemical composition of components). Cr, Mo, and V should also follow the same pattern of increased concentration with O_2 if the steel degradation hypothesis is correct, however unlike the 4 metals above they form oxyanions (chromate, molybdate, and vanadate) in the presence of O_2 which then sorb on FeOx. MnOx might also form. The MnOx/FeOx deposits are fresh and likely of large specific area and easily scavenge oxyanions. This is true also for phosphate and maybe for borate. Co concentrations, similarly to the metal cations, are higher when O_2 is present; however it is not present in the reactor components. An alternate explanation is that the metals, sorbed to FeOx grain coatings, are released when the pH is dropped as CO_2 is added (ZPC of Co is higher than most, see Dzomback and Morel, 1990). They are more thoroughly released when O_2 is added and those forming oxyanions are then sorbed back on newly formed FeOx surfaces. TiO_2's are also

recognized as good sorbers and anatase has been observed in non-negligible amounts in the rock samples, although it is likely detrital. However the strong increase in sorbing behavior when O_2 is added suggests that anatase does not play a big role in the process (its specific surface area is likely small compared to that of FeOx consistent with its detrital origin)

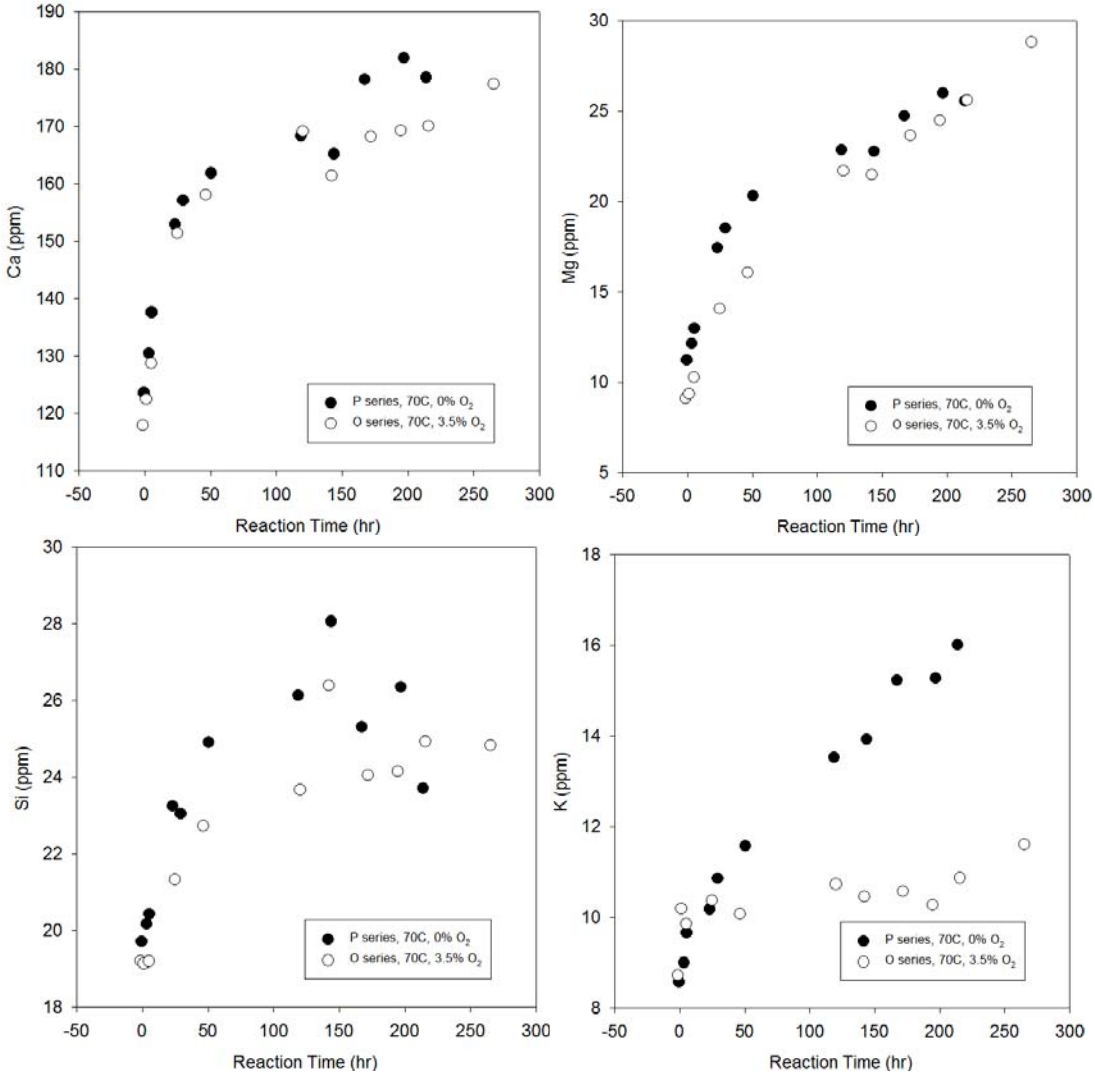

Figure 31. Cranfield, 70°C, 200 bars, with and without O_2 – P and O series – Major elements

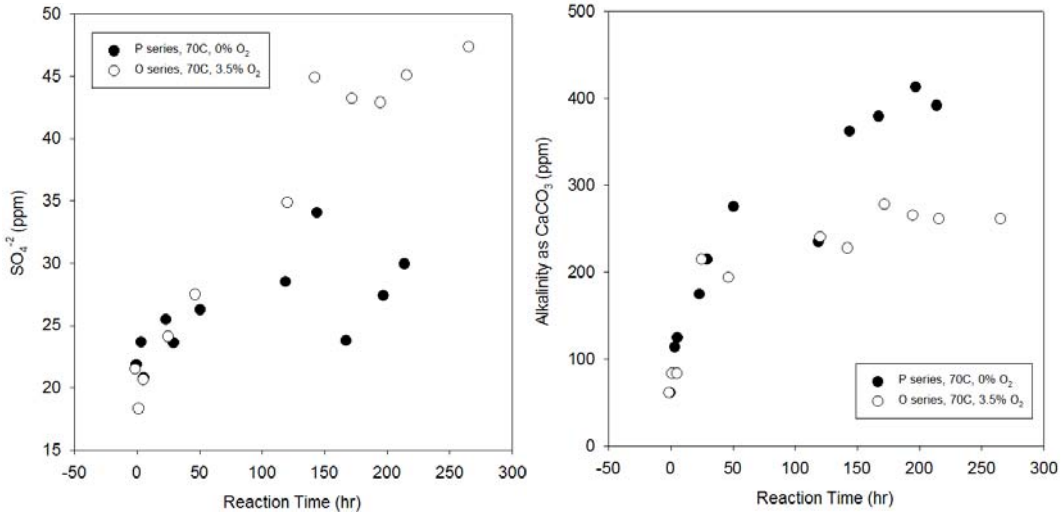

Figure 31. Cranfield, 70°C, 200 bars, with and without O_2 – P and O series – Major elements (continued)

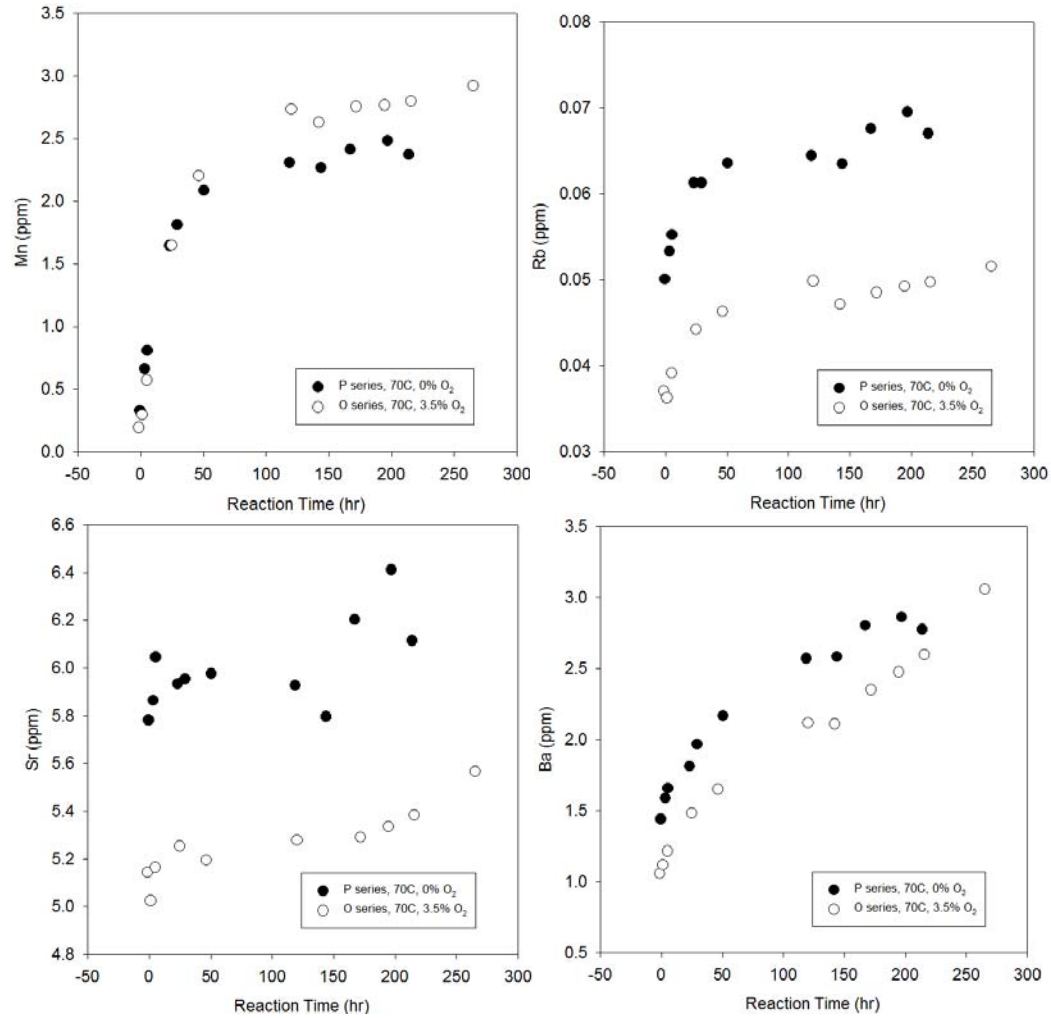

Figure 32. Cranfield, 70°C, 200 bars, with and without O_2 – P and O series – trace elements

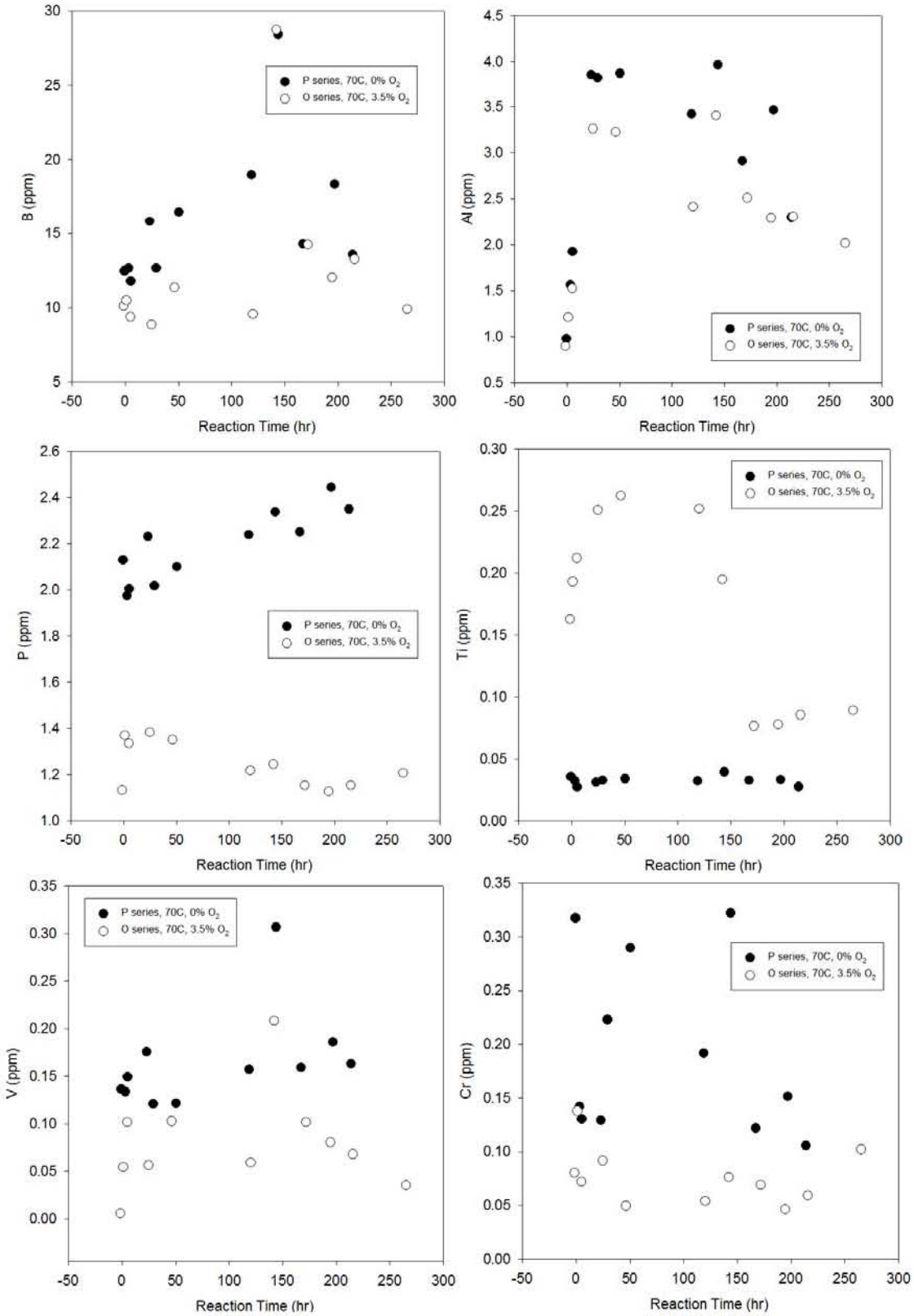

Figure 32. Cranfield, 70°C, 200 bars, with and without O_2 – P and O series – trace elements (continued)

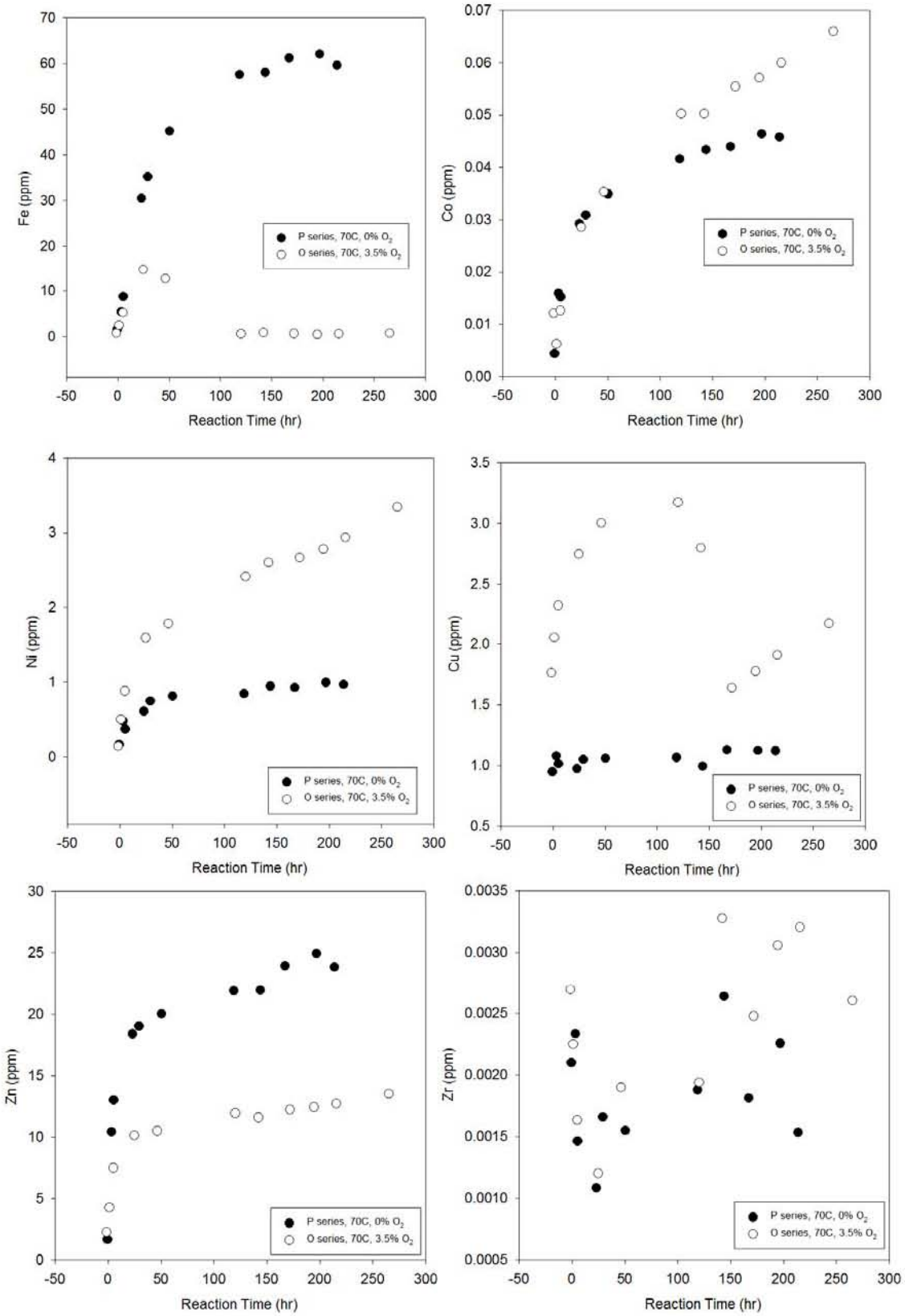

Figure 32. Cranfield, 70°C, 200 bars, with and without O_2 – P and O series – trace elements (continued)

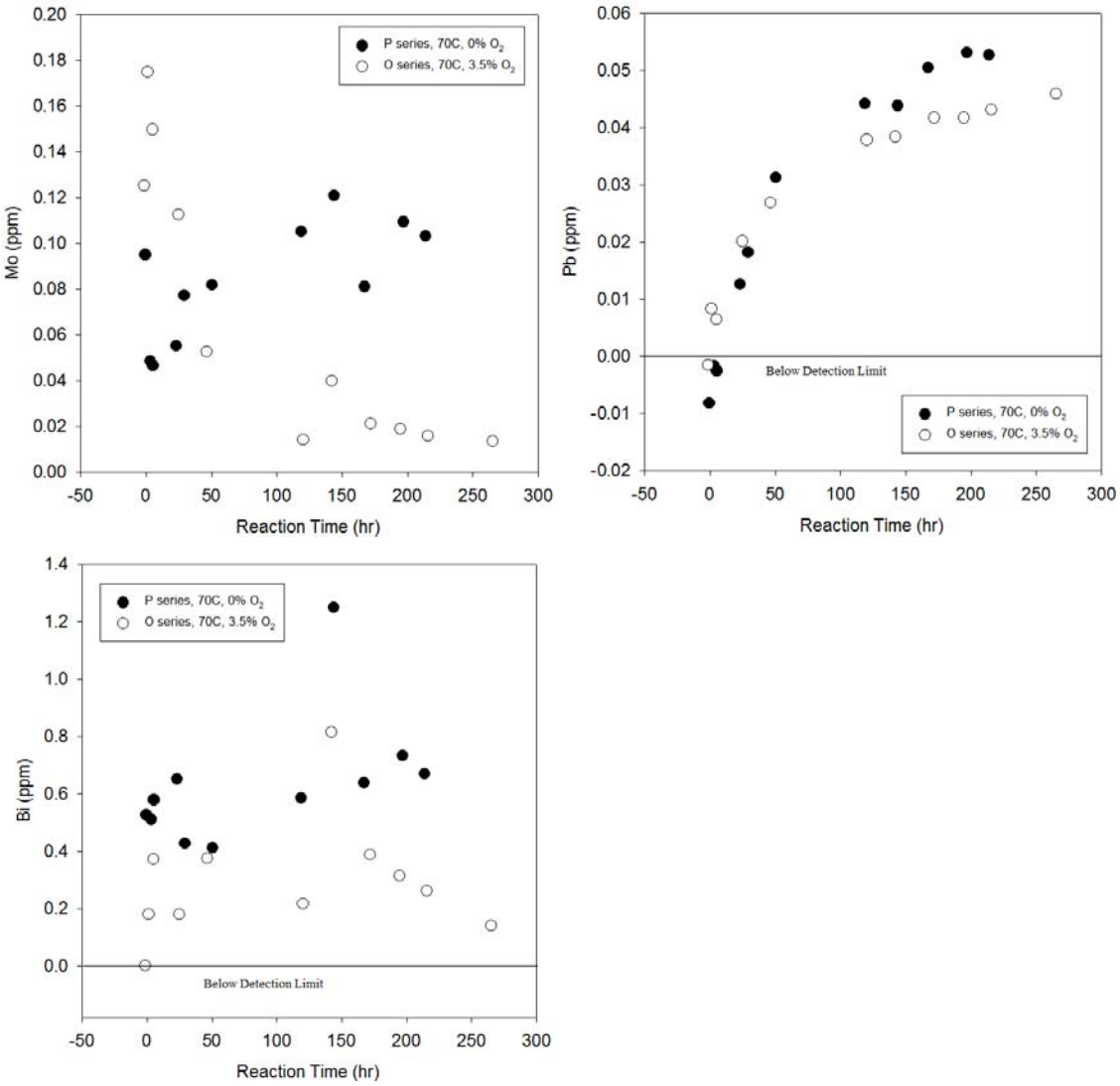

Figure 32. Cranfield, 70°C, 200 bars, with and without O_2 – P and O series – trace elements (continued)

III1.2.4.2 Modeling Results (Cranfield)

In this section we show that we can explain Ca and Mg concentrations by carbonate dissolution (Figure 33). K-feldspar dissolution does not entirely explain K, Si, and Al concentrations.

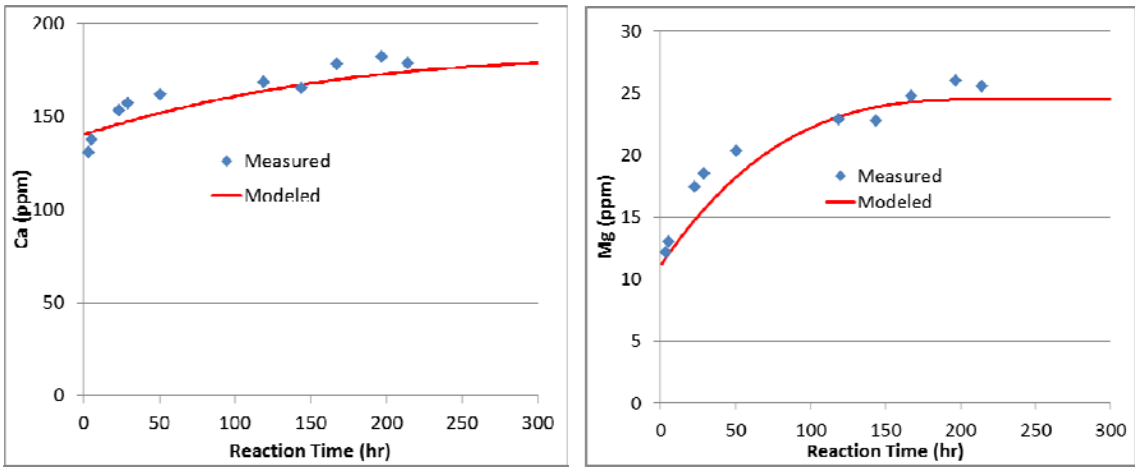

Figure 33. Comparison of measured and modeled major ion concentrations (P series; Cranfield, 70°C, 200 bars, pure CO_2)

III-1-2.5 Kinetics Evaluation (Cranfield)

Reactions are fast and happen in a matter of days. Release rates are plotted on Figure 34 (units are mmol/L/hr/g). When corrected for sample mass, amount of fluid, and CO_2 partial pressure, rate of Ca and Mg dissolution are essentially the same with or without O_2. Early rate of increase in sulfate aqueous concentration appears the same with or without O_2 (maybe desorption due to competition with bicarbonate) but at later times no-O_2 rate drops off while O_2 rate stays level, likely due to the impact of pyrite dissolution. In the no-O_2 case K releases are fast but drop off very quickly whereas when O_2 is present the slowly declining rate is more level. This suggests there are probably two sources for K.

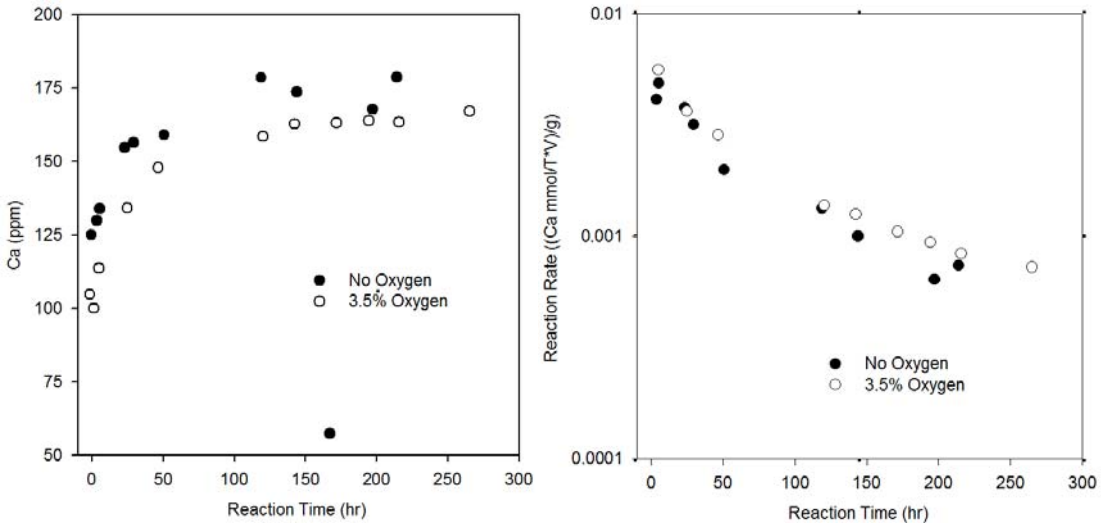

Figure 34. Cranfield (P and O series, 70°C, 200 bars, with and without O_2)

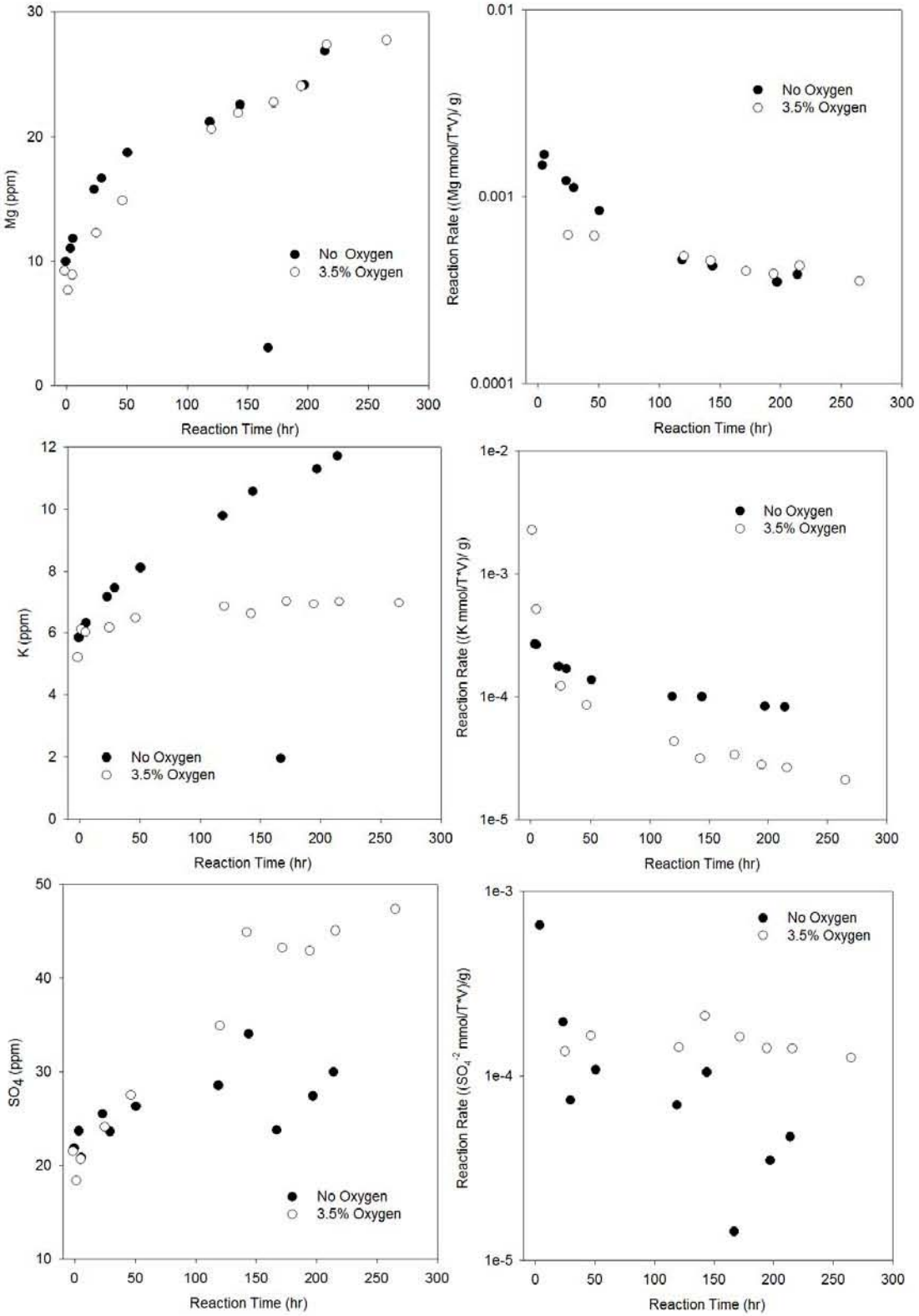

Note: concentrations do not match exactly concentrations presented in Figure 32 because IC data were used to plot them as opposed to ICP-MS for this figure

Figure 34. Cranfield (P and O series, 70°C, 200 bars, with and without O_2) (continued)

III-1-3 Cardium Sands

III-1-3.1 Description of Unreacted Sample (Cardium)

The samples studied (ARC-PC-3 and 4) were kindly provided by ARC and were sampled from core of the Cardium Sands located in the Pembina Area. The rock is described as coming from the parasequences 3 and 4 and associated with a shoreline depositional environment. Our petrographic observations are consistent with a study by Machemer and Hutcheon (1988). Description that came with the samples stated that "the mineralogy of the Cardium sand units is primarily chert, quartz, and clay minerals such as illites, smectites and chlorites. Siderite is also commonly found within each lithofacies." This description was confirmed by our own XRD analysis. The fine grained sandstone sample contains 75.5 % of quartz and approximately 17% of clay minerals (kaolinite and illite) (Table 14). These minerals are relatively unreactive. It also contains relatively reactive mineral phases, such as iron/magnesium carbonates, potassium feldspar and plagioclase. These minerals show relatively smooth and clean grain surface in the original samples (Figure 35).

Table 14. XRD mineral composition of Cardium core sample for reaction experiments

Sample	Quartz	Kaolinite	Illite	Albite	K-feldspar	Siderite	Total
ARC-PC-3	75.5	10.4	6.5	2.5	4.2	0.9	100.0

Figure 35. Unreacted Cardium sample

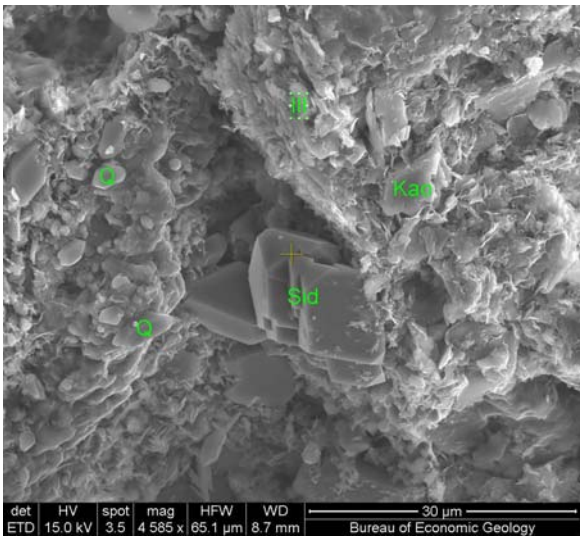

Figure 35A. Siderite crystal with smooth and clean surface in unreacted sample.

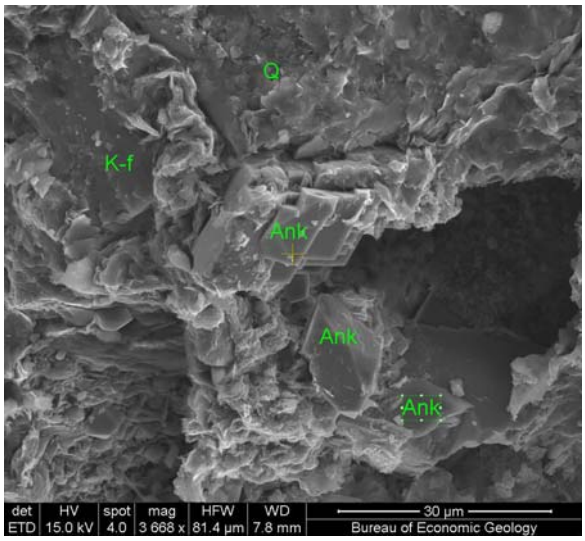

Figure 35B. Smooth ankerite rhombs in unreacted sample.

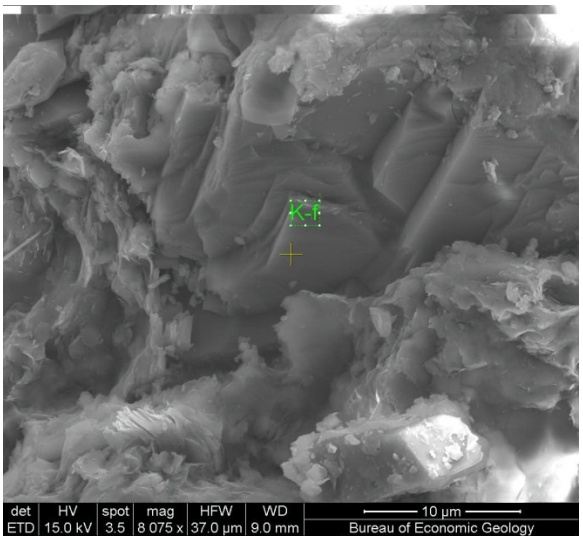

Figure 35C. K-feldspar grain showing clean steps at grain

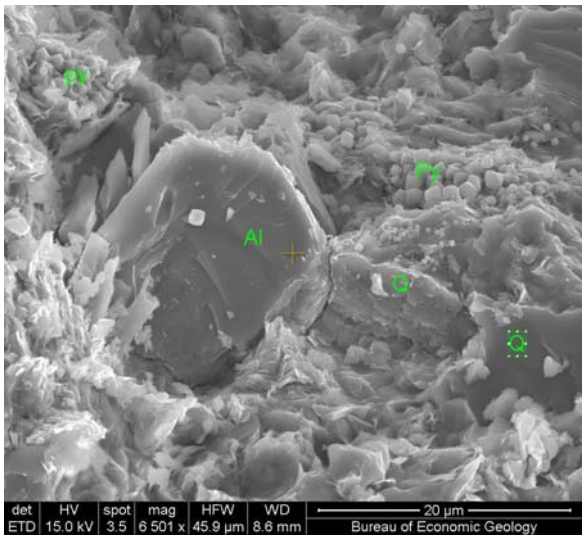

Figure 35D. An albite grain with smooth surface.

III-1-3.2 Description of Sample Reacted with brine and CO_2 (Cardium)

We performed two experiments on ~8 g of rock fragments with CO_2 at 200 bars (corresponding to a depth of ~6,000 ft) and at 70 and 100°C in equilibrium with a 1.88 molal NaCl brine (~100,000 ppm). On the surface of the reacted sample, carbonate minerals were severely corroded. An iron-rich ankerite grain shows crystal cavities due to dissolution. Compared to the relatively complete crystals in the unreacted sample (Figure 35A and B), it is certain the carbonate minerals were leached by the acid brine. Small clay flakes are often seen in on the surface of corroded grains (Figure 36A). These clays may be new precipitates during the experiment. K-feldspar and plagioclase (mostly albite) grains show more dissolution features than the unreacted sample. Feldspar grains often show corrosion pits and holes (Figure 36B and C). Small clay flakes are usually found nearby (Figure 36C), indicating that they may be reaction products of feldspar dissolution. For example, Figure 37A shows that a K-feldspar grain was corroded from inside and only a thin skin remained. Kaolinite can often be seen in the vicinity of corroded feldspar grains (Figure 37C). Kaolinite may be reaction products of feldspar dissolution. Most calcite was dissolved at the reaction surface and only a trace amount remained to be seen (Figure 37D).

Energy dispersive spectrometry (EDS) coupled with SEM was used to conduct semi-quantitative chemical analysis on sample surface. Areas of 1.48×1.28 cm were randomly chosen and scanned to derive average element concentrations (Figure 37). Comparison between the unreacted and reacted samples shows relative change of cation concentrations. In the unreacted sample, calcium is detectable by EDS (Figure 37B); the sample reacted with CO_2, however, shows no Ca peak, indicating carbonate dissolution.

Figure 36. Cardium sample reacted with brine and CO_2.

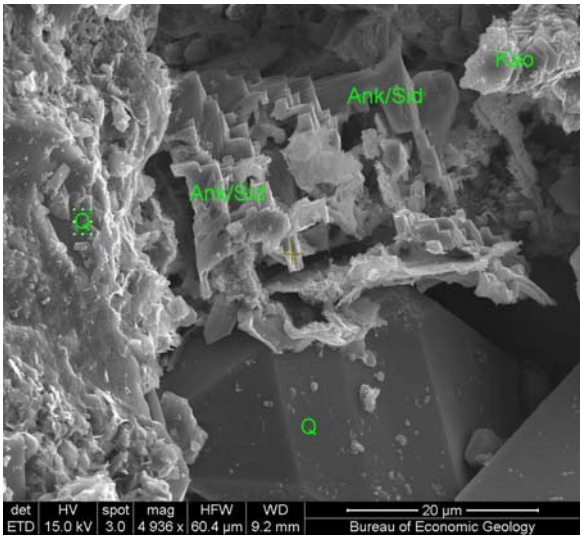

Figure 36A. Reacted sample showing corroded ankerite crystals.

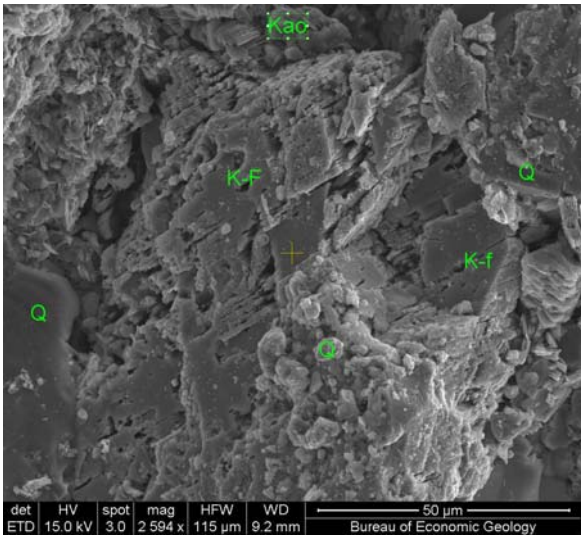

Figure 36B. K-feldspar with corrosion pits in reacted sample.

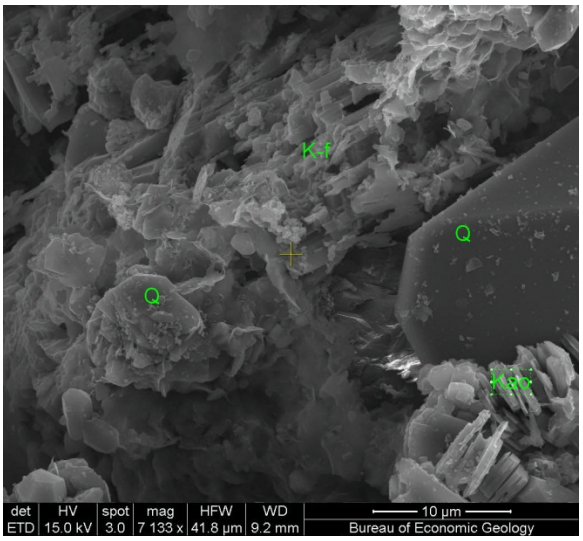

Figure 36C. A corroded K-feldspar grain with clay flakes (possibly new precipitates) littered on surface.

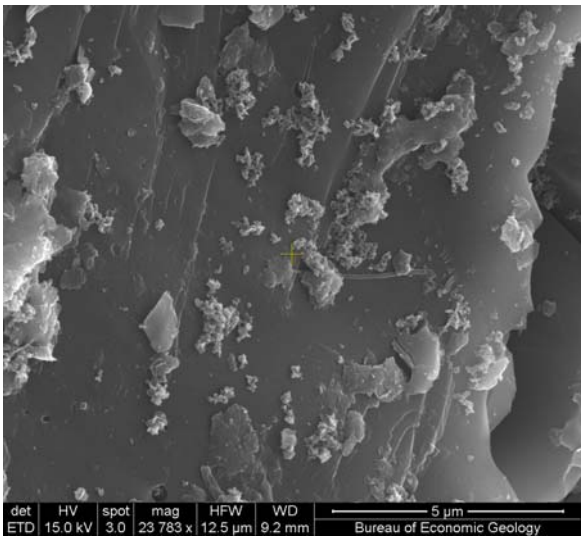

Figure 36D. Iron oxides and illite flakes on a quartz surface.

Figure 37. Cardium sample reacted with brine and CO_2 (EDS data)

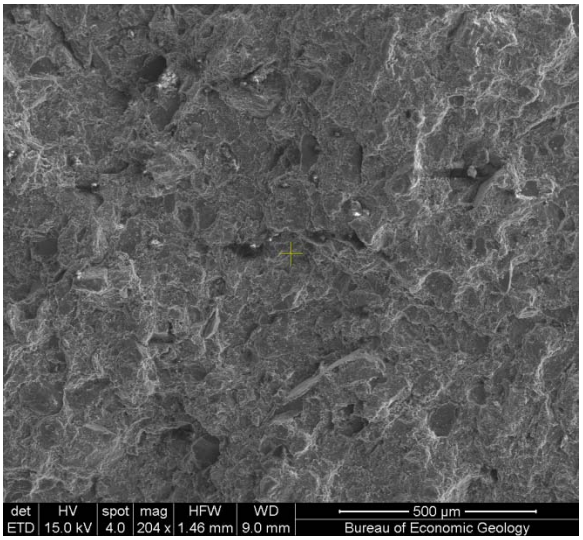

Figure 37A. EDS scan area (1.48×1.28 cm) of unreacted sample surface.

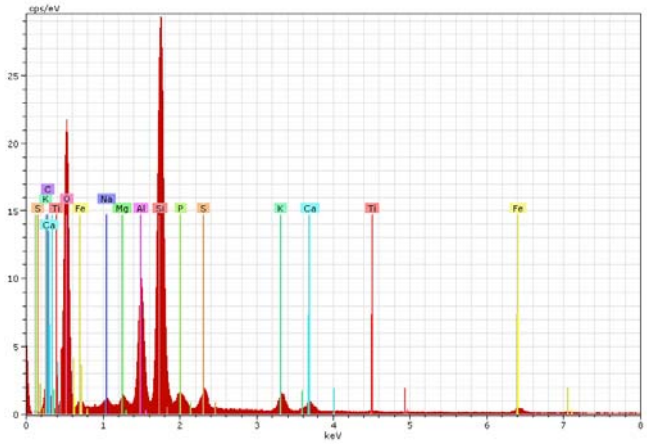

Figure 37B. EDS full frame scan of unreacted sample area of Figure 37A. Surface area chemical composition: Ca, 1.4 %; Na, 0.8 %; K, 1.8 %; Mg, 0.6 %; Fe, 2.6 %; Ti, 0.4%

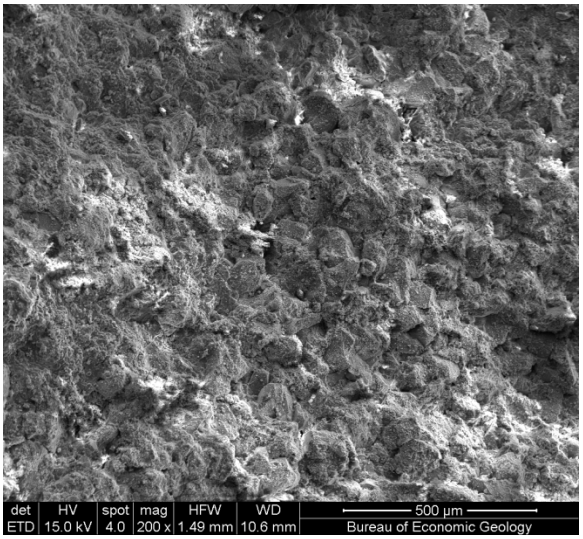

Figure 37C. EDS scan area (1.48×1.28 cm) of sample surface reacted with CO_2 and maybe O_2.

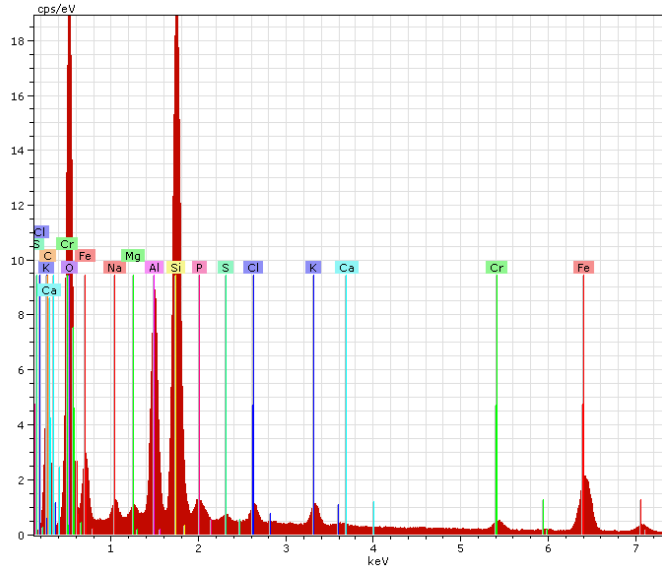

Figure 37D. EDS full frame scan of reacted sample area of Figure 37C, showing lower Ca peak and higher Fe peak. Cr is also detected (some steel dissolution from residual O_2). Surface chemical composition: Ca, 0%; Na, 0.5 %; K, 0.7 %; Mg, 0.1 %; Fe, 11.9 %; Ti, 0 %, Cr, 1.0%.

III-1-3.3 Description of Sample Reacted with Brine, CO_2 and O_2 (Cardium)

As expected, experiments showed quick calcite dissolution and slower feldspar dissolution as two major mineral reactions. Results from the experiments with and without O_2 show some different reactions for the Cardium Sands, Alberta sample which consists of quartz (62.3%), kaolinite (15.0%), illite (12.7%), K-feldspar (7.1%), plagioclase (2.8%) and trace amount of pyrite, siderite, and other minerals. Compared with the sample reacted with pure CO_2, the presence of O_2 has caused pyrite oxidation and produced FeOx which precipitated on the surface of reacted rock chips. We are confident that the FeOx patches do result from geochemical reactions with the rock not steel corrosion that was observed in previous experiments before the experimental setup change.

Aqueous chemical results suggest faster dissolution of carbonate and feldspar minerals when O_2 is present. The unreacted and reacted rock samples were carefully examined using SEM equipped with an X-ray energy dispersive spectrometry system which enables semi-quantitative mineral chemical analysis. Besides dissolution of carbonates and feldspar dissolution caused by CO_2, pyrite appeared to be largely consumed in the O_2 experiment. Small amount of pyrite is present as framboids in the original rock sample (Figure 38A). Individual pyrite crystals appear mostly as fresh-looking octahedrons. In the reacted sample of the O_2 experiment, pyrite is almost absent. The rare remaining crystals no longer show perfect crystalline outline and they are covered by small flaky iron oxides (Figure 38B). Iron oxide flakes are ubiquitously present on mineral surfaces, which make the reacted rock chip appear red on surface (Figure 38C and D). Figure 38C shows a corroded albite mineral surface littered with iron oxide flakes of ~100s nanometer in size. The close up SEM image (Figure 38D) shows the flakes occur in clusters which grow on smooth quartz surface. Based on above evidence, iron oxide is likely produced from oxidation of pyrite as captured by Equations 1 and 2.

$$2FeS_2 + 2H_2O + 7O_2 \rightarrow 2Fe^{2+} + 4H^+ + 4SO_4^{2-} \quad (1)$$

$$4Fe^{2+} + O_2 + 4H^+ \rightarrow 4Fe^{3+} + 2H_2O \quad (2)$$

Sulfate is the other reaction product, which can be observed in the water chemistry from the reaction experiment. Pyrite oxidation is the only O_2 related mineral reaction we observed. It impact will depend the abundance of pyrite in the reservoir rock. If abundant pyrite exists, O_2 impurity would be consumed relatively quick (in several days to weeks). The produced iron oxides would precipitate on to mineral surfaces. Their impact on permeability is likely to be small for the rock type tested in this experiment, primarily due to their small size (100s nanometer).

Figure 38. Cardium sample reacted with brine, O_2 and CO_2.

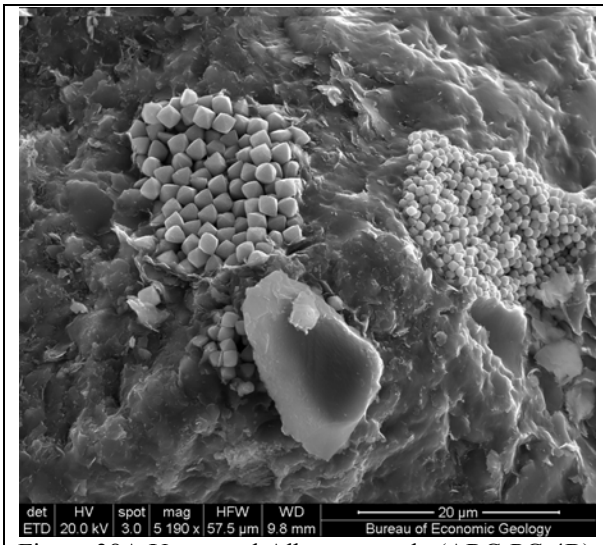

Figure 38A Unreacted Alberta sample (ARC-PC-4B). Small amount of pyrite present as fresh-looking octahedrons.

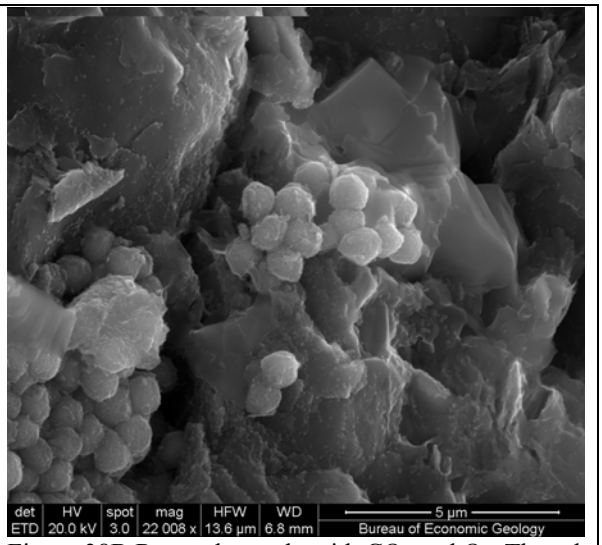

Figure 38B Reacted sample with CO_2 and O_2. Though it is impossible to quantify its abundance, pyrite is extremely rare in reacted sample compared to the original sample. Pyrite crystals covered by tiny flakes of iron oxide which may be derived from pyrite oxidation.

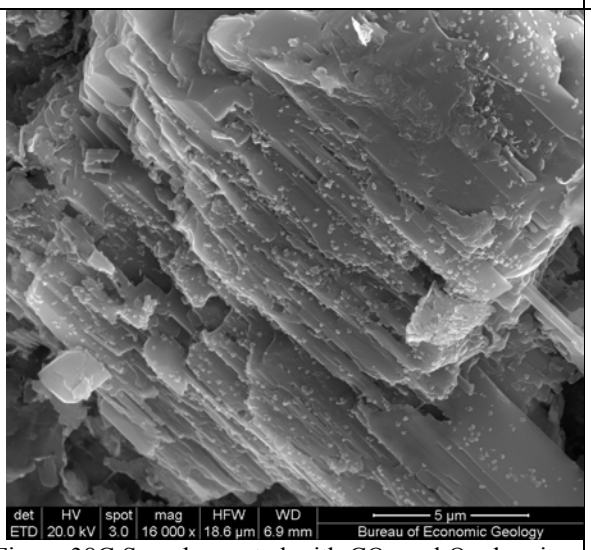

Figure 38C Sample reacted with CO_2 and O_2 showing a corroded albite grain with scattered iron oxide flakes on its surface.

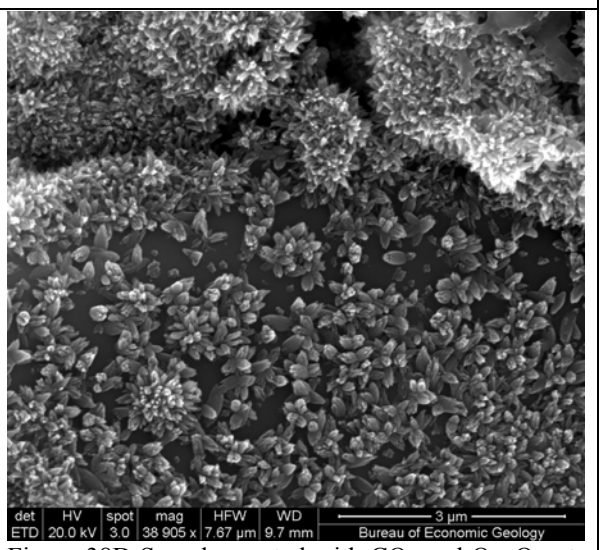

Figure 38D Sample reacted with CO_2 and O_2. Quartz grains covered by clusters of iron oxide flakes.

III-1-3.4 Analysis of Time Series (Cardium)

III1.3.4.1 Presentation of Results (Cardium)

Unlike the Miocene samples, which contained ~10% calcite, the Cardium Sands, Alberta sample mineralogy is dominated by relatively unreactive quartz and clay minerals with a small percentage of feldspars and siderite. Therefore the large increases in alkalinity and Ca

concentrations seen in the Miocene samples are not seen in the Cardium samples, but the effects of Fe-carbonate dissolution are seen (Figure 39). Generally, the Cardium samples show a more gradual increase in alkalinity, Fe and Si concentrations in the aqueous solution that is a result of carbonate dissolution dominated by Fe carbonates (siderite $–FeCO_3$- and ankerite $–CaFe(CO_3)_2$- have been identified in SEM analyses) and feldspar weathering. Ca aqueous concentrations are likely to originate from slowly dissolving ankerite or possibly plagioclase (the observed composition tends towards the more stable albite pole but it is likely to contain Ca) as Ca concentrations do not show the retrograde solubility behavior. Calcite-rich Miocene sample displays a Ca concentration >1000ppm and an associated Sr concentration of 4, Cranfield results are 180and 4 ppm. For the Cardium sands, Ca aqueous concentration are still<40 ppm after 4000 hours (with 0.6 ppm Sr). Almost all elements (Ca, Mg, Mn, Fe, Co, Ni, Zn, Pb, Ti as well as K and Rb) follow the same pattern: faster release rates at 100°C to reach a higher asymptotic plateau. Sr and Ba fall also in this group although trends are not as well-defined. Si concentration follows a similar trend but there is clearly authigenic silicates being formed kaolinite likely and maybe illite as well (but no drop in K concentration) as secondary clay minerals have been observed forming towards the end of the experiment. Al concentrations increase sharply at early times to decrease fast after a few hours and faster yet for the 100°C case. Trace elements such as B (borate), P (phosphate), maybe V (vanadate, data are unclear), Cr (chromate), and Mo (molybdate) all produce oxyanions (and they are the only ones of the analyzed elements) and all display a drop in aqueous concentration. The most likely explanation is that the oxyanions sorb on the edges of the newly formed kaolinite platelets. Only Cu shows a decrease in concentration that does not form an oxyanion.

The increase in alkalinity seen in the Cardium samples cannot be completely explained by Fe carbonate dissolution. There are likely multiple sources of alkalinity. All possible sources are: the dissolution of Fe carbonates, the dissolution of Mg and Ca carbonates, and feldspar weathering. Carbonate dissolution will produce two moles of alkalinity for every mole of carbonate dissolved while the weathering of a mole of feldspar will produce a mole of alkalinity. The experiment run at 100^0C shows slightly higher alkalinity than the experiment run at 70^0C. The molar increase in alkalinity correlates well with the molar increase of (Fe+Mg+Ca) multiplied by 2 + the molar increase in K series (Figure 40b, alkalinity expressed as bicarbonate vs. 2*(Fe + Mg+ Ca) + K expressed in mmol/L) suggesting these multiple sources of alkalinity are present. The increase in alkalinity is likely due to the combination of Fe, Mg, and Ca carbonate dissolution and K-feldspar weathering with Fe carbonate dissolution being an important contributor.

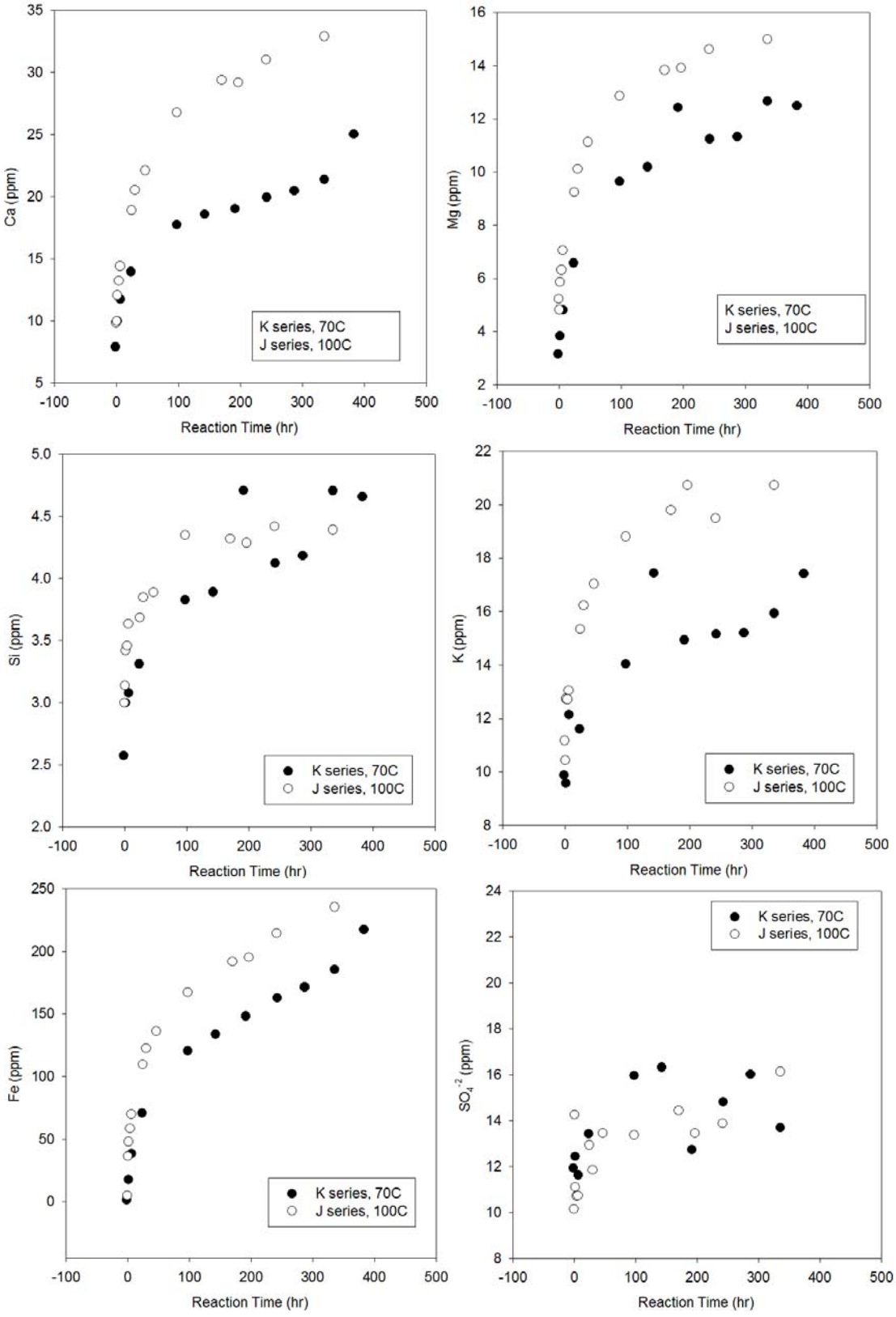

Figure 39. Impact of temperature (J and K series, Cardium, pure CO_2).

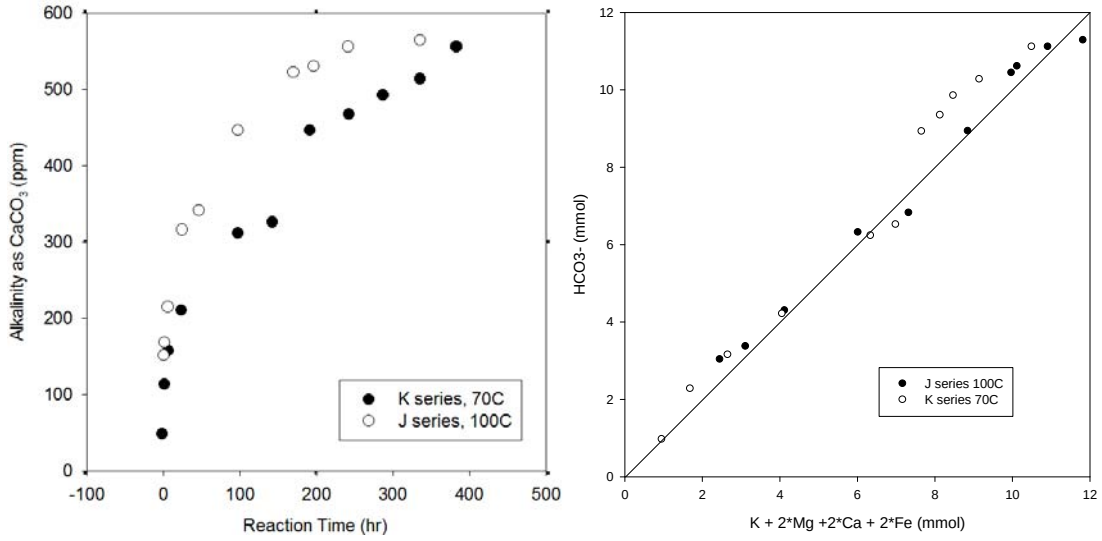

Figure 40. Alkalinity vs. reaction time (J, K series, Cardium, pure CO_2)

Impact of O_2

Comparison between the K (pure CO_2) and N (CO_2+O_2) series runs at 70^0 C and 200 bars show the effects of O_2 on aqueous geochemistry during reaction of saline brine and reservoir mineralogy in the presence of super-critical CO_2. (Figure 41). Although we have only one run to access the effects of O_2 on solution chemistry it appears that O_2 may significantly increase the dissolution rates of carbonates and silicates and oxidation of pyrite. For all elements analyzed, the release rate and final elemental concentration where higher in the experiment with O_2. This is likely related to the decrease in pH following pyrite dissolution. Br- concentrations did not experience the increase (and is not involved in water rock interactions) strongly suggesting that evaporation is not the source of the increase.

All elements (Ca, Mg, Si, K and Rb, Sr, Ba, Ti, Cu, Zn, Pb, and maybe Bi) show a concentration increase by a factor of at least 2 or 3 concomitant with the sharp increase in sulfate concentration from 15 ppm with no O_2 to ~100 ppm related to pyrite oxidation. The drop in pH sped up the degradation of Fe carbonates and feldspars. Alkalinity does not display such a large increase. Al also underwent the sharp increase in concentration but went back to low levels quickly suggesting the generation of authigenic silicates (most likely kaolinite that was actually observed). Fe and, to a lesser degree, Mn exhibit a quick drop in aqueous concentration symptomatic of the precipitation of FeOx and MnOx (Mn and Fe concentrations followed that of Ca in the non-O_2 case). As has been observed in previous experiments oxyanions sorb on newly created oxide surfaces as shown by a drop in B (borate), P (phosphate), V (vanadate), Cr (chromate, an alternative explanation would be co-precipitation with Fe to form oxides), Mo (molybdate). Ni concentrations become low in the presence of O_2 and Ni may precipitate with Fe whereas Co concentrations are higher when O_2 is present.

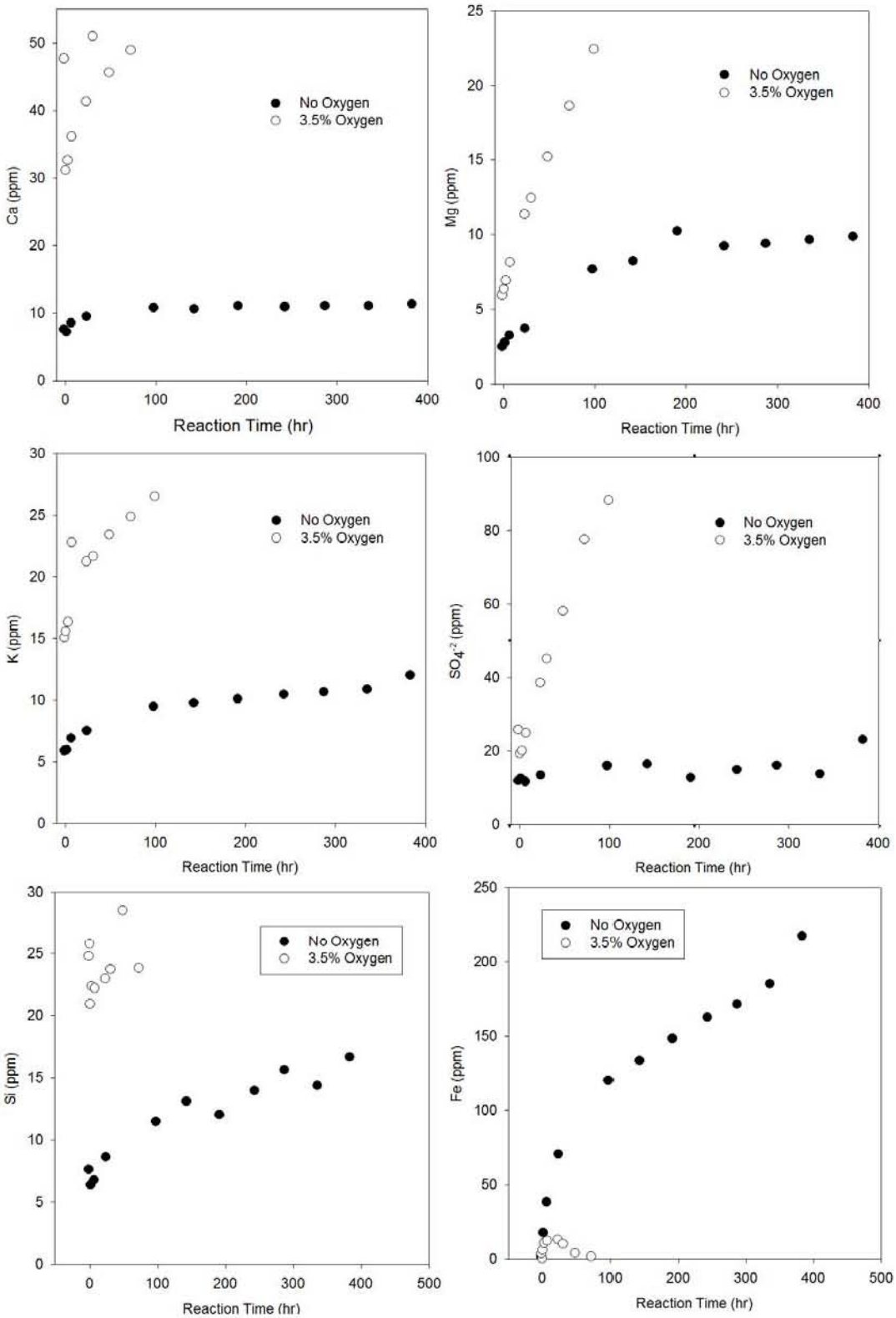

Figure 41. Comparison of pure CO_2 vs. O_2+CO_2 results (Cardium) – Major elements

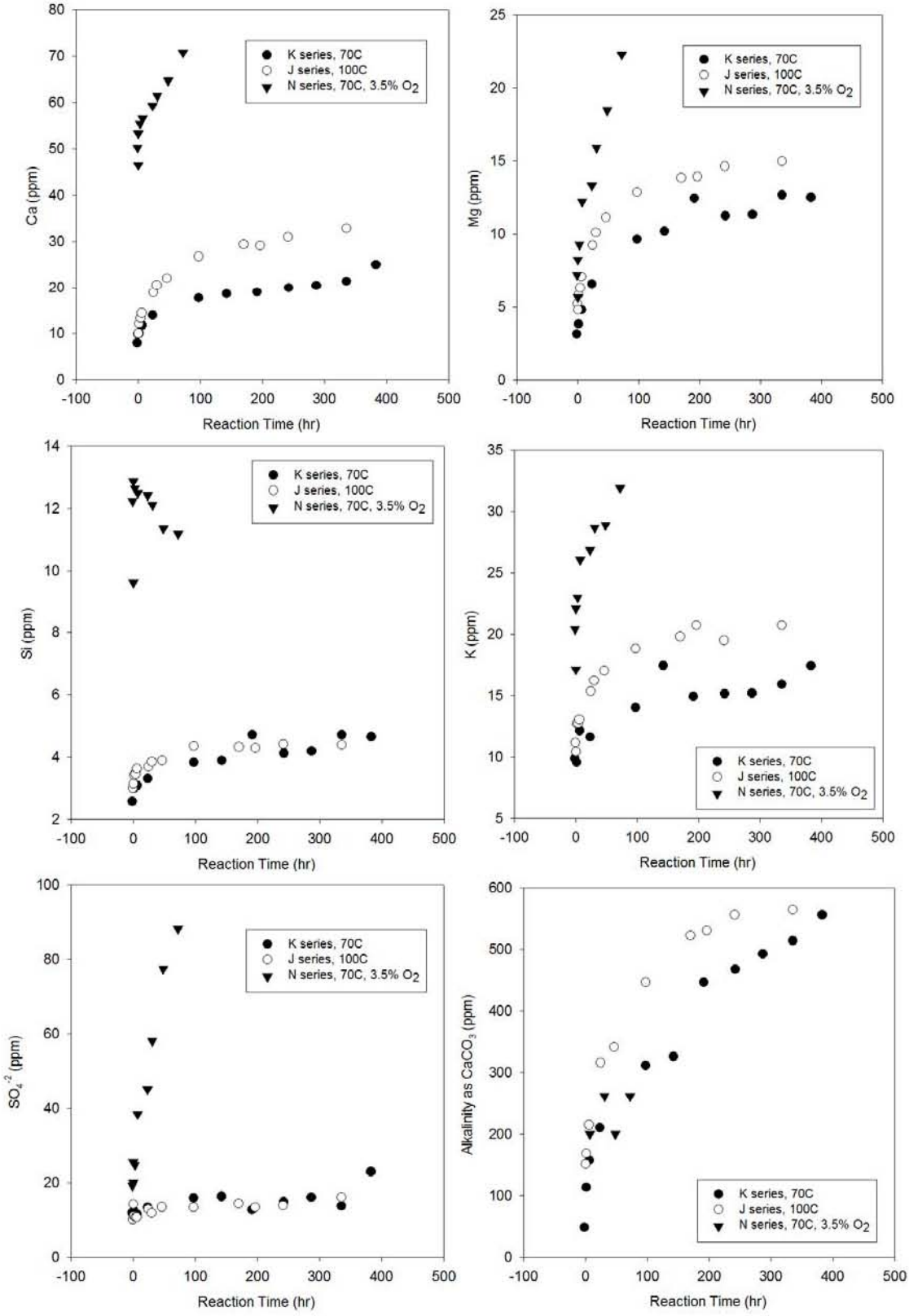

Figure 42. Cardium (K, J, and N series, 70/100°C, with and without O_2)

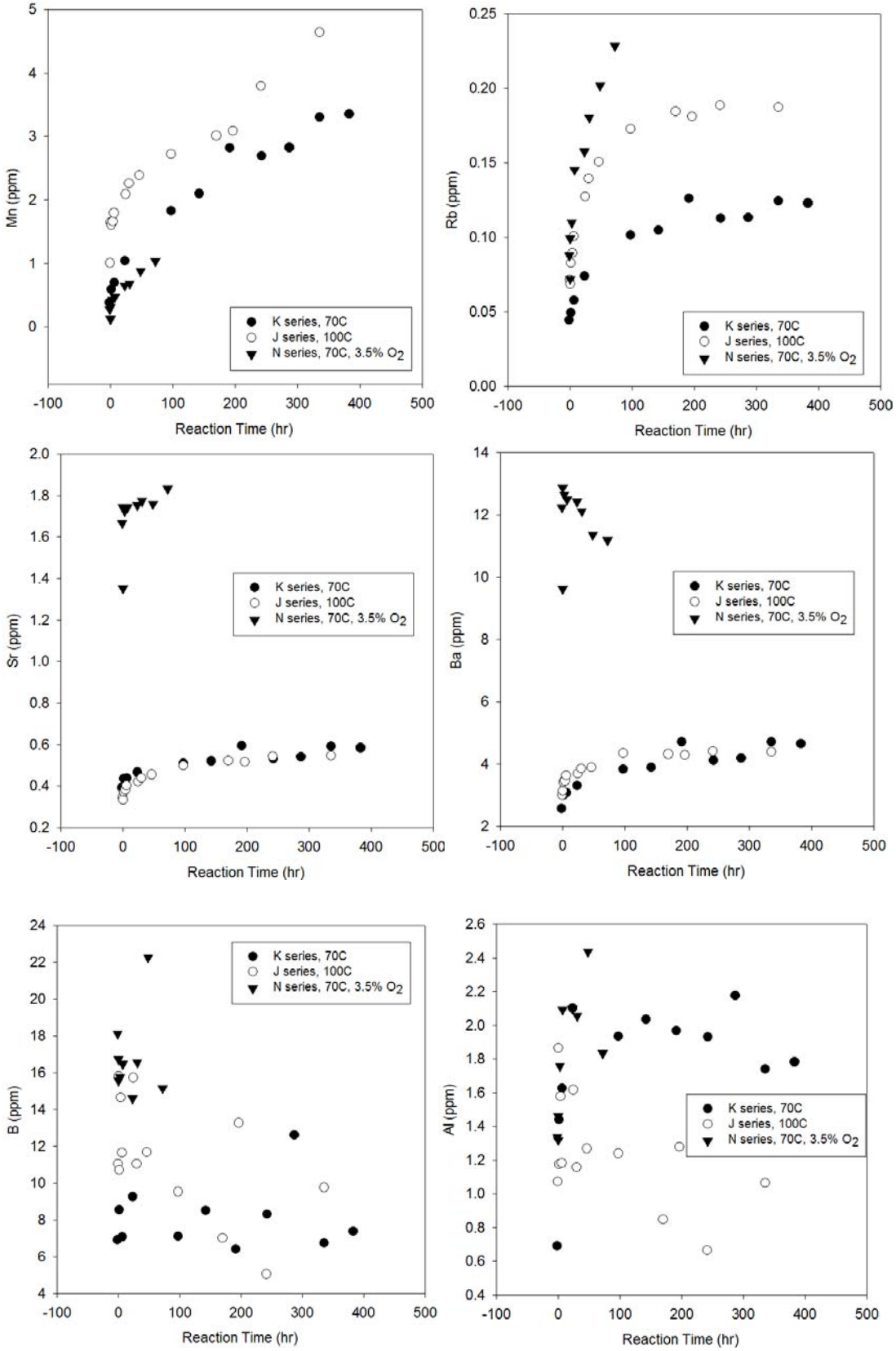

Figure 42. Cardium (K, J, and N series, 70/100°C, with and without O_2) (continued)

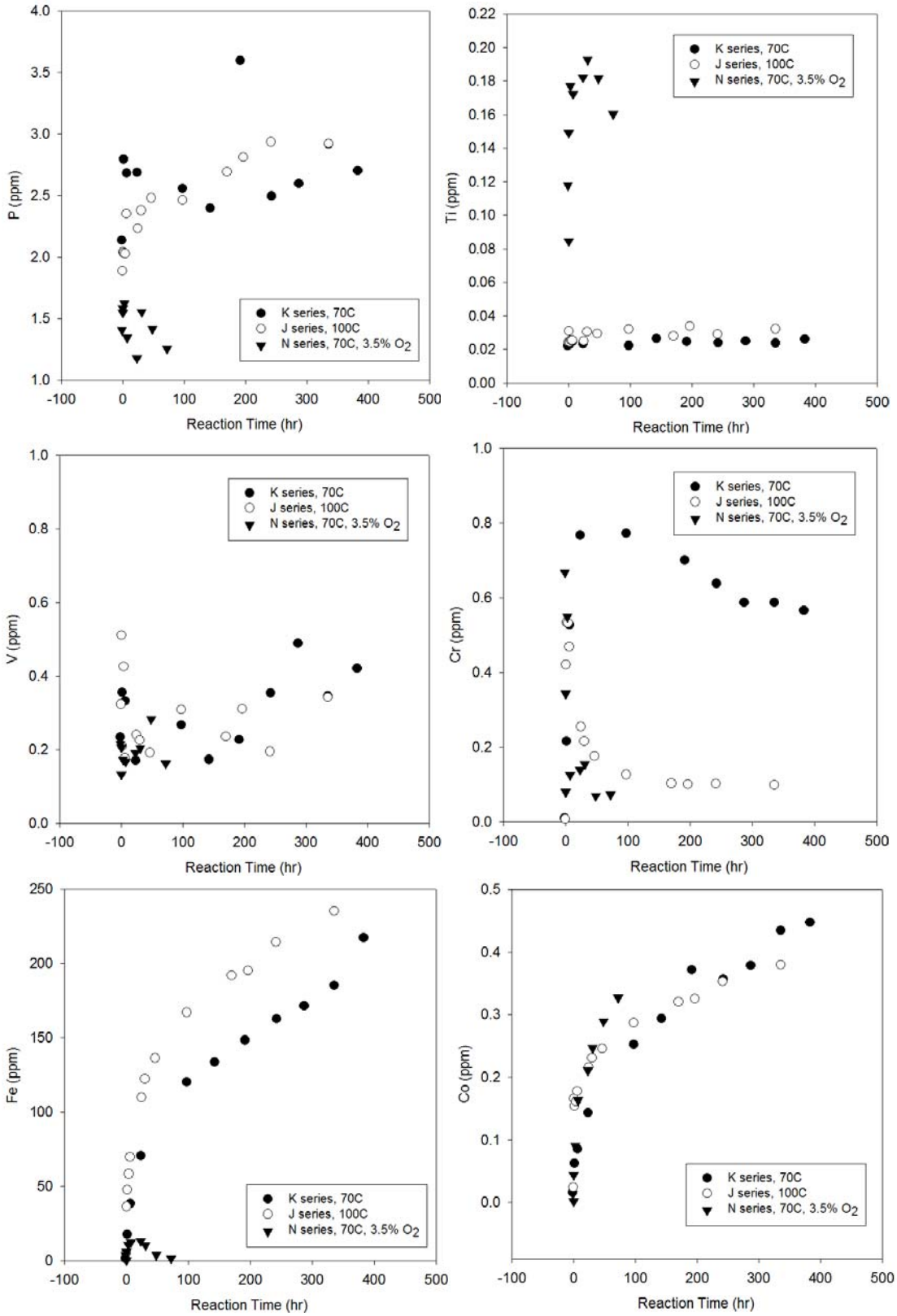

Figure 42. Cardium (K, J, and N series, 70/100°C, with and without O_2) (continued)

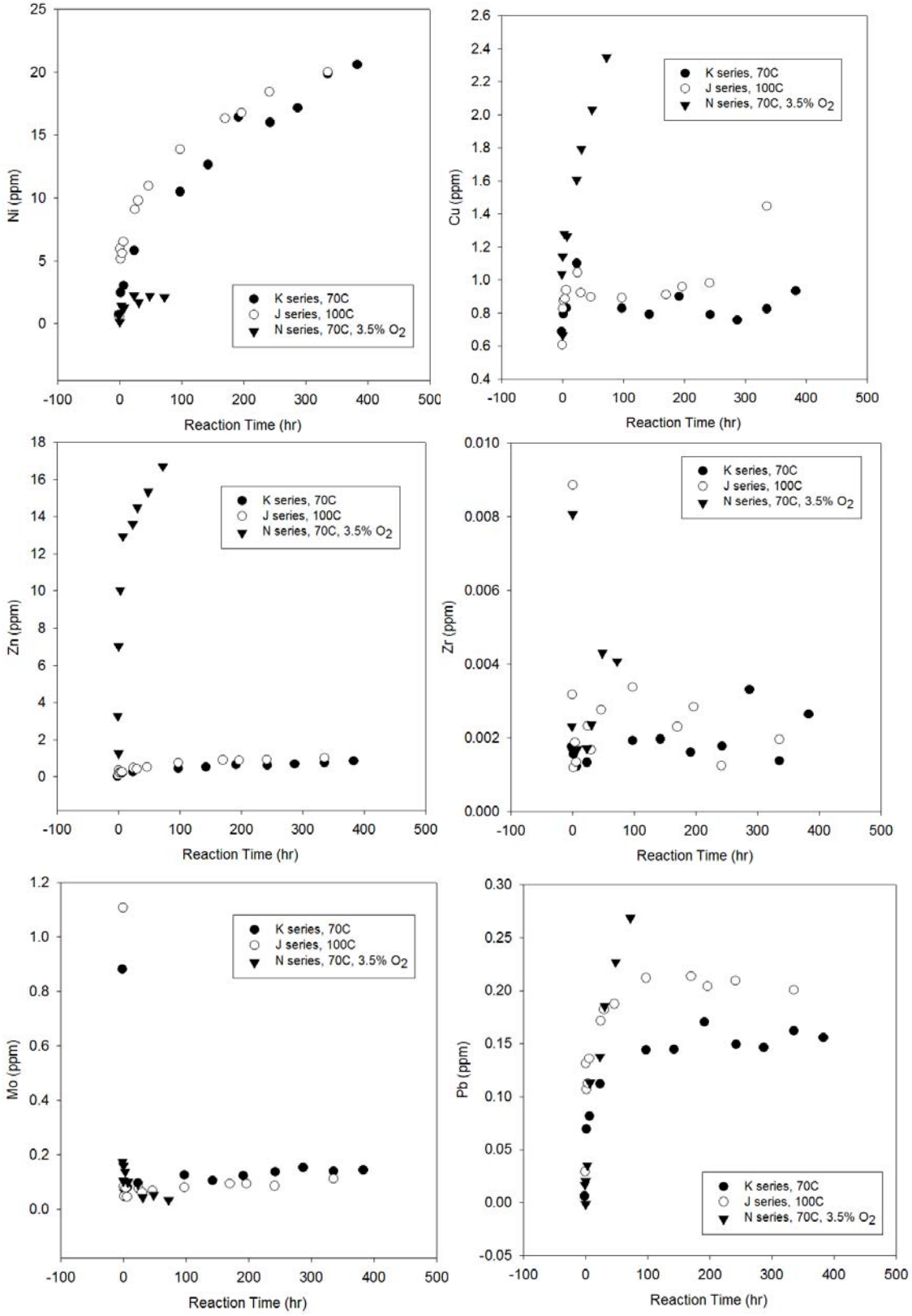

Figure 42. Cardium (K, J, and N series, 70/100°C, with and without O_2) (continued)

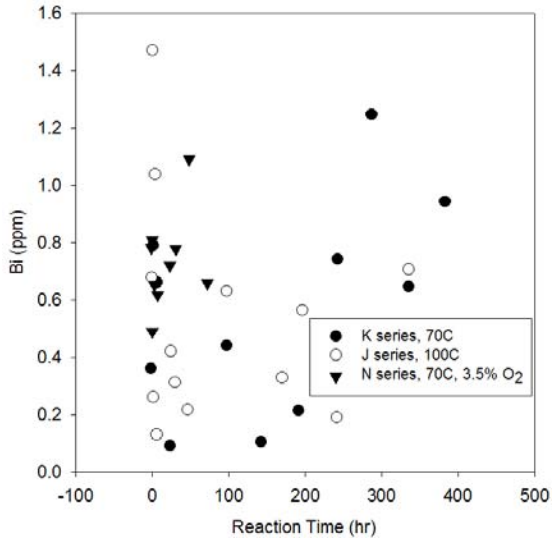

Figure 42. Cardium (K, J, and N series, 70/100°C, with and without O_2) (continued)

III1.3.4.1 Modeling Results (Cardium)

In this section we confirmed that our descriptive understanding of the processes are internally consistent and that the system can be modeled as feldspar and carbonate dissolution and kaolinite precipitation (Figure 34).

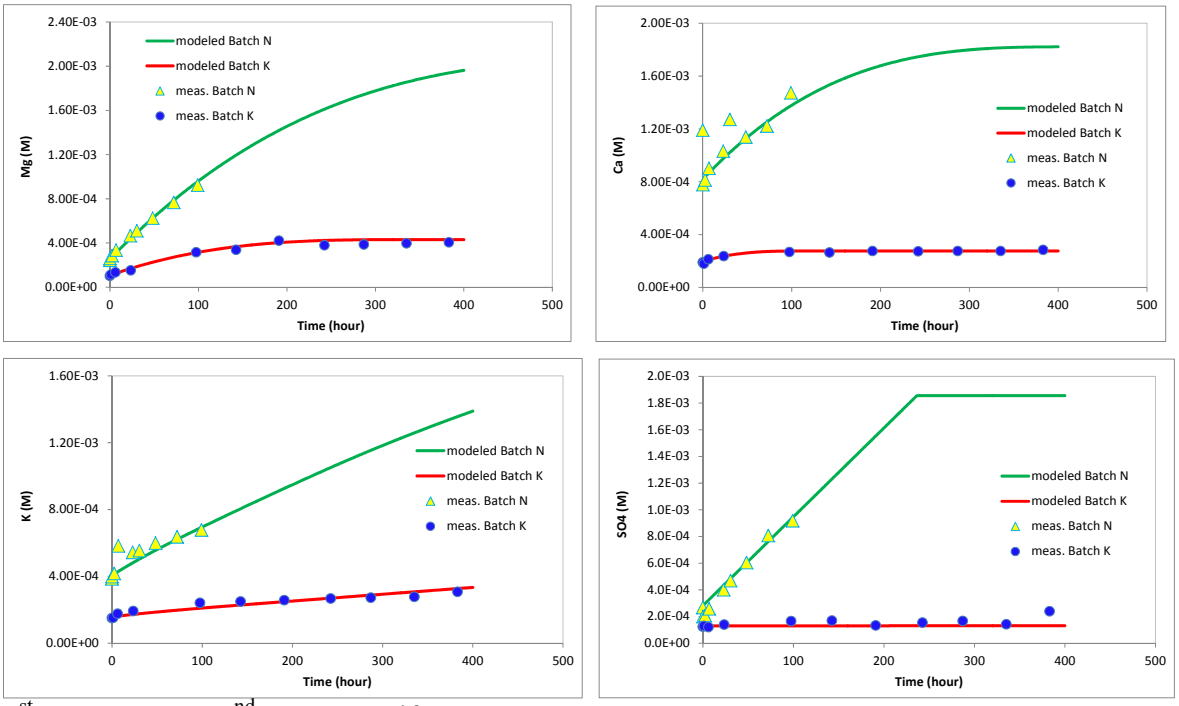

1st row: Mg, Ca; 2nd row: K, sulfate

Figure 43. Comparison of measured and modeled major ion concentrations (N and K series; Cardium, 70°C, 200 bars, CO_2 with and without O_2)

III-1-3.5 Kinetics Evaluation (Cardium)

Reactions are relatively fast but not as fast as in the Cranfield and Miocene case, especially for Ca and Mg. the main release mechanism of those cations is through siderite/ankerite and plagioclase dissolution, slower than calcite dissolution. In the following figures (Figure 44; units are mmol/L/hr/g), raw concentration data are plotted on the left-hand side whereas rates corrected for amount of rock, water, and CO_2 partial pressure are displayed on the right-hand side. Species analyzed are Ca, K, Mg, and sulfate. Rates with O_2 are always higher (different from Miocene and Cranfield) because of the pH drop owing to pyrite dissolution. No pH measurement was made during the experiments.

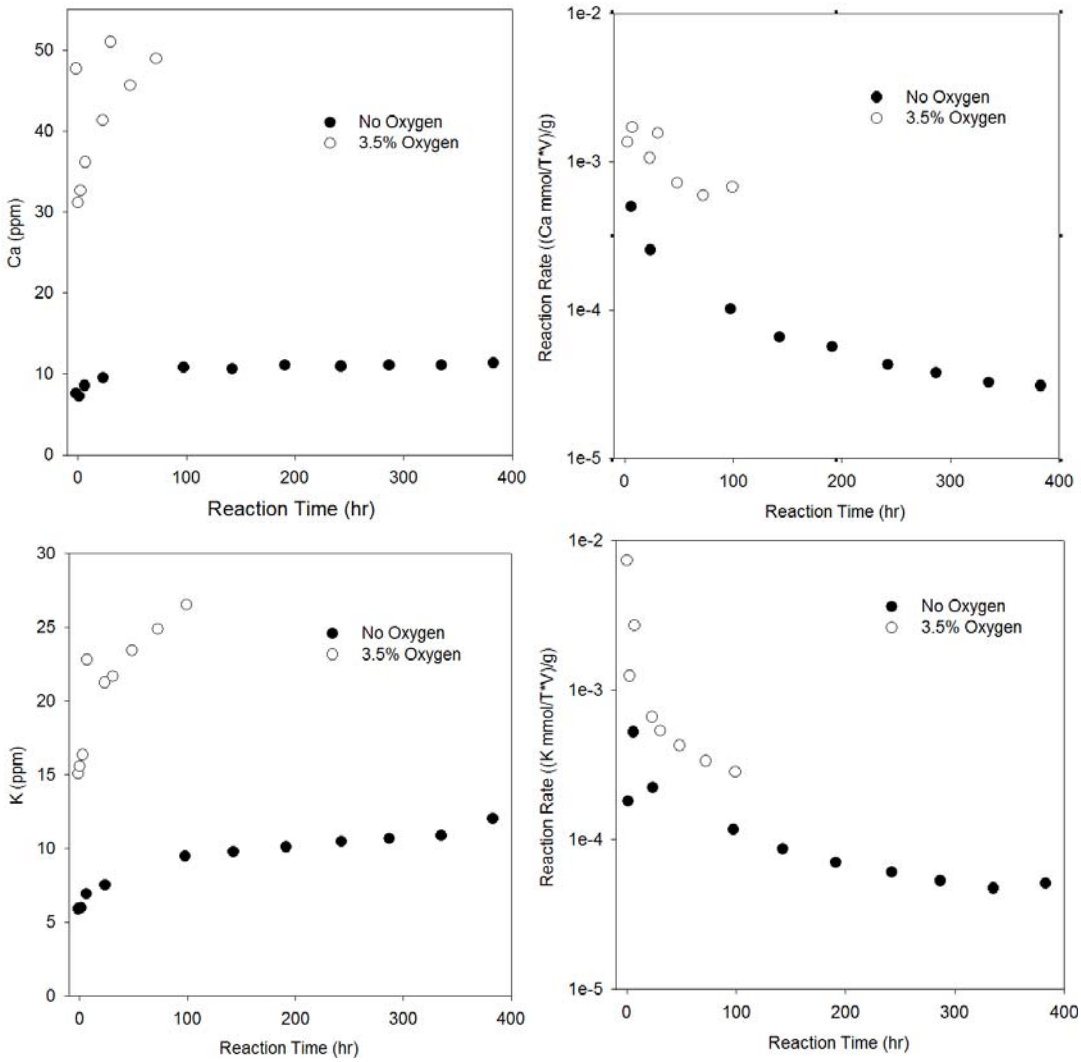

Figure 44. Cardium (K and N series, 70°C, 200 bars, with and without O_2)

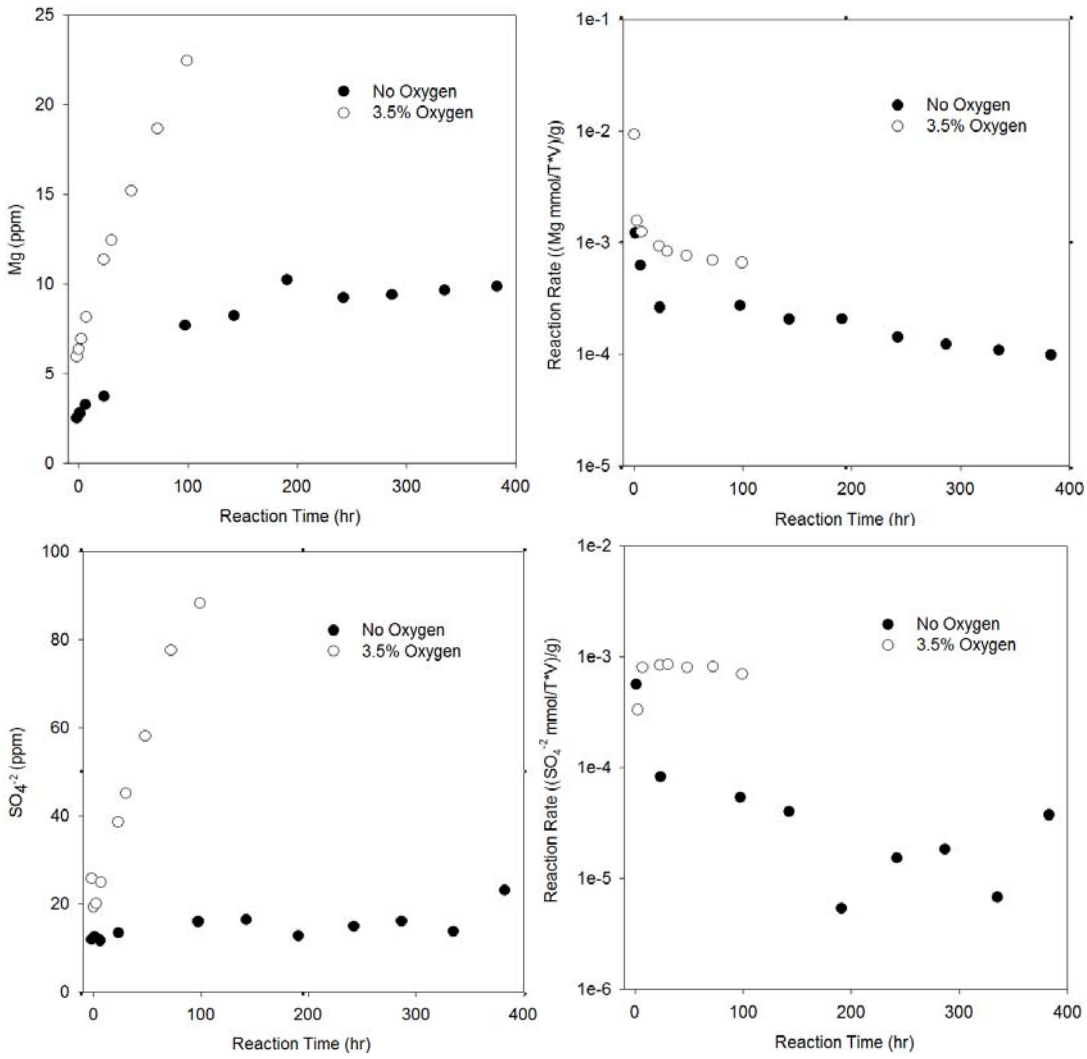

Figure 44. Cardium (K and N series, 70°C, 200 bars, with and without O2) (continued)

III-1-4 Conclusions

We performed several experiments with clastic rock samples of various composition (Figure 45; Table 15). In addition to quartz, the Miocene sample is dominated by calcite (11.8%) and feldspars (31.6%), Cardium dominated by clays (16.9%) with some feldspar (6.7%) and siderite (~1%), and Cranfield dominated by chlorite (20.2%) with some clays (9.3%). Both the Miocene and Cardium samples show evidence of pyrite. The "dirty sandstone" Miocene sample allows for investigating carbonate behavior with and without O_2 whereas the relatively clean and non-reactive Cardium sample is a good candidate to investigate feldspar behavior without the overprint of carbonates. The Cranfield sample with abundant clay minerals dominated by chlorite is even less reactive vis-à-vis CO_2. Minerals sensitive to the presence of O_2 should be pyrite (present in the Miocene and Cardium samples), siderite (present in the Cardium sample), and chlorite (abundant in the Cranfield sample). They all contain ferrous iron-bearing minerals.

Table 15. Summary of sample mineralogical composition

	Offshore Miocene, TX Well OCS-G-3733 Depth 9205 ft	Cardium Sands, AB Well unknown* Depth unknown*	Cranfield, MS Tuscaloosa Formation Well CFU31F-3 Depth 10,476.6 ft
Quartz	43.5%	75.5%	66.9%
Calcite	11.8%		
Siderite		1%	
Microcline	15.2%	4.2%	
Albite	18.4%	2.5%	1.8%
Chlorite			20.2%
Kaolinite	6.2%	10.4%	7.3%
Illite	5.0%	6.5%	2.0%
Pyrite	trace	trace	
Anatase			1.8%
Total	100.1%	100.1%	100%

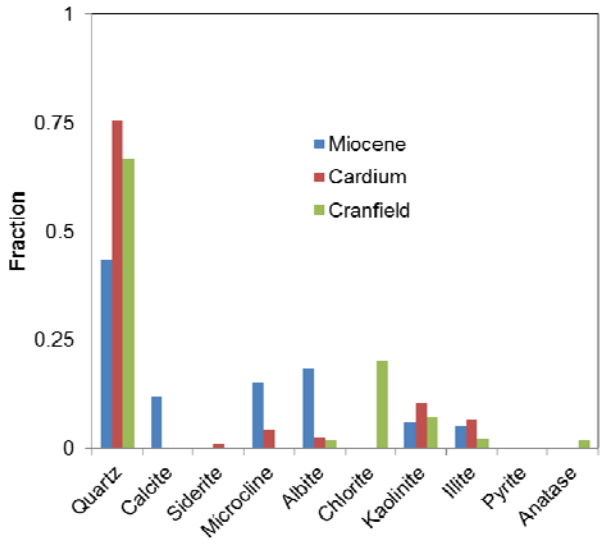

Figure 45. Summary of sample mineralogical composition

We observed the impact of temperature and of O_2, which we chose as the most reactive impurity. With no surprise we observed an increase in release rates with increasing temperature. At one point in the course of the project we thought that O_2 may enhance rates but it turned out to be an experimental artifact. O_2 has an impact if there is (1) redox-sensitive mineral species and (2) ferrous iron-bearing minerals (pyrite, chlorite, siderite, ankerite, ferroan dolomite or calcite, maybe glauconite which contains mostly ferric Fe but some ferrous Fe too). The general chemical evolution of samples is a drop in pH when CO_2 is injected. The pH drop may be mitigated or reduced by buffering species, such as carbonates. It may also favor the dissolution of other species such as feldspars. Once reduced species have been mobilized and are in solution, O_2 can oxidize them. A clear example is siderite or pyrite dissolution with iron hydroxides and allied species (FeOx) precipitating.

A preliminary ranking of relative release rates is presented in Table 16. The table presents results from major ion concentration that can be for the most part related to a single reaction. Approximate readings at time ~0 from the kinetics plots presented earlier are reported in the first row of each category (element and with or without O_2). The second row in each cell represents the release rate relative to the pure CO_2 Miocene 70°C for that particular element (relative rate of 1). Relative release rates are more significant than absolute rates. It is well-known that reaction progress in the field is generally slower than in the laboratory. Our batch experiments tried to minimize this effect by using relatively coarse rock fragments but the fluid is considerably more able to homogenize and contact rock surface in the batch mode than in an actual porous medium. It can be observed that there are orders of magnitude differences in terms of release rates. Miocene 70°C is the fastest release rate for both Mg and Ca; this is due to the influence of carbonates. Release rates are also a strong function of the amount of carbonates in the samples (even if rates are scaled by the amount of solid). Presence of O_2 has a minimal impact, maybe decreasing slightly the release rate most likely because of decrease in CO_2 partial pressure. On the other hand, sulfate and K releases clearly increase in presence of O_2.

Table 16. Approximate ranking of early-time release rate (mmol/L/g/hr) and relative rates

		Miocene 70°C	Miocene 100°C	Cranfield 70°C	Cardium 70°C
Ca	Pure CO_2	~0.5 ***1***	~0.5 *1*	~0.008 *0.016*	~0.0008 *0.0016*
	$CO_2 + O_2$	~0.4 *0.8*	~0.4 *0.8*	~0.008 *0.016*	~0.002 *0.004*
Mg	Pure CO_2	~0.02 ***1***	~0.02 *1*	~0.002 *0.1*	~0.0008 *0.04*
	$CO_2 + O_2$	~0.01 *0.5*	~0.009 *0.45*	~0.001 *0.05*	0.005 *0.025*
K	Pure CO_2	~0.002 ***1***	nd -	~0.001 *0.5*	~0.0008 *0.4*
	$CO_2 + O_2$	~0.005 *2.5*	~0.005 *2.5*	~0.005 *2.5*	~0.002 *1*
SO_4	Pure CO_2	~0.0008 ***1***	~0.0002 *0.25*	nd -	~0.0002 *0.25*
	$CO_2 + O_2$	~0.002 *2.5*	~0.002 *2.5*	nd -	~0.001 *1.25*

To have an impact on permeability by clogging pores, redox-sensitive minerals must be abundant enough. Only chlorite fits this description. However chlorite attack is thorough only at very low pH, below 1 (Simon and Anderson, 1990) at which point it will let gelatinous amorphous ferric FeOx precipitate. Values of pH in the experiments are closer to 3. The presence of pyrite, that will be oxidized by O_2, would help in dropping the pH. However the rock must lack buffering capacity carried by carbonates. Positive impact of the presence of both pyrite and chlorite in seals is likely more favorable for the same reason that reaction products may obstruct pores. The seal at Cranfield contains both (Lu, personal communication, 2012). A reference search using University literature search tools to find formations with abundant chlorite and relatively abundant pyrite with little carbonate was not successful. It seems that only mostly seal rocks fit this description despite the fact that pyrite usually accompanies chlorite in reducing conditions that are probably needed for chlorite precipitation (Dr. Milliken's communication, BEG, 2012; Grossman et al., 1979; Morad, 1986). Cretaceous sandstones such as the Norphlet and Tuscaloosa Formations are two units that have chlorite cements. Some of the South Texas Frio and Vicksburg sandstones also have chlorite, but not as much and also usually with quite a bit of

calcite and zeolites (Dr. Milliken's communication, BEG, 2012; Burton et al., 1987; Grigsby, 2001).

Table 17. Trace element impact

Element	Site	Pure CO_2	O_2 + CO_2	Impurity lower risk?	MCL*100 (ppb)	Problem?
V	Miocene	<400ppb	<200ppb	yes	5000ppb**	no
	Cardium	<500ppb	<200ppb	yes		
	Cranfield	<200ppb	<150ppb	yes		
Cr^^	*Miocene*	*<600ppb*	*<1.5ppm*		*1000ppb*	*yes*
	Cardium	*<800ppb*	*<200ppb*	*yes*		
	Cranfield	*<350ppb*	*<100ppb*	*yes*		
Co	Miocene	<500ppb	<300ppb			
	Cardium	<500ppb	<500ppb			
	Cranfield	<50ppb	<100ppb			
Ni^^	*Miocene*	*<15ppm*	*<10ppm*		*7ppm***	*yes*
	Cardium	*<25ppm*	*<3ppm*			
	Cranfield	*<1ppm*	*<4ppm*			
Cu	Miocene	<1.6ppm	<1.3ppm		150ppm	no
	Cardium	<1.5ppm	<3ppm			
	Cranfield	<1.0ppm	<3ppm			
Zn	Miocene	<800ppb	<50ppm		500ppm**	no
	Cardium	<2ppm	<30ppm			
	Cranfield	<25ppm	<15ppm			
Mo	Miocene	<3000ppb	<700ppb	yes	7000ppb**	
	Cardium	<200ppb	<150ppb	yes		
	Cranfield	<120ppb	<20ppb	yes		
Pb	Miocene	<80ppb	<200ppb		1500ppb	no
	Cardium	<250ppb	<500ppb			
	Cranfield	<60ppb	<50ppb			
Bi	Miocene	<1300ppb	<800ppb	yes		
	Cardium	<1000ppb	<800ppb	yes		
	Cranfield	<80ppb	<50ppb	yes		
As	Miocene	<10ppb	<5ppb		1000ppb	no
	Cardium	<10ppb	<5ppb			
	Cranfield	nd	<10ppb			
Se	Miocene	<5ppb	<10ppb		5ppm	no
	Cardium	<1ppb	<10ppb			
	Cranfield	nd	<5ppb			
Cd	Miocene	<6ppb	nd		500ppb	no
	Cardium	nd	<5ppb			
	Cranfield	nd	nd			
Sb	Miocene	<10ppb	nd		600ppb	no
	Cardium	nd	nd			
	Cranfield	nd	<2ppb			

Note: using 70°C and 3.5% O2 data (D, R, K, N, P, O series with input for S series to correct for higher O_2 in R series; an upper limit of the long-term trend is used not necessarily the highest concentration/spike

^^: Ni and Cr concentrations are suspicious because the likelihood of steel degradation

**: secondary standard only or proposed action level (state or federal) or WHO drinking water guidelines

Trace elements

Trace elements follow expected behavior for the most part. They are released by carbonates and feldspar dissolution (and sometimes, an experimental artifact, by reactor components exposed to O_2). Some are then sorbed by existing or newly created sorbing material such as FeOx and clays. One way to assess the importance of trace elements mobilization is to compute their concentration in a mixture brine/freshwater mimicking dilution of leaking brine in a freshwater aquifer (Table 17).

The dilution has to be large to bring down the TDS of the mixture to ~1000 mg/L. Above this TDS threshold the water would not be consumed because it would be too salty. The danger would then be that a domestic well, for example, would tap water that would still meet TDS standards but lead to ingesting toxic trace metals, possibly for a long period of time. The approach followed here is to simply divide the concentration by a factor of 100. This amount of dilution would be needed to go from the ~100,000 mg/l brine to the 1,000 mg/L potable water. We compared the experimental values to EPA MCL's (http://water.epa.gov/drink/contaminants/index.cfm). It can be seen that oxyanion-building elements performed better when O_2 is present. Among all elements of the table, Cr and Ni only seem to cause a problem in case of leakage but they are major component of the stainless steel reactor components (Table 4) and very likely results from degradation of the steel. It should be noted that the resident brine may contain some amount of trace elements.

Comparison of corrected Ca values:

Comparison of Ca and Mg concentrations in experiments with and without O_2 show the experiments run without O_2 generally have slightly higher Ca and Mg concentrations and release rates. This may be a result of lower CO_2 fugacity in reactions run with O_2. Palandri and Kharaka (2004) report the reaction rates are a function of the activity of H+ raised to the reaction order with respect to H+ (n_1 in following equation):

$$\frac{dm}{dt} = -(A_{acid} e^{\frac{-E_{acid}}{RT}} a_{H^+}^{n_1} + A_{neut} e^{\frac{-E_{neut}}{RT}} + A_{base} e^{\frac{-E_{base}}{RT}} a_{H^+}^{n_3})$$

The Ca and Mg data in the O_2 experiments was corrected for the lower CO_2 fugacity using the following equation:

Ca corrected = Ca measured × (CO_2 fugacity no oxygen/CO_2 fugacity with oxygen)^{n_1}

It was assumed that Ca and Mg originated from calcite dissolution which has a reaction order value of n_1=1. CO_2 fugacity was calculated using the geochemical program Win Prop with the volume of fluid, volume of gas, temperature, pressure and percentages of O_2 and CO_2 as inputs. Figure 46 displays Ca vs. reaction time and Ca release rate vs. reaction time plots. Mg vs. reaction time and Mg release rate vs. reaction time show similar results and are not included. The O_2 experiments corrected for CO_2 fugacity show Ca concentrations very similar to experiments run with no O_2 for all experiments except the Cardium Formation experiment. The similarity between the no-O_2 and CO_2 fugacity corrected results in Ca vs. reaction time plots suggests O_2, by itself, does not significantly alter the extent of calcite dissolution. The concentrations of Ca and Mg are likely more strongly controlled by CO_2 fugacity which in turn alters reactive fluid pH

values. The differences between the O_2 and no-O_2 Cardium experiments are likely due to inter-sample mineralogy. Ca and Mg release rates are also very similar between experiments run with and without O_2, but the no O_2 experiments appear to have slightly higher release rates. Because the release rate is calculated by the change in Ca and Mg concentrations over time and not absolute concentrations there is little difference between corrected and uncorrected O_2 experimental release rates. Calcite dissolution rates that control Ca and Mg concentrations are likely controlled by CO_2 fugacity

Miocene, 70°C, 200 bars (D and R series):

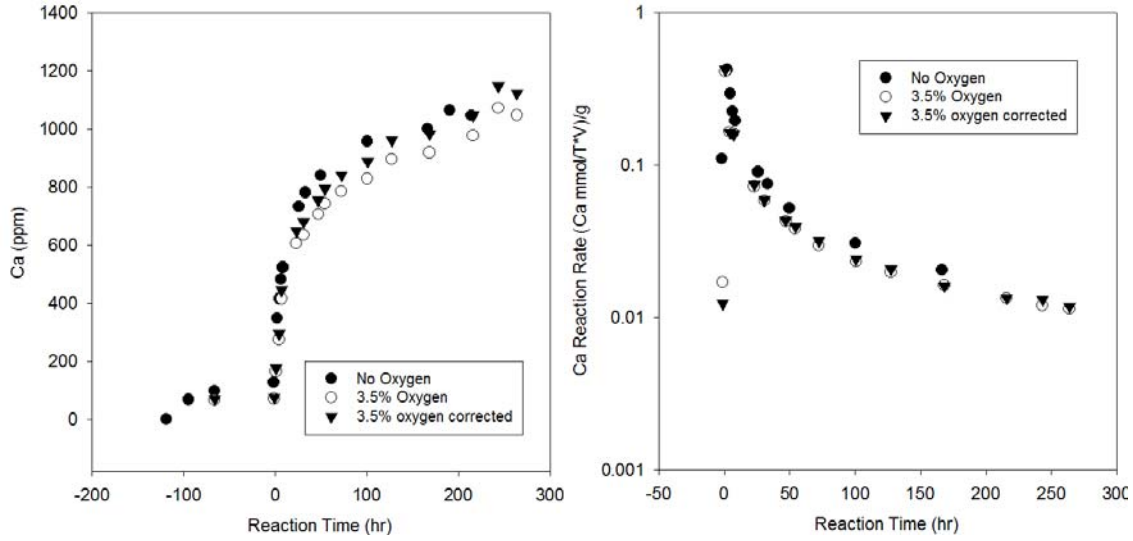

Miocene, 100°C, 200 bars (L and S series):

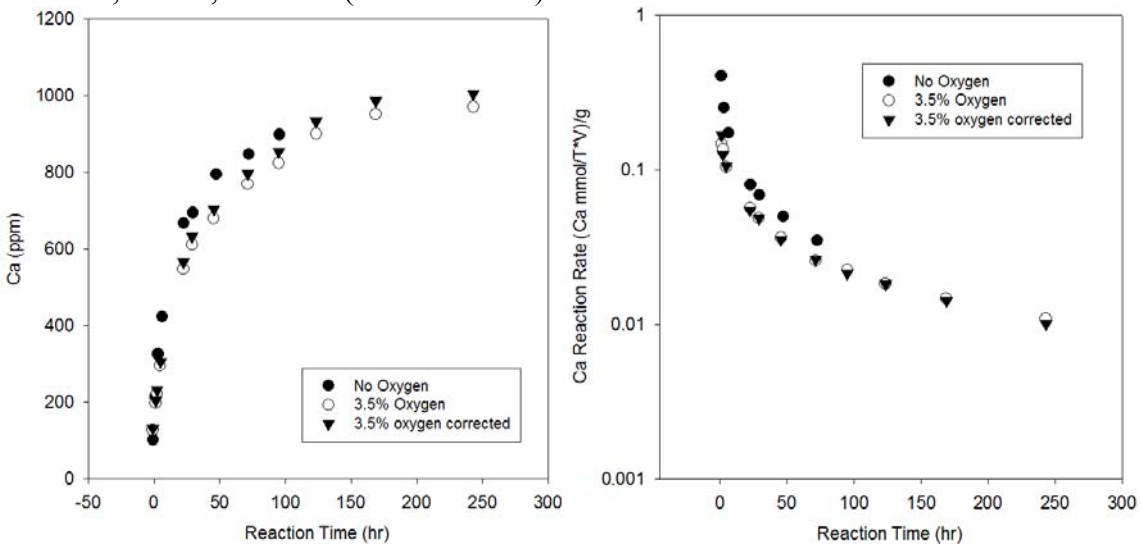

Figure 46. Impact of O_2 on CO_2 fugacity and carbonate dissolution

Cranfield, 70°C, 200 bars (P and O series):

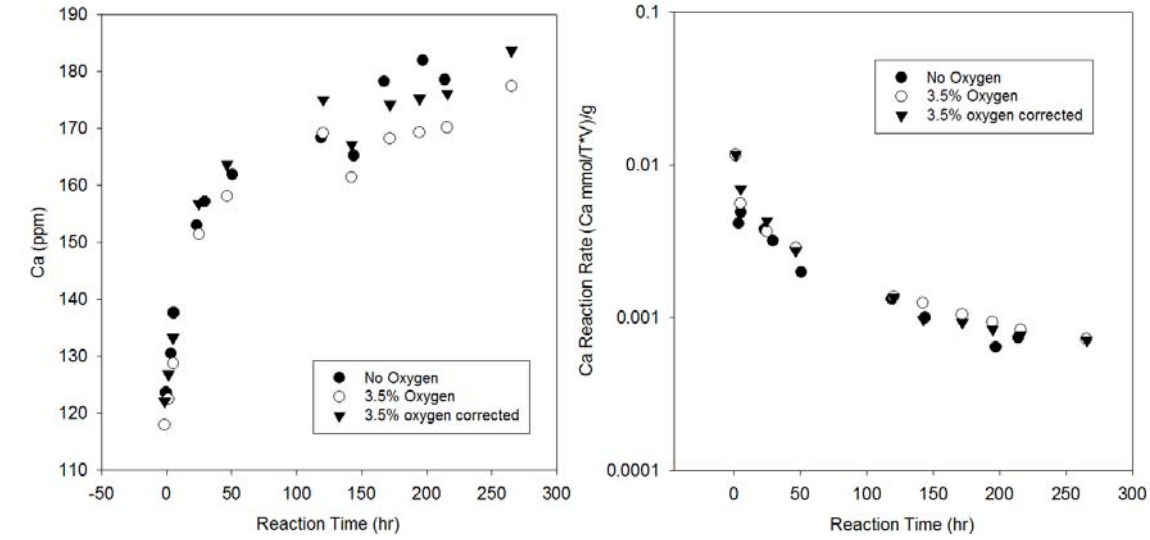

Cardium 70°C, 200 bars (K and N series):

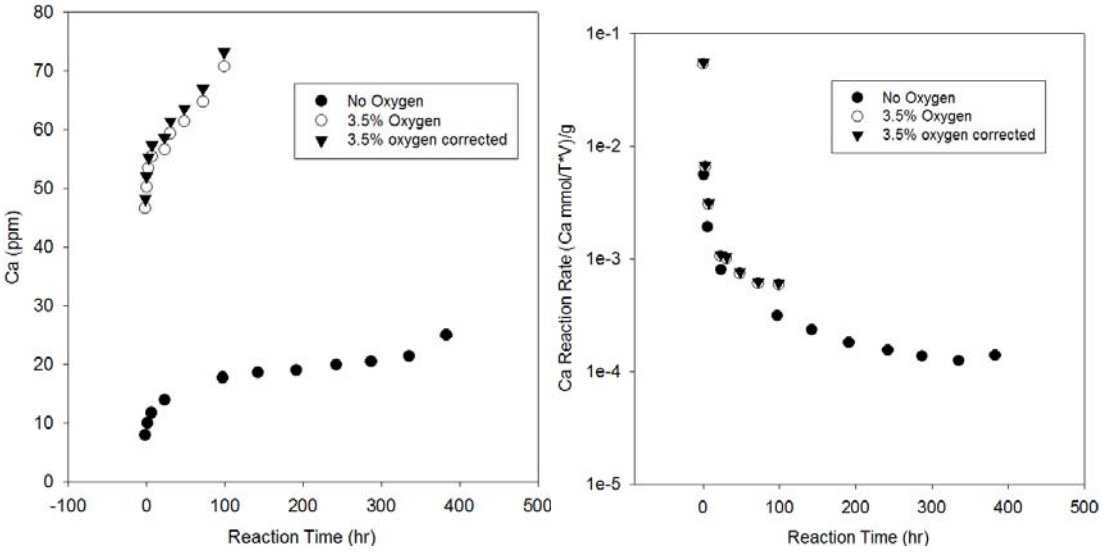

Figure 46. Impact of O_2 on CO_2 fugacity and carbonate dissolution (continued)

III-2. Acid species

This subtask was added in 2011 after discussion with ACPP members and is fully documented in Appendix D. The desktop study investigated the impact on CO_2 sequestration processes of trace and minor reactive acid species not dealt with in the laboratory autoclave experiments. In particular, we characterized the concentration threshold below which the species can be neglected by performing numerical geochemical simulations. Species included HCl, SO_2, NO, and NO_2 present in the waste stream of oxyfuel power plants.

Results suggest that ~1000 ppm for the Frio setting and ~100 ppm for the deeper Cranfield setting are the threshold values beyond which the pH starts dropping significantly beyond that of

CO_2 alone (if no buffering capacity – if buffering capacity, no impact). In this case, trace impurities seem to have a bigger impact at depth than in shallower zones. Typical concentrations of HCl and NOx species are likely below the threshold values but SO_2 concentration is likely higher (Table 3). When considering only the pair CO_2 + trace gas, redox conditions can also change becoming more reducing with SO_2 in the CO_2 stream and more oxidizing with NOx.

III-3. Reactive Transport Modeling

III-3-1 RTM Model Description

The Cardium Sands reservoir depth is approximately 1600m (~5230 ft) at a pressure of ~2400 psi and temperature of 60°C. Porosity of the formation is ~16%. Permeability is relatively low and in the 10-30 md range. Resident water is releatively fresh at ~10,000 ppm and dominated by Na, Cl, and bicarbonate ions. Initial and boundary concentrations are displayed in Table 18. The model system is represented by a 100-m strip discretized into 100 cells, each being 1m in length. The model is intended to simulate the porosity changes at the CO_2 front which is represented by a brine equilibrated with CO_2 and O_2. A uniform and constant average velocity of 0.1 m/yr and effective porosity of 0.16 were used along the entire cross section, which is only valid in the absence of temporal porosity variation. A longitudinal dispersivity of 1 m was assigned to the model. Molecular diffusion coefficient is assumed to be 1×10^{-10} m^2/s. Boundary concentrations were calculated by equilibrating initial brine composition with 98% CO_2 and 2% O_2 under total pressure of 2400 psi (fugacity of CO_2 and O_2, calculated with WINPROP, are 80.1 and 5.14 atm, respectively) and temperature of 60 ºC, corresponding to a depth of ~5000 ft.

Table 18. RTM initial brine compositions and boundary concentrations

Components	Initial Concentration	Boundary Concentration
Al (mole/kg of H_2O)	1.00e-08	1.00e-08
Ca (mole/kg of H_2O)	6.89e-04	6.89e-04
Cl (mole/kg of H_2O)	2.02e-01	2.02e-01
K (mole/kg of H_2O)	6.58e-05	6.58e-05
Mg (mole/kg of H_2O)	2.66e-03	2.66e-03
Na (mole/kg of H_2O)	2.02e-01	2.02e-01
Si (mole/kg of H_2O)	4.21e-04	4.21e-04
Fe (mole/kg of H_2O)	1.10e-05	1.10e-05
C(4) (mole/kg of H_2O)	7.17e-03	1.26e0
O(0) (mole/kg of H_2O)		8.75e-03
Br	0.00	1.00e-5
pH	7.3	3.84
pE	-2.77	14.87

The geochemical model considers 7 primary minerals and 3 secondary minerals (Table 19). Mineral dissolution and precipitation were simulated with kinetic theory and reaction rates are given by (Palandri and Kharaka, 2004):

$$\frac{dm}{dt} = -SA\left[\begin{array}{l} k_{acid}^{298.15K} e^{\frac{-E_{acid}}{R}\left(\frac{1}{T}-\frac{1}{298.15K}\right)} a_{H^+}^{n_1}\left(1-\Omega^{P_1}\right)^{q_1} \\ +k_{neut}^{298.15K} e^{\frac{-E_{neut}}{R}\left(\frac{1}{T}-\frac{1}{298.15K}\right)}\left(1-\Omega^{P_2}\right)^{q_2} \\ +k_{base}^{298.15K} e^{\frac{-E_{base}}{R}\left(\frac{1}{T}-\frac{1}{298.15K}\right)} a_{H^+}^{n_3}\left(1-\Omega^{P_3}\right)^{q_3} \end{array}\right] \quad (1)$$

where *SA* is reactive surface area, $k_{acid}^{298.15}$, $k_{neutral}^{298.15}$, $k_{base}^{298.15}$ are rate constants for acid, neutral and base conditions at 298.15 K; E_{acid}, $E_{neutral}$, E_{base} are activation energies (J mol^{-1}), *T* is temperature (K), *R* is the gas constant, Ω is mineral saturation index, p and q are empirical and dimensionless parameters which were assumed to be 1 in this study, a_{H+} is activity of H^+ in water and *n* is a parameter estimated from experiments. From Eq. (3), it can be seen that mineral reaction rate includes three mechanisms. Parameters for calculating reaction rates of minerals are listed in Table 19 (Palandri and Kharaka, 2004). Note that, for pyrite dissolution, the reaction rate is given by:

$$\frac{dm}{dt} = -SA\left[k_{acid}^{298.15K}\, e^{\frac{-E_{acid}}{R}\left(\frac{1}{T}-\frac{1}{298.15K}\right)} a_{H^+}^{n_1} a_{Fe^{3+}}^{n_2} (1-\Omega^{p_1})^{q_1} + k_{neut}^{298.15K}\, e^{\frac{-E_{neut}}{R}\left(\frac{1}{T}-\frac{1}{298.15K}\right)} a_{O_2}^{n_3} (1-\Omega^{p_2})^{q_2}\right] \quad (2)$$

where n_1, n_2, and n_3 are -0.5, 0.5, and 0.5, respectively.

Table 19. Parameters for calculating kinetic rate constants of minerals

	Mass (%)	Neutral mechanism		Acid mechanism			Base mechanism		
		k (mol/m^2/s)	*E*(kj/mol)	*k* (mol/m^2/s)	*E*(kj/mol)	n_1	*k* (mol/m^2/s)	*E*(kj/mol)	n_3
Primary Minerals									
Quartz	75.3	1.023×10^{-14}	87.7						
Kaolinite	10.4	6.918×10^{-14}	22.2	4.898×10^{-14}	65.9	0.777	8.913×10^{-18}	17.9	-0.472
Illite	6.5	1.660×10^{-13}	35	1.047×10^{-11}	23.6	0.34	3.020×10^{-17}	58.9	-0.4
Albite	2.5	2.754×10^{-13}	69.8	6.918×10^{-11}	65.0	0.457	2.512×10^{-16}	71	-0.572
K-feldspar	4.2	3.890×10^{-13}	38	8.710×10^{-11}	51.7	0.5	6.310×10^{-22}	94.1	-0.823
Siderite	0.9	1.260×10^{-9}	62.76	1.590×10^{-4}	45.0	0.9			
Pyrite	0.2	2.82×10^{-5}	56.9	3.02×10^{-8}	56.9				
Secondary Minerals									
Magnesite		4.571×10^{-10}	23.5	4.169×10^{-7}	14.4	1.0			
Dawsonite		1.260×10^{-9}	62.76	1.590×10^{-4}	45.0	0.9			
Dolomite		2.951×10^{-8}	52.2	6.457×10^{-4}	36.1	0.5			
Fe(OH)$_3$		n/a	n/a	n/a	n/a	n/a	n/a	n/a	

Note: all rate constants are listed for dissolution

III-3-2 RTM Detailed Results

We added bromide as a conservative tracer to check the proper behavior of the system. Figure 47 shows bromide concentrations through time at distances of 0.5 m, 49.5 m and 99.5 from the left boundary where brine saturated with CO_2 and O_2 was injected into the 1-D domain. It can be seen that bromide arrives at 99.5 m after ~1000 years, which was expected because brine velocity is 1 m/year and it confirmed that the flow component of the model works properly.

Brine pH is mainly dominated by advection suggesting impacts of mineral dissolution, such as that of albite and K-feldspar are very trivial (Figure 48). Migration of pH fronts is very similar to that of dissolved inorganic carbon (Figure 49). However, the oxidation front (dissolution of O_2 in brine) was significantly retarded (Figure 50) because of dissolution reactions with pyrite and siderite. Brine showed oxidized condition (pE=~11) at the distance of 0.5 m after about 1700

years. Note that in the 1-D model, no gas phase was considered. In reality, oxidation front could move much faster because O_2 in the gas phase can migrate as fast as that of CO_2.

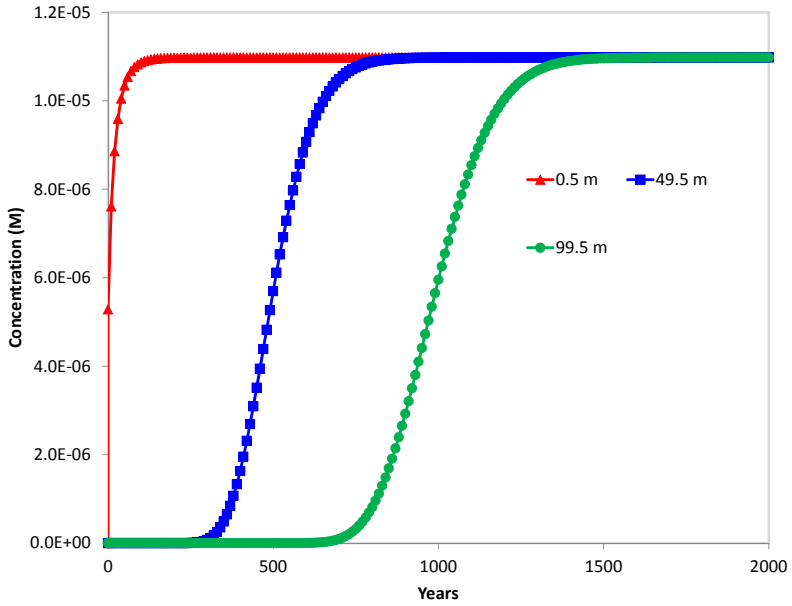

Figure 47. Time variations of Br concentrations at distances of 0.5 m, 49.5 m, and 99.5 m from the inlet.

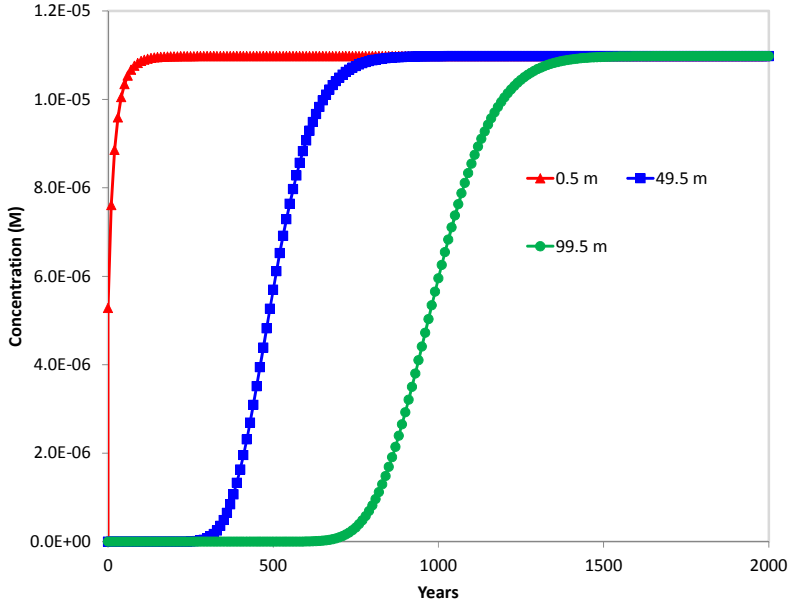

Figure 48. Time variations of pH at distances of 0.5 m, 49.5 m, and 99.5 m from the inlet

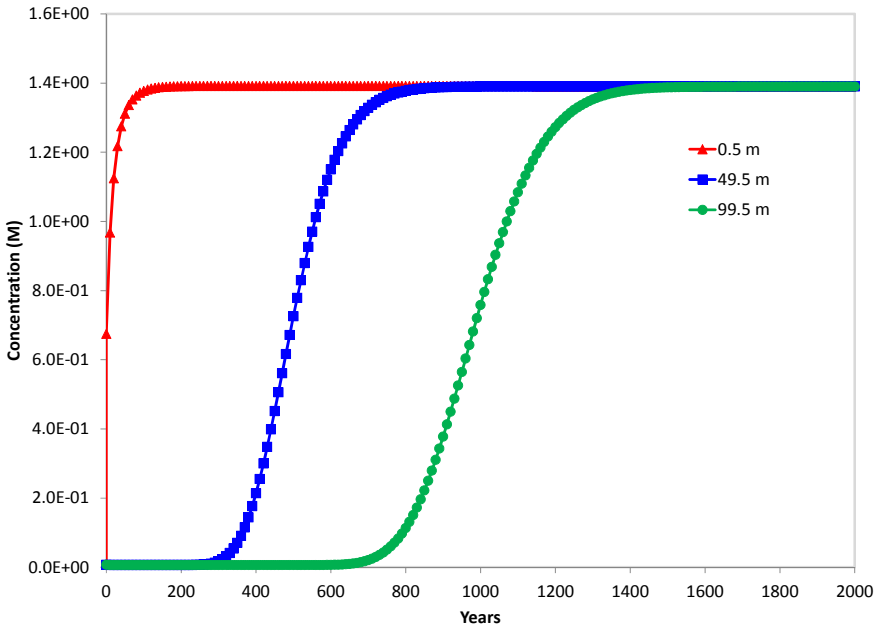

Figure 49. Time variations of dissolved inorganic carbon at distances of 0.5 m, 49.5 m, and 99.5 m from the inlet

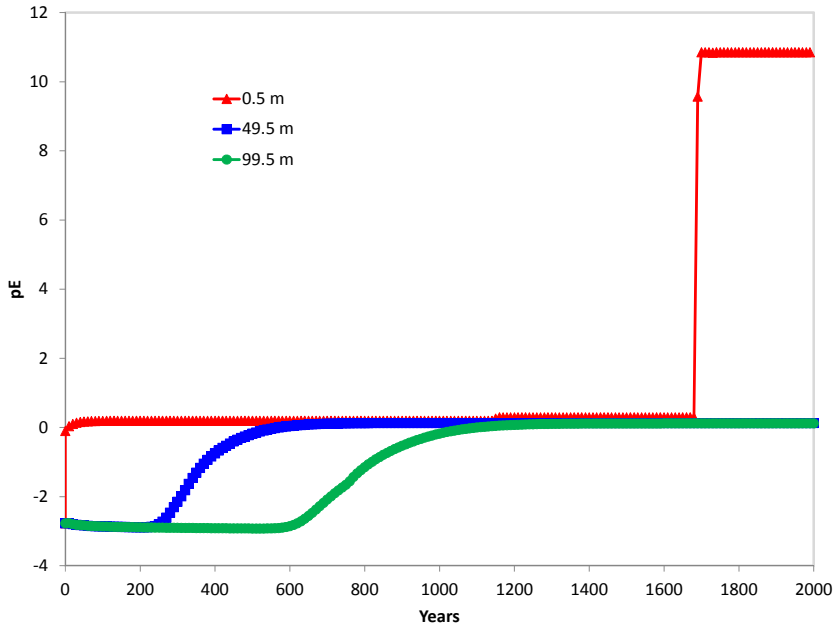

Figure 50. Time variations of pE at distances of 0.5 m, 49.5 m, and 99.5 m from the inlet

Initial and background concentrations of Na are 0.202 M. Because of albite dissolution, Na concentrations are higher than their initial and background concentrations (Figure 51). Initial and background concentrations of K are 6.58×10^{-5} M. It can be seen that K concentrations have increased because of K-feldspar dissolution (Figure 52).

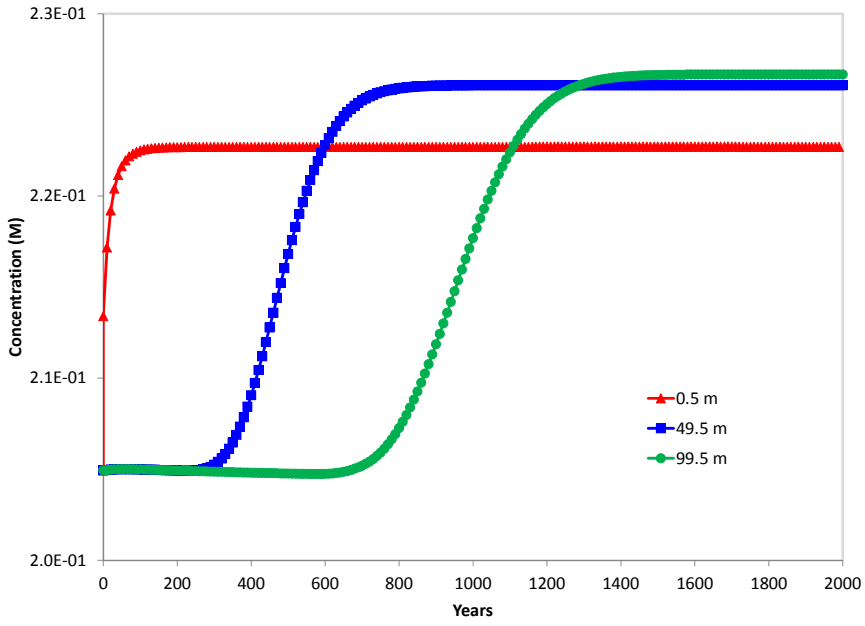

Figure 51. Time variations of Na concentrations at distances of 0.5 m, 49.5 m, and 99.5 m from the inlet

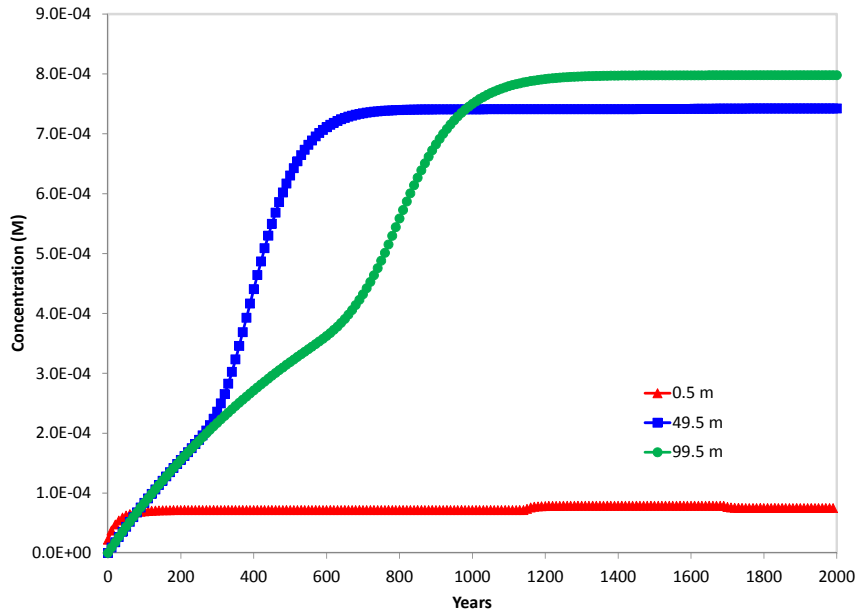

Figure 52. Time variations of K concentrations at distances of 0.5 m, 49.5 m, and 99.5 m from the inlet

Initial and boundary concentrations of total Fe (Fe^{2+} + Fe^{3+}) are 1.1×10^{-5} M. Dissolution of siderite and pyrite raised Fe concentration (Figure 53). Figure 54 shows saturation indices of O_2(g) at distances of 0.5 m, 49.5 m and 99.5 m to the left boundary. Dissolved oxygen is clearly retarded. This is consistent with the pE breakthrough times shown in Figure 50.

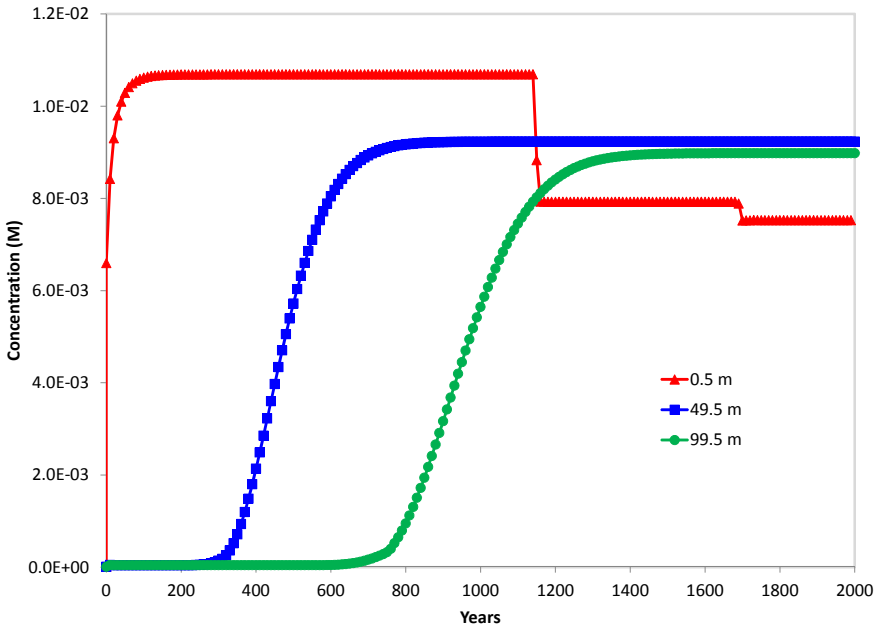

Figure 53. Time variations of total Fe concentrations at distances of 0.5 m, 49.5 m, and 99.5 m from the inlet

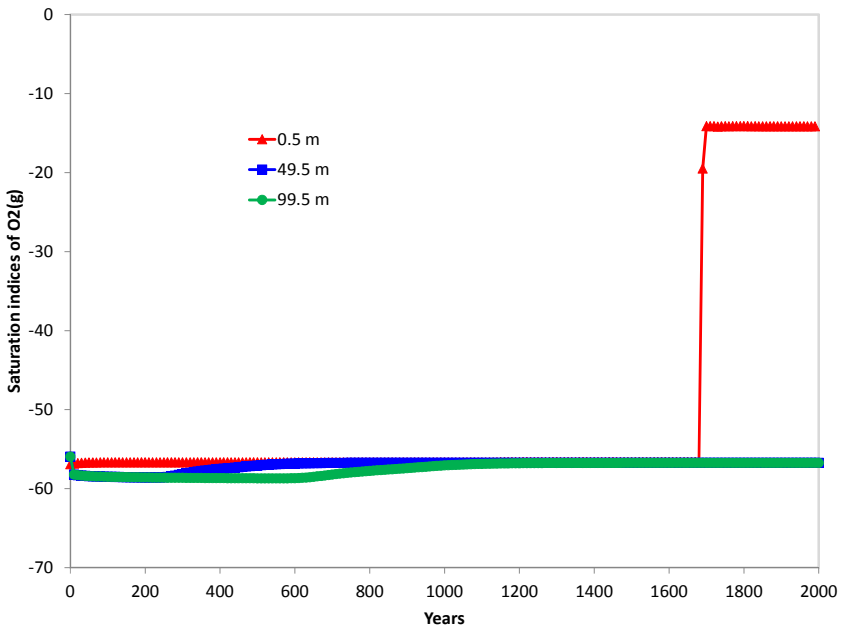

Figure 54. Time variations of saturation indices of oxygen at distances of 0.5 m, 49.5 m, and 99.5 m from the inlet

Figure 55 through Figure 59 show solid mass of albite, K-feldspar, kaolinite, siderite and pyrite at distances of 0.5 m, 49.5 m, and 99.5 m from the inlet of the 1-D domain. Albite and K-feldspar dissolve due to low pH. The closer to the inlet and to the source of CO_2, the more impact on albite and K-feldspar dissolution (Figure 55 and Figure 56). Note that, in agreement with general geological observations, albite dissolution is faster than K-feldspar dissolution.

Dissolution of albite and K-feldspar lead to precipitation of kaolinite as observed in the autoclave samples next to feldspar crystals (Figure 57).

Siderite was exhausted after about ~1100 years and pyrite was exhausted after about 1600 years at distance of 0.5 m from the inlet, suggesting that oxidation of siderite and pyrite is slow. However, dissolution rate of pyrite and siderite could depend on groundwater velocity and reactive surface areas. It will be interesting to conduct sensitivity analysis to see impacts of the two parameters on dissolution of pyrite and siderite. Siderite appears to being oxidized faster than pyrite (Figure 58 and Figure 59). Secondary minerals listed in Table 19 that were allowed by the model to precipitate, and could have precipitated during the runs, did not precipitate over time.

Oxidation and dissolution of pyrite and siderite liberates significant amounts of iron. It is unclear what the stable form of iron oxide at reservoir conditions is but, in general, oxyhydroxides (FeOx) (we used $Fe(OH)_3$ as a proxy) precipitate first and then convert into goethite or hematite. $Fe(OH)_3$, observed in the batch experiments, did not precipitate in our model because the pH remained too low. An interesting debate is the timing of the iron mineral precipitation in the autoclave samples: does it happen during the experiment or as the sample is depressurized (at least some precipitation occurs during the experiment because we observed sorption of oxyanions).

Porosity change can be evaluated based on solid mass of each mineral over time at different distances. Figure 60shows porosity calculated at the different distances to the left boundary. It appears that change in porosity is mainly dominated by dissolution of pyrite and siderite in rocks and precipitation of kaolinite. Precipitation of iron oxyhydroxides Relative change in porosity at distance of 0.5 m from the inlet is <1% over 2000 years. Applying Carmen-Kozeny empirical

$$\frac{k_{new}}{k_{old}} \sim \left(\frac{(1-n)^2}{n^3}\right)_{new} \times \left(\frac{(1-n)^2}{n^3}\right)^{-1}_{old} \quad (3)$$

Formula (Eq. 3), with a porosity change from 0.16 to 0.161 yields a decrease in permeability of 2%. Assuming a porosity change of 2% to 0.18 to take into account massive FeOx precipitation would yield a 16% decrease in permeability.

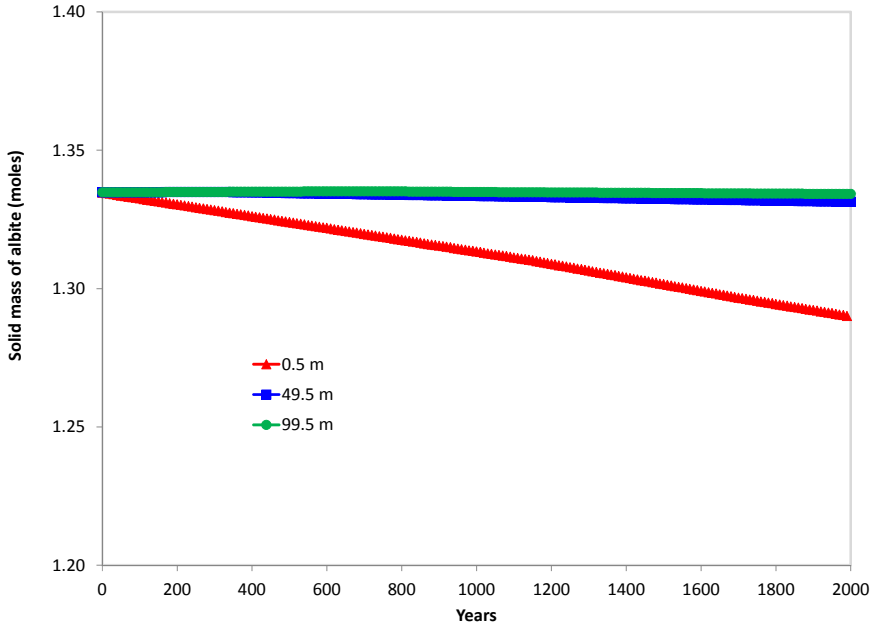

Figure 55. Mass of albite at distances of 0.5 m, 49.5 m, and 99.5 m from the inlet

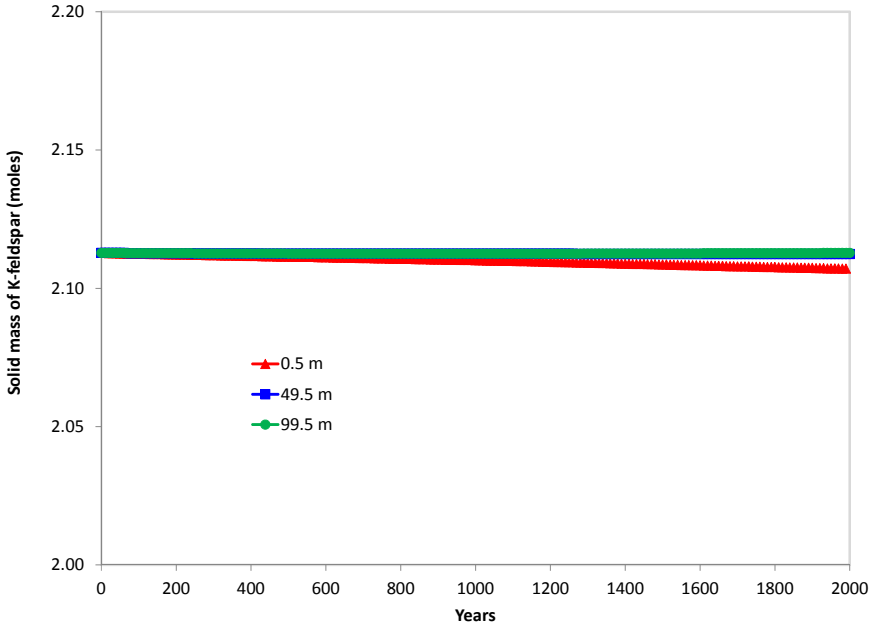

Figure 56. Mass of K-feldspar at distances of 0.5 m, 49.5 m, and 99.5 m from the inlet

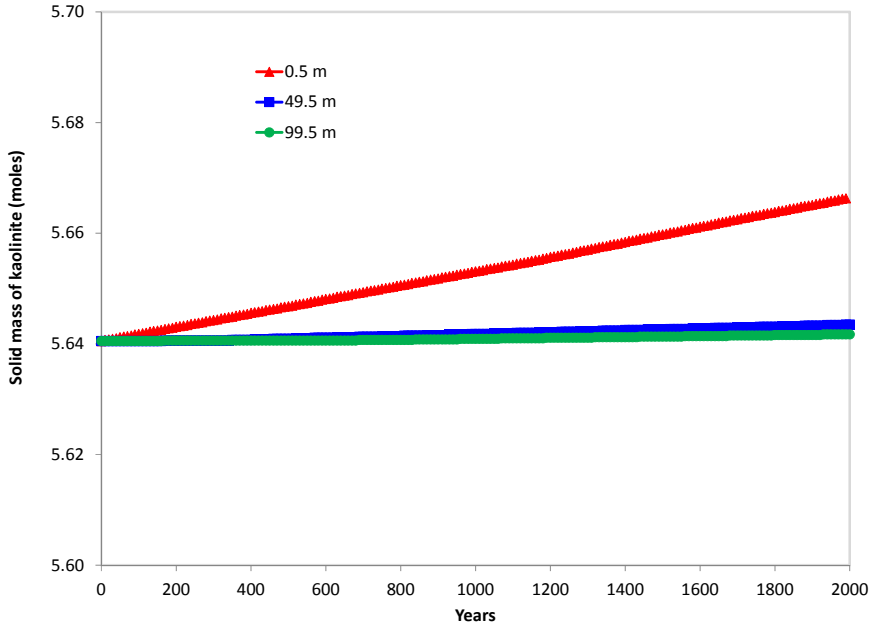

Figure 57. Mass of kaolinite at distances of 0.5 m, 49.5 m, and 99.5 m from the inlet

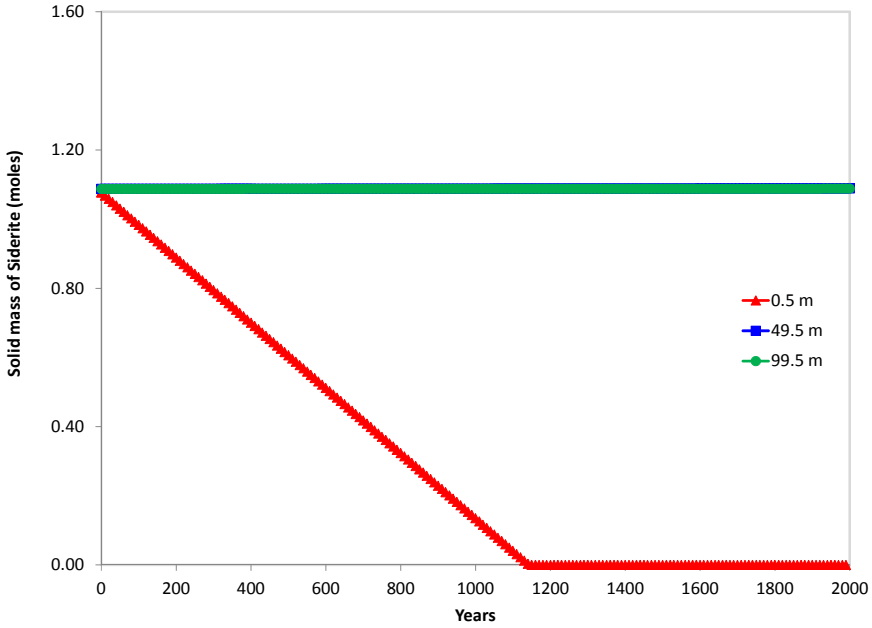

Figure 58. Mass of siderite at distances of 0.5 m, 49.5 m, and 99.5 m from the inlet

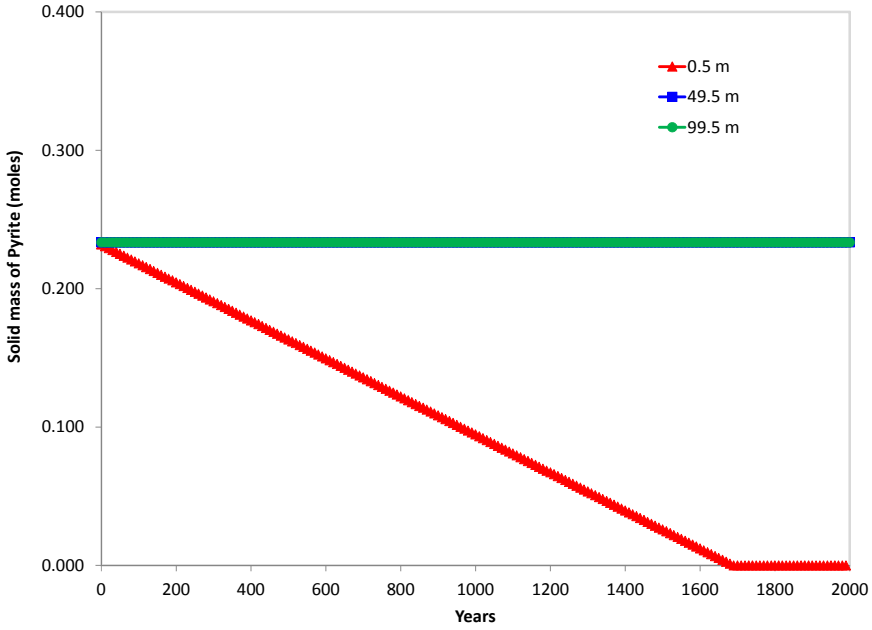

Figure 59. Mass of pyrite at distances of 0.5 m, 49.5 m, and 99.5 m from the inlet

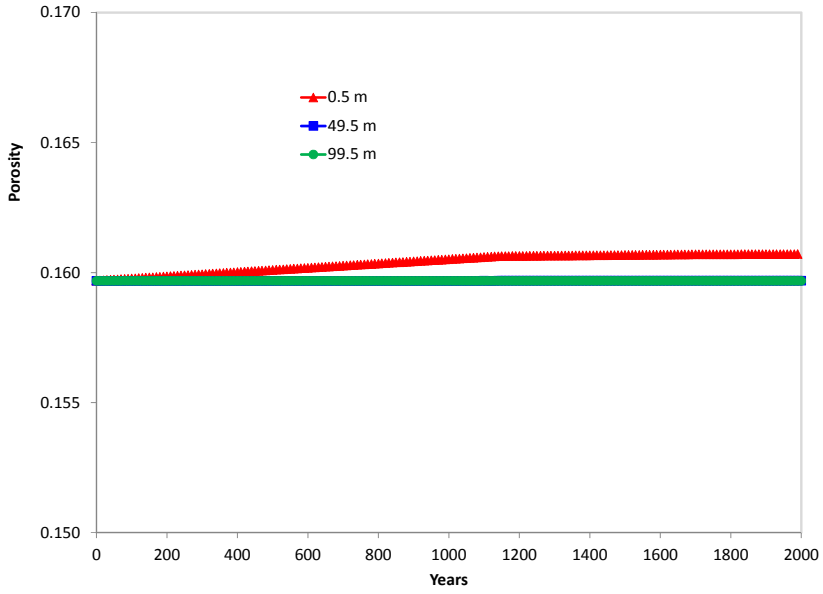

Figure 60. Porosity at distances of 0.5 m, 49.5 m, and 99.5 m from the inlet

IV. Discussion and Conclusions

This report documents the findings of the autoclave experiments exploring the impact of O_2 impurity introduced with super-critical CO_2 on reservoir rock mineralogy and aqueous geochemistry. It complements an earlier report focused on the impact of likely common impurities in the CO_2 stream on the plume flow behavior (Nicot and Solano, 2012). Details on the autoclave findings are presented previously in Section III-1-4 (p.86). In addition to the autoclave experiments dedicated to the impact of O_2, we also investigated the likely impact of other acid species (see Table 2 for list). More acid species could speed up dissolution processes but they are unlikely to change the nature of ultimate reaction products and their spatial distribution. In addition, trace elements are minimally impacted by addition of O_2, some become somewhat more mobile but several are immobilized further. *The overall conclusion is that reactive impurities are unlikely to cause widespread problems in a clastic reservoir* (however they could on well and surface materials if not designed properly when exposed to the ubiquitous presence of water in the subsurface). Whereas gas plume behavior can be impacted by non-compressible impurities in the far-field, geochemical effects from reactive impurities are likely to be observed only in the near field close to the well where dissolved impurities have not been diluted or fixed by reactions and there is continuous exposure to fresh reactive impurities (which may concentrated through dehydration phenomena noted with CO_2 injection). As available solid phases are consumed by reactive gases, the front or fronts expand outward from the injection well and gases are dispersed through a larger volume minimizing or eliminating geochemical impacts.

In any case, the reactive transport model suggests that porosity would not change much because of the balance between precipitation and dissolution. An interesting question that cannot be answered here is the impact on dissolution/precipitation reactions on permeability , particularly whether precipitants tend to concentrate more in pore throats where the impact on permeability would be greater than occurrence in the main pore bodies. SEM and other images suggest that precipitates are fairly well distributed on surfaces or are concentrated around dissolved crystals. An approach to predicting such impacts on permeability without performing coreflood experiments may entail modeling of the thermodynamic direction of the important reactions as a function of pressure at the microscale. Fluid pressure is higher on pore throats walls and lower within the pore body. Such microscale pressure distribution might control the location of the growing authigenic minerals.

There are many important aspects not treated in this document such as:

- O_2 and microbial growth
- Relationship between geochemistry and flow
- Interactions among dissolution products; Catalytic poisoning (e.g., inhibition of precipitation and dissolution reactions)
- Behavior of reducing gases
- Impact of O_2 on carbonate rocks

O_2 can enhance microbial growth in the reservoir. The aerobic microorganisms would be, in that case, imported from the surface as indigenous organisms are anaerobic. Such a case has been

documented at Ketzin, Germany where CO_2 has been injected at shallow depth (~650 m) (Morozova et al., 2011; Wandrey et al., 2011). We did not investigate such reactions in this document.

Beyond the obvious potential impact on permeability, impurities, in particular O_2, can also impact flow via changes in relative permeability and residual saturation related to the CO_2 supercritical phase itself. Minerals exposed to the flowing fluids may have their surfaces altered which produces a subsequent change in wettability (Jun et al., 2013).

Although implicitly included into the release rates, it is also important to understand the effect of those elements whose concentration in aqueous solution are increased by mineral reactions to act as poisons to later mineral precipitation or dissolution. For example, sulfate has been described as limiting calcite precipitation in laboratory (Flaathen et al, 2011). Magnesium has been observed to delay calcite precipitation (e.g., Tracy et al., 1998; Zhang and Dawe, 2000) and phosphates can limit precipitation to a fraction of what it would be without them (e.g., Svensson and Dreybrodt, 1992).

If O_2 can co-exist with reducing gases such as CH_4 or CO or H_2 or H_2S in a pipeline with no or little liquid water, the subsurface offers a different outcome. All gases will dissolve into the brine according to their solubility and possibly react with one another. Even a pure stream of a binary O_2-CO_2 mixture may encounter hydrocarbons in a dissolved phase. The compounds CH_4 and other higher hydrocarbon are common in basins favorable for CO_2 sequestration (Buckley et al., 1958). One of the problem is to determine how fast O_2 will react with CH_4 or CO or H_2 and how much of it will be consumed. And whether the reactions (that do not happen in the atmosphere or a gas phase without a catalyst) can be activated in the aqueous phase with a variety of potential mineral reactive surfaces. A simple physical armoring process is also possible in which precipitates would prevent further dissolution.

A key follow up to this study would entail assessment of how carbonate rocks would react to a CO_2 stream with O_2 and other impurities. At this point the answer is unclear, the Rousse (France) injection was done in a dolomite reservoir (see p.7) and O2 has little impact but reservoirs with large amount of ankerite and siderite would liberate and mobilize large amount of ferrous iron that would then precipitate as FeOx in the presence of O_2. Other important future work could include varying salinity, different binary system (CO_2+CO and impact of FeOx coatings), other co-injectant to form a ternary system (CO_2 + O_2+ SO_2 for example), more rock types (including seal material), and use of pure minerals to extract true kinetics laws, and additional pressure / temperature pairs to assess linearity of release rates.

V. References

Aimard, N., Prevende, C., Cieutat, D., Sanchez-Molinero, I., and Tsiava, R., 2008, The Integrated CO_2 Pilot in the SW of France (Oxycombustion and Geological Storage): A Potential Answer to CO_2 Mitigation in Bitumen Production, SPE 117600

Allen, D.E., B.R. Strazisar, Y. Soong, and S.W. Hedges, 2005, Modeling carbon dioxide sequestration in saline aquifers: Significance of elevated pressures and salinities, Fuel Processing Technology, 56, p.1569-1580.

Berger, P. M., Roy, W. R., and Mehnert, E., 2009. Geochemical Modeling of Carbon Sequestration, MMV, and EOR in the Illinois Basin. Energy Procedia, 1, No. 1, 3437-3444.

Birkholzer, J., Apps, J. A., Zheng, L. Zhang, Y., Xu, T., Tsang, C-F., 2008, Water quality effects caused by CO2 intrusion into shallow groundwater, US Environment Protect Agency (EPA), Lawrence Berkeley National Laboratory, LBNL-1251E.

Breit, G. N., 2002, Produced Waters Database, digital information available at: http://energy.cr.usgs.gov/prov/prodwat/index.htm, last accessed 02/2013

Buckley, S. E., C. R. Hocott, and M. S.Taggart, Jr., 1958, Distribution of hydrocarbons in subsurface waters, AAPG SP 18: Habitat of Oil, p.850-882.

Burton, J. H., D. H. Krinsley, and K. Pye, 1987, Authigenesis of kaolinite and chlorite in Texas Gulf Coast sediments, *Clays and Clay Minerals,* 35(4), 291-296

CMG, 2011, WinProp User's Guide – Version 2011. Computer Modelling Group Ltd, Calgary.

Corvisier, J., A.-F. Bonvalot, V. Lagneau, P. Chiquet, S. Renard, J. Sterpenich, and J. Pironon, 2012, Impact of co-injected gases on CO_2 storage sites: geochemical modeling of experimental results, 11th International Conference on Greenhouse Gas Control Technologies (GHGT11), International Energy Agency Greenhouse Gas R&D programme, Kyoto, Japan, November 18–22, 2012, 12p.

Dashtgard, S.E., M. B.E. Buschkuehle, B. Fairgrieve, and H. Berhane, 2008, Geological characterization and potential for carbon dioxide (CO2) enhanced oil recovery in the Cardium Formation, central Pembina Field, Alberta, Bulletin of Canadian Petroleum Geology, 56(2), p.147-164

Dzombak, D. A. and F. M. M. Morel. 1990. Surface complexation modeling: Hydrous Ferric Oxide. Wiley-Interscience, New York, 393p.

Flaathen, T. K., E. H. Oelkers, S. R. Gislason, and P. Aagaard, 2011, The effect of dissolved sulphate on calcite precipitation kinetics and consequences for subsurface CO_2 storage, GHGT10 Amsterdam, Energy Procedia, 4, p.5037-5043.

Heeschen, K., Risse, A., Ostertag-Henning, C., and Stadler, S., 2011. Importance of co-captured gases in the underground storage of CO2 : Quantification of mineral alterations in chemical experiments. Energy Procedia, 4, No., 4480-4486.

Hodgson, G.W., and B.L. Baker, 1959, Geochemical aspects of petroleum migration in Pembina, Redwater, Joffre, and Lloydminster oil fields of Alberta and Saskatchewan, Canada, AAPG Bulletin, 43(2). p.311-328

Hosseini, S. A., H. Lashgari, J.-W. Choi, J.-P. Nicot, J. Lu, S. D. Hovorka, 2013, Static and Dynamic Reservoir Modeling for Geological CO2 Sequestration at Cranfield, Mississippi, U.S.A., International Journal of Greenhouse Gas Control, dx.doi.org/10.1016/j.ijggc.2012.11.009

Girard, J.-P., P. Chiquet, S. Thibeau, M. Lescanne, and C. Prinet, 2012, Geochemical assessment of the injection of CO2 into Rousse depleted gas reservoir. Part I: Initial mineralogical and geochemical conditions in the Mano reservoir, 11th International Conference on Greenhouse Gas Control Technologies (GHGT11), International Energy Agency Greenhouse Gas R&D programme, Kyoto, Japan, November 18–22, 2012, 7p.

Grigsby, J. D., 2001, Origin and growth mechanism of authigenic chlorite in sandstones of the lower Vicksburg formation, South Texas, Journal of Sedimentary Research, 71(1), p.27–36

Grossman, R. H., R. S. Liebling, and H. S. Scherp, 1979, Chlorite and its relationship to pyritization in anoxic marine environments, Journal of Sedimentary Petrology, 49(2), p.611-614

IEAGHG, 2011, Effects of Impurities on Geological Storage of CO_2, 2011, report 2011/04 prepared by CanmetENERGY, Natural Resources Canada, June 2011, 63 pages + Appendices.

Jacquemet, N., Le Gallo, Y., Estublier, A., Lachet, V., von Dalwigk, I., Yan, J., Azaroual, M., and Audigane, P., 2009. CO2 streams containing associated components--A review of the thermodynamic and geochemical properties and assessment of some reactive transport codes. Energy Procedia, 1, No. 1, 3739-3746.

Johnson, J., Anderson, G., and Parkhurst, D., 2000, Database 'thermo.com.V8.R6.230,' Rev. 1.11. Lawrence Livermore National Lab, Livermore, Calif.

Jun, Y.-S., D. E. Giammar, and C. J. Werth, 2013, Impacts of Geochemical Reactions on Geologic Carbon Sequestration, Environ. Sci. Technol, dx.doi.org/10.1021/es3027133

Koenen, M., Tambach, T. J., and Neele, F. P., 2011. Geochemical effects of impurities in CO2 on a sandstone reservoir. Energy Procedia, 4, No., 5343-5349.

Krause, E. F., H. N. Collins, D. A. Nelson, S. D. Machemer, and P. R. French, 1987, Multiscale Anatomy of a Reservoir: Geological Characterization of Pembina-Cardium Pool, West-Central Alberta, Canada, American Association of Petroleum Geologists Bulletin, 71(10), p.1233-1260.

Lu, J, Mickler, P., Yang, C., and Treviño, R., 2011, "Task 7.0: Mineralization Containment" in Interim Project Progress Report (October 31, 2011: Reporting period July 1 – September 30, 2011) for U.S. Department of Energy ARRA study (American Recovery and Reinvestment Act), *Gulf of Mexico Miocene CO_2 Site Characterization Mega Transect*,, R. Trevino ed.; Conducted under funding agreement DE-FE0001941; 52p.

Lu, J., Kharaka, Y. K., Thordsen, J. J., Horita, J., et al., 2012, CO_2-rock-brine interactions in Lower Tuscaloosa Formation at Cranfield CO2 sequestration site, Mississippi, U.S.A., Chemical Geology, v. 291, p. 269-277.DOI: 10.1016/j.chemgeo.2011.10.020.

Machemer, S. D. and I. Hutcheon, 1988, Geochemistry of early carbonate cements in the Cardium formation, Central Alberta, Journal of Sedimentary Petrology, 58(1), p.136-147.

Matter, J. M., T. Takahashi and D. Goldberg, 2007, Experimental evaluation of in situ CO_2-water-rock reactions during CO_2 injection in basaltic rocks: Implications for geological CO_2 sequestration, Geochemistry, Geophysics, Geosystems, 8(2), 10.1029/2006GC001427

Melrose, J. C., F. Johnson, R. A. Georqe, and H. Groeneveld, 1976, Water-Rock Interactions in the Pembina Field, Alberta, SPE#6049, 12pp.

Michael, K. and S. Bachu, 2001, Fluids and pressure distributions in the foreland-basin succession in the west-central part of the Alberta basin, Canada: Evidence for permeability barriers and hydrocarbon generation and migration, AAPG Bulletin, 85(7), p. 1231–1252

Mickler, P., Lu, J., Yang, C., 2012, "Task 7.0: Mineralization Containment" in Interim Project Progress Report (October 30, 2012: Reporting period July 1 – September 30, 2012) for U.S. Department of Energy ARRA study (American Recovery and Reinvestment Act), *Gulf of Mexico Miocene CO_2 Site Characterization Mega Transect*, R. Trevino ed.; Conducted under funding agreement DE-FE0001941; 58p.

Morad, S., 1986, Pyrite-chlorite and pyrite-biotite relations in sandstones, Sedimentary Geology, 49, p.177-192

Morozova, D., Zettlitzer, M., Let, D., et al., 2011, Monitoring of the microbial community composition in deep subsurface saline aquifers during CO2 storage in Ketzin, Germany, 10th International Conference On Greenhouse Gas Control Technologies, Amsterdam, The Netherlands, Energy Procedia, 4, p. 4362-4370

Monne, J. and C. Prinet, 2012, Lacq-Rousse Industrial CCS reference project: Description and operational feedback after two and half years of operation., 11th International Conference on Greenhouse Gas Control Technologies (GHGT11), International Energy Agency Greenhouse Gas R&D programme, Kyoto, Japan, November 18–22, 2012, 10p.

Nicot, J. -P., and Solano, S. V., 2012, Impact of CO_2 impurities on storage performance and assurance; Tasks 1 and 2: Plume dynamics: The University of Texas at Austin, Bureau of Economic Geology, contract report prepared for CO_2 Capture Project Phase III (CCP3), 155 p.

Nicot, J.-P., S. Solano, J. Lu, P. Mickler, K. Romanak, C. Yang, and X. Zhang, 2011, Potential Subsurface Impacts of CO_2 Stream Impurities on Geologic Carbon Storage, 11th International Conference on Greenhouse Gas Control Technologies (GHGT11), International Energy Agency Greenhouse Gas R&D programme, Kyoto, Japan, November 18–22, 2012, 8p.

Palandri, J. L. and Kharaka, Y. K., 2004, A compilation of rate parameters of water-mineral interaction kinetics for application to geochemical modeling. U.S. GEOLOGICAL SURVEY, Menlo Park, California

Parkhurst, D. L. and Appelo, C. A. J., 1999, User's guide to phreeqc (version 2)— a computer program for speciation, batch-reaction, one-dimensional transport, and inverse geochemical calculations. U.S. Geological Survey

Renard, S., J. Sterpenich, J. Pironon, P. Chiquet, M. Lescanne, and A. Randi, 2011, Geochemical study of the reactivity of a carbonate rock in a geological storage of CO_2: implications of co-injected gases, 10th International Conference On Greenhouse Gas Control Technologies, Amsterdam, The Netherlands, Energy Procedia, 4, p.

Simon, D. E. and M. S. Anderson, 1990, Stability of Clay Minerals in Acid, SPE paper #19422, 12p.

Soong, Y., Goodman, A. L., McCarthy-Jones, J. R., and Baltrus, J. P., 2004. Experimental and simulation studies on mineral trapping of CO2 with brine. Energy Conversion and Management, 45, No. 11-12, 1845-1859.

Strazisar, B. R., Zhu, C., and Hedges, S. W., 2006. Preliminary modeling of the long-term fate of CO2 following injection into deep geological formations. Environmental Geosciences, 13, No. 1, 1-15.

Svensson, U., Dreybrodt, W., 1992. Dissolution kinetics of natural calcite minerals in CO2– water systems approaching calcite equilibrium. Chem. Geol. 100, 129– 145.

Taber, J. .J, 1985, Fate of small concentrations of SO_2, NO_x, and O_2 when injected with CO_2 into oil reservoirs, Argonne National Laboratory, ANL/CNSV-50, 30p.

Tarkowski, R. and Uliasz-Misiak, B., 2007. Reservoir rock reaction to CO2 - An experiment to estimate their use for carbon dioxide geological sequestration needs. Gospodarka Surowcami Mineralnymi-Mineral Resources Management, 23, No. 3, 109-117.

Tracy, S.L., Williams, D.A., Jennings, H.M., 1998. The growth of calcite spherulites from solution: II. Kinetics of formation. J. Cryst. Growth 193, 382– 388.

USDOE, 2012, CO2 Impurity Design Parameters, Quality Guidelines for Energy Systems Studies, NETL report DOE/NETL-341/011212, January 2012, 17p.

Wandrey, M., Pellizari, L., Zettlitzer, M., and Wuerdemann, H., 2011, Microbial community and inorganic fluid analysis during CO2 storage within the frame of CO2SINK - Long-term experiments under in situ conditions, 10th International Conference On Greenhouse Gas Control Technologies, Amsterdam, The Netherlands, Energy Procedia, 4, p.3651-3657.

Wang, J., D. Ryan, E. J. Anthony1, N. Wildgust, and T. Aiken, 2011, Effects of Impurities on CO2 Transport, Injection and Storage, 10th International Conference On Greenhouse Gas Control Technologies, Amsterdam, The Netherlands, Energy Procedia, 4, p. 3071–3078.

Wilkinson, M., Simmonds, M., Allam, R. and White, V., 2003, Oxyfuel Conversion of Heaters and Boilers for CO2 Capture, 2nd National Conference on Carbon Sequestration, May 5-8, Washington, DC.

Wilkinson, M., Boden, J., Panesar, R. and Allam, R., 2001, CO2 Capture via Oxyfuel Firing: Optimization of a Retrofit Design Concept for a Refinery Power Station Boiler, 1st National Conference on Carbon Sequestration, May 15-17, Washington, DC.

Xie, M., Bauer, S., Kolditz, O., Nowak, T., and Shao, H., 2006. Numerical simulation of reactive processes in an experiment with partially saturated bentonite. Journal of Contaminant Hydrology, 83, No. 1-2, 122-147.

Zanganeh, K., Shafeen, A. and Thambimuthu, K., 2004, A comparative Study of Refinery Fuel Gas Oxy-Fuel Combustion Options for CO2 Capture using Simulated Process Data, Proceedings of the 7th International Conference on Greenhouse Gas Control Technologies (GHGT-7), Vancouver, Canada.

Zhang, Y., Dawe, R.A., 2000. Influence of Mg{2+} on the kinetics of calcite precipitation and calcite crystal morphology. Chem. Geol. 163 (1–4), 129– 138.

VI. Appendix A: Experimental Setup

VI-1. Description of the Experimental Setup

Since its beginnings in April of 2010, the Experimental Group for Investigations of Supercritical CO_2 Interactions in Geologic Reservoirs at the UT Bureau of Economic Geology has sought to develop a program that addresses many of the experimental challenges currently being overlooked by much of the scientific community. These challenges include; 1) experimental flexibility, 2) rapid and reliable data collection, and 3) sampling integrity. The team engaged in discussions with other scientists doing high pressure/temperature fluid rock reaction experiments at Chevron, Stanford, and NETL to appreciate challenges and impediments. Since we had no infrastructure to begin with, we committed to build a system that was cutting edge by collaborating with experts in parallel industries such as Thar Process, Inc, a global leader in supercritical fluid technology and Dionex Corporation, a leader in chromatography and extraction systems for separating, isolating, and identifying the components of chemical mixtures. We have worked closely with these experts to design, develop and fabricate an experimental system that we believe has the innovative analytical and experimental capabilities to deliver superior results in supercritical CO_2 research.

After the experimental infrastructure was established, methods development and validation was a top priority to ensure that the data collected were reliable. This involved designing and fabricating additional extraction apparatus, performing numerous trial and error experiments to validate that measurement of CO_2 solubility was correct. Once the system was calibrated and validated, solubility experiments began under varying conditions. Numerous developmental challenges have been met and overcome along the way.

The system that we have built is a high-pressure (≤ 400 bars), high-temperature (≤ 150°C) batch and flow-through column reaction system designed to deliver aliquots of sample from both brine and supercritical CO_2 phases from a reactor directly into analytical apparatus for closed-system measurement. The technique for closed-system measurement is critical for maintaining the integrity of the high pressure-temperature (PT) sample. We are not aware of other research institutions currently conducting these types of experiments. The system is designed with; (1) 250-ml stirred reactor vessel capable of performing batch or column flow-through experiments, (2) pump apparatus for delivering supercritical CO_2 into the system with capability for mixing additional gases of interest for reaction, and (3) innovative closed collector system that separately samples supercritical CO_2 and brine components and quickly delivers them directly into analytical instruments without contamination with O_2 and with minimal disturbance to the sample, and (4) two ion chromatographs for direct analysis of anions and cations in brine.

The Supercritical Fluid Reaction (SFR) system enables rapid reaction of multiple compounds with supercritical CO_2. The system can be operated in a static, pressure control mode (batch) or a dynamic flow control mode (column). The automated supercritical reaction system is integrated with the appropriate heat exchangers and high pressure pumps necessary to pressurize CO_2 to supercritical conditions (31° C and 73.8 bars) and beyond and to mix other fluid components at these pressures (Figures 1 and 2). The bulk CO_2 delivery system, with mass flow meter, enables delivery of steady flow rates (from 50 to 350 g/min) of high pressure CO_2 to the reactor. The

pumps can be used in combination with other high pressure components and are therefore perfect for delivering mixed gases to the reactor. The capability for mixing gases is important for research on gas impurities.

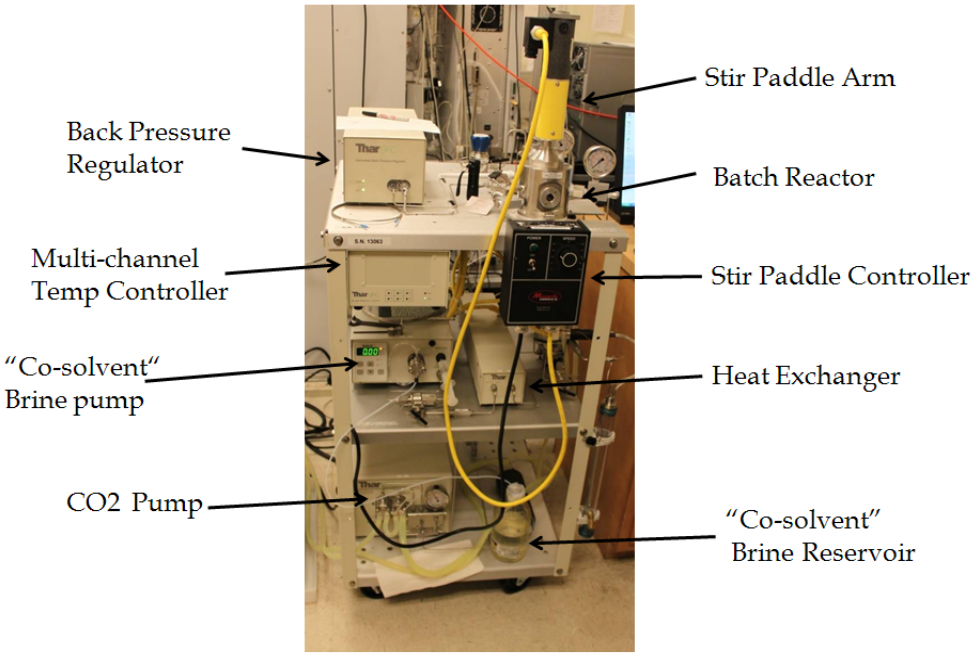

Figure 1. Integrated supercritical reaction system capable of gas mixing.

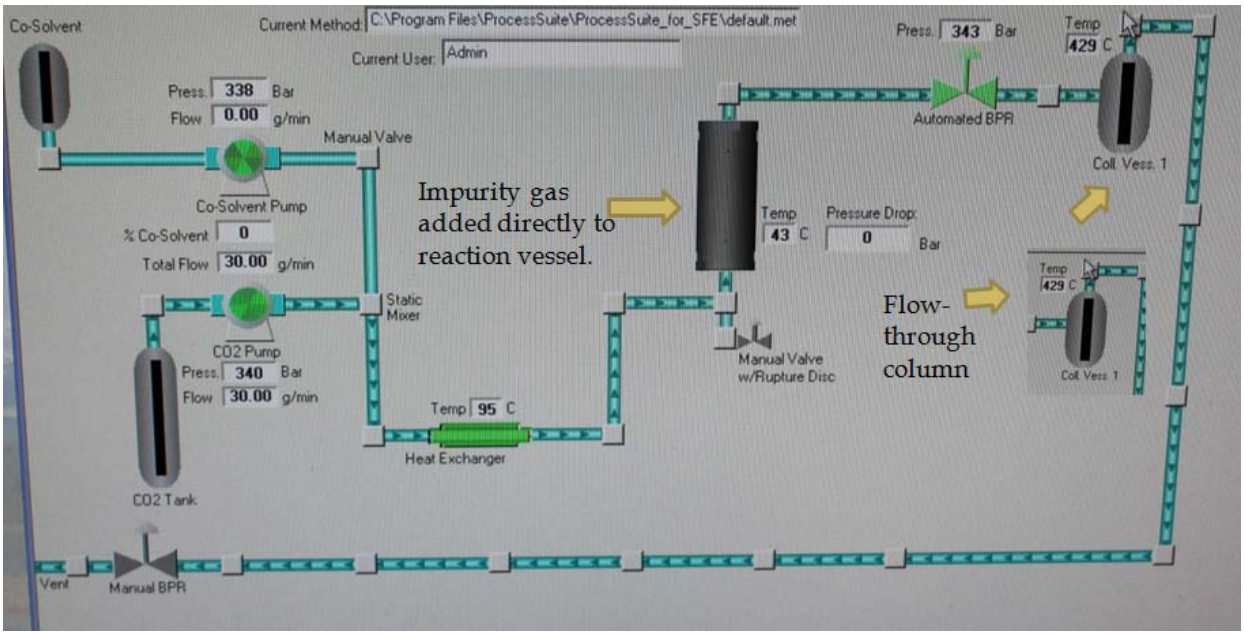

Figure 2. Automated system for high PT reactions of multiple phases.

Sampling the fluid components of the system for geochemical analysis has proven to be problematic for many researchers conducting these types of experiments (i.e. Kaszuba et. al., 2005, 2003, Rosenbauer et. al., 2005; Toews et al, 1995), and contamination of the system with atmosphere is commonly neglected. When sampled with a conventional diptube, fluids are

subjected to an oxygenated atmosphere which creates immediate oxidation of the system and skews results. We have worked closely with Dionex Corporation to develop innovative sampling methods that will directly and independently deliver brine samples to the analytical apparatus without oxygen contamination perturbing the system from its reaction state. This is difficult because the system must be ramped down in pressure and temperature before analysis, and this causes flashing and freezing of the supercritical CO_2 which may cause icing of the transfer lines causing mechanical problems and altering chemical results.

For sampling of the aqueous phase (Figure 3), an innovative system has been designed to directly sample brine from the reactor, automatically dilute (500:1 or 1000:1) the sample and pump it into two ion chromatographs, one with capabilities for analyzing cations and one for analyzing anions. Samples will not encounter O_2 during sampling and analysis due to real-time closed-system analysis over the course of the reaction. In addition, the ease of sampling and analysis will drastically cut experiment times and increase productivity.

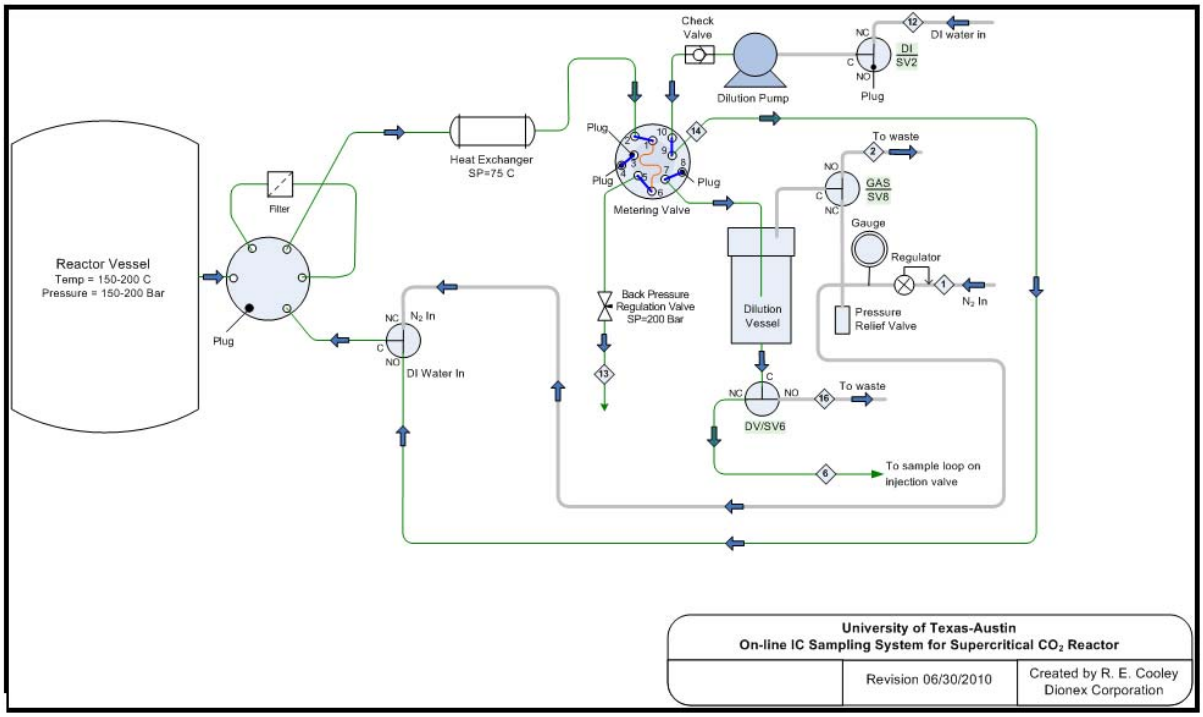

Figure 3. Schematic for innovative brine sampling system developed by scientists at Dionex and the BEG. The system will allow brine to be sampled directly from the reactor in a non-oxygenated setting, diluted and analyzed for anions and cations.

VI-2. Validation of the Experimental Setup

The first measurements performed on the new system were to match known values of CO_2 solubility at high pressure and temperature conditions. A large degassing glass apparatus for measuring gas dissolved gas in brine during reaction was designed by BEG scientists and made by the glass shop of Chemistry Department of The University of Texas at Austin. As shown in Figure 4, it has been connected with vacuum line, liquid sample container, pressure gauge, gas sample container, water bath circulator, drainage valve. Total volume of the degassing glass

apparatus is 931.4ml, including 924ml glass body and 7.4ml connection joints, which is determined by filling known volume of de-ionized water into the apparatus.

Figure 4. Picture of degassing glass apparatus in BEG gas geochemistry laboratory

Two sets of experiments have been conducted in order to evaluate the suitable conditions for CO_2 solubility measurement by means of integrating our high temperature and pressure apparatus, liquid sampling container and degassing glass apparatus.

CO_2 solubility measurement in de-ionized water at 20.7 MPa (3000psia) and 35°C

Identify the equilibration of CO_2 dissolution through pressure profile

Figure 5 shows the CO_2 pressure profile in the high PT reactor during the course of reaction of CO_2 and water. The profile shows pressure variations during charging the reactor with CO_2 using a CO_2 pump and also shows pressure drops caused when water and dissolved gas is sampled into the liquid sampling container. One of the key experimental elements is to quantify CO_2 dissolution by monitoring gas pressure change during the course of CO_2 dissolution into deionized water. The second element is to determine if liquid sampling reaches completion and is representative of conditions in the reactor. Figure 5a shows the pressure profile during charging of the reactor to 3900 psi and pressure loss upon dissolution of CO_2 into water. The first part of the graph represents initial charging of the reactor with subsequent pump shutdown and CO_2 dissolution into deionized water with stirring. This is a "static mode" without constant supply of CO_2 which necessitates a relatively long time to reach the equilibration of CO_2 dissolution. We also applied the "dynamic mode" (second part of the graph) in which a constant CO_2 supply to the reactor is maintained with a CO_2 pump during the course of CO_2 dissolution. It was found that the dynamic mode takes a relatively short time to reach equilibration of CO_2 dissolution. We recommend that static mode can be used at the beginning of experimental run, and the dynamic mode can be applied to maintain CO_2 at a designated pressure after the first

liquid sampling is completed. This technique will allow multiple sampling events over the course of a reaction without the need for setting up new experiments for each measurement.

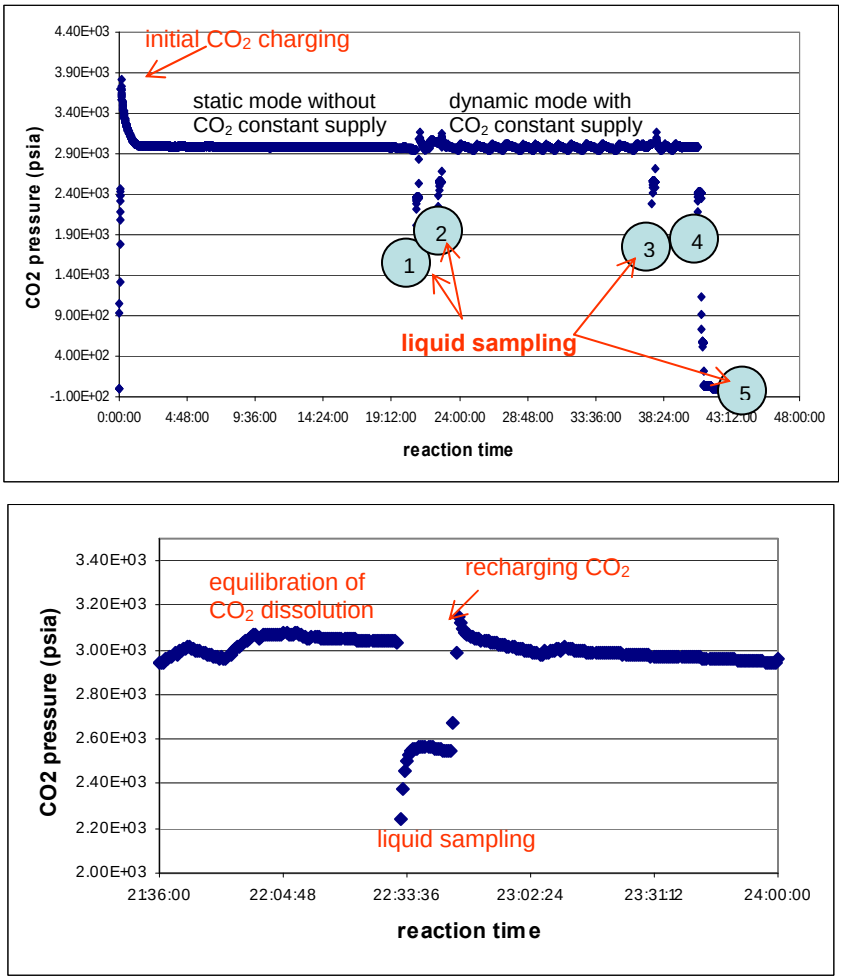

(b)

Figure 5. The change of CO_2 pressure in the reactor over the course of CO_2 dissolution and sampling

Determine the equilibration of liquid sample container through pressure profile

Figure 5b zooms in the pressure change in the reactor before and after taking the first liquid sample. The lines connecting the reactor and the liquid container are evacuated before opening the valve between the reactor and the lines during sampling. In CO_2 dissolved liquid sampling, the gas pressure in the reactor drops when the sampling lines are opened to the sampling container. When in dynamic mode, the CO_2 pump responds to the pressure drop during sampling and automatically recharges the reactor to the designated reaction pressure. Duplicate liquid samples may be taken over time for degassing measurements.

CO_2 solubility measurement through the degassing of gas dissolved liquid

Table 1 shows the preliminary results of the measured dissolved CO_2 amount at CO_2 pressure of 3000 psia and 35°C. In the table, ΔP is the measured pressure difference in the gas extraction apparatus before and after degassing of CO_2 dissolved in deionized water, and ΔW is the

measured weight of fluids sampled which is calculated by subtracting the measured weight of the empty liquid sampling cell from that of the full liquid sampling cell after sampling. It is assumed that the reacted liquid sample totally degasses in the extraction apparatus and that the change of ΔP is entirely attributed to dissolved CO_2. Under this assumption, an extremely high CO_2 solubility measurement was obtained for sample 5 which is the CO_2 pressure around 1.0 bar in reactor (it is highlighted in green in Table 1).

Table 1. Measured CO_2 solubility at P_{CO2} = 3000psi and 35°C

Sample ID	Reactor condition		Degassing apparatus condition				CO_2 solubility (mole CO_2/L H_2O)	
	P_{CO2} (bar)	T (°C)	ΔP (psi)	T (K)	ΔW (g)	ΔV (ml)	w/o H2O correction	w/ H2O correction
(1)	210.54	35	1.37	297.7	2.32	1.85	1.545	1.094
(2)	207.89	35	1.33	297.7	2.33	1.8	1.500	1.049
(3)	206.99	35	1.42	296.7	2.31	1.8	1.607	1.154
(4)	204.68	35	1.32	297.9	2.32	1.8	1.488	1.037
(5)	0.99	35	0.47	298.2	1.76	1.3	0.529	0.078

We collected the degassed gas of sample (5) and conducted a gas compositional analysis using the GC. Gas compositional analysis shows that CO_2 is about 14.8%, air (N_2+O_2) 0.3%. Total detected gas molar volume percent is only about 15% percent. The rest of 85% should be water vapor, which cannot be detected with our GC configuration. Given total degassed pressure is 0.47psi, CO_2 partial pressure in total degassed gas is about 0.07psi and water vapor pressure is estimated 0.40psi under our vacuum degassing apparatus configuration. The difference in the measured solubility of CO_2 in deionized water with and without the correction of water vapor pressure is significantly large (Table 1). Therefore we need to modify our system to minimize the contribution of water vapor pressure and accurately determine CO_2 partial pressure in the degassed gas with GC.

Helium experiment to quantify the contribution of water vapor to ΔP

Instead to loading CO_2 in the reactor, high pressure helium gas was loaded to quantify the contribution of water vapor to Δ*P***.** Helium should experience only slight dissolution compared to CO_2. Table 2 summarizes our results.

There is a large variation in the measured helium solubility after a correction is made for water vapor assuming a constant vapor pressure of 0.4psi for each run. This suggests the water vapor pressure might vary for each run. Therefore, we collected gas samples for (1) to (4) in Table 2, to determine variations in water vapor contribution.

Based on the measured partial pressure of helium in the degassed gas, we calculated the helium solubility in deionized water at high pressure. The helium solubility is from 0.58 to 0.86 mole helium/liter of H_2O. It gives a reasonably a consistent measurement for four times.

Table 2. Dissolved helium measurement in deionized water at 35°C

Sample ID	Reactor condition		Degassing apparatus condition				He solubility (mole He/L H_2O)	
	P_{He} (bar)	T (°C)	ΔP (psi)	T (K)	ΔW (g)	ΔV (ml)	w/o H2O correction	w/ H2O correction
(1)	146.57	35	0.41	295.6	2.3	1.85	5.12	0.123
(2)	133.95	35	0.45	297.4	2.3	1.85	5.59	0.621
(3)	127.05	35	0.59	297.6	11.5	10.1	1.46	0.472
(4)	113.95	35	0.56	297.5	11.5	10.8	1.39	0.397

Table 3. GC analysis result for degassed samples in table 2

Sample ID	He(%)	Air(%)	Calculated H_2O vapor(%)
1	16.8	24.8	58.4
2	10.4	23.8	65.8
3	48.8	12.7	38.5
4	44.3	6.6	49.1

Results of CO_2 dissolution in brine.

We completed experiments of CO_2 solubility in synthetic brine with three different salinities, different temperatures and pressures. About 81 datasets of CO_2 solubility in brine were measured. The experimental data of CO_2 solubility were compared to the results of two models: Duan's model and the Winprop model which were used to simulate CO_2 solubility in brine at the experimental conditions. Preliminary results show that CO2 solubility in brine estimates using the two models match well with the experimental data in pure water (salinity is equal to 0) (see Figure 6), but overestimates the experimental data as salinity of brine increases (Figures 7 and 8). However, Winprop can provide better results of CO_2 solubility than Duan's model. In addition to the Duan's model and Winprop, we are going to use other geochemical model tools, such as Geochemist workbench and/or Phreeqc to simulate the experimental data from the geochemical point of view.

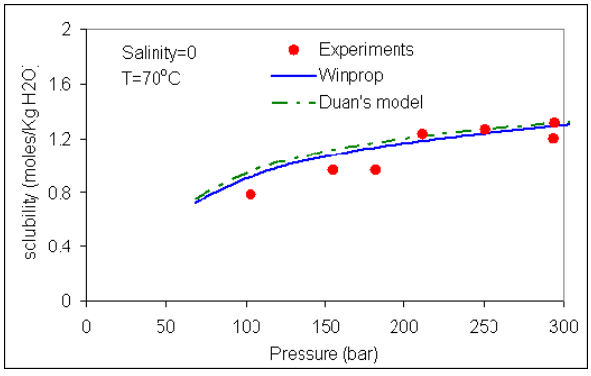

Figure 1 Comparison of experimental CO_2 solubility measured in water (salinity=0) with results of Duan's model and Winprop.

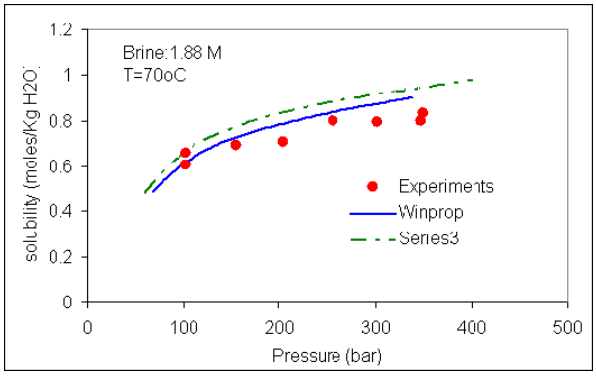

Figure 2 Comparison of experimental CO_2 solubility measured in water (salinity=1.88M) with results of Duan's model and Winprop.

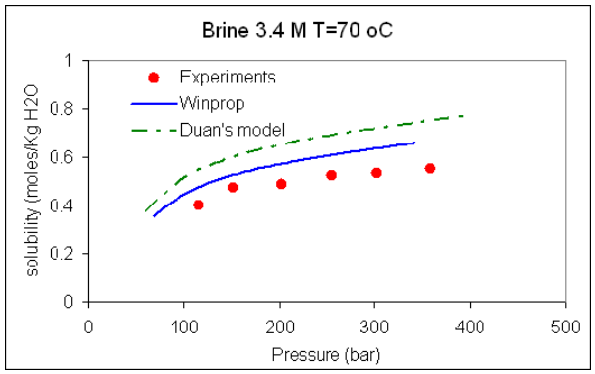

Figure 7. Comparison of experimental CO_2 solubility measured in water (salinity=3.4 M) with results of Duan's model and Winprop.

VI-3. References

Kaszuba, J. P., Janecky, D. R., and Snow, M. G., 2003, Carbon dioxide reaction processes in a model brine aquifer at 200C and 200 bars: implications for geologic sequestration of carbon: Applied Geochemistry, v. 18, p. 1065-1080.

Kaszuba, J. P., Janecky, D. R., and Snow, M. G., 2005, Experimental evaluation of mixed fluid reactions between supercritical carbon dioxide and NaCl brine: Relevance to the integrity of a geologic carbon repository: Chemical Geology, v. 217, p. 277-293.

Rosenbauer, R. J., Koksalan, T., and Panandri, J. L., 2005, Experimental investigation of CO2-brine-rock interactions at elevated temperature and pressure: Implications for CO_2 sequestration in deep-saline aquifers: Fuel Processing Technology, v. 86, p. 1581-1597.

Toews, K. L., Shroll, R. M., and Wal, C. M., 1995, pH-Defining Equilibrium between Water and Supercritical CO_2. Influence on SFE of Organics and Metal Chelates: Analytical Chemistry, v. 67, no. 22, p. 4040-4043.

VII. Appendix B: Literature Review

by Changbing Yang (adapted by J.-P. Nicot), April 2011

Potential Impacts of Geochemical Interactions amoung Rocks, Fluids, CO_2 and Impurities on Geological CO_2 Sequestration —A literature review of reactive transport in deep saline aquifers during CO_2 injection with impurities

Table of Contents

VII-1. Introduction

The CCP3 CO_2 impurities project is interested in understanding behavior of trace impurities such as N_2, O_2, H_2, CO, Ar, and SOx. Co-injection of supercritical CO_2 with impurities, especially SO_2, may affect mineralogical sequestration reactions, injectivities, seal properties near injection wellbores and long term performance of geological CO_2 sequestration, compared to injection of pure supercritical CO_2. Although their importance has been acknowledged for some time, such impacts of co-injection of CO_2 with impurities on geological carbon sequestration have rarely

been addressed extensively (Jacquemet et al., 2009). Apps (2006) reviewed potential impurities and hazardous elements which may originate from combustions of two types of power plants: conventional and IGCC. He pointed out that it would be more cost-effective if those impurities could be disposed together with supercritical CO_2. Sass et al. (2005) did a literature review that focused on SOx and NOx impurities in flue gas and assessed the effects of impurities in CO_2 streams on above-ground processing equipment. Jacquemet et al. (2009) briefly reviewed geochemical properties and numerical modeling of CO_2, impurities, brine, and reservoir rocks interactions, mainly based on three papers only: Xu et al. (2007), Knauss et al. (2005) and Gunter et al.(2000) since very few research results have been reported in the literature.

Wang et al. (2011) addressed a number of key issues related to effects of impuritiesin CO_2 streams on geological storage of CO_2. The authors reported (1) that non-condensable impurites such as N_2, O_2 and Ar may greatly reduce CO_2 storage capacity of geological formations, and there is a maximum reduction of the storage capacity at a certain pressure under a given temperature. By contrast, impurities that are more condensable than CO_2, such as SO_2, can increase the storage capacity, but there is a maximum increase at a certain pressure under a given temperature; (2) that change of density caused by non-condensable gas impurities results in lower injectivity of impure CO_2 into geological formations. However, above a threshold pressure range the injectivity could reach the level of pure CO_2 due to lowered viscosity; (3) that non-condensable impurities increase the buoyancy of the CO_2 plume. This would negatively affect the efficiency of solubility trapping and residual trapping of CO_2; and (4) thatthe effect of SO_2 on reduction of rock porosity and hence CO_2 injectivity would be much smaller than previously thought. The authors concluded that impurities have important impacts on CO_2 storage capacity, storage integrity, injectivity, and other factors.

A commented bibliography, not necessarily comprehensive, follows. We discuss the likely geochemical processes resulting from co-injection of supercritical CO_2, SO_2 and NOx, as well as results rom several laboratory experiments reported in the literature. We then evaluate past numerical modeling efforts assessing impacts of impure CO_2 on geological CO_2 sequestrations. Please note that discusssions often refer to flue gas of conventional coal-fired power plants rather than the oxygas waste injection stream of interest to this study (hence, the present study being carried out). It also sometimes refer to shallow fresh-water aquifer conditions and not to deep subsurface saline aquifers because of lack of reported or published information on the latter.

VII-2. Potential geochemical processes during co-injection of supercritical CO_2 with impurities

VII-2-1 H_2S

Although H_2S is not listed as a gas of interest, it is relevant to examine its impact in the subsurface, in particular pH changes. There are currently over 50 CO_2 injection projects in Alberta and North East British Columbia, Canada where H_2S has been co-injected into oil fields for enhancing oil production (acid gas injection). The impact of injecting H_2S as a co-injectant with CO_2 on the geochemistry of a saline aquifer has been investigated by Gunter et al. (2000), Knauss et al. (2005), Xu et al. (2007) and on interactions in the CO_2-H_2S-rock-well cement system have been discussed by Jacquemet et al. (2005) and Jacquemet et al. (2008). The most significant response to the presence of H_2S is the precipitation of pyrite through sequestration of Fe(II) from chlorites, and reduction of Fe(III) in iron oxides, i.e., hematite and goethite.

$$2H_2S + Fe^{2+} \leftrightarrow FeS_2 + 4\,H^+ \quad (1)$$

Because H_2S is quite soluble in the aqueous phase, a substantial fraction of that co-injected with CO_2 will partition into the formation waters and interact with the rocks.

VII-2-2 SO_2

The estimated concentration of SO_2 from a conventional power plant when deliberately recovered and incorporated with CO_2 in the injectate, ranges from 0.15 – 2 vol.% (Apps, 2006). Upon injection, SO_2 would dissolve into the pore waters, since SO_2 is extremely soluble in the aqueous phase. Ellis et al. (2010) summarized three different scenarios of geochemical processes when SO_2 reacts with the brine phase. The first one is that of SO_2 hydrolosis,

$$SO_2 + H_2O \leftrightarrow H_2SO_3 \quad (2)$$

This reaction produces only a weak acid, sulfurous acid. This process represents the case with no mechanism for oxidation of SO_2. When oxidizing conditions exist, SO_2 is oxidized following the reaction:

$$SO_2 + H_2O + 0.5\,O_2 \leftrightarrow H_2SO_4 \quad (3)$$

This produces sulfuric acid, a very strong acid.As mentioned by Ellis et al. (2010), in otherwise natural conditions, it is unlikely that O_2 is sufficient amount to drive this process since a typical fugacity of oxygen in deep saline formations is on order of 10^{-63} bar. Knauss et al. (2005) pointed out that although O_2 may be insufficient to oxidize very much SO_2, there are other thermal dynamically favored oxidants present in aboundance: pyrite, MnO, and water itself,

$$FeS_2 + SO_2 + 2H_2O \leftrightarrow Fe^{2+} + 2\,S^- + 4\,H^+ + SO_4^{2-} \quad (4)$$

and

$$SO_2 + 2\,H_2O \leftrightarrow H_2(g) + 2H^+ + SO_4^{2-} \quad (5)$$

The third scenario is that, under reservoir conditions, SO_2 is unstable with respect to its reaction products with the aqueous phase and will decompose (Apps, 2006):

$$4SO_2 + 4H_2O \leftrightarrow 3H_2SO_4 + H_2S \quad (6)$$

This process is also called as SO_2 disprorportionation which is typically associated with hydrothermal systems (Ellis et al., 2010). The sulfur in SO_2 is both oxidized to sulfate and reduced to sulfide in a ratio of 3:1. This reaction has been previously modeled as dominant mechanism of acid formation in the context of SO_2 co-injection during geological carbon sequestration (Palandri and Kharaka, 2005; Xu et al., 2007). The resulting sulfuric acid will attack almost all host rock minerals with the exception of quartz, leading to dramatic changes in mineralogy, and the precipitation of secondary sulfates and hydroxy-sulfates, and amorphous silica. Xu (2007) reported that most injected SO_2 is ultimately trapped as sulfate by alumite precipitation, yielding a peak volume fraction of 7%, with additional contributions by anhydrite and as minimal sulfide in the form of pyrite based on numerical modeling results.

It is unclear how this discussion will apply to the problem at hand since O_2 is present in the injection stream. SO_2 behavior and fate will ultimately depend on the respective initial amounts, respective solubility values, solubility kinetics, and SO_2 oxidation kinetics.

VII-2-3 NO_x

During oxidative combustion in a conventional coal-fired power plant, NO with minor N_2O is the primary NO_x components which are derived primarily from the nitrogen containing functional groups in the original coal. NO_2 could also form in the stack gases following combustion. NO is an oxidizing agent, and would be reduced in stages by organic material in the saline aquifer if present (Apps, 2006):

$$NO + \text{organic material} \leftrightarrow N_2 + CO_2 + H_2O \quad (7)$$

$$N_2 + \text{organic material} \leftrightarrow NH_3 + CO_2 \quad (8)$$

The conversion of N_2 to NH_3 is likely to be very slow in the absence of nitrogen fixing biota, but there are very limited data on the kinetics of these reactions. In fact, availability of organic matter in the deep brine formations may limit the two processes and therefore induce alternative decomposition pathways, such as reaction with co-injected SO_2, either directly, or through the agency of the H_2S decomposition product (Apps, 2006). The end product, NH_3, will hydrolyze to form $NH4^+$ and OH^-. $NH4^+$ may exchange with ions in the interlayer of clay or be adsorbed on the clay surfaces.

VII-2-4 Other gases

The gases contain small amounts of N_2, Ar, H_2, CO, and O_2. N_2 and Ar gases are the two most inert gases which may be co-injected with supercritical CO_2. The two gases may dissolve into brine or stay in the gas phase for long periods of time. Less is known about the behavior of the other gas components. Compared to SO_2, NOx, and CO_2, H_2, CO, and O_2 are relatively inactive. O_2, co-injected with supercritical CO_2, may dissolve into brine and therefore may alter the redox potential of brine. However, such change in redox potential may be subtle. Dissolved O_2 may react with ions in brine, such as dissolved Fe^{2+} and Mn^{2+}. As described above, O_2 can also oxidize SO_2 and indirectly impacts the formation pH. Solubilities of H_2 and CO are relative small, compared to that of O_2. H_2 could be used by bacteria if they are present in the storage formations. The possible reaction path, mediated by microorganisms, is (Chapelle et al., 2002):

$$4\,H_2 + CO_2 \rightarrow CH_4 + 2H_2O \quad (9)$$

CO, typically produced from partial oxidation of coals in power plants, is a good reducing agent, and therefore may reacted with iron oxides in the aquifer materials as well.

VII-3. Laboratory experimental simulation of interactions of CO_2, impurites and rocks

Many laboratory experimental simulations of interactions among rocks and supercritical CO_2 alone or with H_2S as one component have been reported (Bateman et al., 2005; Credoz et al., 2009; Dupraz et al., 2008; Dupraz et al., 2009a; Dupraz et al., 2009b; Kaszuba et al., 2003; Kaszuba et al., 2005; Ketzer et al., 2009; Liteanu and Spiers, 2009; Perrin and Benson, 2010; Pironon et al., 2007; Regnault et al., 2009; Regnault et al., 2005; Rosenbauer et al., 2005). However, to date, very limited information on laboratory experimental simulations of rocks and supercritical CO_2 with impurities such as SO_2 and NOx exists. In the following section, we will review some laboratory experimental simulations of the CO_2-SO_2-rock system presented by Mandalaparty et al.(2009), Sass et al. (2003), Heeschen et al. (2011), Summers et al. (2004), and Murphy et al. (2010). The last two references focused on sequestration, performed at ground

level, not in the subsurface, of supercritical CO_2 (+ SO_2) and selected reactive minerals. However, their experimental results may be interesting for studying impact of interactions between the CO_2+SO_2 supercritical mixture and rocks on geological carbon sequestration, so the two references are very briefly reviewed in the following section. It is worthwile noting that some other laboratory experiments related to aqueous sulfide and supercritical CO_2 may be reported in the literature, however, we will restrict ourselve to the four references.

VII-3-1 Laboratory experiments presented by Mandalaparty et al.(2009)

Experimental apparatus used by Mandalaparty et al.(2009) consists of series of four reactors made of 316-grade stainless steel, which were rated for 4000 psi at 600°C. It is interesting to note that the reactor used in this study has a provision for retrieving the rock sample without disturbing it through a detachable cap at the bottom. A single cylinder high pressure positive displacement pump is used to pressurize CO_2 in the reactor and high-pressure needle valves are used to control flow of CO_2. Dry CO_2 (drawn from a CO_2 cylinder equipped with a siphon) was used in all their experiments. A bench top temperature controller with SPECVIEW was used to controll the experimental temperature. Rock samples are 'dirty sandstone' comprised of equal proportions of calcite, dolomite, quartz, microcline, andesine and chlorite. The mineral grains were angular to circular in shape and ranged in size from 80-100 μm. about 3 grams (~0.5 g of each mineral) of rock was used in each experiment. Brine was prepared using high purity nano-filtered de-ionized (DI) by adding laboratory grade NaCl. After about 7 cc of CO_2 was injected into the reactor, the pressure of the experimental system to 2200 psi and eventually decreased to 2000 psi over a period of 37 hrs. Then the total pressure of the system stabilized around 2000 psi for the duration of the experiment. They reported that the pressure showed few fluctuations and may be attributed to changes in the ambient temperature in the laboratory.

Total four sets of experiments were carried out at different conditions with different feed gas compositions. Three sets were conducted with rocks and CO_2 alone with different experimental temperature and initial pH. One set was conducted with 90% CO_2 and 10% SO_2. The rock sample analysis was carried out using X-ray diffraction (XRD), scanning electron microscope (SEM) and energy dispersive X-ray spectroscopy (EDS) analyses.

Mandalaparty et al.(2009) reported that (1) experiments with brine, rocks and supercritical CO_2 alone revealed that the initial time period was dominated by dissolution of minerals like calcite. As the reactions progressed, reprecipitation causes the calcium ion concentration to decrease; and (2) presence of SO_2 changes the fundamental chemistry of the system as described next.

Ca concentration increased throughout the experiment with a final increase of almost 80% (Figure 1). This increase is almost 1.5 times greater than the increase observed in the experiments with CO_2 as pure gas. The most significant observation with presence of SO_2 gas as impurity in CO_2 gas is the change in pH values. The pH of the system was 1.9 after 14 days, 2.48 after 37 days whereas, in the experiment of CO_2 as pure gas, pH decreased to approximately a value of 4.5 after 27 days and then stablized at around 6.7. This experimental result is consistent with the numerical modeling result reported by Elis et al. (2010). However, the pressure of CO_2 + SO_2 was maintained at 600 psi through the experiment which may be lower than pressures under reservoir conditions (Figure 2). Mandalaparty et al.(2009) were also able to quantify the mineral changes in terms of weight before and after the experiment based on XRD analysis (Table 1). As expected, precipitation of anhydrite (calcium sulfate) is observed later in time according to the following reaction:

$$SO_4^{2-} + Ca^{2+} \leftrightarrow CaSO_4 \quad (10)$$

Table 1. Quantitative estimates of changes in composition of the minerals (wt%) before and after the experiment (CO_2 + SO_2) from XRD analysis after 37 days (Mandalaparty et al., 2009)

Mineral	Initial (wt%)	Reacted (wt%)
Andesine	17	15
Calcite	17	2
Dolomite	12	8
Quartz	19	22
Chlorite	16	13
Microcline	18	23.7

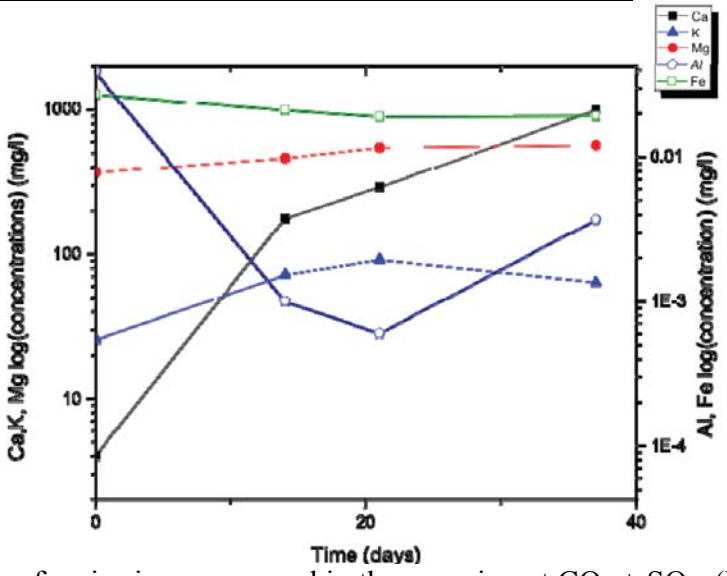

Figure 1. Concentrations of major ions measured in the experiment CO_2 + SO_2 (Mandalaparty et al., 2009)

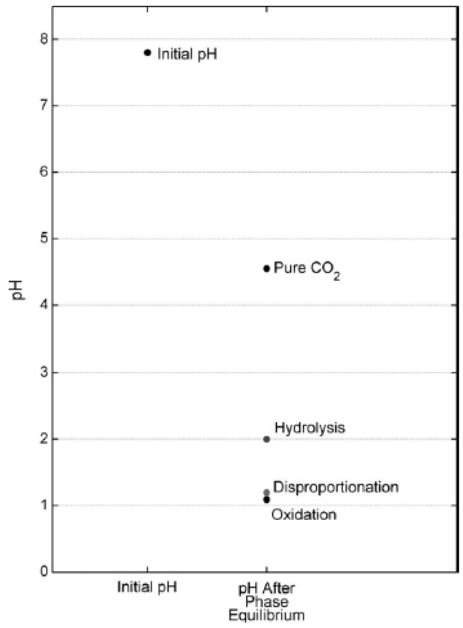

Figure 2. Phase equilibrium brine pH results for CO_2 + SO_2 and CO_2 alone for an initial alkalinity of 3.75 10^{-2} M (Ellis et al., 2010).

VII-3-2 Laboratory experiments presented by Sass et al. (2003)

Sass et al. (2003) conducted a set of batch experiments to study the potential for long-term sequestration of CO_2 in a deep, regional host rock formation; and to evaluate the compatibility of overlying caprock with injected CO_2 with regard to its effectiveness as a barrier against upward migration of the injectate. The researchers also conducted experiments to test the effects of SO_2 impurity and to evaluate if SO_2 impedes carbon sequestration or produces byproducts that may potentially impact the sequestration processes.

The reaction vessels are made of chemically resistant Hasteloy^{TM} C-276 and lined with PTFE-Teflon inserts. Each vessel has a one-liter internal capacity to be filled with brine solution and rock samples (or solid minerals). The experiments ran for time periods ranging from 30 to 90 days. Gas compositions were analyzed at the end of each experiment.The reacted solution was analyzed for total organic carbon, alkalinity, pH, ORP, sulfate, chloride, and metals. The solids were rinsed two times and then anaylzed by several techniques, including optical microscopy, x-ray diffraction (XRD), scanning eletron microscopy (SEM) and EDS, and x-ray photoelectron spectroscopy (XPS). In the SO_2 experiments, pyrite was added to maintain a chemically reducing environment and to provide a source of iron. Concentrations of SO_2 in the CO_2 and SO_2 mixture were typical of flue gas from coal combustion when desulfurization is not used.

Results of the experiments with pure CO_2 show no indications of carbon trapping reactions and no behavior that would adversely affect injecivity. Results of the experiments with CO_2 and SO_2 mixture increased iron leachability. Sass et al. (2003) could not find processes other than increasing iron leachability and suggested that the potential benefits of co-injeting SO_2/CO_2 mixed waste could be considered to determine whether this practice is economically favorable.

VII-3-3 Laboratory experiments presented by Heeschen et al. (2011)

Heeschen et al. (2011) conducted a set of high-pressure and high-temperature experiments to elucidate mineral and fluid alterations and quantify kinetic rates for the mineral–fluid–CO_2 co-injected gas system within the COORAL project "CO_2 Purity for Separation and Storage". Their unstirred batch-reactor system can be used to conduct four contemporaneous experiments at precisely defined P-T conditions of up to P≤590 bar and T≤350°C. Experiments were conducted using three components: (1) natural mono-minerals, (2) salt solutions representing brines of deep saline aquifers in Northern Germany and (3) binary gas mixtures of CO_2 plus one accessory gas. The reaction cell is made of gold with volumes up to 130 ml which allow the addition or removal of fluids throughout the experiment without altering the experimental conditions. However, the authors only reported the experimental results of CO_2-brine-dolomite. Experiments for CO_2 with trace gases are still under way.

VII-3-4 Laboratory experiments presented by Summers et al. (2004)

One of the objectives of the laboratory experiments conducted by Summers et al. (2004) is to investigate the effect of a small percentage of SO_2 in the CO_2 stream on the mineral-carbonation sequestration approach with two types of rock samples: olivine from the Twin Sisters deposit in northwestern Washington State (TSO) and basalt from an outcrop of the Columbia River Basalt

Group (CRB) in north-central Oregon. TSO is forsterite, the magnesium-rich member of the olivine family. CRB contains lesser but significant amounts of magnesium (Mg), calcium (Ca), and ferrous iron (Fe^{2+}). The TSO and CRB feed materials were initially ground to a nominal size of less than 75 microns in laboratory-scale rod and/or ball mills. In each experiment, 167 grams of mineral were combined with a 0.64M $NaHCO_3$ and 1M NaCl carrier solution in a 15%-solids slurry and fed to a 2-liter autoclave. The system was then purged with CO_2, pressurized to 150 psi (10 atm) gas (CO_2 or CO_2 + SO_2), stirred at 1000 rpm, heated to the test temperature of 185° C (the warm-up period was 1 hr), and held at temperature and pressure for 1hr (TSO) or 6 hr (CRB).

One interesting result reported in the study was that SO_2 in the mixed gas did not inhibit the carbonation reaction initiated by CO_2 and may have enhanced it slightly, perhaps by increasing the solubility of Mg. They reported that SO_2 had little effect on the chemistry of the solid products of the carbonation reactions and solid sulfates did not form to any significant extent. This result is different than that oberved in the laboratory experiment conducted by Mandalaparty et al.(2009). One of the possible reasons could be that the different mineral assemblage of the rock samples used in the two laboratory experiments.

Since no mineral reactions were observed, Summers et al. (2004) concluded that the amount of SO_2 taken into solution is determined by the volume and solubility limits of the solution. In contrast, the quantity of CO_2 sequestered is dictated by the quantity of cations available for carbonation and the kinetics of the carbonation reaction.

VII-3-5 Laboratory experiments presented by Murphy et al. (2010))

Murphy et al. (2010) conducted two types of experiments (ex-situ experiments and in-situ experiments) to study the reaction between supercritical CO_2 and water containing ferrihydrite and sodium sulfide. A high pressure micro-reactor cell was used and has a capability for the collection of ATR-FTIR spectra at elevated pressure and temperature.

Experimental results by Murphy et al. (2010) illustrated that if reservoir rocks contain iron oxyhydroxide, such as the Frio “C” sandstone in the South Liberty oil field (Kharaka et al., 2006), SO_2 (or H_2S) injection will lead to the formation of siderite in the presence of supercritical CO_2. The time scale for iron reduction and the transformations of the ferric minerals during exposure to supercritical CO_2 is relatively short. However, it must be noted that in the reservoir conditions (temperature and pressure) may be different from the conditions in the laboartory and therefore they suggested that more laboratory experiments may need to be conducted to explore reductive mechanisms utilizing H_2S and SO_2 in geological sequestration.

VII-4. Numerical evaluation of co-injection of CO_2 with impurities for geological carbon sequestration

Numerical modeling of geochemical impacts on storage of co-sequestration of CO_2 with impurities has been rarely addressed (Jacquemet et al., 2009). The possible reasons are (1) little or no data exists on transport properties, heat capacity, solid-gas interficial tensions and thermal properties of multicomponent gas mixtures; and (2) current numerical codes are limited in their ability to perform such simulations. These numerical modeling studies of co-injection of CO_2 and impurities reported in the literature are based on some assumptions in order to overcome the

codes limitations such as inability to include H_2S into the non-aqueous phase (Jacquemet et al., 2009).

VII-4-1 Numerical codes

There are several numerical codes which could to be used for simulating geochemical impacts of co-injecting CO_2 with impurities on geological CO_2 sequestration. There are: TOUGHREACT (Xu et al., 2007), STOMP (Bacon et al., 2009; White and Oostrom, 2006), CrunchFlow (Steefel, 2009), PHREEQC (Parkhurst and Appelo, 1999), and PATHARC.94 (Gunter et al., 2000).

TOUGHREACT introduces reactive chemistry into the multiphase fluid and heat flow code TOUGH2 (Pruess et al., 2004). More information on the TOUGHREACT can be found at the website (http://www-esd.lbl.gov/TOUGHREACT/). A new fluid property module, ECO2N, based on work by Spycher and Pruess (2005), provides an accurate description of the thermophysical properties of mixtures of water and CO_2 under conditions typically encountered in saline aquifers of interest for CO_2 disposal ($10°C \leq T \leq 110°C$; $P \leq 600$ bars). TOUGHREACT can take into account changes in porosity and permeability due to mineral dissolution and precipitation (but not field-proven to our knowledge). A broad range of subsurface thermal–physical–chemical processes are considered under various thermohydrological and geochemical conditions of pressure, temperature, water saturation, ionic strength, and pH and Eh. Further details on the process capabilities are given in Xu et al. (2006). It must be noted that in oreder to use TOUGHREACT, the user need to directly assume dissolved amount of H_2S and SO_2 in brine in order to simulate co-injection of CO_2 with impurities of H_2S and SO_2 gas as the software cannot compute it from equilibrium with a gas phase. .

CrunchFLow (or CRUNCH in Knauss et al., 2005) is a computer software package for simulating multicomponent, multi-dimensional reactive transport in porous media (Steefel, 2009). The features of the code include: simulation of advective, dispersive, and diffusive transport in up to two dimensions using the global implicit (GIMRT) option or three dimensions using time-splitting of transport and reaction (OS3D); non-isothermal transport and reaction; unsaturated transport with gas-aqueous phase exchange; multicomponent aqueous complexation; kinetically-controlled mineral precipitation and dissolution; multicomponent ion exchange on multiple sites; multicomponent surface complexation on multiple sites with or without an electrostatic correction based on the double layer model. Site densities are linked to mineral concentrations which may evolve; microbially-mediated reactions based on Monod type formulations; multicomponent diffusion with an electrochemical migration term to correct for electroneutrality where diffusion coefficients of charged species differ; multiple options (equilibration with a gas or mineral phase, total concentration, fixed activity) for initialization of boundary and initial conditions. For simulating co-injection of CO_2 with impurities (H_2S and SO_2), CrunchFLow assumes CO_2, H_2S and SO_2 as dissolved gas phases into brine for simulating coinjection of CO_2 with those impurities (Knauss et al., 2005).

STOMP-WCS-R is a simulator for water, CO_2, salt and reactions (White and Oostrom, 2006). Entrapment of CO_2 with imbibing water conditions can be modeled with the hysteretic two-phase k-s-p functions. Supercritical CO_2 has the role of a gas in these two-phase k-s-p relations. Geochemical simulations were performed with the batch geochemistry solution module ECKEChem (Equilibrium-Conservation-Kinetic Equation Chemistry).

PHREEQC and its allied reactive transport model, PHAST, has the more complete chemical database and accounts for a wide range of geochemical reactions including redox reactions (Parkhurst and Appelo, 1999). PHREEQC does not include a real gas approach for solubility calculation. SCALE2000 includes a real gas approach for calculating the solubility of the mixture CO_2-H_2S-H_2O-CH_4-N_2, but without considering redox reactions. PATHARC.94 is a numerical code for simulating reaction paths in a batch experiment (Gunter et al., 2000). No real gas approach is considered in the simulations.

VII-4-2 Numerical modeling conducted by Knauss et al (2005)

Knauss et al. (2005) presented the results of 1-D reactive transport simulation to investigate the impact of mixtures of dissolved CO_2, H_2S or SO_2 on carbon sequestration in the Frio Fm., TX. The model mineralgy and modal aboundances are based on average of 12 peterographic and XRD analysis for Frio Fm. sand samples. Total of 8 primary minerals and 8 secondary minerals were considered in the model and assumed to proceed kinetically. The "TST-like" formulation is used to describe kinetics of mineral dissolution/precipitation. Reaction constants used in the numerical simulations are listed in Table 2. The authors pointed out that lack of kinetic data concerning dawsonite dissolution precipitation is a problem.

Since Pitzer equations were not implemented in CrunchFlow, the extended Debye-Huckel formalism was used for calculating activity coefficients of aqueous species. Their simulations suggest that relatively high concentration of H_2S co-injected with CO_2 would not adversely impact injectivity compared to the injection of CO_2 alone (Figure 3). However, SO_2 does make a significant difference due to the lower pH (Figure 3). Co-injection of a very small amount of SO_2 (10^{-6} bar partial pressure) would lead to a brine pH of unity and enhanced mineral dissolution. This extreme acidification was attributed to the formation of sulfuric acid.

Knauss et al. (2005) also evaluated how efficient CO_2 sequestration is when either H_2S or SO_2 is present as an impurity. Results displayed in Table 3 suggest that the CO_2 only and the CO_2 and H_2S cases are virtually identical in terms of the C inventory. In the case of CO_2 and SO_2 more carbon remains in the fluid and less has been trapped as mineral. Numerical results also indicate that anhydrite will precipitate when SO_2 is co-injected with CO_2 and may potentially leads to porosity loss. Due to the code limitation, the authors could not evaluate this impact on injectivity.

Table 2 Kinetic data used in the simulations of Knauss et al. (2005)

Mineral	logk	Ea	n	Mineral	logk	Ea	n
	(mol/m2as)	(kcal)			(mol/m2as)	(kcal)	
Albite	-9.69	14.3	0.5	Kaolinite	-11.6	15	0.17
Albite	-12	16.2	0	Kaolinite	-13	15	0
Anhydrite	-2.76	7.65	0.11	Magnesite	-4.36	4.54	1
Labradorite	-8.86	15.9	0.5	Magnesite	-9.35	15	0
Labradorite	-12	16.2	0	Muscovite	-11.7	5.26	0.4
Barite	-7.19	7.65	0.11	Muscovite	-13	15	0
Calcite	-1.16	4.54	1	Pyrite	-8	15	0
Calcite	-6.19	15	0	Quartz	-13.9	20.9	0
Chalcedony	-12.7	16.5	0	Siderite	-3.01	5	0.9
Clinochlore	-11.6	15	0	Siderite	-8.9	15	0
Dawsonite	-7	15	0	Strontianite	-3.03	10	1

K-feldspar	-9.45	12.4	0.4	Strontianite	-7.35	10	0
K-feldspar	-12	13.8	0				

Table 3 Carbon inventory after a 100-year simulation in three cases

	Pre-injection	CO_2	CO_2+H_2S	CO_2+SO_2
Fluid(mol)	1.04	186	185	259
Mineral (mol)	190	287	284	228

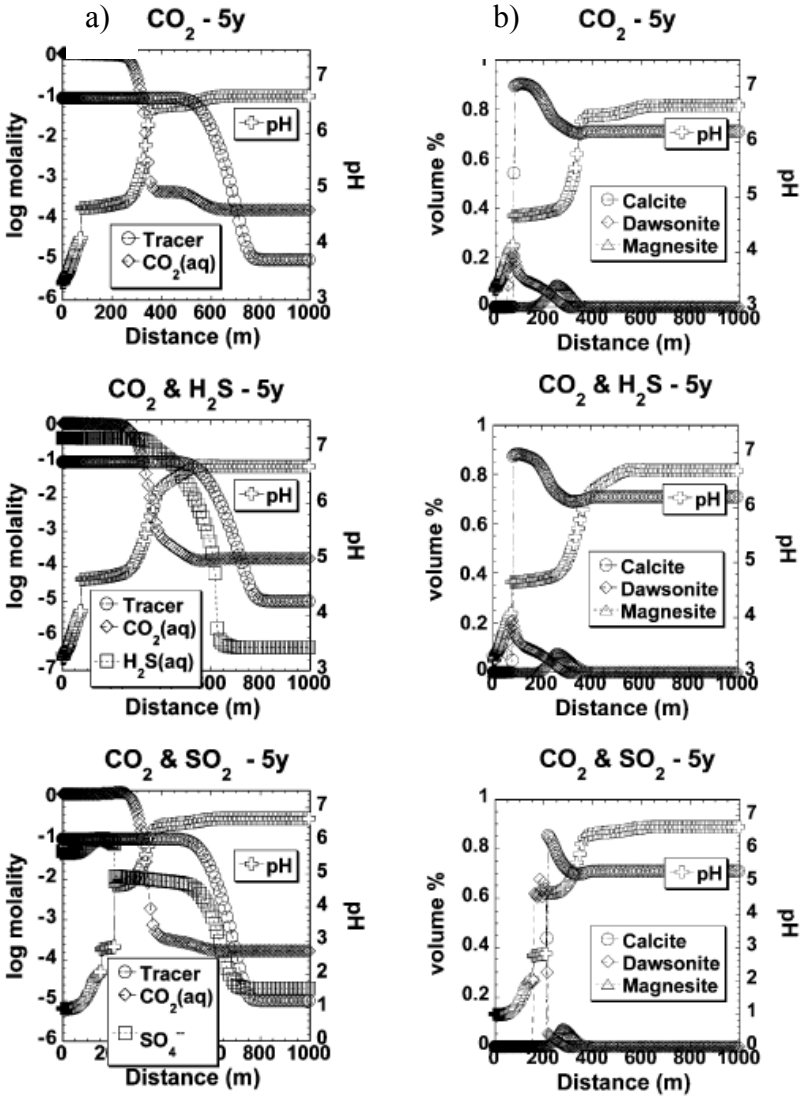

Figure 3. a) Molal concentrations and pH and b) Volume percent of carbonate minerals throughout the domain at the end of the injection phase (5 years) (Knauss et al., 2005).

VII-4-3 Numerical modeling conducted by Xu et al (2007)

Xu et al. (2007) simulated injection and mineral trapping of CO_2 with H_2S and SO_2 in a sandstone formation which is typical of those encountered in Gulf Coast aquifers using TOUGHREACT. The model domain is a 1-D radial region surrounding an injection well.

Mineral reactions are assumed to proceed kinetically. Multiphase flow was considered for CO_2, and brine. However, because of code limitation, either H_2S or SO_2 was assumed to be a dissolved phase in brine. Kinetic rate for mineral reactions used in Xu et al. (2007) models are listed in Table 4.

Table 4. Parameters for calculating kinetic rate constants of minerals (Xu et al., 2007)

Mineral	A (cm^2/g)	Parameters for kinetic rate law							
		Neutral mechanism		Acid mechanism			Base mechanism		
		k^{25} (mol/m^2/s)	E (kJ /mol)	k^{25}	E	n (H^+)	k^{25}	E	n (H^+)
Quartz	9.1	1.023×10^{-14}	87.7						
Kaolinite	108.7	6.918×10^{-14}	22.2	4.898×10^{-12}	65.9	0.777	8.913×10^{-18}	17.9	−0.472
Illite	108.7	1.660×10^{-13}	35	1.047×10^{-11}	23.6	0.34	3.020×10^{-17}	58.9	−0.4
Oligoclase	9.1	1.445×10^{-12}	69.8	2.138×10^{-10}	65	0.457			
K-feldspar	9.1	3.890×10^{-13}	38	8.710×10^{-11}	51.7	0.5	6.310×10^{-12}	94.1	−0.823
Na-smectite	108.7	1.660×10^{-13}	35	1.047×10^{-11}	23.6	0.34	3.020×10^{-17}	58.9	−0.4
Chlorite	9.1	3.02×10^{-13}	88	7.762×10^{-12}	88	0.5			
Hematite	12.9	2.512×10^{-15}	66.2	4.074×10^{-10}	66.2	1			
Magnesite	9.1	4.571×10^{-10}	23.5	4.169×10^{-7}	14.4	1			
Dolomite	9.1	2.951×10^{-8}	52.2	6.457×10^{-4}	36.1	0.5			
Low-albite	9.1	2.754×10^{-13}	69.8	6.918×10^{-11}	65	0.457	2.512×10^{-16}	71	−0.572
Siderite	9.1	1.260×10^{-9}	62.76	6.457×10^{-4}	36.1	0.5			
Ankerite	9.1	1.260×10^{-9}	62.76	6.457×10^{-4}	36.1	0.5			
Dawsonite	9.1	1.260×10^{-9}	62.76	6.457×10^{-4}	36.1	0.5			
Ca-smectite	108.7	1.660×10^{-13}	35	1.047×10^{-11}	23.6	0.34	3.020×10^{-17}	58.9	−0.4
Alunite	9.1	1.000×10^{-12}	57.78				1.000×10^{-12}	7.5	−1.0
Opal-A (dissolution)	9.1	4.900×10^{-13}	76						
Opal-A (precipitation)	9.1	3.800×10^{-10}	49.8						
Pyrite	12.9	$k^{25}=2.818\times10^{-5}$		$k^{25}=3.02\times10^{-8}$					
		$E_a=56.9$		$E_a=56.9$					
		n (O_2(aq))=0.5		n (H^+)=−0.5, n (Fe^{3+})=0.5					

Xu et al. (2007) conducted two groups of simulations. The first group of three simulations corresponds to the combinations of injected gases (CO_2 only, CO_2+H_2S, and CO_2 +SO_2). The second group of simulations examined sensitivities to reaction rates by decreasing the magnitude of the rate constant (or surface area) of oligoclase, chlorite, and opal-A each by one order of magnitude.

Xu et al. (2007) concluded that the co-injection of H_2S, compared to injection CO_2 alone, does not significantly affect pH distribution, mineral alteration, or CO_2 mineral sequestration. This is consistent with Knauss et al. (2005). The co-injection of SO_2 can result in a substantially different pH distribution and mineral alteration. A larger and more strongly acidified zone will form with co-injection of SO_2. Secondary sulfates and pyrite will precipitate at a radial distances ranging from 50 to 150 m. The authors also found that co-injection of SO_2 could inhibit ankerite precipitation (see Figure 4). However, it does precipitate in significant amounts together with dawsonite in the region immediately peripheral to the acidified zone, each occupying volume fractions of about 3%.

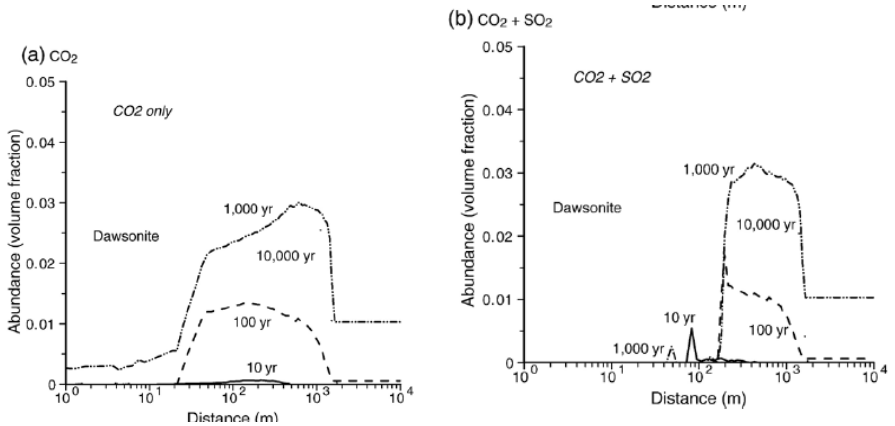

Figure 4. Variation of dawsonite abundance with time (Xu et al., 2007)

Xu et al. (2007) suggested that porosity increases significantly in the acidified zones where mineral dissolution dominates. With co-injection of SO_2, the porosity increases from an initial 0.3 to 0.43 after 100 years. It is interesting to note that within the CO_2 mineral-trapping zone, the porosity decreases to about 0.28 for both cases of CO_2 alone and CO_2+SO_2, because of precipitation of secondary carbonates in the rock matrix. They authors reported that precipitation of secondary sulfates at the acidification front causes the porosity to decrease to 0.23 which is due to the maximum precipitation of alunite.

For both CO_2 alone and CO_2 + SO_2 injection cases, Xu et al. (2007) found that the patterns and amounts of carbonate mineral precipitation in the CO_2 trapping zone are similar, although the acidified zone resulting from injection of CO_2 extends only to a radial distance of 50 m from the well bore, compared with that resulting from the co-injection of SO_2, which extends to 200 m. CO_2 is sequestered mainly as precipitation of ankerite and dawsonite, together with a small amount of siderite. After 10,000 years, CO_2 mineral trapping could reach about 40–50 kg/m^3 of injection zone host rock, which is very close to the maximum possible for the specified host rock mineralogy.

Xu et al. (2007) concluded that most injected SO_2 was ultimately trapped as sulfate by alunite precipitation, with additional contributions by anhydrite and as minimal sulfide in the form of pyrite. Pyrite also forms during co-injection of CO_2 and H_2S.

VII-4-4 Numerical modeling by Bacon et al. (2009)

Bacon et al. (2009) performed numerical simulations of pilot-scale CO_2 injection at two host formations in the midwestern United States (Rose Run and Copper Ridge) with co-sequestration of SO_2 to assess the competing effects of dolomite dissolution and anhydrite precipitation on formation hydraulic properties. As mentioned previously, the numerical code, STOMP, was used (Bacon et al., 2009). The geochemical model considers 14 carbonate, silicate and sulfate aqueous species, and four mineral species. The mineral composition of the formation was assumed from average observed values from the ELAN analysis (Figure 5). It can be seen two host formations have significant differences in mineral compositions.

a) b)

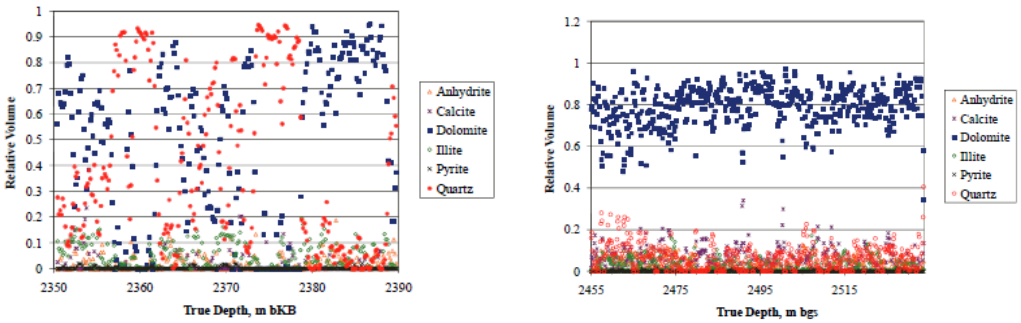

Figure 5. Mineral Proportions of a) the Rose Run Formation and b) the Copper Ridge Formation

Table 5. Reaction rates used in the numerical simulations of Bacon et al. (2009)

Kinetic Reaction	Log Equilibrium Coefficient at 54°C	Intrinsic Rate Constant, k_0, mol m^{-2} s^{-1}	Activation Energy, E_a, kJ mol^{-1}
Anhydrite = $Ca^{2+} + SO_4^{2-}$	-4.67	2.07×10^{-1}	14.3
Calcite = $-H^{+} + Ca^{2+} + HCO_3^{-}$	1.42	2.03×10^{-2}	23.5
Dolomite = $-2H^{+} + Ca^{2+} + Mg^{2+} + 2HCO_3^{-}$	1.53	$4.13\times10^{+1}$	52.2
Quartz = SiO2(aq)	-3.54	$2.79\times10^{+2}$	90.1

Kinetic mineral dissolution/precipitation reactions were assumed to be governed by Transition State Theory. Table 5 lists the reaction rates used in the numerical simulations of Bacon et al. (2009). A 2-D axisymmetric domain was considered in the numerical simulations. Co-sequestration of SO_2 was simulated by adding 1 percent SO_2 by mass to the injected CO_2.

Bacon et al. (2009) reported that the largest increases in anhydrite mass are seen close to the injection well because anhydrite precipitates more rapidly than the other minerals considered in the study when SO_2 is co-injected with CO_2. Their numerical results suggest that the change in anhydrite mass is as high as 14.2 percent for the Rose Run and 60.5 percent for the Copper Ridge injections (Figure 6). It can be seen that different host formations could result in sequestration of SO_2. Finally they concluded that the addition of SO_2 to the injection results in the precipitation of anhydrite near the well. For a 330,000 metric ton injection of CO_2, with a 100-year recovery period, mineral dissolution/precipitation does not significantly affect the rate of carbon sequestration in, or the formation properties of, the Rose Run and Copper Ridge formations.

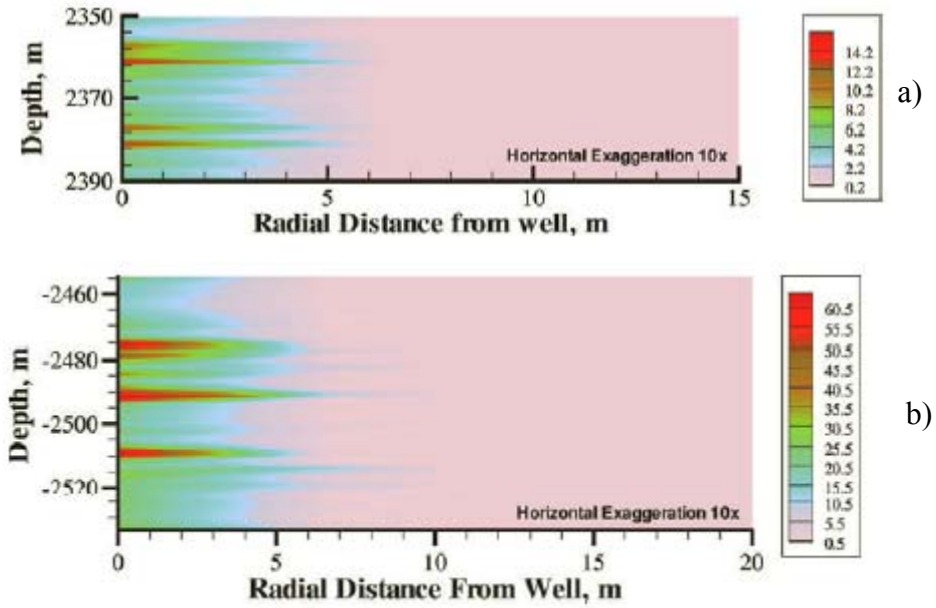

Figure 6. Percentage change in anhydrite mass 100 years after injection of CO_2 and SO_2 in a) the Rose Run Formation and b) the Rose Run Formation

VII-4-5 Numerical modeling conducted by Koenen et al. (2011)

Koenen et al. (2011) reported geochemical modeling results of effects of impurities in CO_2 on a sandstone aquifer. The geochemical modeling was performed with PHREEQC. Two possible CO_2 streams from pre-combustion and oxyfuel (semi-purified) capture technology were simulated to address the effects of impurities on storage (Table 6). In the pre-combustion stream some hydrocarbons are present and assumed to be chemically inert. N_2 and Ar are also assumed to be chemically inert.

Table 6. CO_2 streams with impurities from a pre-combustion and an oxyfuel capture technology (Koenen et al., 2011)

	pre-combustion (mole %)	Semi-purified oxyfuel (mole %)
CO_2	99.64	98.0
N_2	0.077	0.7
O_2	0.0045	0.7
H_2	0.14	-
CO	0.03	0.005
H_2S	0.00014	-
SO_2	-	0.007
NO	-	0.01
Ar	-	0.6

Mineralogy considered in the model is taken from the mineralogical composition of a potential Dutch CO_2 storage field (Table 7). The authors concluded that (1) besides CO_2, H_2S, NO and SO_2 can lower the pH of the pore water on the short-term. If accumulation near the injection well results in very high concentrations in the brine, the pH decrease can cause enhanced short-term dissolution of calcite, but without significant effects on the porosity due to the low amount of brine present in a gas field; (2) impurities do not result in significant differences in long-term mineral changes compared to the pure-CO_2 case, except when surplus amounts of O_2 are present. Presence of O_2 in the CO_2 could result in the formation of nontronite and alunite, at the expense

of siderite and pyrite. Due to the low reaction rate of these minerals, the effects would only occur in the long-term. Instead of a slight increase in porosity in the absence of O_2 which occurs in the other scenarios, the porosity change is negligible; and (3) the effects caused by H_2S, SO_2, NO and O_2 would only be significant in case of accumulation of these impurities near the injection well. Whether accumulation could occur depends on the kinetics of aqueous species dissolution, on gas flow and on diffusion within the CO_2 plume and the brine.

Table 7. Mineral compositions used in the geochemical modeling by Koenen et al. (2011)

	Reservoir composition (wt%)	Reservoir composition (moles)
Quartz	83.0	144.4
Muscovite	1.0	0.3
Glauconite	1.0	0.2
Kaolinite	4.0	1.6
K-Feldspar	2.0	0.3
Calcite	0.5	0.5
Halite	0.2	0.4
Pyrite	0.2	0.2
Illite	8.1	2.2
Dawsonite		0.1727
Dolomite-ord		0.0089

VII-4-6 Other numerical modeling effort

There are several peer-reviewed papers of interest, such as Gunter et al. (2000) and Ellis et al. (2010). Gunter et al. (2000) used a batch geochemical model to simulate the interaction of industrial waste streams comprising CO_2 and H_2S with the minerals in typical carbonate and sandstone aquifers from the Alberta Basin, Canada. Their results show that these acid gases can be neutralized with formation of secondary minerals, such as calcite, siderite, anhydrite/gypsum and pyrrhotite. As expected, siliciclastic aquifers demonstrate better "mineral trapping" characteristics for CO_2 than carbonate aquifers, because high-pressure CO_2 enhances carbonate dissolution.

Due to limitations of numerical codes, most numerical simulations dicussed in the previous sections did not account for the factor that dissolution rate of the injected SO_2 into brine could be a limiting factor for brine acidification. Crandell et al. (2010) has shown that mass transfer limitations of SO_2 through the supercritical CO_2 phase may be important. Their work suggested that SO_2 within the supercritical CO_2 plume near the phase boundary is quickly depleted and a thick zone of depletion can be developed. This zone may further create resistance for dissolution of SO_2 into brine. They predicted that by taking into account this limiting factor, less than one third of the injected SO_2 will dissolve into brine after 100 years.

Ellis et al. (2010) presented numerical modeling to understand magnitude and time scale of brine acidification for the case of SO_2 co-injection during geological carbon sequestration in deep saline formations. They analyzed three SO_2 reaction scenarios: hydrolysis, oxidation, and disproportionation. Two extreme cases were simulated: rapid dispersion of SO_2 in a slowly advecting brine phase and diffusive transport of SO_2 in a stagnant brine phase. In reality, transport SO_2 could be a combination of the two extreme cases. It must be noted that this model did not account for mineral reactions for buffering the low pH caused by interactions of SO_2 and brine.

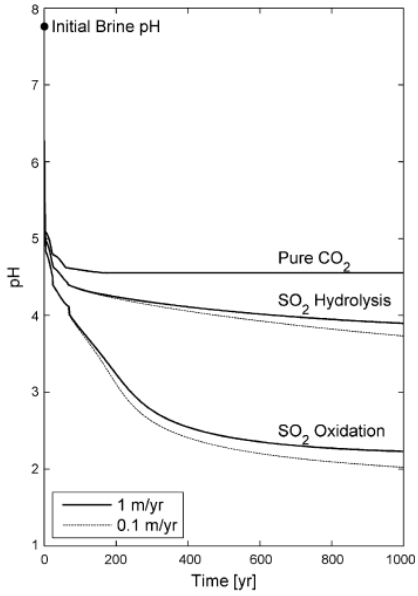

Figure 7. Brine pH results for SO_2 hydrolysis and SO_2 oxidation reaction scenarios for diffusion-limited SO_2 dissolution into an advecting brine (Ellis et al., 2010). For reference, pH results for the case of a pure CO_2 injection plume are also shown.

One of the interesting results reported by Ellis et al. (2010) is that different SO_2 reaction scenarios can lead to different evoluation of pH in the case of diffusion limited SO_2 dissolution into brine (Figure 7).

Ellis et al.(2010) also confirmed that SO_2 co-injection during geologic carbon sequestration has the potential to cause enhanced brine acidification. However, they argued that the magnitude, onset, and spatial extent of this acidification may not be significant. If SO_2 mass transfer limitations were not considered, it is possible that brine pH values are close to unity. Based on numerical resutls, they predicted that 73–90% of the injected SO_2 will remain within the supercritical CO_2 phase after 1000 years. If potential oxidants are not present in the aquifer, severe brine acidification will occur only if SO_2 disproportionation is favorable. Finally they concluded that the co-injection of a small amount of SO_2 may not cause rapid, severe widespread brine acidification and therefore SO_2 co-injection may be a viable option for mitigating SO_2 emissions from power plants. Their results indicated that if dissolution limitations are not taken into account, brine pH will be overestiamted and the dissolution limitation of SO_2 should be seriously considered in any geochemical modeling effort investigating SO_2 co-injection.

Wei and Li (2011) used the COMSOL-multi-physics software 3.5a to simulate injection of CO_2 and N_2 gas mixture in an aquifer to demonstrate the effect of N_2 on the migration process of CO_2. The numerical results show that preferential CO_2 solubility in brine compared to that of N_2 results in CO_2 being stripped off at the leading edge of the displacement front of fluid mixture containing N_2 that advances in the aqueous phase. The authors also reported that the chromatographic partitioning process of CO_2 in gas phase can separate N_2 and trap CO_2 in aquifer during preferential flow process, which caused by preferential solubility and mineral trapping during the CO_2 displacement process.

Jacquemet et al. (2011) simulate the intrusion of CO_2 and impurities from oxycombustion capture in a freshwater aquifer model based on a glauconitic sandstone aquifer with the reactive transport code TOUGHREACT. An unfavorable scenario in which the co-injectant gases present

maximal contents in SOx, NOx and O_2, were modeled. Model results indicate that acidification and carbonation of water induces Fe- and Mn-bearing minerals dissolution that increases the concentration of these metals in water. Contamination by sulfates is due to the SO_2 oxidation by O_2, both of these components being carried by the contaminant gas. The vertical extent of contamination is enhanced by both the upward migration of gaseous CO_2 and downward migration of dense carbonated water. The presence of SO_2 and NO in the contaminant gas, even in very low concentrations, induces a negative local pH shift of 1 unit by comparison with a pure-CO_2 contaminant gas. This pH shift has consequences on Fe and Mn release amplitude. The code does not allow realistic modeling of the fate of NOx in the aquifer.

VII-5. Summary

This short preliminary literature review report reviewed potential impacts of geochemical interactions among brine, rocks and CO_2 with impurities coinjected on geological carbon sequestration. We first reviewed possible geochemical processes when coinjection of impurities with CO_2 into deep brine formation, espeically SO_2, H_2S, and NOx. Then several laboratory experiments which were conducted to study SO_2 coinjection were reviewed. Finally, we reviewed numerical evaluation of coinjection of impurities (H_2S and SO_2) based on several publications in literature and numercial tools used in the numerical simulations.

VII-6. References

Apps J.A. 2006. A Review of Hazardous Chemical Species Associated with CO2 Capture from Coal-Fired Power Plants and their Potential Fate during CO2 Geologic Storage, Lawrence Berkeley National Laboratory, Berkeley, California. pp. 60.

Bacon D.H., Sass B.M., Bhargava M., Sminchak J., Gupta N. 2009. Reactive transport modeling of CO2 and SO2 injection into deep saline formations and their effect on the hydraulic properties of host rocks. Energy Procedia, 13283-3290.

Bateman K., Turner G., Pearce J., M., Noy D., J., Birchall D., Rochelle C., A. 2005. Large-Scale Column Experiment: Study of CO2, Porewater, Rock Reactions and Model Test Case. Oil & Gas Science and Technology - Rev. IFP, 60161-175.

Chapelle F.H., O'Neill K., Bradley P.M., Methe B.A., Ciufo S.A., Knobel L.L., Lovley D.R. 2002. A hydrogen-based subsurface microbial community dominated by methanogens. Nature, 415312-315.

Crandell L.E., Ellis B.R., Peters C.A. 2010. Dissolution Potential of SO2 Co-Injected with CO2 in Geologic Sequestration. Environmental Science & Technology, 44349-355. DOI: 10.1021/es902612m.

Credoz A., Bildstein O., Jullien M., Raynal J., Pétronin J.-C., Lillo M., Pozo C., Geniaut G. 2009. Experimental and modeling study of geochemical reactivity between clayey caprocks and CO2 in geological storage conditions. Energy Procedia, 13445-3452.

Dupraz S., Parmentier M., Menez B., Guyot F. 2008. Experimental study of biomineralization processes relevant to CO2 geological sequestration. Geochimica et Cosmochimica Acta, 72A233-A233.

Dupraz S., Parmentier M., Ménez B., Guyot F. 2009a. Experimental and numerical modeling of bacterially induced pH increase and calcite precipitation in saline aquifers. Chemical Geology, 26544-53.

Dupraz S., Menez B., Gouze P., Leprovost R., Benezeth P., Pokrovsky O.S., Guyot F. 2009b. Experimental approach of CO2 biomineralization in deep saline aquifers. Chemical Geology, 26554-62. DOI: 10.1016/j.chemgeo.2008.12.012.

Ellis B.R., Crandell L.E., Peters C.A., 2010. Limitations for brine acidification due to SO2 co-injection in geologic carbon sequestration. International Journal of Greenhouse Gas Control, 4, p.575–582.

Gunter W.D., Perkins E.H., Hutcheon I. 2000. Aquifer disposal of acid gases: modelling of water-rock reactions for trapping of acid wastes. Applied Geochemistry, 151085-1095.

Heeschen K., Risse A., Ostertag-Henning C., Stadler S. 2011. Importance of co-captured gases in the underground storage of CO2 : Quantification of mineral alterations in chemical experiments. Energy Procedia, 44480-4486.

Jacquemet N., Pironon J., Caroli E. 2005. A New Experimental Procedure for Simulation of H2s + CO2 Geological Storage. Application to Well Cement Aging. Oil & Gas Science and Technology - Rev. IFP, 60193-203. DOI: 10.2516/ogst:2005012.

Jacquemet N., Pironon J., Saint-Marc J. 2008. Mineralogical changes of a well cement in various H2S-CO2(-brine) fluids at high pressure and temperature. Environmental Science & Technology, 42282-288. DOI: 10.1021/es070853s.

Jacquemet N., Picot-Colbeaux G., Vong C.Q., Lions J., Bouc O., Jérémy R. 2011. Intrusion of CO2 and impurities in a freshwater aquifer -- Impact evaluation by reactive transport modelling. Energy Procedia, 43202-3209.

Jacquemet N., Le Gallo Y., Estublier A., Lachet V., von Dalwigk I., Yan J., Azaroual M., Audigane P. 2009. CO2 streams containing associated components--A review of the thermodynamic and geochemical properties and assessment of some reactive transport codes. Energy Procedia, 13739-3746.

Kaszuba J.P., Janecky D.R., Snow M.G. 2003. Carbon dioxide reaction processes in a model brine aquifer at 200 °C and 200 bars: implications for geologic sequestration of carbon. Applied Geochemistry, 181065-1080.

Kaszuba J.P., Janecky D.R., Snow M.G. 2005. Experimental evaluation of mixed fluid reactions between supercritical carbon dioxide and NaCl brine: Relevance to the integrity of a geologic carbon repository. Chemical Geology, 217277-293.

Ketzer J.M., Iglesias R., Einloft S., Dullius J., Ligabue R., de Lima V. 2009. Water-rock-CO2 interactions in saline aquifers aimed for carbon dioxide storage: Experimental and numerical modeling studies of the Rio Bonito Formation (Permian), southern Brazil. Applied Geochemistry, 24760-767.

Kharaka Y., Cole D., Hovorka S., Gunter W., Knauss K., Freifeld B. 2006. Gas-water-rock interactions in Frio Formation following CO2 injection: Implications for the storage of greenhouse gases in sedimentary basins. Geology, 34577 - 580.

Knauss K.G., Johnson J.W., Steefel C.I. 2005. Evaluation of the impact of CO2, co-contaminant gas, aqueous fluid and reservoir rock interactions on the geologic sequestration of CO2. Chemical Geology, 217339-350.

Koenen M., Tambach T.J., Neele F.P. 2011. Geochemical effects of impurities in CO2 on a sandstone reservoir. Energy Procedia, 45343-5349.

Liteanu E., Spiers C.J. 2009. Influence of pore fluid salt content on compaction creep of calcite aggregates in the presence of supercritical CO2. Chemical Geology, 265134-147.

Mandalaparty P., Deo M., Moore J., McPherson B. 2009. Carbon dioxide sequestration: Effect of the presence of sulfur dioxide on the mineralogical reactions and on the injectivity of CO2+SO2 mixtures, University of Utah, Institute for Clean and Secure Energy. pp. 53.

Murphy R., Lammers K., Smirnov A., Schoonen M.A.A., Strongin D.R. 2010. Ferrihydrite phase transformation in the presence of aqueous sulfide and supercritical CO2. Chemical Geology, 27126-30.

Palandri J.L., Kharaka Y.K. 2005. Ferric iron-bearing sediments as a mineral trap for CO2 sequestration: Iron reduction using sulfur-bearing waste gas. Chemical Geology, 217351-364.

Parkhurst D.L., Appelo C.A.J. 1999. User's guide to phreeqc (version 2)— a computer program for speciation, batch-reaction, one-dimensional transport, and inverse geochemical calculations, U.S. Geological Survey pp. 310.

Perrin J.-C., Benson S. 2010. An Experimental Study on the Influence of Sub-Core Scale Heterogeneities on CO2 Distribution in Reservoir Rocks. Transport in Porous Media, 8293-109.

Pironon J., Jacquemet N., Lhomme T., Teinturier S. 2007. Fluid inclusions as micro-samplers in batch experiments: A study of the system C-O-H-S-cement for the potential geological storage of industrial acid gas. Chemical Geology, 237264-273. DOI: 10.1016/j.chemgeo.2006.06.026.

Pruess K., García J., Kovscek T., Oldenburg C., Rutqvist J., Steefel C., Xu T. 2004. Code intercomparison builds confidence in numerical simulation models for geologic disposal of CO2. Energy, 291431-1444.

Regnault O., Lagneau V., Schneider H. 2009. Experimental measurement of portlandite carbonation kinetics with supercritical CO2. Chemical Geology, 265113-121.

Regnault O., Lagneau V., Catalette H., Schneider H. 2005. Experimental study of pure mineral phases/supercritical CO2 reactivity. Implications for geological CO2 sequestration. Comptes Rendus Geoscience, 3371331-1339. DOI: 10.1016/j.crte.2005.07.012.

Rosenbauer R.J., Koksalan T., Palandri J.L. 2005. Experimental investigation of CO2-brine-rock interactions at elevated temperature and pressure: Implications for CO2 sequestration in deep-saline aquifers. Fuel Processing Technology, 861581-1597.

Sass B., Monzyk B., Ricci S., Gupta A., Hindin B., Gupta N. 2005. Impact of SOx and NOx in Flue Gas on CO2 Separation, Compression, and Pipeline Transmission, Carbon Dioxide Capture for Storage in Deep Geologic Formations, Elsevier Science, Amsterdam. pp. 955-981.

Sass B.M., Gupta N., Chattopadhyay S., Ickes J., Byrer C.W. 2003. Evaluation of CO2 Sequestration in Saline Formations Based on Geochemical Experiments and Modeling, in: J. Gale and Y. Kaya (Eds.), Greenhouse Gas Control Technologies - 6th International Conference, Pergamon, Oxford. pp. 1641-1644.

Spycher N., Pruess K. 2005. CO2-H2O mixtures in the geological sequestration of CO2 center dot. II. Partitioning in chloride brines at 12-100 degrees C and up to 600 bar. Geochimica et Cosmochimica Acta, 693309-3320. DOI: 10.1016/j.gca.2005.01.015.

Steefel C.I. 2009. CRUNCHFlow: Software for Modeling Multicomponent Reactive Flow and Transport, USER'S MANUAL, Lawrence Berkeley National Laboratory, Berkeley, CA. pp. 91.

Summers C., Dahlin D., Ochs T. 2004. The Effect of SO2 on Mineral Carbonation in Batch Tests, 29th International Technical Conference on Coal Utilization & Fuel Systems, Coal Technology Association, Clearwater, Florida. pp. 10.

Wang J., Ryan D., Anthony E.J., Wildgust N., Aiken T. 2011. Effects of impurities on CO2 transport, injection and storage. Energy Procedia, 43071-3078.

Wei N., Li X.C. 2011. Numerical studies on the aquifer storage of CO2 containing N2. Energy Procedia, 44314-4322.

White M.D., Oostrom M. 2006. STOMP: Subsurface Transport Over Multiple Phases , Version 4.0, User's Guide, Pacific Northwest National Laboratory, Richland, Washington. pp. 120.

Xu T., Sonnenthal E., Spycher N., Pruess K. 2006. TOUGHREACT--A simulation program for non-isothermal multiphase reactive geochemical transport in variably saturated geologic media: Applications to geothermal injectivity and CO2 geological sequestration. Computers & Geosciences, 32145-165.

Xu T., Apps J.A., Pruess K., Yamamoto H. 2007. Numerical modeling of injection and mineral trapping of CO2 with H2S and SO2 in a sandstone formation. Chemical Geology, 242319-346.

VIII. Appendix C: Supplementary Detailed Description of Core Samples

By Jiemin Lu (adapted by J.-P. Nicot)

VIII-1. Offshore Miocene

Excerpts from Lu, J., 2011, "Task 7.0: Mineralization Containment" in Interim Project Progress Report (October 31, 2011: Reporting period July 1 – September 30, 2011) for U.S. Department of Energy ARRA study (American Recovery and Reinvestment Act), *Gulf of Mexico Miocene CO_2 Site Characterization Mega Transect*,, R. Trevino ed.; Conducted under funding agreement DE-FE0001941; 52p.

This section describes results of a petrographic study done independently from CCP3 but for which CCP3 partly funded the autoclave experiment. The task was to evaluate the rate of mineralization in the injection formation and the potential effects on injection and storage by using laboratory experiments and numerical modeling. The potential rock samples for the laboratory reaction experiment was chosen and analyzed from a Miocene core from Matagorda Island area. The characterization efforts include core description, quantitative XRD mineralogical analysis, petrographic and diagenetic analyses, and core plug porosity and permeability measurements.

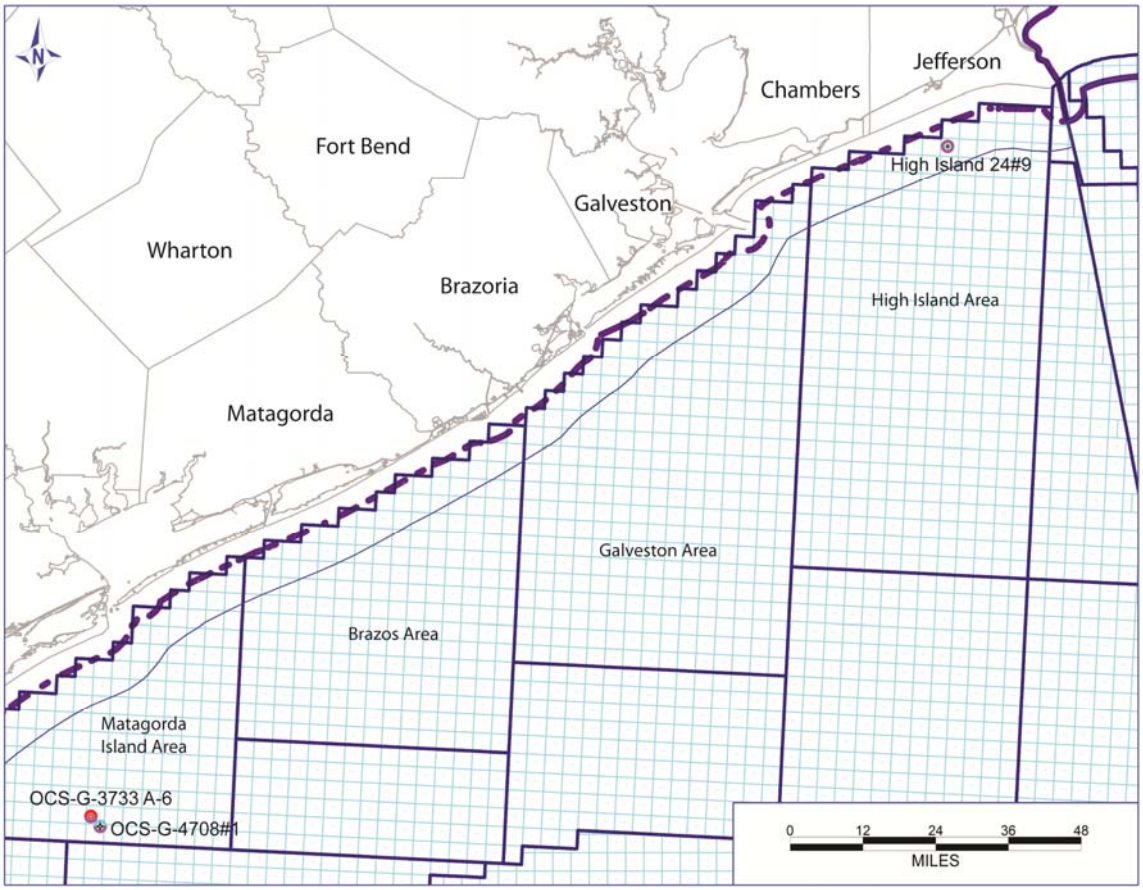

Fig.1 Location of Miocene cores studied.

VIII-1-1 Core and samples

Information on available drill cores in Texas state water and coastal areas was obtained from Integrated Core and Log Database of Austin Core Research Center (CRC) at Bureau of Economic Geology, The University of Texas at Austin. Potential cores were examined and scrutinized for suitable age and locations. In total, three Miocene cores were chosen and studied in details, two from Matagorda Island, OCS-G-3733 A-6 (API: 427034015800) and OCS-G-4708 #1 (API: 427034012600), and the other from High Island 24L #9 (API: 427083031600) (Fig. 1). The core of Well OCS-G-3733 A-6 was studied specifically for Task 7. The rest two were analyzed for seal characterization.

The core of OCS-G-3733 A-6 is approximately 200 ft long ranging from 9100 to 9212 ft. It contains mainly fine-grained sandstone of delta fringe (Fig. 2A) interbedded with muddy siltstone of pro-delta deposits (Fig. 2B) in the Lower Miocene. Sedimentary log is shown in Fig. 3. The core is comprised of three packages of fine-grained sandstone, siltstone/mudstone of 20, 50 and 40 feet thick upward. The sandstones are grey, greenish and occasionally brown in color. The majority of the sandstones are featureless and uniform with locally abundant burrows. Some show erosive bottom and cross-beddings. The siltstone and mudstone are usually dark grey to brownish in color, calcareous, and locally shaly. Siltstone contains small lenticular sand bodies.

In total, 24 plugs were drilled from the core, among which ten were selected for porosity/ permeability tests, representing a variety of microfacies (fine-grained sandstone, very fine-grained sandstone, and siltstone). 23 samples were analyzed by XRD for mineral composition and examined for petrography and diagenesis using light microscope and Scanning Electron Microscope (SEM).

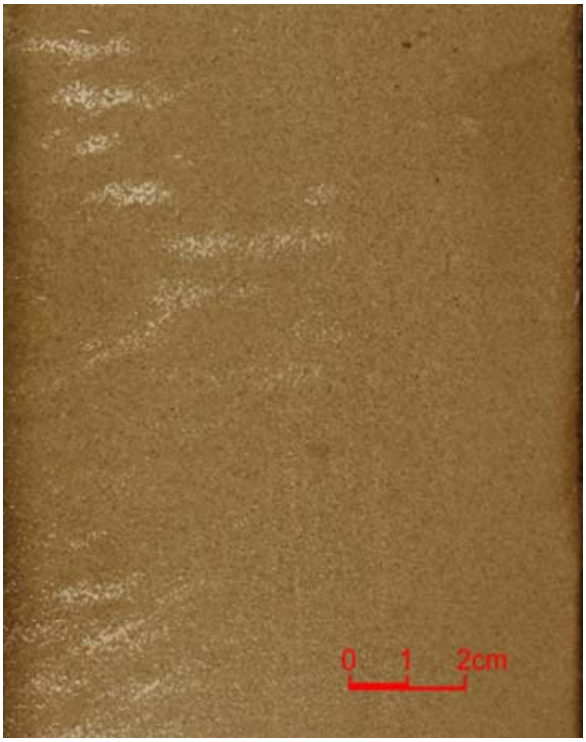

Fig. 2A Uniform fine-grained sandstone at 9128 ft, Well OCS-G-3733 A-6, Matagorda Island.

Fig. 2B Burrowed siltstone, 9155 ft, Well OCS-G-3733 A-6, Matagorda Island.

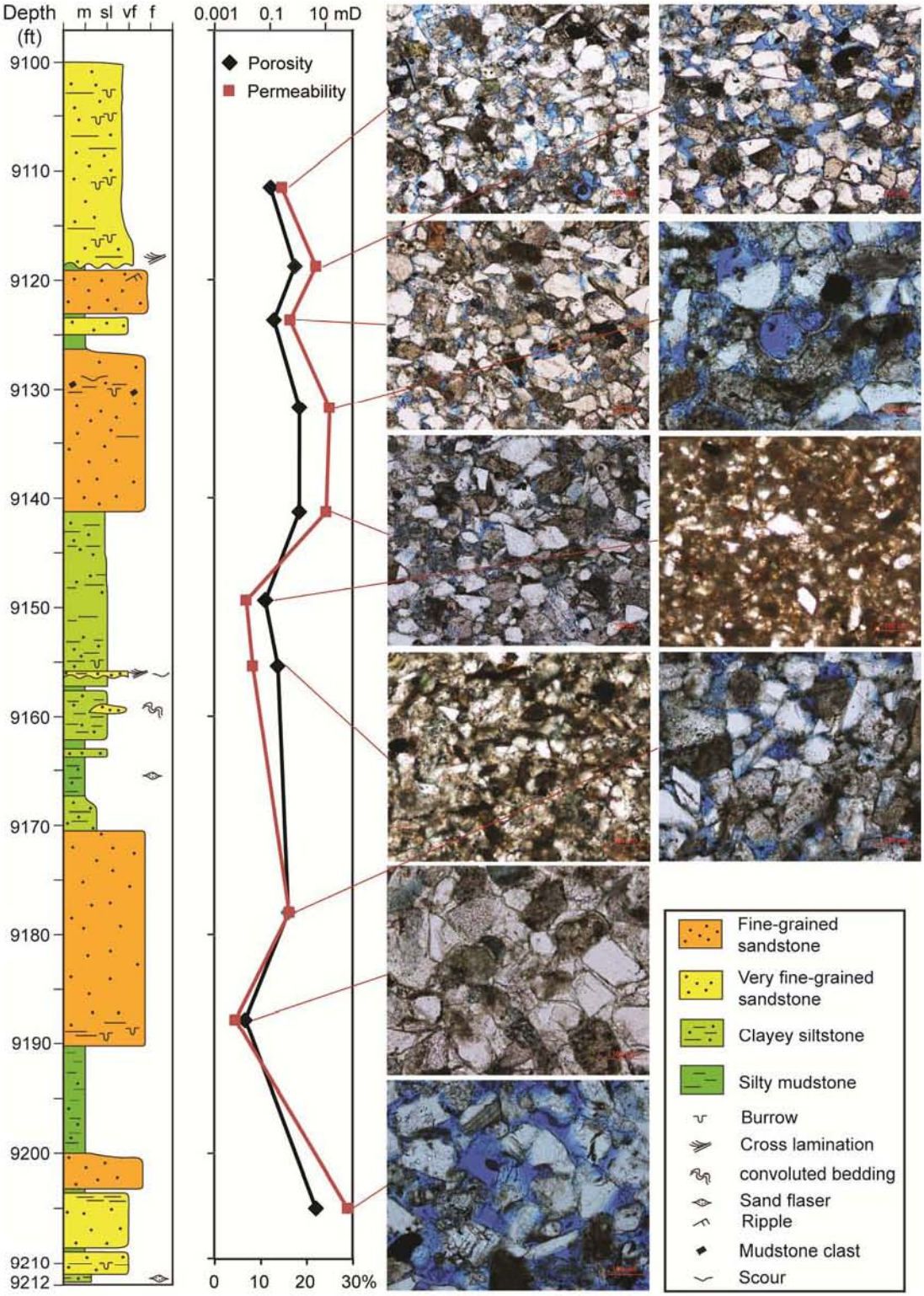

Fig. 3 Sedimentary log of Well OCS-G-3733 A-6, Matagorda Island Area, plotted with porosity and permeability and thin section photomicrographs.

VIII-1-2 XRD mineralogy

VIII-1-2.1 Method

Using random-powder X-ray diffraction, core samples were analyzed quantitatively for mineral composition. Random powders were prepared by means of wet grinding and spray drying (Hillier, 1999). Representative parts of each core sample were first disintegrated using a TEMA ball mill for 1 min. For further wet grinding, approximately 5 g of powder samples was transferred to a McCrone Micronizing Mill, and 13 mL of a 0.5% (wt/vol) aqueous solution of polyvinyl alcohol was added to the mill. Addition of a single drop of 1-octanol (CH3[CH2]7OH) prevented foaming during wet grinding and reduced the introduction of air bubbles into the dried granules. Each sample was ground for 12 min to reduce particle size sufficiently to less than 10 mm. The drying chamber of the spray drier was heated until exit air temperature reached 130 to 140°C, and a sheet of A2 paper was placed beneath the chamber to collect the dried droplets when a slurry sample was sprayed from top. X-ray diffraction analysis of 14 samples was conducted on a Bruker AXS D8 diffractometer at the University of Texas at Austin. Diffraction patterns were recorded by step scanning from 2 to 75° 2q, with a step size of 0.016° counting for 1 s per step. Bruker's Eva software was used to identify mineral phases. Quantitative analysis was conducted using Topas 3, a personal computer software based on the Rietveld method (Bish, 1994).

Table 1 XRD mineralogical composition of core samples. Sandstone samples in orange; mudstone and siltstone samples marked in green.

Depth (ft)	Quartz	Kaolinite	Calcite	Illite	Albite	K-feldspar	Siderite	Chlorite	Pyrite	Total
Well OCS-G-3733 A-6, Matagorda Island. API: 427034015800										
9100	33.6	4.9	12.3	14.6	21.2	12.4			1.1	100.0
9109	45.6	2.9	11.9	9.2	21.7	8.8				100.0
9111.6	42.1	1.9	24.1	7.2	10.8	13.9				100.0
9118	41.4	1.8	21.2	4.4	25.2	6.0				100.0
9118.8	42.9	2.6	22.2	6.5	13.3	12.7				100.0
9123.7	32.3	1.7	32.9	3.8	14.8	14.5				100.0
9128	40.0	3.3	20.6	4.4	16.1	14.1	1.5			100.0
9131.8	36.1	2.2	27.4	4.1	15.2	14.0	1.0			100.0
9141.3	36.8	2.8	22.2	5.4	16.9	14.8	1.2			100.0
9143	32.4	4.4	17.6	12.3	14.5	18.9				100.0
9149.4	32.8	4.0	18.0	11.8	14.1	18.4	0.9			100.0
9155.4	32.2	3.7	20.4	10.4	15.0	18.3				100.0
9156.3	30.4	4.8	18.7	13.0	14.4	18.7				100.0
9162.7	17.2	11.6	23.2	30.0	2.8	15.1				100.0
9171.8	28.7	1.7	38.1	5.5	13.6	12.4				100.0
9178	34.7	2.6	23.4	4.9	18.7	15.7				100.0
9179.6	36.8	3.1	16.4	5.9	21.1	16.8				100.0
9187.8	23.5	1.4	43.0	3.3	13.2	13.0		2.7		100.0
9191.5	22.8	10.0	19.1	25.5	4.9	17.7				100.0
9198	20.4	10.3	22.4	25.7	4.2	17.0				100.0
9203	44.0	2.7	11.9	6.0	18.9	16.6				100.0
9205	43.5	6.2	11.8	5.0	18.4	15.2				100.0
9208	42.5	4.4	15.5	4.8	17.0	5.9				100.0

VIII-1-2.2 Results

XRD mineral compositions of the samples are shown in Table 1. Minerals identified include quartz, K-feldspar, albite, illite, kaolinite, calcite, and siderite. Overall, the samples show similar compositions. Abundances of quartz, albite, calcite and clay minerals show relatively larger variations than other mineral. Quartz is the most dominant detrital mineral (17- 46%, average 34.5%), followed by calcite (12-43%, average 21.5%), albite (3-25%, average 15%) and K-feldspar (6-19%, average 14.8%). Average abundance of illite and kaolinite are 9.7% and 4.1%, respectively. In siltstone samples, abundances of illite and kaolinite are 18.4% and 7.0% respectively, compared with 5.9% and 2.9% for sandstone samples. Chlorite was only detected in one sandstone (9187.8 ft) in this core, while the core of Well OCS-G-4708#1contains 11% of chlorite in siltstone samples and 5% in sandstone samples. Calcite abundance is high in this well with an average of 22%, similar to that of Well OCS-G-4708#1 (19%). Small amount of siderite (less than 2%) was also detected in several samples.

VIII-1-3 Petrography and Diagenesis

VIII-1-3.1 Method

Thin section transmitted-light microscopy

A total of 25 petrographic thin sections from Well OCS-G-3733 A-6 were prepared and studied using transmitted-light optical microscope. Sections were polished following surface impregnation with a low-viscosity impregnation medium. The thin sections were examined in both transmitted light (plane and polarized) and in bright-field reflected light.

Scanning Electron Microscope (SEM) with Energy Dispersive Spectrometry (EDS) elemental mapping

Eleven highly polished thin sections from Well OCS-G-3733 A-6 were made and examined using BSE imaging after the samples had been coated with carbon. Secondary electron (SE) and back-scattered electron (BSE) modes were applied. The analyses were carried out using a field-emission SEM, an FEI Nova™ NanoSEM 430, at The University of Texas at Austin. A system of two energy dispersive X-ray detectors was used in conjunction with SEM to produce elemental maps of individual view areas.

VIII-1-3.2 Results

The sandstones of the core are usually moderately to poorly sorted and poorly rounded (e.g. Fig. 4A). Major framework grains include quartz (average 38%), plagioclase (17%) and K-feldspar (13%). Calcite with an average of 22% exists as detrital grains, fossils and cements (Fig. 4B). Clay minerals are mostly illite (6%) and kaolinite (3%) as pore-filling (Fig. 4C) and mineral replacing habits. Metamorphic and volcanic rock fragments are up to 5% and are usually deformed and altered (Fig. 4D).

Compaction and grain rearrangement are the earliest diagenetic events. Compaction evidence includes deformation of ductile components such as rock fragments and mica minerals (Fig. 4D), pressure dissolution (Fig. 4E), and fracturing of brittle grains. Calcite cementation is the next important diagenetic event. Calcite cements mostly occur as pore-filling (Fig. 4F) with occasional mineral replacing habits. Abundance of calcite cements varies significantly among samples. Some samples contain less than 5 % calcite cements (e.g. sample at 9128 and 9205 ft,

Fig. 4G and H), while others have over 20% (Sample 9187.8 ft, Fig. 4I). Mineral dissolution is not significant in most of samples, but it enhances porosity locally (Fig. 4H). It is difficult to determine the pre-existing minerals when they are totally dissolved, but the presence of partially corroded feldspar grains suggests that some dissolution is associated with feldspar minerals (4J). A minor contributor of secondary porosity is calcite grains.

Clay precipitation and replacement of rock fragments and detrital minerals are the next diagenetic event. Kaolinite usually occurs as pore-filling habit (Fig. 4C). Trace amount of chlorite can be seen as replacement of mineral (Fig. 4D) or rock fragment.

Siltstone samples are tightly compacted and poorly sorted. They contain high content of clay and matrix materials filling in intergranular space (Fig. 4K and L). The detrital grains are usually poorly rounded (Fig. 4K). Calcite cementation is abundant (Fig. 4M). Clay minerals (illite and kaolinite) usually occur in intergranular space and foraminifera test (Fig. 4N). Mineral dissolution is less evident in siltstones.

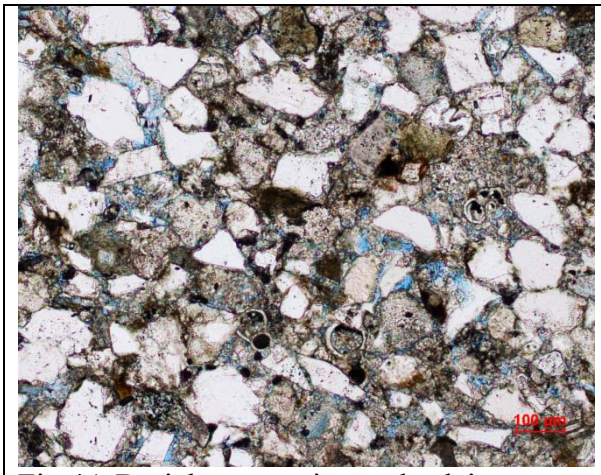

Fig 4A Burial compaction and calcite cements greatly reduced porosity in fine-grained sandstone. Poorly rounded, moderately sorted. 9123.7 ft, Well OCS-G-3733 A-6. Porosity: 12.8%, permeability: 0.53 mD.

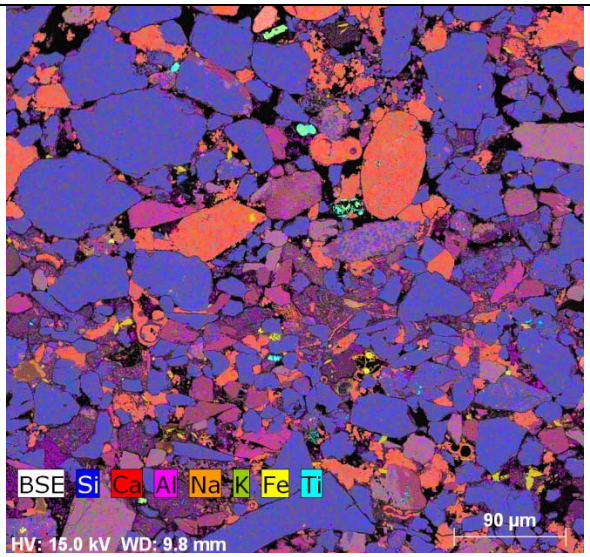

Fig. 4B Abundant calcite occurs as detrital grains, fossils and cements. 9118.8 ft, OCS-G-3733 A-6.

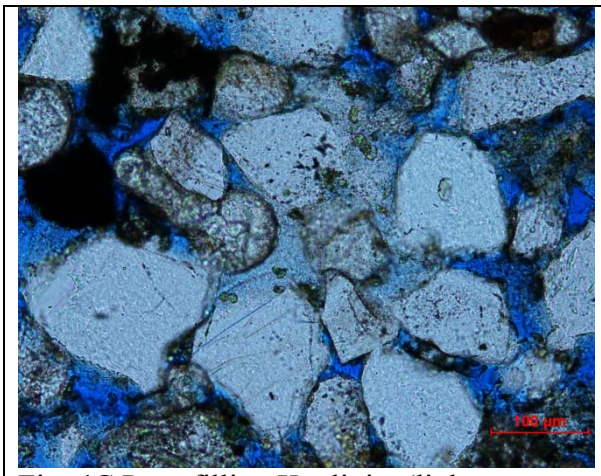

Fig. 4C Pore-filling Kaolinite (light grey between mineral grains). 9128 ft, Well OCS-G-3733 A-6.

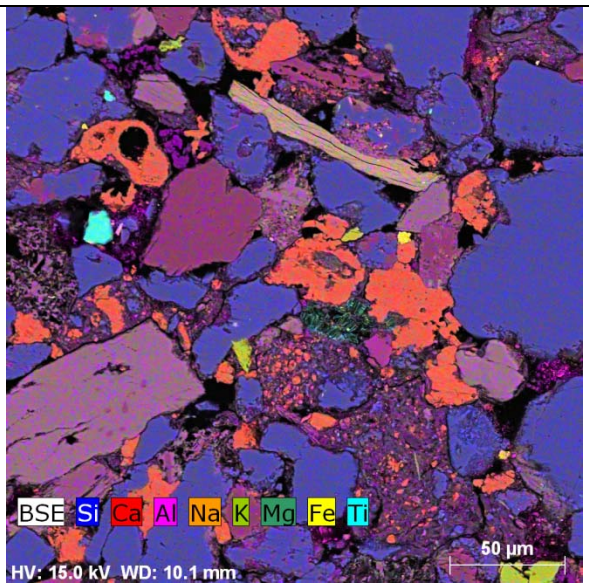

Fig. 4D A deformed rock fragment in low right corner. A mica grain deformed and replace by chlorite in the upper part of the image. 9118.8 ft, OCS-G-3733 A-6.

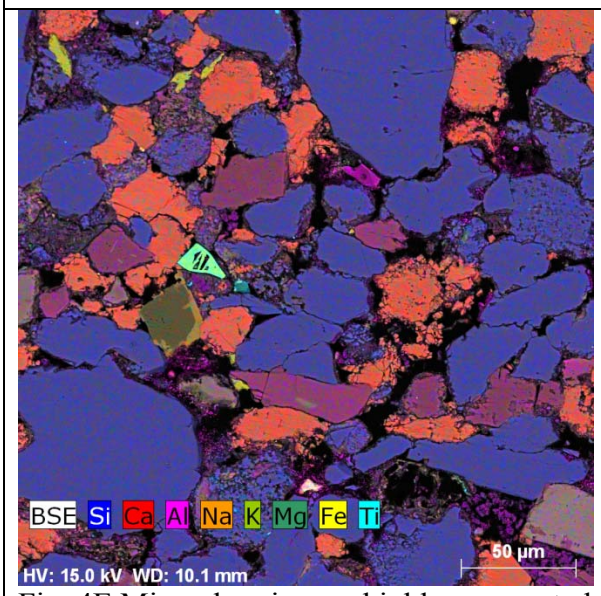

Fig. 4E Mineral grains are highly compacted pressure solution is evident along quartz grain (blue) contact. 9118.8 ft, OCS-G-3733 A-6.

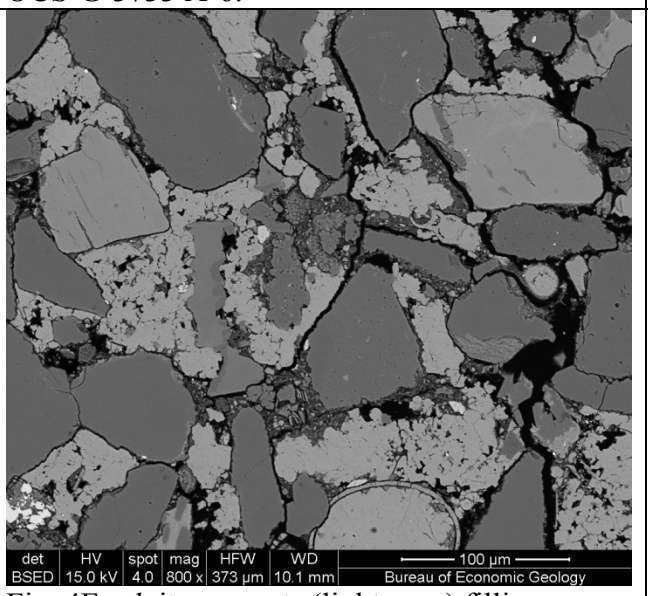

Fig. 4F calcite cements (light grey) filling pores and foram test. 9111.6 ft, OCS-G-3733 A-6.

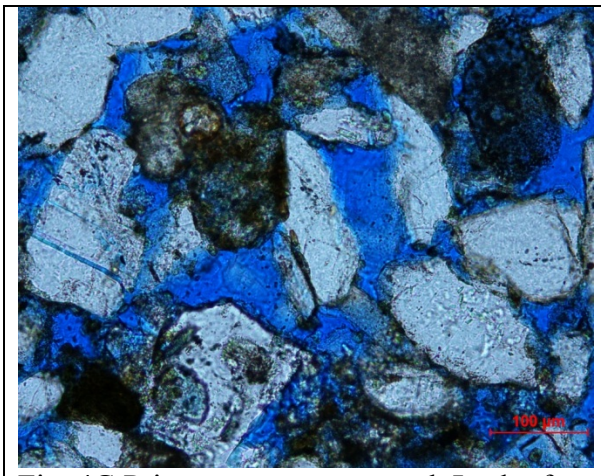

Fig. 4G Primary pores preserved. Lack of carbonate cements. 9128 ft, OCS-G-3733 A-6.

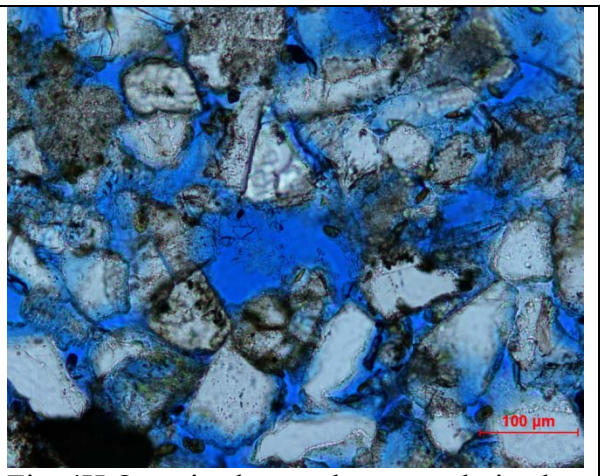

Fig. 4H Oversized secondary pore derived from mineral dissolution. Free of calcite cements. Porosity: 22.0%; permeability: 62.7 mD. 9205 ft, OCS-G-3733 A-6.

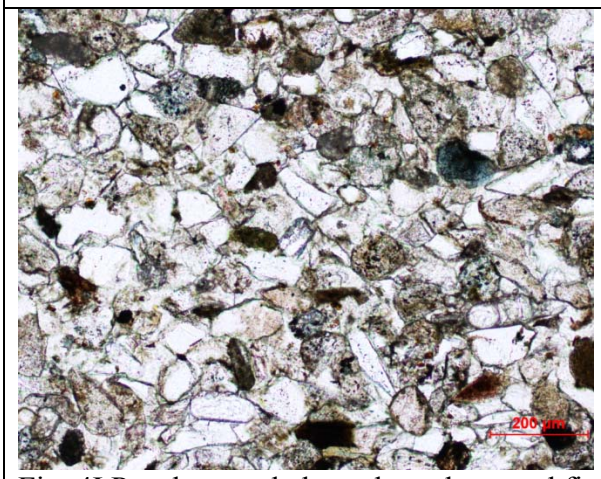

Fig. 4I Poorly rounded, moderately sorted fine-grained sandstone. Porosity completely diminished by cementation. 9187.8 ft, OCS-G-3733 A-6. Porosity: 6.57%, permeability: 0.005 mD.

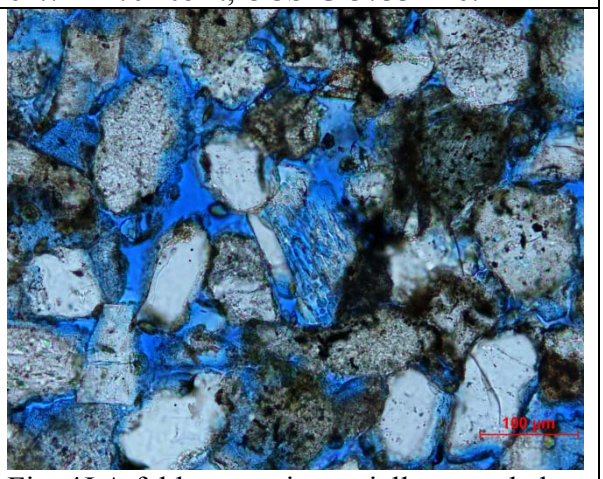

Fig. 4J A feldspar grain partially corroded. 9205 ft, Well OCS-G-3733 A-6.

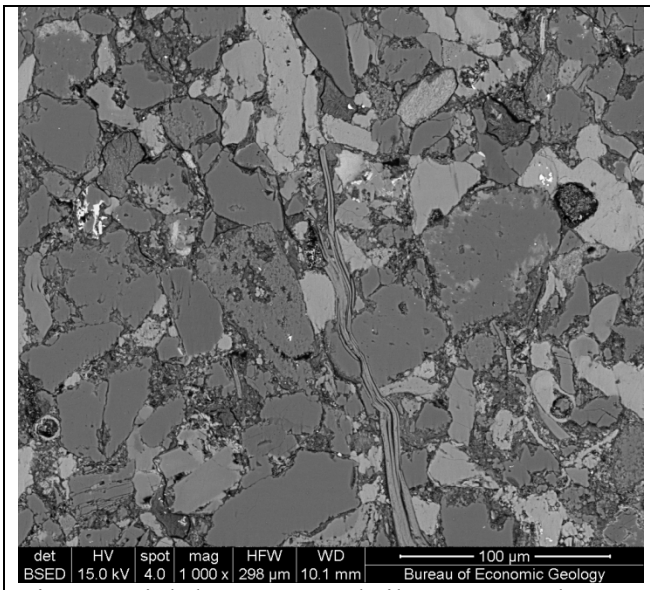

Fig. 4K Tightly compacted siltstone. Poorly rounded grains and abundant clay size matrix reduce porosity. 9155.4 ft, Well OCS-G-3733 A-6.

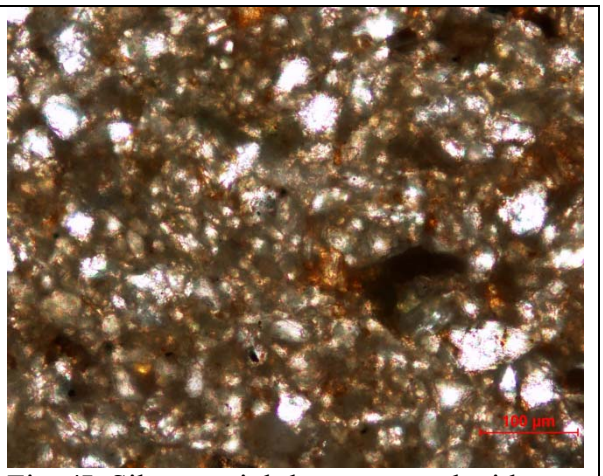

Fig. 4L Siltstone tightly compacted with higher clay content abundance. 9149.4 ft, Well OCS-G-3733 A-6. Porosity: 10.9%, permeability: 0.01 mD.

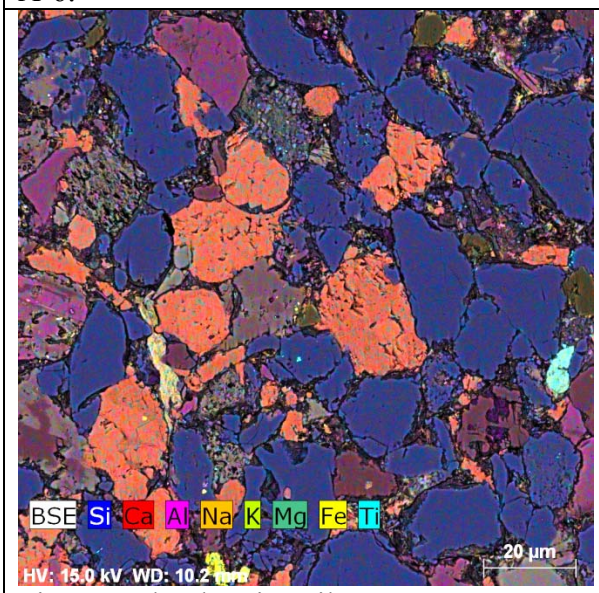

Fig. 4M Clay-bearing siltstone. Low permeability (0.02 mD). Clay and calcite cements reduced porosity and permeability. 9155.4 ft, OCS-G-3733 A-6.

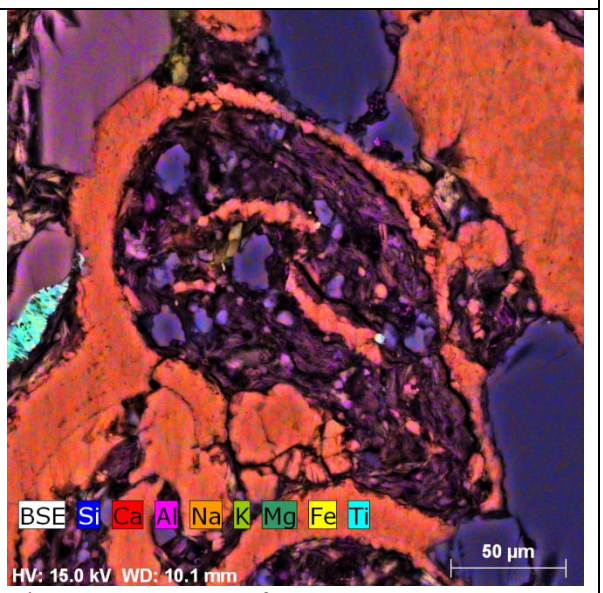

Fig. 4N 4O 9155.4 ft, OCS-G-3733 A-6. Illite, clay size particles and calcite cements filling up a foraminiferal test.

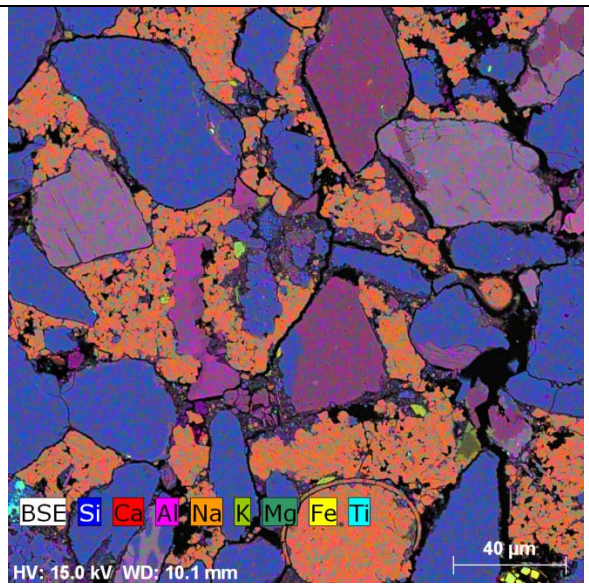

Fig. 7A Abundant calcite cements and calcite fossils (most are foraminiferas) with occasional dolomite rhombs. 9111.6 ft, OCS-G-3733 A-6. Porosity: 12.1; permeability: 0.265 mD.

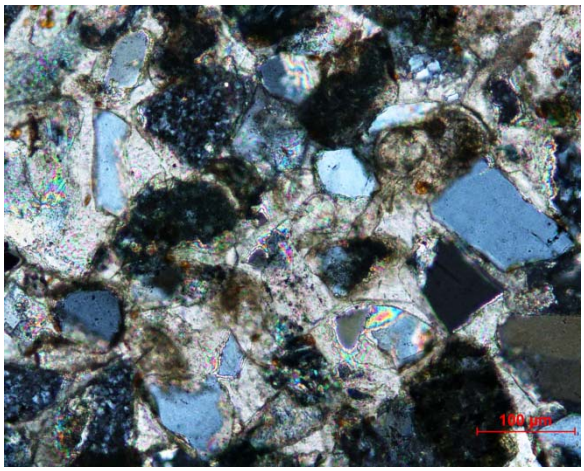

Fig. 7B Porosity completely diminished by calcite cements. 9187.8 ft, OCS-G-3733 A-6. Porosity: 6.57%, permeability: 0.005 mD.

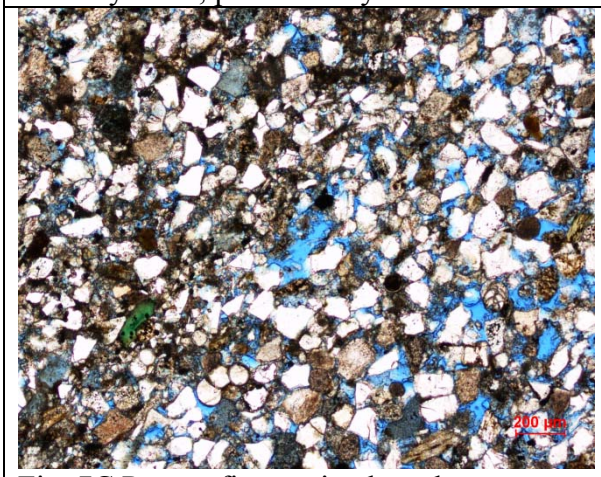

Fig. 7C Porous fine-grained sandstone interlaminated with matrix-abundant sandstone. 9118.8 ft. OCS-G-3733 A-6.

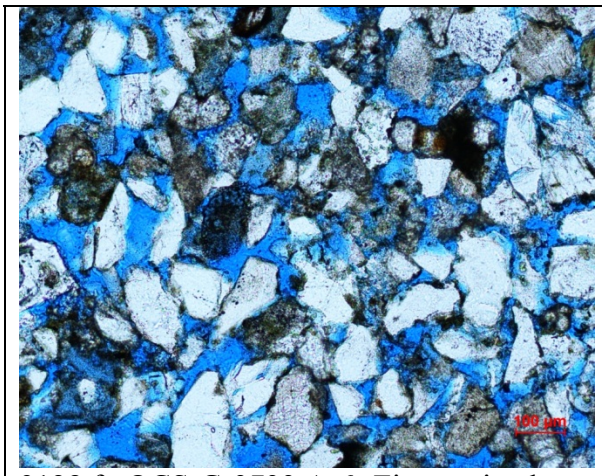

9128 ft, OCS-G-3733 A-6. Fine-grained sandstone, poorly rounded. Mostly primary pores. Secondary porosity locally important. Little cementation. Abundant detrital calcite/fossil fragment.

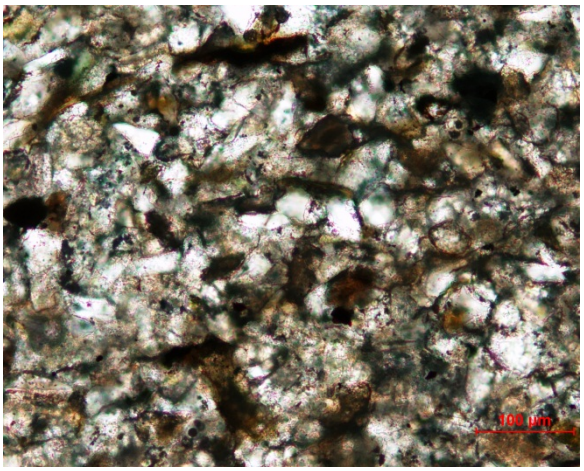

Tightly compacted siltstone. Poorly rounded grains and abundant clay size matrix reduce porosity. 9155.4 ft, Well OCS-G-3733 A-6.

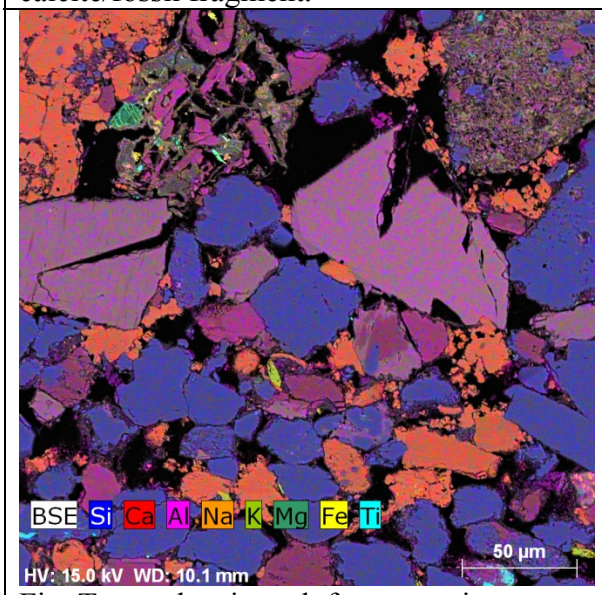

Fig. Two volcanic rock fragments in upper part of the image. The one on left is partially dissolved and replaced. 9118.8 ft, OCS-G-3733 A-6.

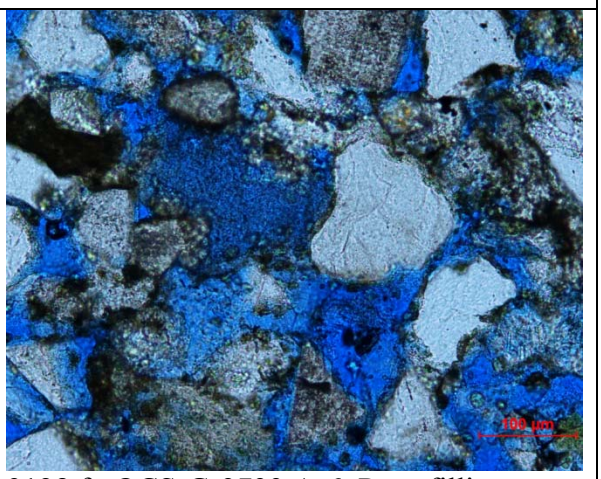

9128 ft, OCS-G-3733 A-6. Pore-filling, grain lining, and pore lining chlorite exist.

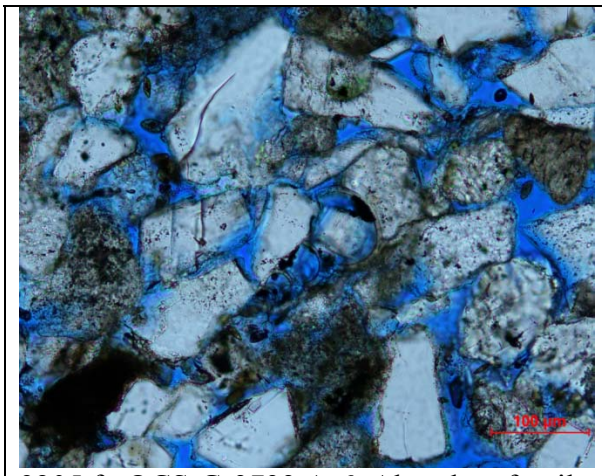 9205 ft, OCS-G-3733 A-6. Abundant fossil fragments. Porosity: 22.0%; permeability: 62.7 mD.	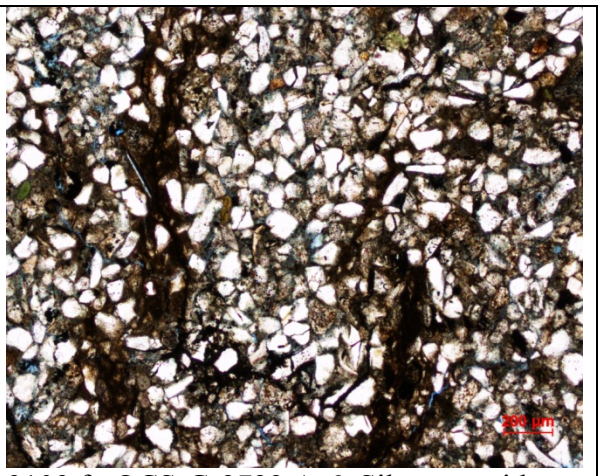 9109 ft, OCS-G-3733 A-6. Siltstone with low porosity. Clay matrix eliminates porosity.

	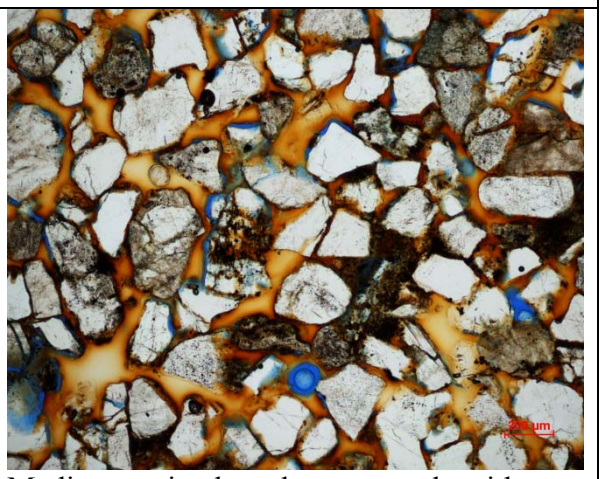 Medium-grained sandstone sample with high porosity (~30%). Brown intergranular material is epoxy used for preserving the loose core. 8555 ft, Well High Island 24L#9.

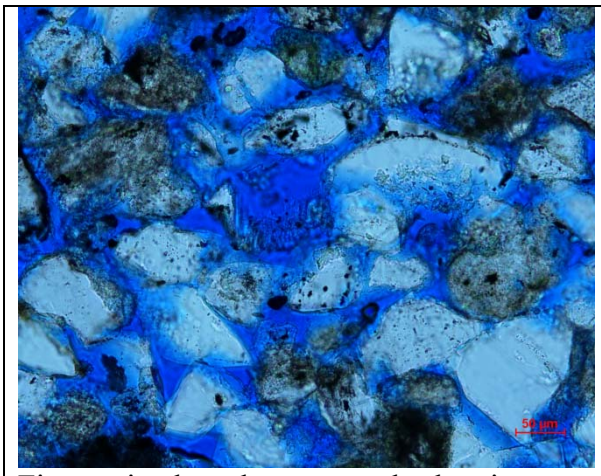

Fine-grained sandstone sample showing high porosity (~25%). A feldspar grain partly corroded, creating secondary pores. 8492 ft, Well High Island 24L#9.

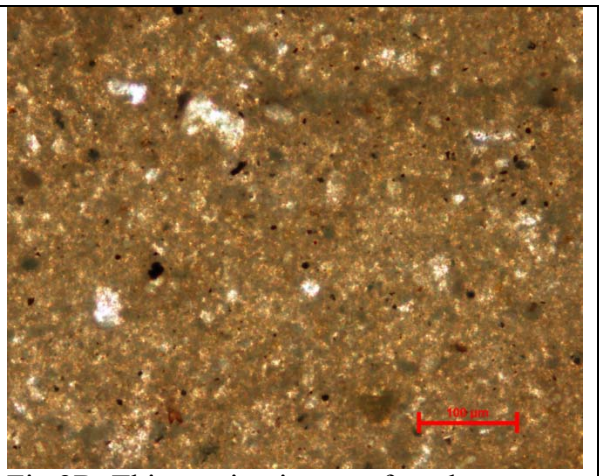

Fig 2B. Thin section image of mudstone overlying a succession of high porosity sandstones, showing abundant clay and low porosity, therefore, high sealing capacity. 8408 ft, Well High Island 24L#9.

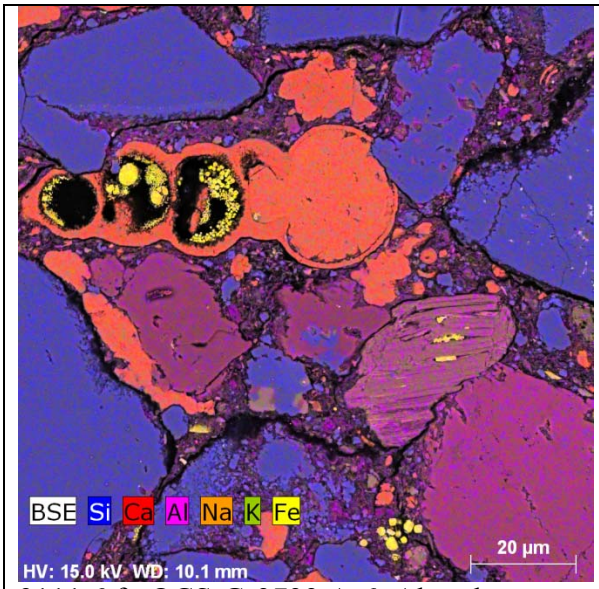

9111.6 ft, OCS-G-3733 A-6. Abundant fossils.

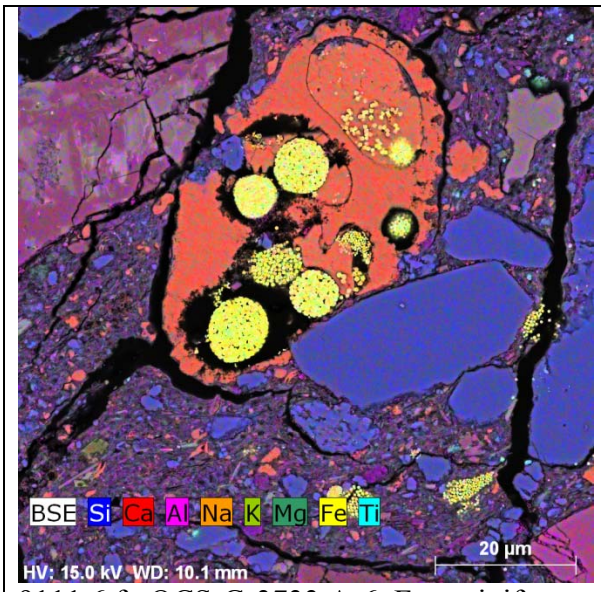

9111.6 ft, OCS-G-3733 A-6. Foraminifera test filled with pyrite and calcite. Abundant clay size matrix.

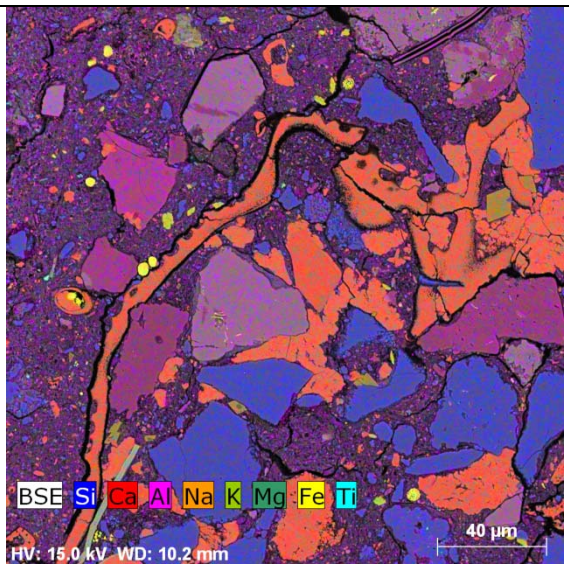

9111.6 ft, OCS-G-3733 A-6. Abundant fossil fragment and calcite cements, occasionally dolomite rhombs. Clay size matrix and calcite cements greatly reduced porosity.

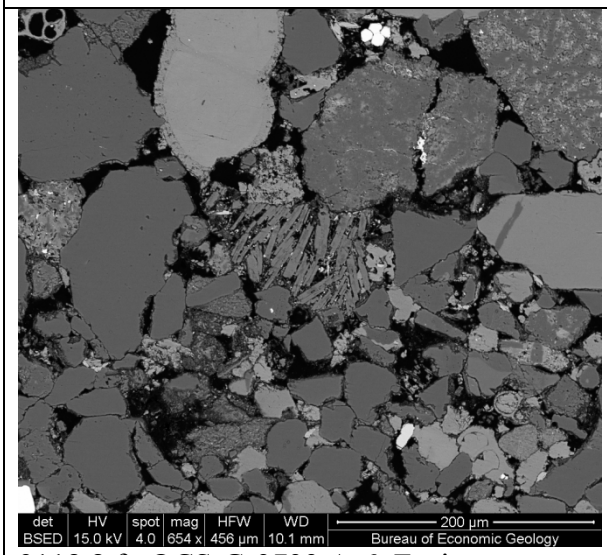

9118.8 ft, OCS-G-3733 A-6. Facies transition from very fine to medium grained sandstone. Abundant calcite fossils.

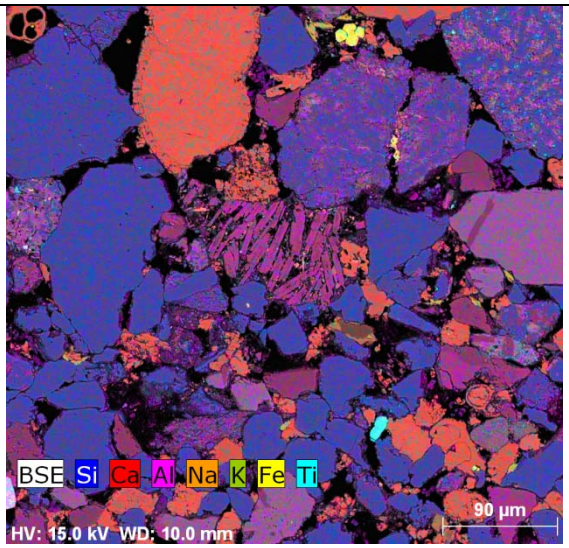

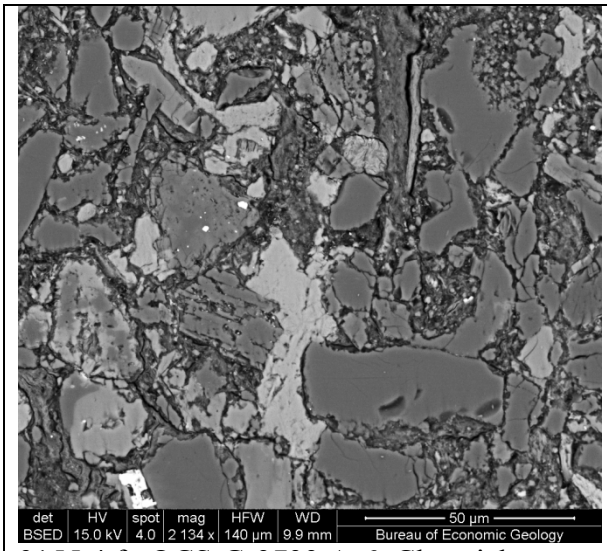

9155.4 ft, OCS-G-3733 A-6. Clay-rich siltstone. Low permeability (0.02 mD).

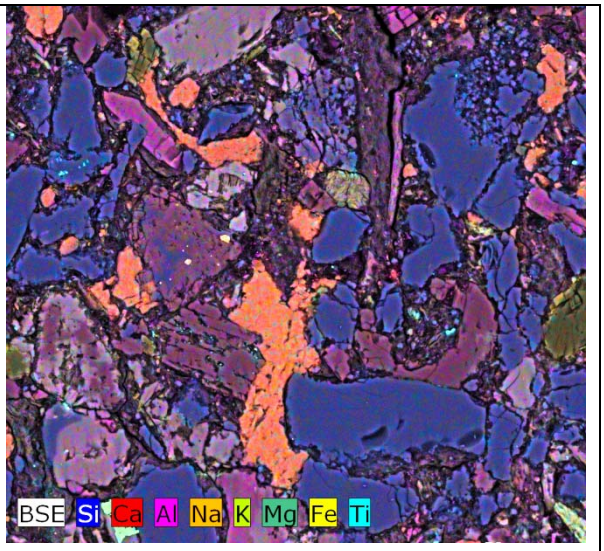

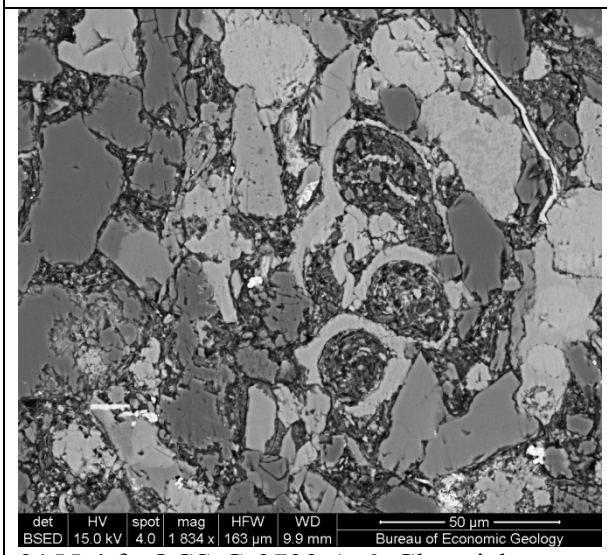

9155.4 ft, OCS-G-3733 A-6. Clay-rich siltstone. Low permeability (0.02 mD). Clay and calcite cements reduced porosity and permeability.

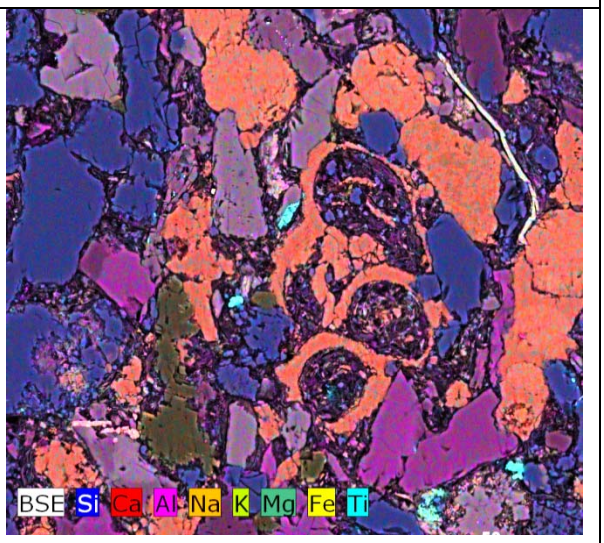

VIII-1-4 Core plug porosity and permeability measurements

VIII-1-4.1 Method

Ten core plugs were analyzed for grain density, porosity, permeability, and fluid saturation at Core Laboratories. The plugs selected were placed in Dean Stark equipment using toluene, followed by Soxhlet extraction cycling between a chloroform/methanol (87:13) azeotrope and methanol. Samples were oven dried at 240° F to weight equilibrium (+/- 0.001 g). Porosity was

determined using Boyle's Law technique by measuring grain volume at ambient conditions and pore volume at indicated net confining stresses (NCS). Permeability to air was measured on each sample using unsteady-state method at indicated NCS. Fluid saturations were determined by the Dean Stark technique using brine (1.032 g/cc density, 50,000 ppm TDS) and oil (0.845 g/cc density, 36° API). Grain density values were calculated by direct measurement of grain volume and weight on dried plug samples. Grain volume was measured by Boyle's Law technique.

VIII-1-4.2 Results

Porosity and permeability are shown in Table 2 and plotted in Fig. 5. They are also plotted with the sedimentary log of the core (Fig. 3). Porosity of the samples ranges from 11% to 22%. The fine-grained sandstone sample at 9187.8 ft has exceptionally low porosity of 6.6%. The very fine-grained sandstone at 9205.0 ft is the most porous sample. Two siltstone samples are at low end of the range with 11% and 14% porosity, respectively.

Porosity is generally correlated with grain size. The samples analyzed show gradually higher porosity from siltstone to very fine-grained sandstone and fine-grained sandstone (Table 1; Fig. 3). The exception to the correlation is the sample at 9187.8 ft. Its low porosity is due to high calcite cementation (43% total calcite). Calcite cementation is the most important porosity-limiting factor based on SEM and XRD studies. XRD measures all calcite phases in bulk samples, such as detrital grains, fossils and cements. Assuming the rock samples contained similar volume of detrital calcite and fossils at time of deposition, measured XRD bulk abundance would reflect relative abundance of cements. The samples show a negative correlation between porosity and calcite content (Fig. 6A). Petrographic studies confirm that calcite cementation is abundant in most samples and is the most important porosity-reducing authigenic mineral (Fig. 7A). The least porous sample at 9187.8 ft contains 43% of calcite, the majority of which is cements (Fig. 4I & 7B). On the other hand, the most porous sample (9205.0 ft) has porosity of 22% and contains the lowest calcite content of 12% (Fig. 6A). Thin section examination shows that the majority of its calcite exists as fossils (mostly foraminiferas) and calcite cementation is sporadic (Fig. 4H & J). Mineral dissolution is evident in this sample and enhances porosity (Fig. 4H & J).

Sample at 9118.8 ft, a fine-grained sandstone, contains porous laminations with low cementation interbedded with tight laminations with abundant calcite cementation and matrix material (Fig. 4B & 7C). Interlamination of heterogeneous facies reduces its overall porosity and permeability (porosity 17.4%; permeability 4.6 mD).

Two siltstone samples (9149.4 and 9155.4 ft) fall below the correlation trend of calcite abundance and porosity. They have lower porosity than sandstone samples with similar calcite abundance. Petrographic examination show that poorly sorted and rounded grains, together with high clay content, results in low porosity (Fig. 4K & L).

Permeability ranges between 0.005 and 63 mD, showing a large variation. Fig. 5 shows a strong correlation between porosity and permeability ($R^2 = 0.85$). Therefore, the diagenetic and depositional factors that control porosity also determine permeability. Abundance of calcite cements and clays are the two most important parameters. Grain size, sorting and rounding also affect porosity and permeability.

Overall, only one sandstone sample out of eight shows good porosity and permeability. The low quality of the sandstones is related to the primary depositional characteristics such as small grain

size, poor sorting, and rounding. The grain size in the core falls between the categories of lower fine to upper very fine sandstone (88-177 μm). The small grain size constrains overall porosity and permeability. The sandstones are mostly poorly to moderately sorted and poorly rounded, which leads to high degree of compaction. The sandstone properties are further affected by diagenesis, especially by carbonate cementation. Calcite cementation greatly reduces porosity and results in high degree of heterogeneity within the core. Mineral dissolution was observed in some samples, but not significant overall. It is well known that diagenesis, especially carbonate cementation, is randomly distributed in subsurface. Cement abundance and the extent of cemented zones (concretions and nodules) are usually not correlated with primary sedimentary beddings and will complicate storage capacity and infectivity.

However, the studied core presents the end member of low-quality sandstones. The study gives insights to the factors and features that damage and improve storage potential. It provides a case study for sandstone characterization and evaluation. The study improves our understanding of elements controlling sandstone quality and ability in selecting storage candidate formations.

Table 2 Conventional core plug analyses. Fine-grained sandstone samples marked in orange; very fine-grained sandstone in yellow; siltstone samples in green.

		Net Confining		Permeability		Saturation		Grain
Sample Number	Depth (ft)	Stress (psig)	Porosity (%)	Klinkenberg (md)	Kair (md)	Oil % Pore Volume	Water	Density (g/cm^3)
1	9111.6	2650	12.10	.152	.265	1.7	29.4	2.679
2	9118.8	2650	17.36	3.60	4.57	4.3	12.2	2.668
3	9123.7	2650	12.83	.375	.527	4.2	15.9	2.674
4	9131.8	2650	18.37	13.3	14.2	2.9	22.4	2.674
5	9141.3	2650	18.35	9.17	10.7	4.3	27.3	2.672
6	9149.4	2650	10.94	.004	.014	5.2	44.3	2.697
7	9155.4	2650	13.66	.007	.023	4.0	26.7	2.684
8	9178.0	2650	15.95	.342	.491	1.7	19.2	2.676
9	9187.8	2650	6.57	.001	.005	3.2	23.4	2.692
10	9205.0	2650	21.94	59.0	62.7	3.3	21.2	2.652

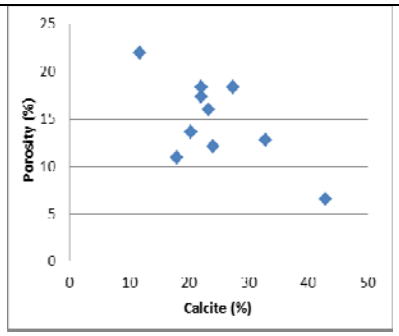

Fig. 6A Porosity vs. calcite abundance of samples of Well OCS-G-3733 A-6, showing negative correlation between porosity and calcite abundance.

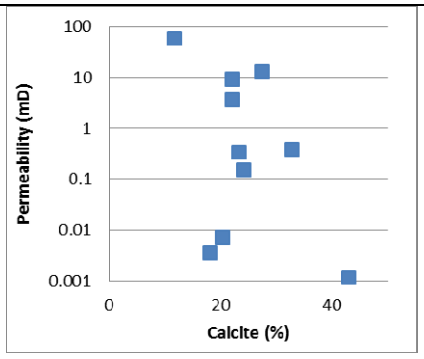

Fig. 6B Permeability vs. calcite abundance of samples of Well OCS-G-3733 A-6, showing weak correlation between permeability and calcite abundance.

VIII-2. Cranfield

The following test is excerpted from a paper by Jiemin Lu [Lu, J., Kharaka, Y. K., Thordsen, J. J., Horita, J., et al., 2012, CO_2-rock-brine interactions in Lower Tuscaloosa Formation at Cranfield CO2 sequestration site, Mississippi, U.S.A., Chemical Geology, v. 291, p. 269-277] documented the petrographic nature of the Cranfield sediments.

The reservoir rock, which is composed mainly of minerals with low reactivity (average quartz 79.4%, chlorite 11.8%, kaolinite 3.1%, illite 1.3%, concretionary calcite and dolomite 1.5%, and feldspar 0.2%), is relatively unreactive to CO_2. Reservoir temperature is ~125°C, and reservoir pressure was 32 MPa at a depth of 3,040 m.

VIII-2-1 Methods of study

Transmitted light microscopy and scanning electron microscopy (SEM)

As part of the geochemical study, a total of 63 thin sections from 4 cores (29-12, 28-1, 31F-2, 31F-3) from the reservoir interval were examined using a light microscope. Samples were examined in both transmitted light (plane and polarized) and in bright-field reflected light. Another 27 thin sections were coated with carbon and examined using a field-emission SEM and an FEI Nova™ NanoSEM 430 at The University of Texas at Austin (UT). The SEM was aided by energy dispersive spectrometry (EDS) for qualitative analysis of elemental composition.

X-ray diffraction (XRD) mineralogy

Thirty-seven core samples from the injection zone of Well 31F-2 were quantitatively analyzed using random-powder X-ray diffraction (XRD), which was prepared by wet grinding and spray drying (Hillier, 1999). Core samples were disintegrated using a TEMA ball mill prior to wet grinding using a McCrone Micronizing Mill. Slurry samples were sprayed through the heated chamber of a spray drier and dried. XRD was conducted on a Bruker AXS D8 diffractometer at UT, and quantitative analysis was performed using Topas 3, which is PC software based on the Rietveld method (Bish, 1994). Sample-preparation methods and analytical parameters can be found in Lu et al. (2011).

VIII-2-2 Results

Mineralogy and petrography

Bulk XRD mineral compositions of core samples are shown in Table 1. Abundance of authigenic mineral phases and rock fragment was estimated by thin-section microscopy and point count. The Lower Tuscaloosa reservoir sandstones are quartz arenite, composed mainly of quartz (79.4%), chlorite (chamosite) (11.8%), kaolinite (3.1%), and illite (1.3%), which have a lower dissolution rate and reactivity than those of K-feldspar and carbonate minerals (Palandri and Kharaka, 2004). The reservoir rock contains small amounts of more active minerals, such as calcite (1.1%), dolomite (0.4%), and albite (0.2%). According to point count, the sandstones contain an average 4.5% of rock fragments that are mostly metamorphic and igneous. Many rock fragments have been dissolved, leaving secondary pores (average 2.3%), and some have been partly replaced by chlorite. Feldspar minerals are rare in thin sections and undetectable by XRD for most samples. Albite was identified by XRD in five samples in the upper part of the reservoir, with an abundance of as much as 2.9% (Table 1). Most chlorite occurs as fibrous coats surrounding detrital grains (Figs. 1A, B), although some occurs as pore-lining and pore-filling

phases. Authigenic kaolinite most commonly occurs as pore-filling vermicular and booklet-stacking patterns. Quartz cement (up to 1% according to point count) is present in the upper part of the reservoir. Calcite and dolomite concretions (some of which are iron rich, according to SEM/EDS analysis) exist in conglomerates in the lower part of the reservoir. In total, four concretions with irregular edges were identified in two cores from the monitoring wells (31F-2 and 31F-3). Under microscope, most calcite and dolomite cements (up to 40%) are poikilotopic and occur as pore-filling and replacing habits. Outside of concretions, carbonate minerals occur only in trace amounts. They are commonly surrounded by grain coating and pore-lining chlorite (Fig. 1C).

VIII-2-3 References

Bish, D.L., 1994. Quantitative x-ray diffraction analysis of soil, in: Amonette, J.E., Zelazny, L.W. (Eds.), Quantitative Methods in Soil Mineralogy. Soil Science Society of America, Wisconsin, pp. 267-295.

Hillier, S., 1999. Use of an air brush to spray dry samples for X-ray powder diffraction.

Lu, J., Milliken, K., Reed, M.R., Hovorka, S., 2011. Diagenesis and sealing capacity of the middle Tuscaloosa mudstone at the Cranfield carbon dioxide injection site, Mississippi. Environ. Geosci. 18, 1-19.

Palandri, J.L., Kharaka, Y.K., 2004. A Compilation of Rate Parameters of Water–Mineral Interaction Kinetics for Application to Geochemical Modeling. U.S. Geological Survey, Open File Report 2004-1068, California, 64 pp.

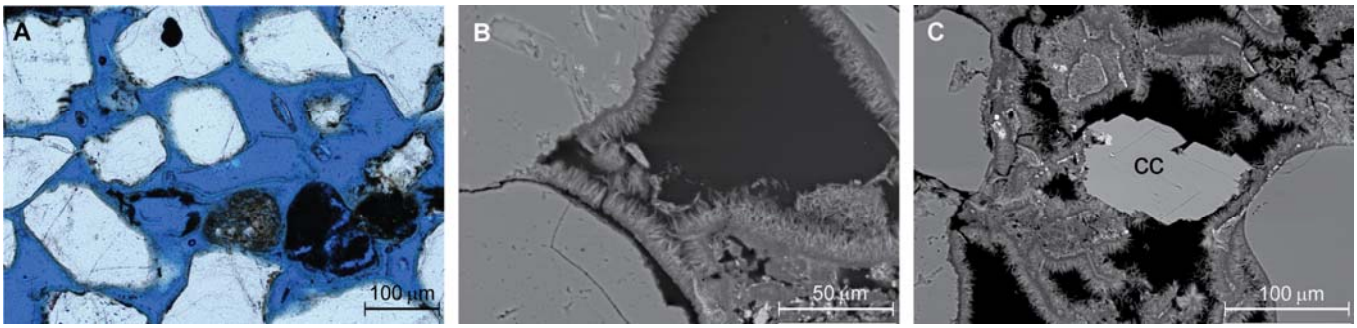

Fig. 1. (A) Light optical microscopic image showing chlorite coating surrounding detrital grains, rock fragments, and secondary pores; 3190.3 m, Well 31F-3; (B) backscattered SEM image showing fibrous chlorite coating surrounding quartz grains; 3190.8 m, Well 31F-2; (C) backscattered SEM image showing rare-occurring calcite (cc) grain confined by chlorite rims, limiting its contact with pore water; 3190.8 m, Well 31F-2.

Table 1. Mineralogy of reservoir sandstone of Well CFU31F-2 determined by XRD. Well location: Latitude: 31.563336; Longitude: -91.140564.

Depth (m)	Quartz %	Kaolinite %	Chlorite %	Illite %	Albite %	Calcite %	Dolomite %	Anatase %
3178.1	77.9	5.1	11.0	1.3		0.5		4.2
3178.9	73.7	4.3	13.8	1.9	2.5			3.7
3179.8	66.9	5.1	18.4	2.8	2.9			4.0
3180.1	77.0	6.0	18.8	2.9	1.0			4.3
3181.1	79.4	3.9	11.0	2.0	0.9			2.8
3181.7	78.6	4.0	11.1	2.1	1.1			3.1
3182.0	74.7	4.6	14.4	2.3				4.1
3183.0	82.0	3.3	9.7	1.8				3.2
3183.8	81.5	3.7	10.1	1.8				2.9
3184.4	85.8	3.3	7.3	1.2				2.5
3184.8	83.9	3.4	8.4	1.3				3.0
3185.2	83.5	3.4	9.0	1.6				2.5
3185.8	83.2	3.3	9.1	1.1				3.3
3187.0	79.3	4.2	11.2	1.2				4.1
3187.6	79.3	3.3	13.0	0.9				3.4
3188.3	80.7	3.1	12.6	1.2				2.5
3188.8	82.3	2.1	12.2	1.0				2.5
3189.3	81.3	2.6	12.0	1.0				3.1
3189.6	82.5	2.7	10.7	1.2				2.9
3190.0	78.8	2.7	14.0	1.3				3.2
3190.1	83.0	2.4	10.7	1.3				2.7
3190.8	81.0	1.5	13.4	1.2				2.9
3190.9*	80.7	1.7	14.1	0.8				2.6
3191.2	75.6	2.5	17.1	1.0				3.7
3191.5	77.9	2.8	15.3	0.9				3.2
3193.2	55.2	1.2	4.7	0.6		36.8		1.5
3193.6	84.6	3.0	8.8	0.8				2.8
3193.9	81.4	2.2	12.8	0.4				3.3
3194.2	85.5	2.5	8.7	0.4		0.5		2.4
3194.9	85.1	2.2	10.1	0.3				2.3
3195.6	85.7	2.0	9.2	0.5		0.6		2.0
3195.9	80.8	2.1	14.0	0.3				2.9
3196.1	82.0	2.2	13.1	0.1				2.7
3196.8	81.9	2.2	12.5	1.2				2.2
3197.7	83.6	1.7	10.5	1.4		0.5		2.3
3199.7	71.2	4.8	10.6	1.9			9.8	1.8
3200.3	70.5	4.7	13.1	1.5			6.5	3.7
Average	79.4	3.1	11.8	1.3	0.2	1.1	0.4	3.0

IX. Appendix D: Acid Species Analysis

by Changbing Yang (adapted by J.-P. Nicot)

Geochemical Modeling of Impacts of Impurities in the CO_2 Stream on Groundwater Chemistry

Summary

This appendix presents preliminary results of two sets of numerical models for assessing impacts of impurities in the CO_2 stream on brine chemistry, especially brine pH and Eh. Gas fugacity is calculated with WINPROP, a phase behavior and property software developed by CMG, and then taken as input to PHREEQC, a geochemical calculation program developed by USGS, for simulating interactions of brine-gases-rocks. One set of numerical models were to evaluate impacts of each of the four acid gases (SO_2, NO, NO_2, and HCl) present in small quantities in the CO_2 stream on brine chemistry. Model results suggest that impacts of acid gases on brine pH can be neglected when concentration of an acid gas in the CO_2 stream is less than a threshold value, for instance, ~1000 ppm for the Frio setting and ~100 ppm for the Cranfield setting for all gases considered. Presence of SO_2 in the CO_2 stream makes the brine more reducing and presence of NO and NO_2 makes the brine more oxidizing. In a second step we modeled brine-rock interactions and an impure CO_2 stream. The choice of the impure CO_2 stream composition is somewhat arbitrary and was made by choosing impurity levels toward the upper bound of their likely range. Preliminary model results show that CO_2, Ar and O_2 are the dominant gases in the gas phase after interactions of brine-rocks-gases and that other gases initially present are consumed and remain only at the trace level. SO_2 and CO are nearly depleted in the gas phase. Simulated brine pH is 3.2 for the Frio setting and 3.0 for the Cranfield setting with no calcite in the model. If calcite is taken into account, simulated brine pH is 4.9 for the Frio setting and 4.2 for the Cranfield setting. Simulated brine Eh ranges from 0.92 volts to 1.03 volts in both settings, showing oxidizing conditions, due to dissolved oxygen in brine. Because of the oxidizing conditions, SO_4^{2-} is dominant among the sulfur species and NO_3^- is dominant among the nitrogen species.

IX-1. Modeling approach

In this study, PHREEQC(Parkhurst and Appelo, 1999), a geochemical calculation program developed by USGS, is used to simulate impacts of impurities in the CO_2 stream, especially acid gases, on brine chemistry and dissolution/precipitation of minerals contained in the aquifer sediments. We were confronted to two initial issues: (1) little information on thermodynamic data of real gas mixture (CO_2 and impurities) is available in the literature and (2) limitations of modeling tools; most numerical models assume that acid gases in the CO_2 stream will completely dissolve in brine and lead to an instantaneous decrease in brine pH (such as SO_2 becoming SO_4^{-2} and H^+) instead of considering the partitioning process and the fact that some fraction of each acid gas will stay in the CO_2 stream. More specifically for the geochemical model we used: although PHREEQC can model different gas compositions in the gas phase, it uses the ideal gas law to describe the interactions among gases and liquid, which may be valid for low pressure and temperature conditions, but may not be valid for reservoir conditions, for example, reservoir pressure is about 1500 psi and temperature is about 59 ^oC in the Frio formation, one of two test cases in this study. So we used WINPROP (CMG, 2011) to calculate gas fugacity under

reservoir conditions and then as input to PHREEQC. Winprop is a model tool developed by CMG to solve equation of state multiphase equilibrium property package featuring fluid characterization, lumping of components, matching of laboratory data through regression, simulation of multiple contact processes, phase diagram construction and solids precipitation.

A batch model, rather than a reactive transport model, is used to evaluate impacts of impurities in the CO_2 stream on brine chemistry and dissolution/precipitation of minerals present in the aquifer sediments. Compared to a reactive transport model, a batch model, without considering dynamic fluid flow, requires less model parameters and is simpler to implement.

A geochemical database which describes chemical reactions is needed for conducting geochemical modeling using either a batch model or a reactive transport model. Nine different geochemical databases with different sets of gases are provided with PHREEQC. Table 1 lists gases included in five of the nine geochemical databases. The LLNL geochemical database (PHREEQC format) includes more gases than the other four geochemical databases. Three acid gases, SO_3, N_2O, and HCN, are not included in any of the nine geochemical databases. Most probably the three acid gases are much less naturally present in geological environments, main focus of PHREEQC users. In the following modeling simulations, these three acid gases are not considered. It should be noted that the geochemical databases may also include other gases, such as Na(g) in the LLNL database. However, those gases may not be present in the CO_2 stream and therefore are not listed in Table 1.

Table 1. Gases included in the five chemical databases

Database	Gas included	Not included
LLNL	CH_4, CO, CO_2, HCL, H_2, H_2S , NO, NO_2, O_2, SO_2, NH_3, Ar, N_2	SO_3, N_2O, HCN
Minteq	CH_4, CO_2, O_2	CO, HCL, H_2, H_2S , NO, NO_2, SO_3, N_2O, HCN, NH_3
Minteq.V4	CH_4, CO_2,H_2S, O_2	CO, HCL, H_2, NO, NO_2, SO_3, N_2O, HCN,NH_3
Phreeqc	CH_4, CO_2, H_2, H_2S , O_2,NH_3, N_2	CO, HCL, NO, NO_2, SO_3, N_2O, HCN
Wateq4f	CH_4, CO_2, H_2, H_2S , O_2,NH_3, N_2	CO, HCL, NO, NO_2, SO_3, N_2O, HCN

Two representative reservoir settings were simulated in this study: the Frio setting (formation in Texas Gulf Coast of Oligocene Age) and the Cranfield setting (formation in the Mississippi Gulf Coast of Cretaceous age). We chose these two settings because BEG led extensive investigations there before and after injecting CO_2. Information about those sites is documented elsewhere. Brine chemistry and reservoir pressure, temperature of the two settings are listed in Table 2. Since measured brine Eh of the two settings are not available, brine Eh is assumed to be 0.32 volts for both brine waters.

Table 2. Brine chemistry and reservoir physical properties

	Frio Setting (Xu et al., 2010)	Cranfield Setting (Lu et al., 2012)
C(4) (Mol/Kg of H_2O)	1.04E-02	6.86E-03
Ca (Mol/Kg of H_2O)	6.09E-03	3.09E-01
Cl (Mol/Kg of H_2O)	1.49E+00	2.84E+00
Fe (Mol/Kg of H_2O)	4.63E-04	1.01E-02
K (Mol/Kg of H_2O)	4.53E-03	1.63E-02
Mg (Mol/Kg of H_2O)	2.20E-02	3.97E-02
Na (Mol/Kg of H_2O)	1.35E+00	2.05E+00
S (Mol/Kg of H_2O)	4.20E-05	4.62E-10

	Frio Setting (Xu et al., 2010)	Cranfield Setting (Lu et al., 2012)
pH	6.7	5.9
Eh	0.32	0.32
Pressure (psi)	1500	4600
Temperature (^{o}C)	59	127.2
Porosity	0.34	0.25
Calcite as buffer for pH (volume ratio)	0.019	0.014

Two sets of numerical models were conducted. Set 1 is to simulate interactions of brine and CO_2 to which is added only one of the four acid gases (SO_2, NO, NO_2, HCl). Concentration of the acid gas varies from 0.0001% to 5% (1 ppm to 500,000 ppm). The objective of the modeling exercise for Set 1 is to assess impacts of the acid gas as impurity in the CO_2 stream on pH and Eh of the brine, as well as change in aqueous species. For comparison, calcite is also considered in the models to evaluate how calcite can buffer brine pH and Eh. For this set of runs, we tried two approaches to calculate gas fugacity of the CO_2 stream. Approach 1 assumes that gas fugacity of the mixture depends on concentration of the acid gas (NO, NO_2, SO_2 and HCl). Approach 2 assumes that gas fugacity is independent of concentration of the acid gas. In Approach 1, gas fugacity for different concentrations of an acid gas in the CO_2 stream are calculated with WINPROP and then as input for PHREEQC. In Approach 2, gas fugacity is calculated with WINPROP only for CO_2 and then as input for PHREEQC. In the PHREEQC model, concentration of an acid gas (NO, NO_2, SO_2 and HCl) is changed from 1 ppm to 500,000 ppm. Since both approaches provide very similar results, results of Approach 2 for the Set 2 runs are presented in this short report.

Set 2 simulates interactions of brine and all possible impurities at once in the CO_2 stream. Gas composition of the CO_2 stream is listed in Table 3. The choice of the impure CO_2 stream composition is somewhat arbitrary and was made by choosing impurity levels toward the upper bound of their likely range. Approach 2 was employed to calculate gas fugacity of CO_2 stream for this set of runs.

Total four runs were conducted by considering different reservoir conditions (Frio setting and Cranfield setting) in case of presence of a buffer (calcite). Description of the four runs is given in Table 4.

Table 3. Gas compositions modeled in Set 2

Gas composition	Percentage (%)	ppm	Gas composition	Percentage (%)	ppm
CO_2	95.944%		HCN	0%	0
HCl	0.001%	10	SO_3	0%	0
NO_2	0.001%	10	N_2O	0%	0
CO	0.030%	300	H_2	0%	0
NO	0.020%	200	H_2S	0%	0
SO_2	0.004%	40			
O_2	2.100%	21000			
N_2	0.200%	2000			
Ar	1.700%	17000			
Total	100%				

Table 4. Description of numerical models of Set 2.

Model	Gas compositions	Reservoir setting	Buffer
Set 2_1	Listed in Table 3	Frio	Without calcite
Set 2_2	Listed in Table 3	Frio	With Calcite
Set 2_3	Listed in Table 3	Cranfield	Without calcite
Set 2_4	Listed in Table 3	Cranfield	With Calcite

IX-2. Results

IX-2-1 Numerical modeling results of Set 1 Runs

The general objective of the modeling is to determine the threshold concentration at which a given impurity starts impacting pH. Brine pH modeled as function of percentage of an acid gas in the CO_2 stream for the Frio setting is shown in Figure 1. No calcite is considered. Note that the pH is low with no impurities because of the CO_2. It is interesting to see that brine pH shows very minor (or little) change when the percentage of an acid gas (SO_2, NO, NO_2, HCl) in the CO_2 stream is less than about 0.1% (1000 ppm). When percentage of an acid gas in the CO_2 stream is higher than 0.1% (1000 ppm), brine pH obviously decreases as increase in concentration of acid gas. Among the four acid gases, SO_2 shows the most impact on brine pH and NO shows the least impact on brine pH for the Frio setting. Model results of brine pH for the Cranfield setting without considering presence of calcite in the aquifer sediments are shown in Figure 2. Brine pH after reacted with CO_2 and the acid gas is slightly lower for the Cranfield setting than for the Frio setting, probably due to the fact that the total reservoir pressure of the Cranfield setting is much higher than that of the Frio setting. Note that for the Cranfield setting, brine pH shows minor (or no) change when concentration of acid gas is less than 0.01% (100 pm). Note that brine pH increases slightly (~0.05 unit) when concentration of NO from 2000 ppm to 10000 ppm and then decreases again. It is unclear why brine pH shows such a behavior for the Cranfield setting. One possibility is numerical instabilities (Parkhurst and Appelo, 1999).

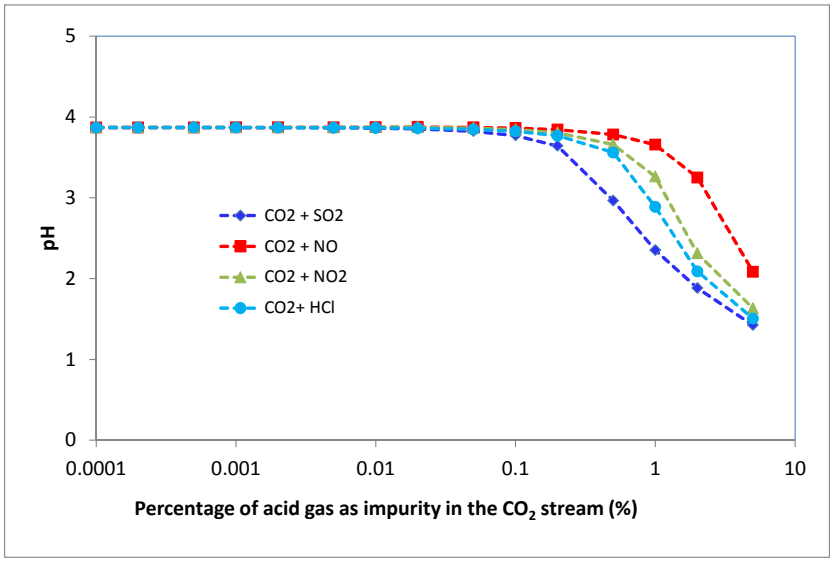

Figure 1. Modeled brine pH as function of percentage of acid gas (NO, NO_2, SO_2, and HCl) in the CO_2 stream without considering calcite as buffer for the Frio setting.

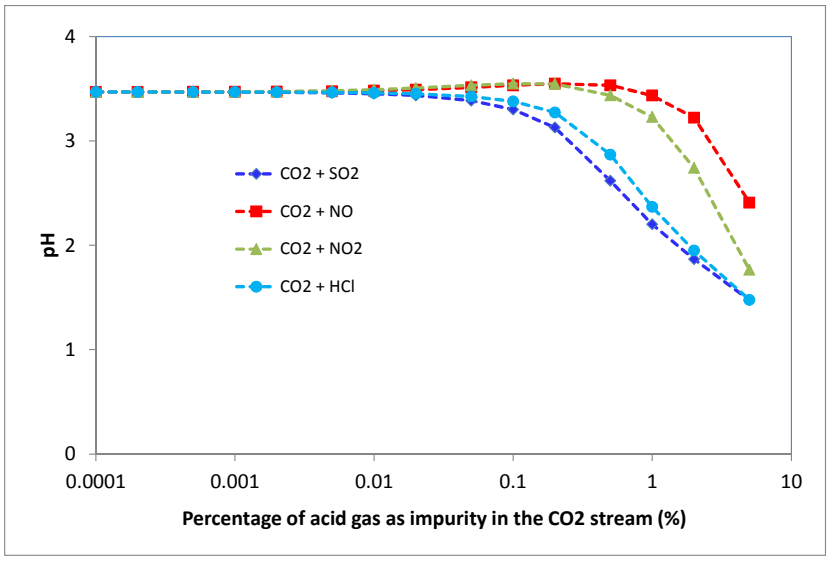

Figure 2. Modeled brine pH as function of percentage of acid gas (NO, NO_2, SO_2, and HCl) in the CO_2 stream without considering calcite as buffer for the Cranfield setting.

In order to further evaluate the impacts of an acid gas as impurity in the CO_2 stream on brine pH, a change in brine pH is calculated (ΔpH)

$$\Delta pH = pH_p - pH_{imp} \quad (1)$$

where pH_{imp} is the brine pH modeled with different concentrations of an acid gas in the CO_2 stream, and pH_p is the brine pH modeled when pure CO_2 is considered. ΔpH represents the contribution of an acid gas as impurity in the CO_2 stream to brine pH. As expected, the higher concentration of an acid gas in the CO_2 stream, the more significant contribution of the acid gas to brine pH, then the greater ΔpH. Figure 3 shows ΔpH as function of an acid gas in the CO_2 stream for the Frio setting without considering calcite as a buffer. It can clearly be seen that ΔpH is almost 0 when percentage of an acid gas is less than 0.1%. ΔpH is close to 0 when NO concentration is less 0.2% (2000 ppm.) As concentration of an acid gas increases to 5%, ΔpH are 2.6 for SO_2, 2.4 for HCl, 2.2 for NO2 and 1.8 for NO. Figure 4 shows ΔpH as function of an acid gas in the CO_2 stream for the Cranfield setting without considering calcite as a buffer. ΔpH is close to 0 when concentration of an acid gas is less than 0.01% (100ppm). Modeling results of brine pH for both the Frio and Cranfield settings suggests that there is a threshold value of the concentration of an acid gas in the CO_2 stream. If concentration of the acid gas is less than the threshold value, impacts of acid in the CO_2 stream on brine pH can be neglected. For instance, the threshold values of the four acid gases are 1000 ppm for the Frio setting and 100 ppm for the Cranfield setting. Obviously the threshold value may depend on reservoir conditions as well as type of an acid gas. Threshold value of NO concentration in the CO_2 stream is 0.2% (2000 ppm) (See Figure 3 and 4).

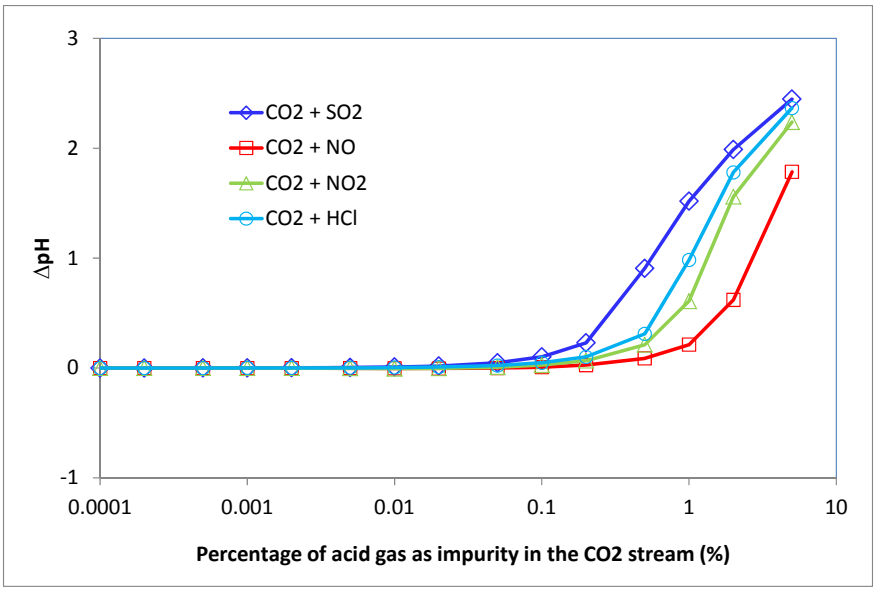

Figure 3. Change in brine pH (ΔpH) as function of percentage of acid gas (NO, NO_2, SO_2, and HCl) in the CO_2 stream without considering calcite as buffer for the Frio setting.

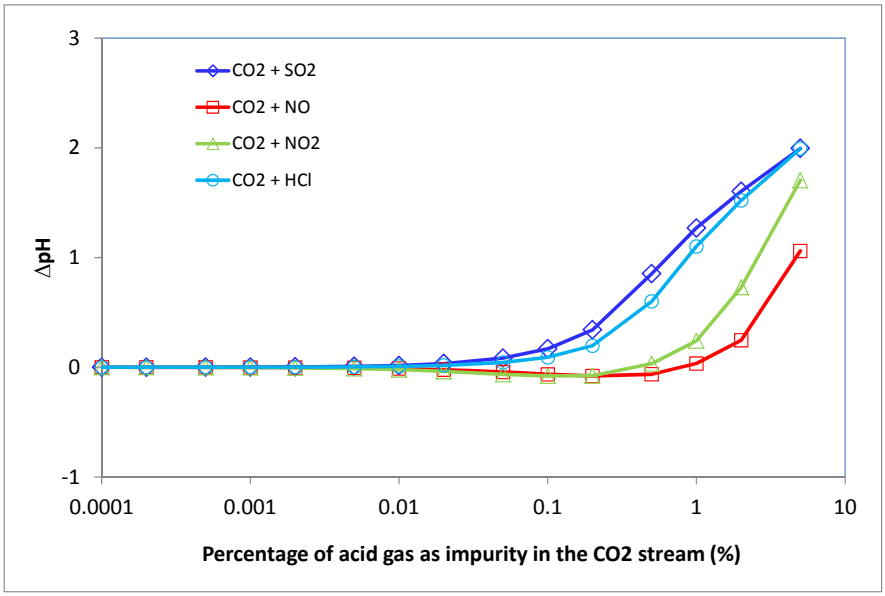

Figure 4. Change in brine pH (ΔpH) as function of percentage of acid gas (NO, NO_2, SO_2, and HCl) in the CO_2 stream without considering calcite as buffer for the Cranfield setting.

Mineral dissolution/precipitation, such as dissolution of silicate and carbonate minerals, may play a role in buffering brine pH. Mineral reactions can be modeled based on either the equilibrium assumption or reaction kinetics. The former assumes that interactions of minerals with brine can be fast enough so that equilibrium can be reached between brine and minerals. The later considers that interactions of mineral with brine are slow and can be expressed with a kinetic law. Since we are interested in how brine pH will be affected if there is a buffer, such as calcite, a simplified model is used by considering calcite in the geochemical models based on the equilibrium assumption. A more comprehensive geochemical model which considers kinetic mineral dissolution could be developed in the future study. For instance dissolution of silicate

minerals can also buffer pH; however reaction rates are much slower. Kinetics should be used for simulating dissolution of silicate minerals. Modeled brine pH values with considering calcite as a buffer are about 4.9 for the Frio setting and 4.2 for the Cranfield setting, regardless of change in concentration of an acid gas in the CO_2 stream. The plots of brine pH modeled with calcite buffer are not shown here.

Potential impacts of an acid gas, NO, NO_2, SO_2 in the CO_2 stream on brine redox potential are also of interest since these acid gases may be either oxidized or reduced when dissolved into brine and change brine Eh. Modeled brine Eh as a function of concentration of an acid gas in the CO_2 stream for the Frio setting is shown in Figure 5. As expected, HCl in the CO_2 stream does not show any impact on brine Eh. Brine Eh increases as increase in concentration of NO or NO_2 in the CO_2 stream. This suggests that brine becomes more oxidizing. Brine thus has stronger corrosion capability to the steel tube of the injection wells. It is interesting that when SO_2 is present in the CO_2 stream brine shows more reducing conditions and therefore may be good for the steel tube of the injection well (ignoring the impact of pH). Figure 6 shows modeled brine Eh as a function of acid gas concentration in the CO_2 stream for the Cranfield setting. Similar conclusions can be drawn from the results of the Frio setting. However, change in brine Eh is slightly smaller for the Cranfield setting than for the Frio setting.

Next, we examine likely explanations for the change in Eh. Dissolution of SO_2 in brine proceeds according to the following reaction,

$$SO_{2(g)} + H_2O \leftrightarrow 2H^+ + SO_3^{2-} \quad (1)$$

However, most SO_3^{2-} is oxidized to SO_4^{2-}. If SO_2 concentration in the CO_2 stream is small, Fe^{3+} is the likely electron acceptor in the brine and is reduced to Fe^{2+}, according to the following reaction,

$$2Fe^{3+} + SO_3^{2-} + H_2O \leftrightarrow 2Fe^{2+} + SO_4^{2-} + 2H^+ \quad (2)$$

So Fe^{3+} concentration in brine decreases and Fe^{2+} concentration increases (Figure 7).

When most Fe^{3+} is reduced to Fe^{2+} or if not initially present (more reducing conditions) SO_3^{2-} from dissolution of SO_2 is partially oxidized to SO_4^{2-} and the rest will be reduced to S^{2-}, based on the following reaction:

$$2SO_3^{2-} + 2H_2O \leftrightarrow 2SO_4^{2-} + S^{2-} + 4H^+ \quad (3)$$

It can be seen that S^{2-} concentration increases as SO_2 concentration in the CO_2 stream increases (Figure 8a). Concentration SO_3^{2-} is small when the redox reactions using Fe^{3+} as an oxidant (figure 8d). Once Fe^{3+} has been consumed, concentration of SO_3^{2-} shows a sharp increase (Figure 8d) and S^{2-} is produced (Figure 8c). Total sulfur aqueous species in brine increases as more SO_2 dissolves into brine (Figure 8a). As S^{2-} concentration increases in brine, pyrite would tend to precipitate, as seen in Figure 9 which shows saturation index of pyrite as a function of SO_2 concentration in the CO_2 stream.

If NO is present in the CO_2 stream, NO uses Fe^{2+} as the most likely electron donor. Fe^{2+} is oxidized into Fe^{3+} when there is enough Fe^{2+} to act as a reductant. The reaction proceeds according to the following equation,

$$3NO(g) + Fe^{2+} \leftrightarrow Fe^{3+} + N_2 + NO_3^- \quad (4)$$

Therefore, Fe^{2+} concentration in brine decreases while Fe^{3+} concentration increases (Figure 10). In addition to Fe^{2+} in brine, NO also uses H_2O as reductant. The sequential reactions proceed according to the following processes,

$$NO(g) + 0.5H_2O + 0.25\,O_2 \leftrightarrow H^+ + NO_2^- \quad (5)$$

$$2NO_2^- + 2H^+ \leftrightarrow 1.5\,O_2 + N_2 + H_2O \quad (6)$$

$$NO_2^- + 0.5\,O_2 \leftrightarrow NO_3^- \quad (7)$$

A complete reaction path can be written by canceling NO_2^- by

$$3NO(g) + 0.5H_2O \leftrightarrow NO_3^- + N_2 + 0.25\,O_2 + H^+ \quad (8)$$

The processes release proton and O_2. Concentrations of NO_3^-, N_2, and O_2 increase as more NO is present in the CO_2 stream (Figures 11 and 12.). In addition, saturation indices of N_2 gas in brine show an increasing trend as more NO is present in the CO_2 stream (Figure 13).

If NO_2 is present in the CO_2 stream, NO_2 can use Fe^{2+} as an electron donor and Fe^{2+} is oxidized into Fe^{3+} when there is enough Fe^{2+} in the brine. The reaction goes through a series of intermediate processes and the overall reaction can be given by:

$$NO_{2(g)} + 4H^+ + 4Fe^{2+} \leftrightarrow 4Fe^{3+} + 0.5\,N_2 + 2\,H_2O \quad (9)$$

Therefore, Fe^{3+} concentration increases while Fe^{2+} decreases as more NO_2 is present in the CO_2 stream (Figure 14). Dissolved N_2 in brine increases (Figure 15) as concentration of NO_2 in the CO_2 stream is increased. Note that the above reaction consumes proton and should lead to increase in brine pH. However, brine dissolution of CO_2 provides enough proton for the reaction in Eq. 9 to proceed. If there is not enough Fe^{2+}, reactive dissolution of $NO_{2(g)}$ can proceed according to the following series of reaction paths,

$$NO_{2(g)} + 0.5H_2O + 0.25\,O_2 \leftrightarrow H^+ + NO_3^- \quad (10)$$

$$2NO_3^- + 2H^+ \leftrightarrow 2.5\,O_2 + N_2 + H_2O \quad (11)$$

In the reaction path above, N_2 and O_2 are produced, which are shown in Figures 15 and 16.

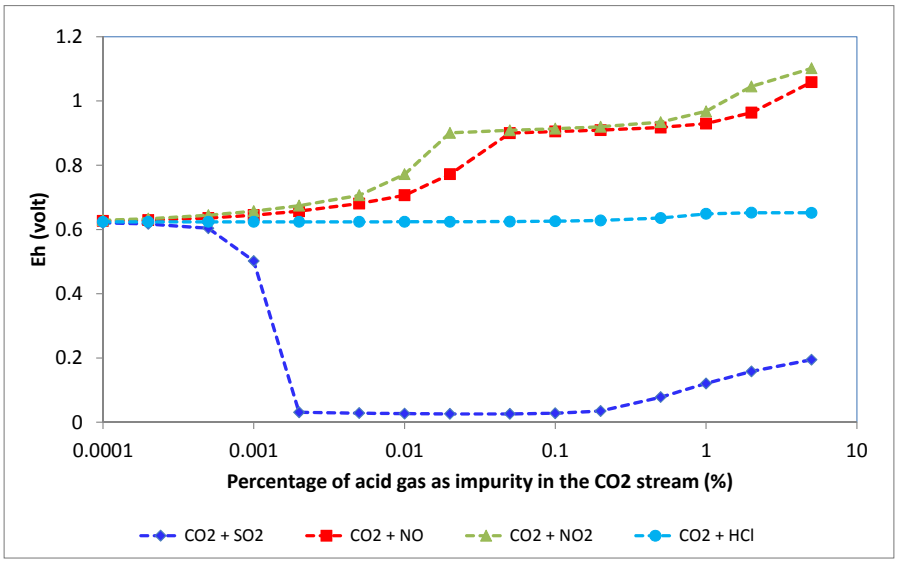

Figure 5. Modeled brine Eh as function of percentage of acid gas in the CO_2 stream for the Frio setting.

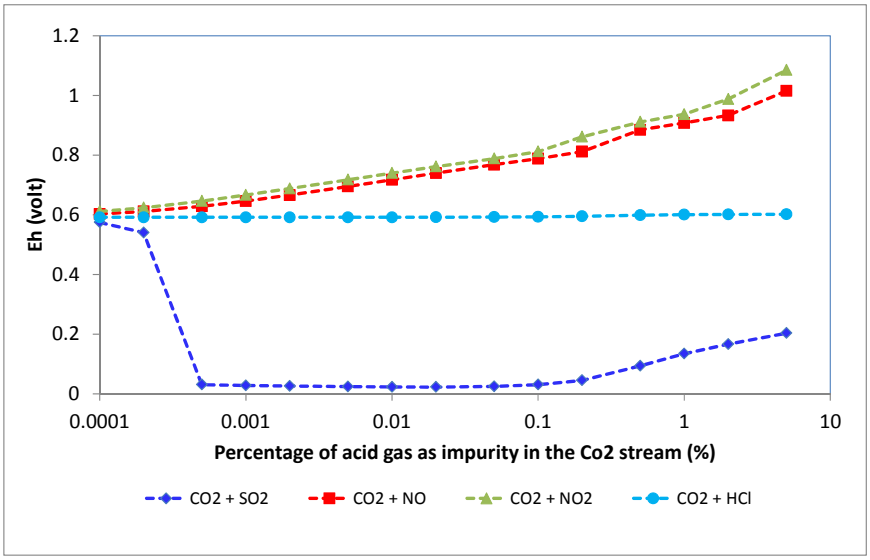

Figure 6. Modeled brine Eh as function of percentage of acid gas in the CO_2 stream for the Cranfield setting.

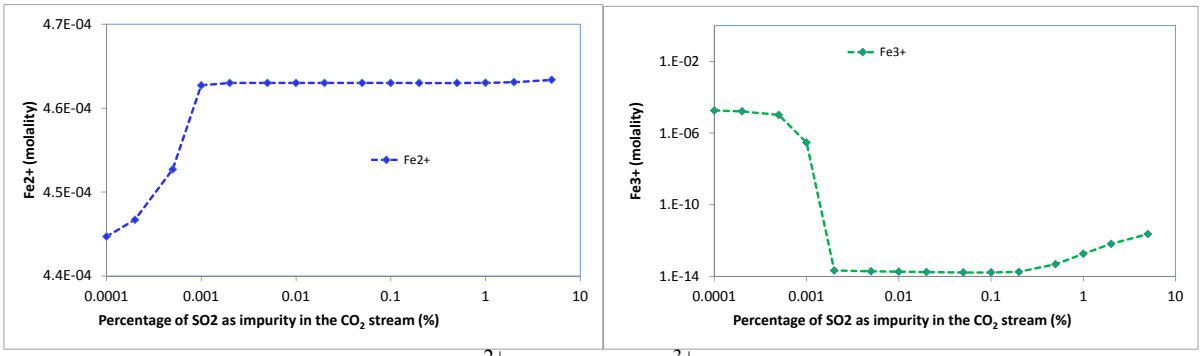

Figure 7. Modeled concentrations of Fe^{2+} (left) and Fe^{3+} as function of percentage of SO_2 in the CO_2 stream for the Frio setting.

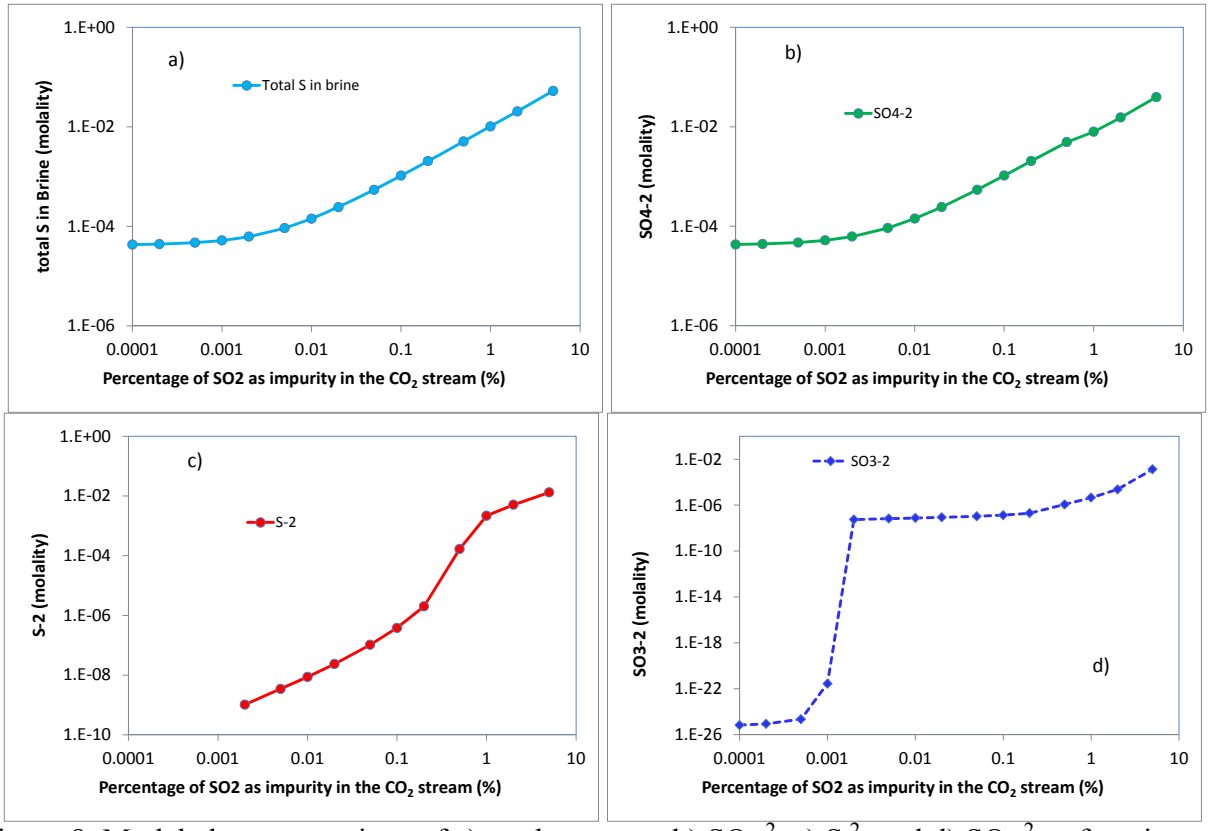

Figure 8. Modeled concentrations of a) total aqueous, b) SO_4^{-2}, c) S^{-2}, and d) SO_3^{-2} as function of percentage of SO_2 in the CO_2 stream for the Frio setting.

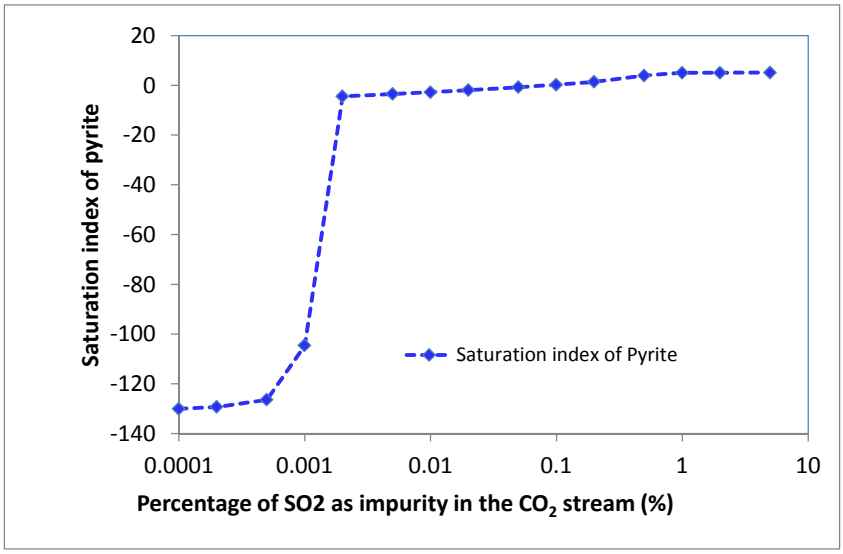

Figure 9. Modeled saturation index of pyrite as a function of percentage of SO_2 in the CO_2 stream for the Frio setting (negative value means pyrite is under saturated with brine and positive value means that pyrite is over saturated with brine and tends to precipitate).

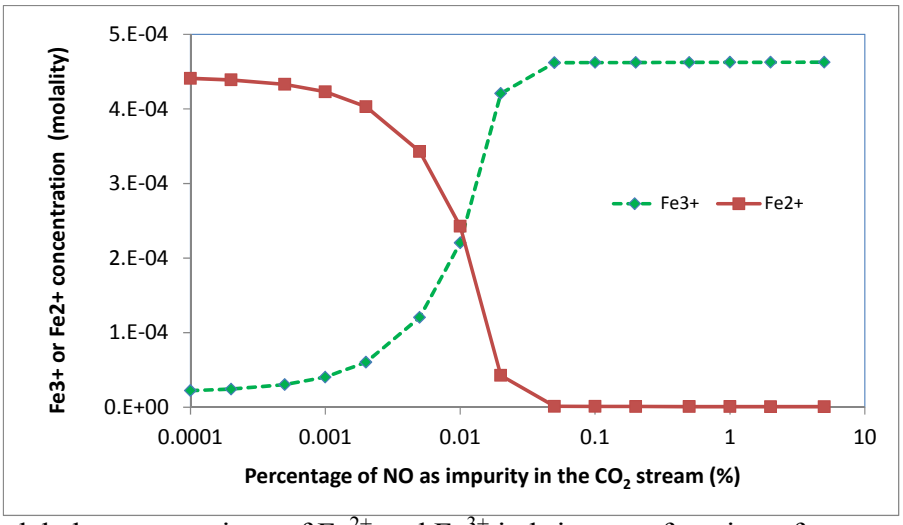

Figure 10. Modeled concentrations of Fe^{2+} and Fe^{3+} in brine as a function of percentage of NO in the CO_2 stream for the Frio setting.

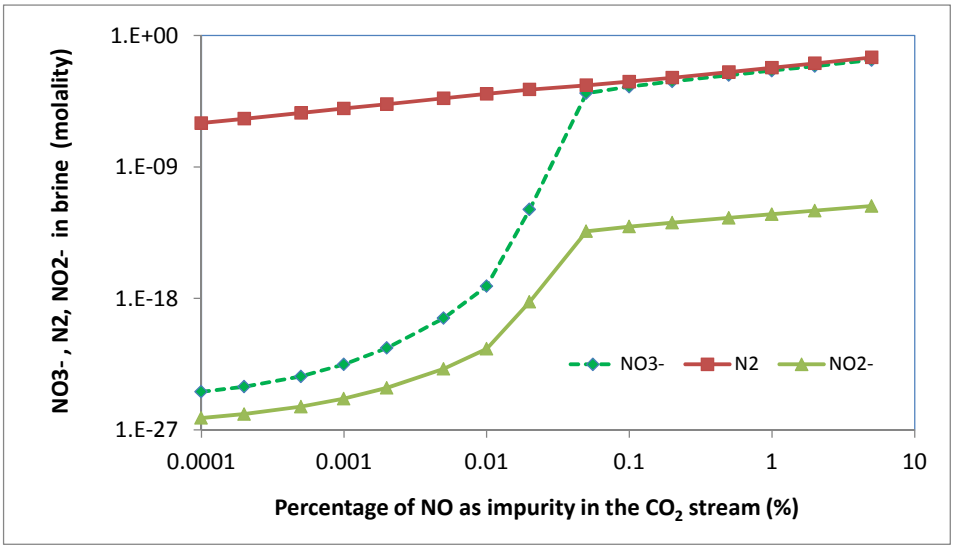

Figure 11. Modeled concentrations of NO_3^-, NO_2^-, and N_2 in brine as a function of percentage of NO in the CO_2 stream for the Frio setting.

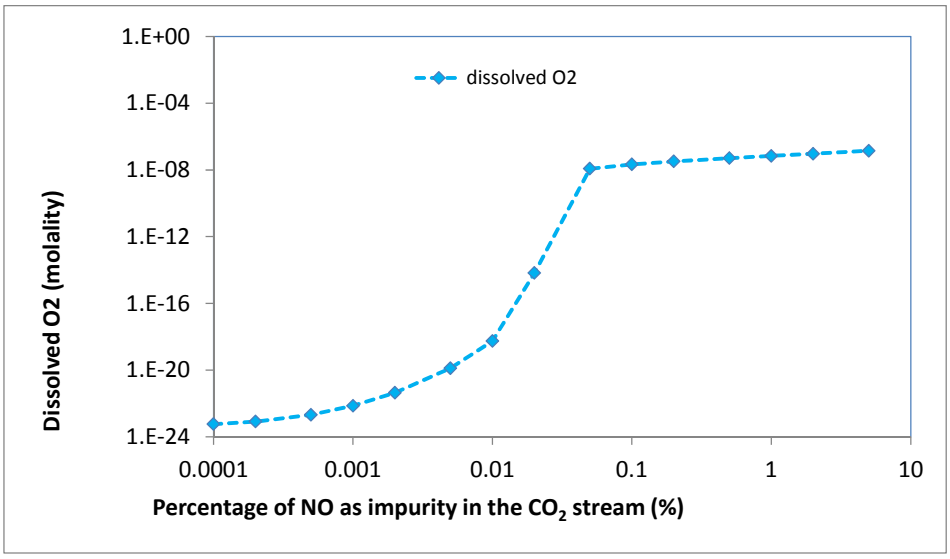

Figure 12. Modeled concentrations of dissolved O_2 as a function of percentage of NO in the CO_2 stream for the Frio setting.

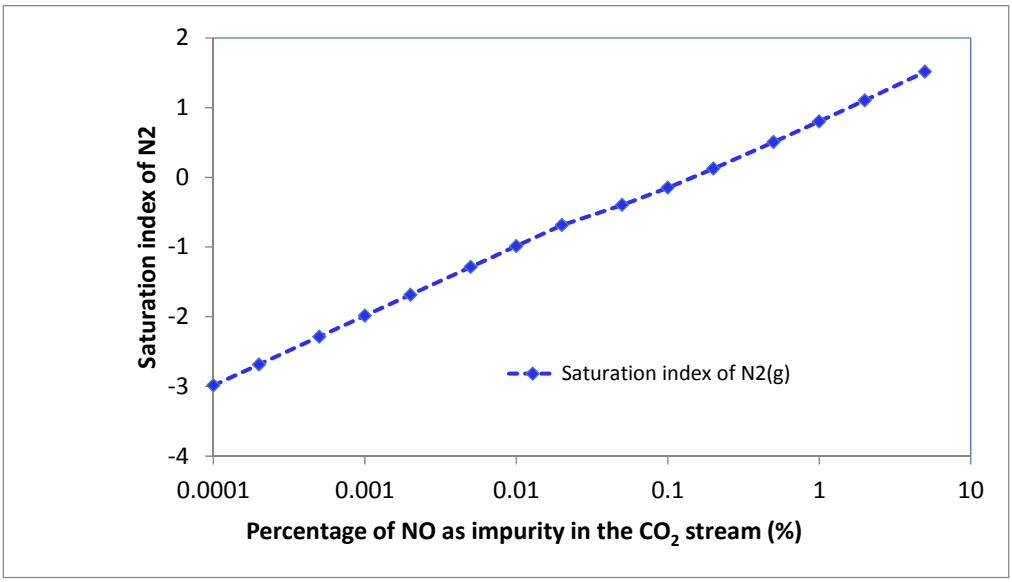

Figure 13. Modeled saturation index of N_2 as a function of percentage of NO in the CO_2 stream for the Frio setting (negative value means N_2 is under saturated with brine and positive value means that N_2 is over saturated with brine and tends to exsolve).

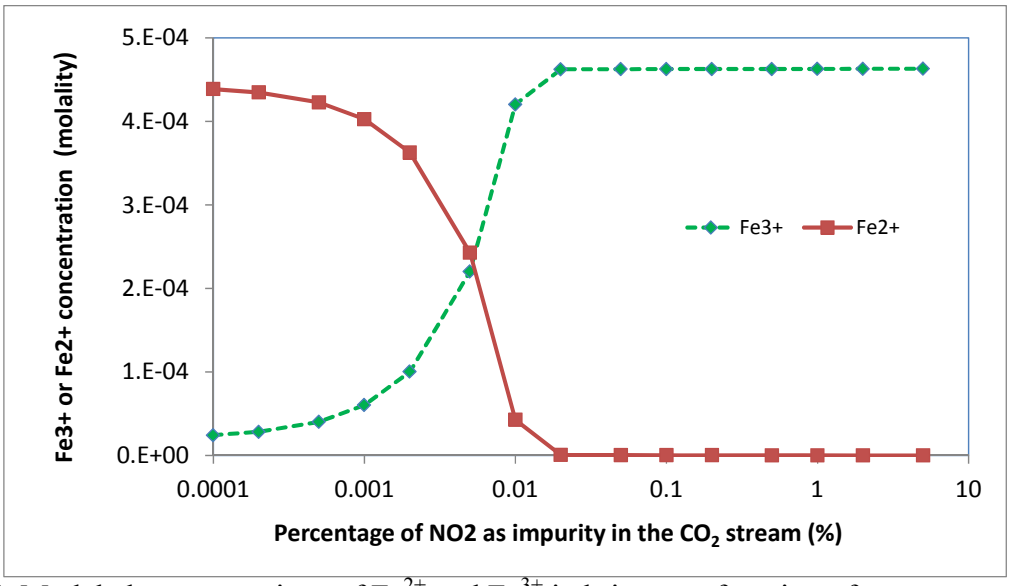

Figure 14. Modeled concentrations of Fe^{2+} and Fe^{3+} in brine as a function of percentage of NO_2 in the CO_2 stream for the Frio setting.

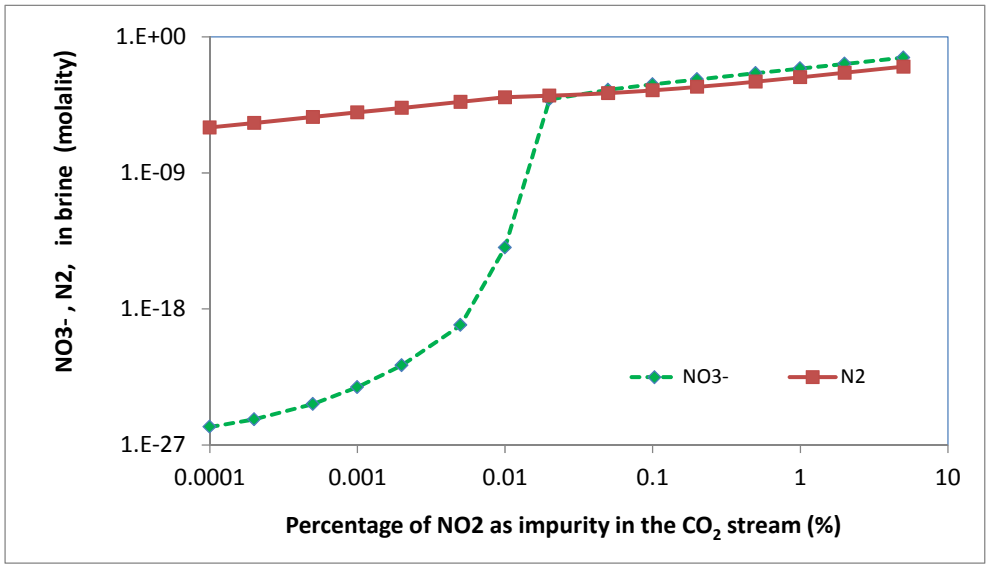

Figure 15. Modeled concentrations of NO_3^-, and N_2 in brine as a function of percentage of NO_2 in the CO_2 stream for the Frio setting.

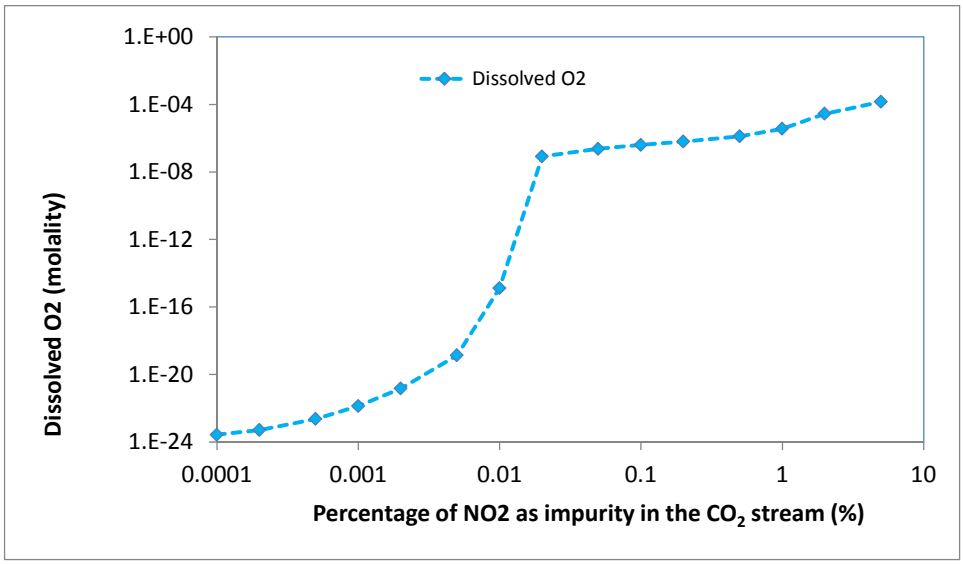

Figure 16. Modeled concentrations of dissolved O_2 as a function of percentage of NO_2 in the CO_2 stream for the Frio setting.

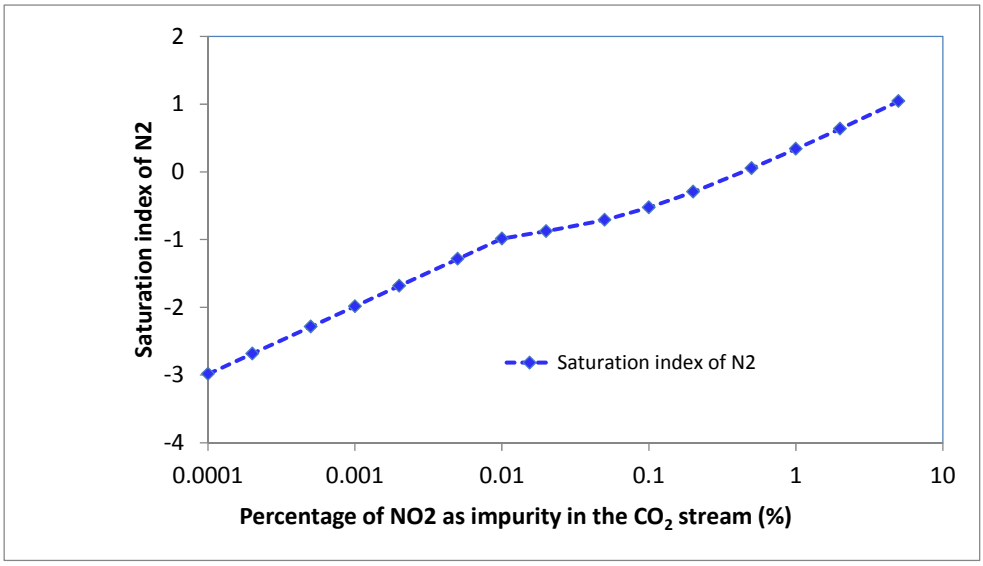

Figure 17. Modeled saturation index of N_2 as a function of percentage of NO_2 in the CO_2 stream for the Frio setting (negative value means N_2 is under saturated with brine and positive value means that N_2 is over saturated with brine and tends to ex-solve).

IX-2-2 Numerical modeling results of Set 2 Runs

In this section we examine rock-water interaction in presence of a realistic CO_2 stream. After the CO_2 stream with impurities contacts the brine, redistribution of gases between gas phase and brine occurs due to dissolution and other geochemical reactions. Partitioning of inert gases, such as argon, N_2, between the gas phase and brine depends on gas solubility, a function of pressure and temperature. For reactive species, such as SO_2, NO, as discussed earlier, redox reactions could potentially occur. Modeling results of gas compositions for the four runs listed in Table 4 are shown in Figures 18 and 19. As expected, CO_2 as the dominant gas in the gas phase reacts

with brine and/or buffer (calcite in this study). Molar percentage of CO_2 left in the gas phase is higher for the Frio setting than for the Cranfield setting. The other two dominant gases left in the gas phase are oxygen and argon. Molar percentages of O_2 and Ar left in the gas phase are higher for the Cranfield setting than for the Frio setting. Calcite dissolution does not seem to have obvious impacts on major gas compositions (CO_2, O_2, and Ar). Figure 18 shows molar percentages of trace gases left in the gas phase, less than 0.003%. For example, CO and SO_2 have been depleted from the gas phase (Figure 19a and b). Most likely CO dissolves into brine and further is oxidized into bicarbonate according to the following reaction,

$$CO_{(g)} + H_2O + 0.25\ O_2 \leftrightarrow H^+ + HCO_3^- \quad (12)$$

Oxidation of CO in the high-PT could proceed kinetically in natural environments. However, in this study all geochemical reactions are simulated based on the equilibrium assumption. Since dissolved oxygen is present in brine, a very strong oxidant, SO_3^{2-}, product of SO_2 dissolution in brine (Eq. 1) is almost completely oxidized into SO_4^{2-} by dissolved oxygen, following the reaction by

$$O_2 + 2SO_3^{2-} \leftrightarrow 2SO_4^{2-} \quad (12)$$

Other gases, such as HCl, N_2, NO, and NO_2 are present in the gas phase at a trace level (Figure 19b).

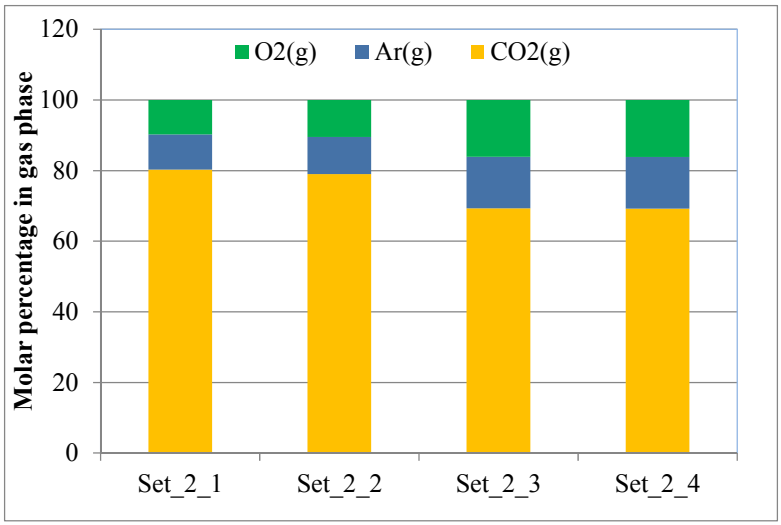

Figure 18. Molar percentage of O_2, Ar, and CO_2 in the gas phase after reacted with brine simulated in the four runs (Table 4).

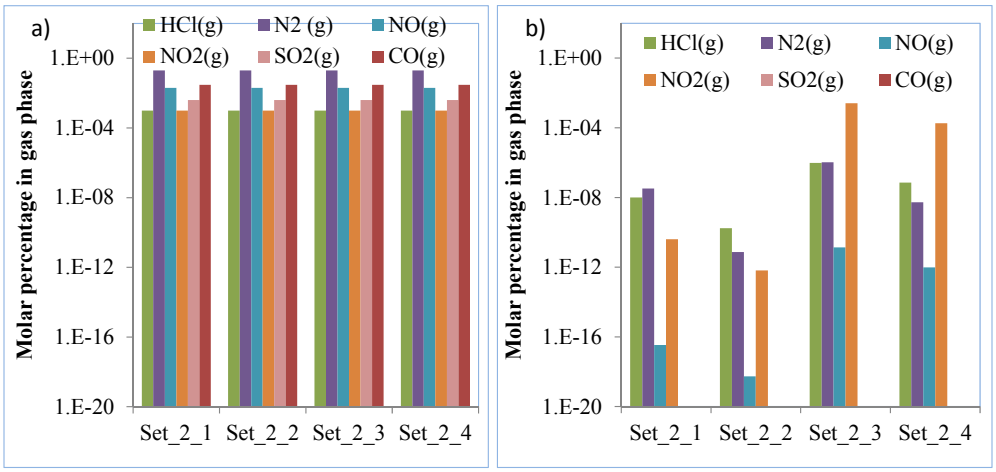

Figure 19. Molar percentage of HCl, N_2, NO, NO_2, SO_2, CO in the gas phase a) before and b) after reacting with the brine simulated in the four runs (Table 4).

Simulated brine pH is similar for both the Frio and Cranfield settings without considering calcite as a buffer. There are about 2 units of difference in pH for the Frio setting and one unit of difference in pH for the Cranfield setting with and without considering calcite as buffer (Figure 20). Brine Eh varies slightly from 0.9 to 1.05 probably because brine Eh is dominated by dissolved oxygen in brine (Figure 20).

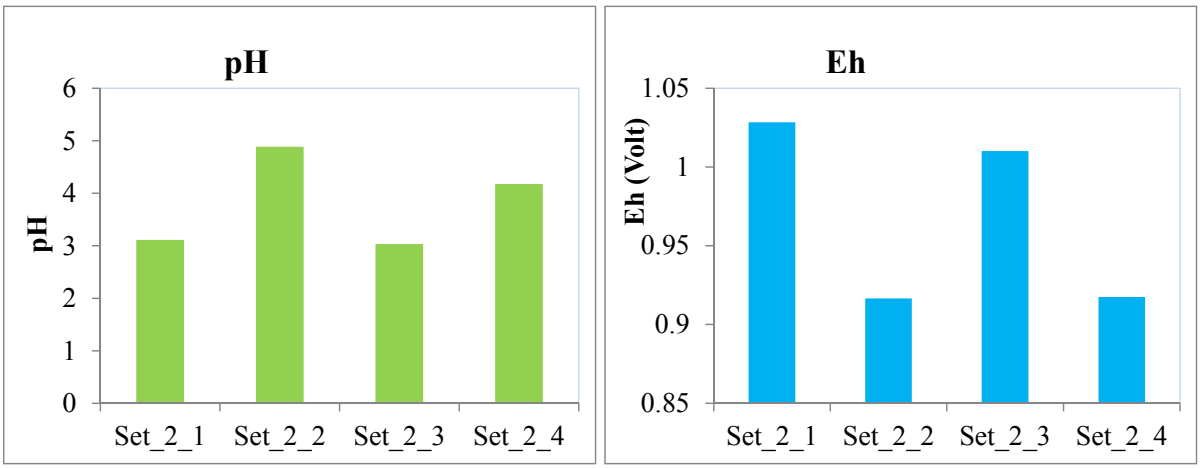

Figure 20. Brine pH (left) and Eh (right) simulated for the four runs (Table 4).

Figure 21a shows distribution of nitrogen species in brine simulated in the four runs. Obviously, NO_3^- is the dominant species in brine and dissolved N_2 holds the second place. Other nitrogen species, such as NO_2^-, NH_3 are at the trace level. Among sulfur species, SO_4^{2-} is dominant species. Most of other sulfur species are not present in brine, suggesting that SO_2 in the CO_2 stream is almost completely oxidized to SO_4^{2-} (Figure 21b). Since brine Eh shows mild oxidizing condition, Fe^{3+} is the dominant iron species in the brine (Figure 21c). Most Fe^{2+} is oxidized into Fe^{3+} for the Frio setting, but not for the Cranfield setting (Figure 21c). Dissolved Ar and O_2 in brine are higher for the Cranfield setting than for the Frio setting, most probably due to the higher pressure of the Cranfield setting (Figure 21d).

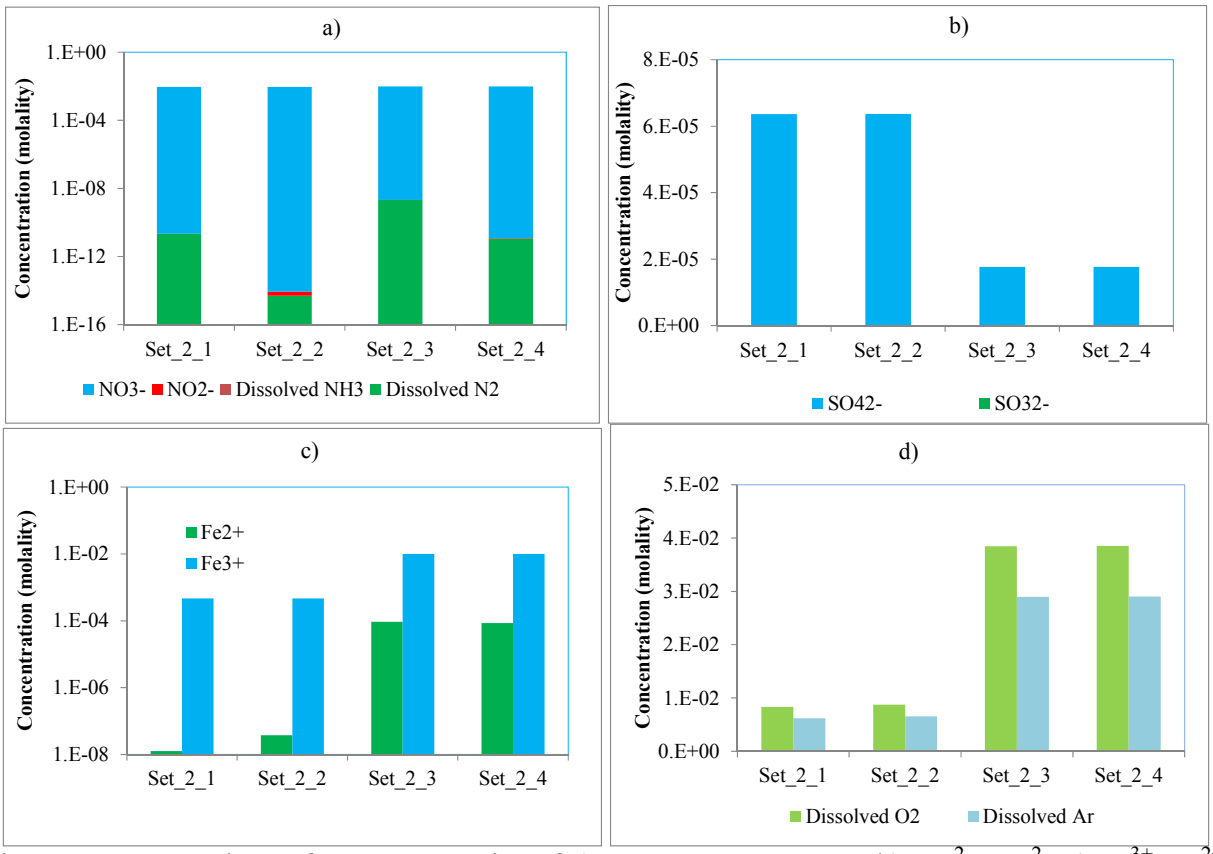

Figure 21. Comparison of aqueous species of a)NO_3^-, NO_2^-, NH_3, N_2, b)SO_4^{2-},SO_3^{2-}, c) Fe^{3+}, Fe^{2+} and d) dissolved O_2 and Ar in brine simulated in the four runs.

IX-3. Proposed future work

Preliminary results of two sets of batch models to evaluate impacts of impurities in the CO_2 stream on brine chemistry for the Frio and Cranfield settings have been presented in the current study. However, due to limitations of the current models, further improvements are needed.

1) The numerical models present in this study need to be calibrated with experimental data either from the literature or the experiments which are being conducted by the BEG team.
2) Phreeqc simulates the gas phase which follows the ideal gas law. Although gas fugacity of the CO_2 stream is calculated from the reservoir pressure and temperature with Winprop and then taken as input to PHREEQC, the equilibrium of the liquid and vapor (gas phase) may not be reached. An improved thermodynamic model which can consider liquid and vapor (including those impurities) as a whole system is needed.
3) Interactions of brine and the CO_2 stream with impurities were simulated with batch models that neglect the transport process of the fluids (brine and the CO_2 stream injected.) Transport models may provide better simulations of interactions of brine and the CO_2 stream injected in the storage formations.
4) Interactions of brine and the CO_2 stream with the aquifer sediments are simplified in the batch model by considering whether a reactive mineral, calcite, is present as a buffer in the sediments. Improved models should consider most reactive minerals, including silicate minerals. Mineral reactions in the improved model should be simulated based on kinetics, rather than assuming equilibrium.

5) Acid gases can potentially change brine to oxidizing conditions, and therefore may accelerate corrosion of the steel tubings of the injection wells. Assessing the corrosion potential of such a brine on tubing and other steel parts will require improved numerical models.

IX-4. References

CMG, 2011. WinProp User's Guide – Version 2011. Computer Modelling Group Ltd, Calgary.

Lu, J. et al., 2012. CO_2–rock–brine interactions in Lower Tuscaloosa Formation at Cranfield CO2 sequestration site, Mississippi, U.S.A. Chemical Geology, 291: 269-277.

Parkhurst, D.L., Appelo, C.A.J., 1999. User's guide to phreeqc (version 2)— a computer program for speciation, batch-reaction, one-dimensional transport, and inverse geochemical calculations. Water-Resources Investigations Report 99-4259, U.S. Geological Survey

Xu, T., Kharaka, Y.K., Doughty, C., Freifeld, B.M., Daley, T.M., 2010. Reactive transport modeling to study changes in water chemistry induced by CO_2 injection at the Frio-I Brine Pilot. Chemical Geology, 271(3–4): 153-164.

IX-5. WINPROP and PHREEQC Input Files

Input file of WINPROP for Set_2_1

```
**FILE NAME:     Frio_CO2_mixture_Frio.dat
*FILENAMES *OUTPUT *SRFOUT *REGLUMPSPLIT *NONE *GEMOUT *NONE
         *STARSKV *NONE *GEMZDEPTH *NONE *IMEXPVT *NONE
*WINPROP     2011.10

**=-=-=Titles/EOS/Units
**REM     Impurities calculation
*TITLE1 ''
*TITLE2 ''
*TITLE3 ''
*UNIT *FIELD
*INFEED *MOLE
*MODEL *PR *1978

**=-=-=Component Selection/Properties
**REM
*NC 16 16

*COMPNAME
'CO2'  'NH3'  'Ar'  'HCN'  'SO3'
'HCl'  'NO2'  'CO'  'H2'  'NO'
'SO2'  'O2'  'H2O'  'N2'  'H2S'
'CH4'

*HCFLAG
3  0  0  0  0
0  0  0  0  0
0  0  2  0  4
1

*PCRIT
72.8  111.324944  48.34  50.0  81.0
81.5001234  99.9950654  34.54  12.93  63.95
77.77  49.741  217.6  33.5  88.2
45.4

*TCRIT
304.2  405.55  150.86  456.7  490.0
```

324.55 430.95 132.92 33.19 180.15
430.75 154.58 647.3 126.2 373.2
187.315

*AC
0.225 0.25 1.0e-006 0.407 0.422
0.1274 0.588 0.04816 0.21599 0.58294
0.24538 0.02218 0.344 0.04 0.1
0.008

*MW
44.01 17.03056 39.948 27.03 80.066
36.46094 46.0055 28.01 2.016 30.0
64.06 32.0 18.015 28.013 34.08
16.043

*VSHIFT
-0.09434672 -1.0 -1.0 0.0 -1.0
-1.0 -1.0 -0.12839472 -0.183709952 -0.12416
-0.05168032 -0.119904 -0.14966408 -0.128388336 -0.11547776
-0.153860496

*ZRA
0.2736 0.2203020645 0.290499915 0.1865512678 0.3956938997
0.3561252501 0.3565942877 0.2864064 0.27214085 0.2409501
0.3884241426 0.2886147 0.2338 0.2905 0.2851
0.2876

*VCRIT
0.094 0.08048919007 0.07439493898 0.1918093191 0.1264010135
0.09139042719 0.08506079479 0.09043812379 0.05732924614 0.05569714176
0.122555914 0.07360158433 0.056 0.0895 0.0985
0.099

*VISVC
0.094 0.08048919007 0.07439493898 0.1918093191 0.1264010135
0.09139042719 0.08506079479 0.09043812379 0.05732924614 0.05569714176
0.122555914 0.07360158433 0.056 0.0895 0.0985
0.099

*OMEGA
0.4572355289 0.4572355289 0.4572355289 0.4572355289 0.4572355289
0.4572355289 0.4572355289 0.4572355289 0.4572355289 0.4572355289
0.4572355289 0.4572355289 0.4572355289 0.4572355289 0.4572355289
0.4572355289

*OMEGB
0.0777960739 0.0777960739 0.0777960739 0.0777960739 0.0777960739
0.0777960739 0.0777960739 0.0777960739 0.0777960739 0.0777960739
0.0777960739 0.0777960739 0.0777960739 0.0777960739 0.0777960739
0.0777960739

*SG
0.818 0.7472276887 0.2110284681 0.6833403985 0.8373993717
0.54365135 0.7739933441 0.1687981166 0.03011300029 0.2741672439
0.7232396172 0.2181727697 1.0 0.809 0.801
0.3

*TB
-109.21 -71.48458148 -303.0717856 42.00103316 39.67839014
-136.8065296 -38.42856034 -314.9227165 -420.3967084 -279.255268
-20.94996578 -299.7406171 212.0 -320.35 -76.63
-258.61

*PCHOR
78.0 42.97062086 114.1211861 74.29953402 233.1099384
103.4441559 132.5414517 77.34626778 4.897261363 83.52
186.4856961 89.7072 52.0 41.0 80.1
77.0

```
*ENTHALPY
4.77805  0.114433  0.000101132  -2.6494e-008  3.4706e-012  -1.314e-016
0.0  -0.06502081025  0.0003410195022  -5.131e-008  0.0  0.0
0.0  0.3575542165  0.000238114619  -5.131e-008  0.0  0.0
0.0  -0.07391684046  0.0004533042157  -7.157365e-008  0.0  0.0
0.0  -0.07274518543  0.0003340878252  -5.131e-008  0.0  0.0
0.0  0.007846577209  0.0003972212148  -5.250445e-008  0.0  0.0
0.0  -0.06709161206  0.0003391922533  -5.131e-008  0.0  0.0
0.0  0.5065427789  -2.395061e-005  -5.131e-008  0.0  0.0
0.0  2.696429775  -0.0174560112  -5.131e-008  0.0  0.0
0.0  0.2254721244  0.0003720103908  -5.131e-008  0.0  0.0
0.0  -0.0742397428  0.0003945658997  -6.153405e-008  0.0  0.0
0.0  0.3398138702  0.0002614768298  -5.131e-008  0.0  0.0
-2.46342  0.457392  -5.2512e-005  6.4549e-008  -2.02759e-011  2.3631e-015
-0.68925  0.253664  -1.4549e-005  1.2544e-008  -1.7106e-012  -8.239e-017
-0.61782  0.238575  -2.4457e-005  4.1067e-008  -1.30126e-011  1.44852e-015
-5.58114  0.564834  -0.000282973  4.17399e-007  -1.525576e-010  1.958857e-014

*HEATING_VALUES
0.0  0.0  0.0  0.0  0.0
0.0  0.0  0.0  0.0  0.0
0.0  0.0  0.0  0.0  0.0
844.2900105

*IDCOMP
1  -19  -20  -10  -11
-12  -13  -14  -15  -16
-17  -18  59  2  0
3

*VISCOR   *HZYT
*MIXVC   1.0

*VISCOEFF
0.1023  0.023364  0.058533  -0.040758  0.0093324
*HREFCOR   *HARVEY

*PVC3    1.2

*BIN
0.0
0.0  0.0
0.0  0.0  0.0
0.0  0.0  0.0  0.0
0.0  0.0  0.0  0.0  0.0
0.0  0.0  0.0  0.0  0.0
0.0
-0.03  0.0  0.0  0.0  0.0
0.0  0.0
-0.1622  0.0  0.0  0.0  0.0
0.0  0.0  0.09
0.0  0.0  0.0  0.0  0.0
0.0  0.0  0.0  -0.03
0.046  0.0  0.0  0.0  0.0
0.0  0.0  0.0  0.0  0.0
0.114  0.0  0.0  0.0  0.0
0.0  0.0  0.0  0.0  0.0
0.0
0.2  0.0  0.0  0.0  0.0
0.0  0.0  0.2  0.563  0.0
0.0  0.0
-0.02  0.0  0.0  0.0  0.0
0.0  0.0  0.012  -0.03  0.0
0.08  -0.0119  0.275
0.096  0.0  0.0  0.0  0.0
0.0  0.0  0.0544  0.1  0.0
0.0  0.0  0.12  0.176
0.103  0.0  0.0  0.0  0.0
0.0  0.0  0.03  0.016  0.0
0.1356  0.05  0.4907  0.031  0.08
```

```
*SALINITY   *MOLAL    0.2

**=-=-=Composition
**REM
**COMPONENT ARRAY
*COMPOSITION   *PRIMARY
95.944  0.0  1.7  0.0  0.0
0.001  0.001  0.03  0.0  0.02
0.004  2.1  0.0  0.2  0.0
0.0

**COMPONENT ARRAY
*COMPOSITION   *SECOND
0.0  0.0  0.0  0.0  0.0
0.0  0.0  0.0  0.0  0.0
0.0  0.0  100.0  0.0  0.0
0.0

**=-=-=OGW/EOS Multiphase Flash
*FLASH
**NC 16 16
*LABEL    'Test'
*FEED  *MIXED 1.0
*KVALUE  *INTERNAL
*LEVEL 4
*OUTPUT 1
*TYPE  *GENERAL 3
*PRES 1500.0
*TEMP 138.2
*DELP 0.0
*DELT 0.0
*STEPP 1
*STEPT 1
*DELZ 0.0
*STEPZ 1

**=-=-=    END
```

Input file of PHREEQC for SET_2_1

```
SOLUTION 1
   temp      59
   pH        6.7
   redox     Fe(2)/Fe(3)
   units     mol/kgw
   density   1.1
   Ca        0.066 Calcite    0
   Mg        0.022
   Na        1.35
   K         0.00453
   Fe        0.000463
   Si        0.00025
   S         4.2e-005
   C         0.0104
   Cl        1.49
   O(0)      4.88e-068
   Al        1.56e-008
   -water    1.0  # kg


GAS_PHASE 1
   -fixed_pressure
   -pressure 69.33975
   -volume 0.3931
   -temperature 59
   CO2(g)    63.718822
   CO(g)     0.041728539
   Ar(g)     2.32881371
```

```
   HCl(g)    0.00067502
   N2(g)     0.28799985
   O2(g)     2.928967582
   NO(g)     0.03092965
   NO2(g)    0.00038248
   SO2(g)    0.001428829

SELECTED_OUTPUT
       -file  Frio_CO2_mixture.sel
#       -pe             false
            -totals         Fe N S C Fe(2) Fe(3) N(0) N(-3) N(3) N(5) S(4) S(6) O(0) Ar C(2) C(4)
USER_PUNCH
  -head CO2 CO2mas No  SI_NO2(g)
 100 PUNCH  mol("CO2"), GAS("CO2(g)"),Gas("NO2(g)"), SI("NO2(g)") SI("N2(g)")
               END
```

Input file of PHREEQC for SET_2_2

```
SOLUTION 1
   temp      59
   pH        6.7
   redox     Fe(2)/Fe(3)
   units     mol/kgw
   density   1.1
   Ca        0.066 Calcite    0
   Mg        0.022
   Na        1.35
   K         0.00453
   Fe        0.000463
   Si        0.00025
   S         4.2e-005
   C         0.0104
   Cl        1.49
   O(0)      4.88e-068
   Al        1.56e-008
   -water    1.0  # kg

EQUILIBRIUM_PHASES 1
   Calcite   0 1.13773   # porosity=0.34, water+gas=1.3931L. VoulmeRock=2.2116 L
                    # V_calcite=0.019, Mass_calcite=2.74288*0.019*2.71*1000=113.8754g=1.13773 moles

GAS_PHASE 1
   -fixed_pressure
   -pressure 69.33975
   -volume 0.393129
   -temperature 59
   CO2(g)    63.718822
   CO(g)     0.041728539
   Ar(g)     2.32881371
   HCl(g)    0.00067502
   N2(g)     0.28799985
   O2(g)     2.928967582
   NO(g)     0.03092965
   NO2(g)    0.00038248
   SO2(g)    0.001428829

SELECTED_OUTPUT
       -file  Frio_CO2_mixture_rock.sel
#       -pe             false
       -totals         Fe N S C Fe(2) Fe(3) N(0) N(-3) N(3) N(5) S(4) S(6) O(0) Ar C(2) C(4)
USER_PUNCH
  -head CO2 CO2mas No  SI_NO2(g)
 100 PUNCH  mol("CO2"), GAS("CO2(g)"),Gas("NO2(g)"), SI("NO2(g)") SI("N2(g)")
END
```

X. Appendix E: Reactive Transport Modeling PHREEQC Input file

by Changbing Yang

```
SOLUTION 0
   temp      60
   pH        3.83
   pe        14.868
   redox     pe
   units     mol/kgs
   density   1
   Mg        0.002657
   Ca        0.0006894
   Cl        0.2023
   Na        0.2024
   C(4)      1.259
   Fe        1.109e-005
   Br        0.00001
   Al        1e-008
   Si        4.21E-04
   O(0)      8.752e-003
   -water    1 # kg

SOLUTION 1-100
   temp      60
   pH        7.3
   pe        -2.774
   redox     pe
   units     mol/kgs
   density   1
   Mg        2.657e-003
   Ca        6.894e-004
   Cl        2.023e-001
   Na        2.024e-001
   C(4)      7.172e-003
   Fe        1.095e-005
   Al        1.0e-8
   Si        4.21E-04
   -water    1 # kg

KINETICS 1-100
-cvode
Quartz
       -parms 1.023e-14
       -m0 173.4043047      # moles in rocks
       -m  173.4043047
Kaolinite
       -parms 6.918e-14 4.898e-12  8.913e-18
       -m0 5.640438449
       -m  5.640438449
Illite
       -parms 1.660e-13 1.047e-11 3.020e-17
```

```
        -m0 2.370629705
        -m  2.370629705
Albite
        -parms 1.445e-12 2.138e-10
        -m0  1.334865
        -m    1.334865
K-feldspar
        -parms 3.89e-13 8.71e-11 6.31e-22
        -m0 2.112796887
        -m  2.112796887
Siderite
        -parms 1.26e-9 1.59e-4
        -m0 1.087677022
        -m  1.087677022
Pyrite
         -parms   2.81838e-5  3.01995e-8       # neutral and acid
  #       -parms 6.45654E-09     # 2.81838e-5
         -m0 0.233393961
         -m  0.233393961
Dawsonite
        -parms 1.26e-9 1.59e-4
        -m0 0.0
        -m  0.0
Magnesite
        -parms 4.571e-10 4.169e-7
        -m0 0.0
        -m  0.0
Dolomite
        -parms 2.951e-8 6.457e-4
        -m0 0.0
        -m  0.0

INCREMENTAL_REACTIONS true

RATES
Quartz
-start
  40  SR_Qu = SR("Quartz")
  45  if (M <= 0 and SR_Qu < 1) then goto 200
  50  k1 = exp(-87.7e3/8.314472*(1/TK - 1/298.15))
  52  SA = 0.01
  55  rate = SA*PARM(1) * (M/M0)^0.67 * (1 - SR_Qu)
  60  moles=rate*TIME
  70  PUT(rate,1)
  200 SAVE moles
-end

Kaolinite
 -start
  40  SR_kao = SR("Kaolinite")
  45  if (M <= 0 and SR_kao < 1) then goto 200
  50  ek1 = exp(-87.7e3/8.314472*(1/TK - 1/298.15))
  52  ek2 = exp(-65.9e3/8.314472*(1/TK - 1/298.15))
  54  ek3 = exp(-17.9e3/8.314472*(1/TK - 1/298.15))
  56  SA = 0.01
  60  r1=ek1*PARM(1)
```

```
  65  r2=ek2*PARM(2)*act("H+")^.777
  67  r3=ek3*PARM(3)*act("H+")^-.472
  70  rate = SA*(M/M0)^0.67 *(1 - SR_kao)*(r1+r2+r3)
  80  moles=rate*TIME
  90  PUT(rate,2)
  200 SAVE moles
 -end

Illite
 -start
  40  SR_Il = SR("Illite")
  45  if (M <= 0 and SR_Il < 1) then goto 200
  50  ek1 = exp(-35e3/8.314472*(1/TK - 1/298.15))
  52  ek2 = exp(-23.6e3/8.314472*(1/TK - 1/298.15))
  54  ek3 = exp(-58.9e3/8.314472*(1/TK - 1/298.15))
  56  SA = 0.01
  60  r1=ek1*PARM(1)
  65  r2=ek2*PARM(2)*act("H+")^.34
  67  r3=ek3*PARM(3)*act("H+")^-.4
  70  rate = SA*(M/M0)^0.67 *(1 - SR_Il)*(r1+r2+r3)
  80  moles=rate*TIME
  90  PUT(rate,3)
  200 SAVE moles
 -end

Albite
 -start
  40  SR_og = SR("Albite")
  45  if (M <= 0 and SR_og < 1) then goto 200
  50  ek1 = exp(-69.8e3/8.314472*(1/TK - 1/298.15))
  52  ek2 = exp(-65.0e3/8.314472*(1/TK - 1/298.15))
 # 54  ek3 = exp(-58.9e3/8.314472*(1/TK - 1/298.15))
  56  SA = 0.01
  60  r1=ek1*PARM(1)
  65  r2=ek2*PARM(2)*act("H+")^.457
#  67  r3=ek3*PARM(3)*act("H+")^-.4
  70  rate = SA*(M/M0)^0.67 *(1 - SR_og)*(r1+r2)
  80  moles=rate*TIME
  90  PUT(rate,4)
  200 SAVE moles
 -end

K-feldspar
 -start
  40  SR_Kf = SR("K-feldspar")
  45  if (M <= 0 and SR_Kf < 1) then goto 200
  50  ek1 = exp(-38.0e3/8.314472*(1/TK - 1/298.15))
  52  ek2 = exp(-51.7e3/8.314472*(1/TK - 1/298.15))
  54  ek3 = exp(-94.1e3/8.314472*(1/TK - 1/298.15))
  56  SA = 0.01
  60  r1=ek1*PARM(1)
  65  r2=ek2*PARM(2)*act("H+")^.5
  67  r3=ek3*PARM(3)*act("H+")^-.4
  70  rate = SA*(M/M0)^0.67 *(1 - SR_Kf)*(r1+r2+r3)
  80  moles=rate*TIME
  90  PUT(rate,5)
```

```
  200 SAVE moles
 -end

Siderite
 -start
  40  SR_si = SR("Siderite")
#  45  if (M <= 0 and SR_si < 1) then goto 200
  50  ek1 = exp(-62.76e3/8.314472*(1/TK - 1/298.15))
  52  ek2 = exp(-45.0e3/8.314472*(1/TK - 1/298.15))
  56  SA = 0.01
  60  r1=ek1*PARM(1)
  65  r2=ek2*PARM(2)*act("H+")^0.9
  70  rate = SA*(1 - SR_si)*(r1+r2)
  80  moles=rate*TIME
  90  PUT(rate,6)
  200 SAVE moles
 -end

Pyrite    # Pandera and Kharaka
  -start
  40  SR_py= SR("Pyrite")
  45  if (M <= 0 and SR_py < 1) then goto 200
  50  ek1 = exp(-56.9e3/8.314472*(1/TK - 1/298.15))
  52  ek2 = exp(-56.9e3/8.314472*(1/TK - 1/298.15))
  56  SA = 0.01
  60  r1=ek1*PARM(1)*act("O2")^.5
  65  r2=ek2*PARM(2)*act("H+")^-0.5*act("Fe+3")^0.5
  70  rate = SA*(1 - SR_py)*(r1+r2)
  80  moles=rate*TIME
  90  PUT(rate,7)
  200 SAVE moles
  -end

Dawsonite
 -start
  40  SR_da= SR("Dawsonite")
 # 45  if (M <= 0 and SR_da < 1) then goto 200
  50  ek1 = exp(-62.76e3/8.314472*(1/TK - 1/298.15))
  52  ek2 = exp(-45.0e3/8.314472*(1/TK - 1/298.15))
  56  SA = 0.01
  60  r1=ek1*PARM(1)
  65  r2=ek2*PARM(2)*act("H+")^0.9
  70  rate = SA*(1 - SR_da)*(r1+r2)
  80  moles=rate*TIME
  90  PUT(rate,8)
  200 SAVE moles
 -end

Magnesite
 -start
  40  SR_Ma = SR("Magnesite")
 # 45  if (M <= 0 and SR_Ma < 1) then goto 200
  50  ek1 = exp(-23.5e3/8.314472*(1/TK - 1/298.15))
  52  ek2 = exp(-14.4e3/8.314472*(1/TK - 1/298.15))
  56  SA = 0.01
  60  r1=ek1*PARM(1)
```

```
 65  r2=ek2*PARM(2)*act("H+")
 70  rate = SA*(1 - SR_Ma)*(r1+r2)
 80  moles=rate*TIME
 90  PUT(rate,9)
 200 SAVE moles
-end

Dolomite
 -start
 40  SR_do = SR("Dolomite")
 # 45  if (M <= 0 and SR_do < 1) then goto 200
 50  ek1 = exp(-52.2e3/8.314472*(1/TK - 1/298.15))
 52  ek2 = exp(-36.1e3/8.314472*(1/TK - 1/298.15))
 56  SA = 0.01
 60  r1=ek1*PARM(1)
 65  r2=ek2*PARM(2)*act("H+")^0.5
 70  rate = SA*(1 - SR_do)*(r1+r2)
 80  moles=rate*TIME
 90  PUT(rate,10)
 200 SAVE moles
-end

TRANSPORT
      -cells          100   #  total length = cells X length
      -length          1.0  # total depth = 100x1.0=100m
      -shifts         200     # =
      -time_step       3.1536e+8 # in seconds
      -flow_direction  forward
      -boundary_cond   flux    flux
      -diffc           1.0e-10
      -dispersivity    1.0   # (m)
      -correct_disp    true
      -punch_cells     1 50 100
      -punch_frequency 1
      -print_cells     1-100
      -print_frequency 1

SELECTED_OUTPUT
      -file  O_run2-spt.sel
      -pe             true
      -totals          Br Ca Mg Na K Si C(4) Al Fe O(0) Fe(3)  Fe(2) S(6)
      -si  O2(g) CO2(g) Quartz Kaolinite Illite Albite K-Feldspar siderite pyrite Dawsonite Magnesite Dolomite
       -kinetic_reactants  Quartz Kaolinite Illite Albite K-Feldspar siderite pyrite Ankerite Dawsonite  Magnesite
Dolomite
 #PRINT
 #       -reset false
USER_PUNCH
  -head     molo2      actFe+3
 100 PUNCH  mol("O2")  act("Fe+3")
END
```

XI. Appendix F: Result Tables

This section presents results from chemical analyses of the solutions in contact with the rock samples through time. Series letters refer to Table 6 and Table 8. The “Trace Elements” group, which is actually ICP-MS measurements, also provides major cation composition. “Major ions” group, except Na and Cl, were measured using IC.

Blue shaded boxes are below the detection limits and the results are not usable. Detection limits are more than a function of the sensitivity of the ICP-MS device; it also depends on the amount of dilution achieved to go from a brine to aqueous concentrations within the calibrated analytical range. Orange shaded boxes are above the calibration range of the ICP-MS and are also suspect.

XI-1. Analytical Results

Offshore Miocene series

Major ions (IC):

Exploratory and sensitivity experiments:

Sample	Reaction time (hrs)	Li (ppm)	Na (ppm)	NH4 (ppm)	K (ppm)	Mg (ppm)	Ca (ppm)	F (ppm)	Cl (ppm)	NO2 (ppm)	Br (ppm)	NO3 (ppm)	PO4 (ppm)	SO4 (ppm)	Alk. (ppm)
A series: CO_2 – 100°C – Miocene – DI water															
A-1	-100.6		27.749		1.850	2.578	25.269								
A-2	-73.0														
A-3	-4.8														
A-4	16.2	1.639	39.981		2.687	13.178	326.860								
A-5	40.4														
A-6	48.2														
A-7	65.2														
A-8	72.7	1.866	39.576		2.319	10.243	388.315								
A-9	87.3														
A-10	117.2														
A-11	139.9		44.423	1.375	4.876	11.859	452.490								
A-12	167.6														
A-13	192.2														
A-14	214.9		43.054	0.936	6.009	14.957	544.953		29.161					12.314	
A-15	264.8		45.868	1.015	6.434	15.214	548.208		30.352			1.250		12.847	
A-16	338.2		44.500	1.213	7.053	15.702	557.290		31.819			1.233		12.904	
A-17	375.8	0.065	55.903	1.156	8.108	17.968	623.938		38.067	1.739		1.739		15.733	
A-18	425.8		44.673	1.556	8.770	18.242	625.975		40.666					16.064	
B series: CO_2 – 100°C – Miocene															
B-1	-75.8	0.0	35909	0.0	0.0	0.0	0.0	0.4	26163	0.0	81.2	3.3	19.2	13.2	
B-2	-21.9	0.0	40279	0.0	9.2	5.6	82.3	0.0	28675	0.0	84.1	0.0	0.0	33.4	
B-3	-0.8	0.0	41177	0.0	9.7	9.5	103.5	0.0	28544	0.0	86.0	0.0	0.0	36.5	
B-4	2.2	0.0	42080	0.0	10.2	12.9	106.3	0.0	28753	0.0	87.6	0.0	25.2	37.5	
B-5	6.0	0.0	38163	0.0	14.3	14.3	407.8	1.8	27107	0.0	78.5	0.0	28.5	37.2	
B-6	30.9	0.0	37840	0.0	9.9	17.1	530.9	0.0	27156	0.0	78.8	0.0	26.4	38.1	

Sample	Reaction time (hrs)	Li (ppm)	Na (ppm)	NH4 (ppm)	K (ppm)	Mg (ppm)	Ca (ppm)	F (ppm)	Cl (ppm)	NO2 (ppm)	Br (ppm)	NO3 (ppm)	PO4 (ppm)	SO4 (ppm)	Alk. (ppm)
B-7	29.3	0.0	38823	0.0	10.7	18.3	737.5	0.0	27719	0.0	82.2	0.0	0.0	39.7	
B-8	43.9	0.0	35606	0.0	10.0	17.5	739.7	0.0	24465	0.0	69.0	3320.3	27.6	34.7	
B-9	51.4	0.0	36362	0.0	10.5	18.4	804.7	0.0	25463	0.0	69.9	3697.4	31.4	34.3	
B-10	71.5	0.0	36497	0.0	10.6	18.7	817.6	0.0	25259	0.0	69.7	3371.1	32.5	36.9	
B-11	148.0	0.0	36252	0.0	10.8	18.9	844.1	0.0	25276	0.0	69.7	4786.9	31.6	36.6	
B-12	165.2	0.1	34854	0.0	10.7	18.7	840.9	0.0	24352	0.0	69.0	4964.8	31.3	36.5	
B-13	235.9	0.0	37243	0.0	11.7	20.1	909.6	0.0	25139	0.0	73.5	3482.0	28.0	38.0	
B-14	265.5	0.1	37620	0.0	12.1	20.4	914.3	0.0	25704	0.0	72.7	4709.6	36.3	39.8	
C series: O_2+CO_2 – 100°C – Miocene															
C-1	-44.1	0.02	37031	0.00	4.09	1.78	33.62	0.00	25159	0.00	73.69	2122.67	44.62	22.55	
C-2	-27.9	0.02	36987	0.00	6.76	5.92	97.68	0.00	25577	0.00	71.55	2657.42	30.38	34.15	
C-3	-3.9	0.02	38561	0.00	7.99	10.74	124.79	0.00	26308	0.00	74.99	4000.57	33.03	35.31	
C-4	2.2	0.02	39931	0.00	8.74	12.12	229.85	0.00	27727	0.00	80.49	4603.10	45.26	41.92	
C-5	3.8	0.03	38423	0.00	8.71	13.47	273.74	0.00	26057	0.00	76.01	3424.13	41.08	41.29	
C-6	6.2	0.03	39889	0.00	9.84	16.73	364.26	0.00	27151	0.00	78.83	4155.82	28.92	44.32	
C-7	8.3	0.03	39178	0.00	9.37	17.59	394.10	0.00	26547	0.00	77.59	4626.65	41.94	46.10	
C-8	19.8	0.03	40185	0.00	10.49	23.46	568.59	0.00	26364	0.00	78.82	1462.42	23.34	48.49	
C-9	48.9	0.04	40945	0.00	11.99	28.01	742.35	0.00	27132	0.00	80.90	2533.64	23.33	58.84	
C-10	92.1	0.04	41148	0.00	13.46	29.05	819.35	0.00	27325	0.00	83.25	3003.63	32.99	64.92	
C-11	188.2	0.10	42653	0.00	16.16	31.28	864.69	0.00	27056	0.00	83.15	2078.85	37.64	71.48	
C-12	242.4	0.06	42661	0.00	17.13	30.72	829.63	0.00	28685	0.00	85.95	4800.77	40.00	75.05	
C-13	259.3	0.05	44758	0.00	17.85	32.31	863.15	0.00	28479	0.00	88.80	2755.98	32.89	75.43	
E series: CO_2 – 100°C – 300 bars - Miocene															
E-1	-77.50	0.02	40,044	0.00	10.57	5.27	99.60	0.00	26,431	0.00	73.60	4331	0.00	49.32	
E-2	-5.00	0.02	40,133	0.00	11.27	6.80	107.07	0.00	26,275	0.00	73.32	5666	0.00	47.93	209.8
E-3	-0.13	0.03	40,805	0.00	8.72	8.59	207.66	0.00	26,146	0.00	73.87	3472	0.00	52.56	
E-4	2.00	0.03	40,290	0.00	8.96	10.42	292.48	0.00	26,132	0.00	77.15	5515	0.00	53.92	
E-5	3.50	0.03	40,848	0.00	9.23	11.36	354.81	0.00	26,488	0.00	77.27	4272	0.00	54.49	1064
E-6	6.00	0.03	40,845	0.00	9.66	12.23	402.12	0.00	26,544	0.00	75.74	4457	0.00	54.19	
E-7	18.75	0.03	43,012	0.00	11.23	15.09	579.56	0.00	27,451	0.00	79.86	3256	0.00	57.84	1743.8
E-8	26.50	0.03	44,218	0.00	12.12	16.16	645.56	0.00	27,985	0.00	83.96	2728	0.00	61.96	1920.7
E-9	43.50	0.04	45,902	0.00	13.00	17.74	740.37	0.00	29,143	0.00	85.08	3993	0.00	63.96	2148.1
E-10	67.42	0.03	45,620	0.00	13.32	18.40	788.13	0.00	28,771	0.00	86.94	2655	0.00	63.52	2299.8

Sample	Reaction time (hrs)	Li (ppm)	Na (ppm)	NH4 (ppm)	K (ppm)	Mg (ppm)	Ca (ppm)	F (ppm)	Cl (ppm)	NO2 (ppm)	Br (ppm)	NO3 (ppm)	PO4 (ppm)	SO4 (ppm)	Alk. (ppm)
E-11	92.83	0.04	45,440	0.00	13.33	18.92	815.77	0.00	28,237	0.00	82.27	3433	0.00	62.76	2451.4
E-12	162.92	0.05	44,078	0.00	13.83	18.97	828.50	0.00	27,657	0.00	82.63	2979	0.00	61.61	2603
E-13	188.37	0.05	44,951	0.00	13.99	19.47	852.45	0.00	27,910	0.00	83.07	3855	0.00	62.42	2608.1

Experiments from Table 6 matrix:

Sample	Reaction time (hrs)	Li (ppm)	Na (ppm)	NH4 (ppm)	K (ppm)	Mg (ppm)	Ca (ppm)	F (ppm)	Cl (ppm)	NO2 (ppm)	Br (ppm)	PO4 (ppm)	SO4 (ppm)	Alk. (ppm)
D series: CO_2 – 70°C - Miocene														
D-1	-94.42	0.00	***43200***	0.00	1.30	0.17	0.54	0.000	***66600***	0.000	72.736	0.000	5.853	
D-2	-94.42	0.02	***43200***	0.00	5.79	2.47	57.57	0.530	***66600***	0.000	69.361	0.000	45.843	
D-3	-66.50	0.02	***43200***	0.00	6.27	3.87	82.15	0.000	***66600***	0.000	70.807	0.000	46.891	
D-4	-1.75	0.02	***43200***	0.00	6.63	4.98	109.10	0.000	***66600***	0.000	70.285	0.000	48.754	190
D-5	2.25	0.02	***43200***	0.00	6.66	8.04	310.41	0.000	***66600***	0.000	68.939	0.000	48.959	
D-6	4.25	0.02	***43200***	0.00	6.85	9.54	392.25	0.000	***66600***	0.000	71.020	0.000	50.045	
D-7	6.25	0.02	***43200***	0.00	6.83	10.11	433.67	0.000	***66600***	0.000	71.602	0.000	48.049	1213
D-8	8.25	0.02	***43200***	0.00	7.03	10.96	488.67	0.000	***66600***	0.000	70.841	0.000	48.534	1352
D-9	25.75	0.02	***43200***	0.00	7.47	13.24	676.37	0.000	***66600***	0.000	73.264	0.000	51.432	1883
D-10	32.83	0.02	***43200***	0.00	7.47	13.53	714.98	0.000	***66600***	0.000	73.908	0.000	52.746	
D-11	49.75	0.02	***43200***	0.00	7.28	13.64	748.08	0.000	***66600***	0.000	73.895	0.000	54.420	2237
D-12	100.25	0.03	***43200***	0.00	8.22	15.85	878.69	0.000	***66600***	0.000	74.473	0.000	52.797	2603
D-13	166.50	0.03	***43200***	0.00	8.84	17.33	967.16	0.000	***66600***	0.000	77.005	0.000	57.660	2755
D-14	190.50													
D-15	214.25													
R series: O_2+CO_2 – 70°C - Miocene														
R-1	-66.25	0.0	43200	0.0	7.6	1.7	57.2	0.0	66600	0.0	4.459	0.000	67.185	
R-2	-1.25	0.0	43200	0.0	8.5	2.1	64.4	0.0	66600	0.0	6.405	0.000	74.801	184.5
R-3	0.75	0.0	43200	0.0	8.6	2.8	160.3	0.0	66600	0.0	2.993	0.000	70.347	345.4
R-4	4.08	0.0	43200	0.0	8.9	4.1	284.9	0.0	66600	0.0	4.483	0.000	71.611	
R-5	7.00	0.0	43200	0.0	9.2	5.8	438.4	0.0	66600	0.0	3.899	0.000	74.069	1027.1
R-6	22.92	0.0	43200	0.0	9.8	8.5	615.7	0.0	66600	0.0	5.162	0.000	78.793	1334.4
R-7	30.75	0.0	43200	0.0	10.1	9.2	664.9	0.0	66600	0.0	4.077	0.000	84.619	1384.9
R-8	46.92	0.0	43200	0.0	10.5	10.6	736.0	0.0	66600	0.0	4.171	0.000	85.699	1718.5

Sample	Reaction time (hrs)	Li (ppm)	Na (ppm)	NH4 (ppm)	K (ppm)	Mg (ppm)	Ca (ppm)	F (ppm)	Cl (ppm)	NO2 (ppm)	Br (ppm)	PO4 (ppm)	SO4 (ppm)	Alk. (ppm)
R-9	54.25	0.0	43200	0.0	10.6	10.7	755.6	0.0	66600	0.0	7.170	0.000	84.541	
R-10	72.25	0.0	43200	0.0	10.5	11.3	775.6	0.0	66600	0.0	6.506	0.000	87.217	1997.5
R-11	100.67	0.0	43200	0.0	11.0	12.6	844.9	0.0	66600	0.0	5.018	0.000	99.302	
R-12	127.25	0.0	43200	0.0	11.5	13.6	904.0	0.0	66600	0.0	4.404	0.000	105.710	2122.8
R-13	168.25	0.1	43200	19.7	12.2	15.3	980.7	0.0	66600	0.0	3.688	0.000	114.587	2216.4
R-14	215.75	0.1	43200	23.8	12.7	16.6	1033.5	0.0	66600	0.0	2.344	0.000	118.557	
R-15	243.25	0.1	43200	27.9	12.7	17.1	1039.2	0.0	66600	0.0	2.511	0.000	122.868	2047
R-16	263.75	0.0	43200	25.2	13.0	17.9	1066.9	0.0	66600	0.0	6.486	0.000	123.703	2375.6
L series: CO_2 – 100°C - Miocene														
L-1	-0.67	0.04	43200	0.00	10.79	3.78	94.45		66600		81.03	0.00	49.86	194.90
L-2	1.00	0.03	43200	0.00	10.58	6.67	212.76		66600		83.09	0.00	49.97	568.60
L-3	3.00	0.04	43200	0.00	10.56	8.77	315.27		66600		80.35	0.00	44.50	846.60
L-4	6.33	0.04	43200	0.00	10.95	10.20	412.47		66600		80.14	0.00	48.02	1112.00
L-5	22.75	0.04	43200	0.00	11.95	13.62	625.09		66600		84.04	0.00	51.85	1731.10
L-6	29.33	0.04	43200	0.00	12.38	14.87	683.00		66600		84.23	0.00	52.11	1844.90
L-7	47.33	0.05	43200	0.00	13.31	16.38	778.67		66600		87.62	0.00	50.65	2097.60
L-8	72.33	0.05	43200	0.00	13.45	17.04	830.13		66600		86.72	0.00	56.83	2325.00
L-9	95.58													2426.10
S series: O_2+CO_2 – 100°C - Miocene														
S-1	-1.1	0.0	43200	0.0	11.9	6.0	117.9		66600		6.2	0.0	62.2	61
S-2	1.2	0.0	43200	0.0	12.0	7.1	181.9		66600		4.7	0.0	60.0	
S-3	2.2	0.0	43200	0.0	12.1	8.1	224.8		66600		5.2	0.0	63.3	310.8
S-4	4.6	0.0	43200	0.0	12.3	9.7	289.4		66600		4.3	0.0	66.1	716
S-5	22.3	0.1	43200	0.0	13.4	17.3	566.5		66600		5.4	0.0	81.5	1137.2
S-6	29.0	0.1	43200	0.0	13.7	18.8	620.3		66600		3.5	0.0	82.0	1432.1
S-7	45.5	0.1	43200	10.3	13.4	21.2	704.5		66600		5.1	0.0	90.8	1440.5
S-8	71.3	0.1	43200	12.9	14.5	25.0	771.7		66600		4.6	0.0	101.2	1478.4
S-9	94.9	0.1	43200	20.1	15.1	28.1	880.3		66600		5.5	0.0	111.3	1819.6
S-10	123.4	0.1	43200	24.7	15.9	30.8	923.8		66600		6.1	0.0	117.1	
S-11	168.8	0.1	43200	53.0	16.3	34.0	999.7		66600		5.0	0.0	133.2	1617.4
S-12	243.1	0.1	43200	111.4	17.5	38.3	1062.2		66600		2.9	0.0	96.7	2198.7
H series: CO_2 – 130°C - Miocene														
H-1	-50.77	0.0	40276	0.0	11.6	1.9	81.0							154.2

Sample	Reaction time (hrs)	Li (ppm)	Na (ppm)	NH4 (ppm)	K (ppm)	Mg (ppm)	Ca (ppm)	F (ppm)	Cl (ppm)	NO2 (ppm)	Br (ppm)	PO4 (ppm)	SO4 (ppm)	Alk. (ppm)
H-2	0.87	0.0	39290	0.0	5.9	2.7	143.2							492.8
H-3	2.28	0.0	38726	0.0	6.8	3.9	193.7							669.7
H-4	5.12	0.0	38322	0.0	7.1	5.3	284.5							821.3
H-5	9.78	0.0	38856	0.0	7.8	6.7	390.3							1124.6
H-6	23.70	0.0	38150	0.0	8.8	8.0	515.6							1453.1
H-7	45.43	0.0	39575	0.0	10.4	9.2	595.7							1630
H-8	117.78	0.0	40933	0.0	13.3	10.3	676.3							1743.8
H-9	141.57	0.1	44857	0.0	15.9	11.9	712.1							1945.9
H-10	169.37	0.1	43563	0.0	15.9	11.4	689.5							2299.8
H-11	193.03	0.0	42730	0.0	16.0	11.0	677.7							2400.8
H-12	217.53	0.0	43178	0.0	16.8	11.2	690.8							2249.2
H-13	288.53	0.0	46577	0.0	20.1	12.4	725.7							2501.9

Major and Trace elements (ICP-MS):

Exploratory and sensitivity experiments:

A series: CO_2 – 100°C – Miocene – DI water

Sample	Reaction time (hrs)	B (ppm)	Mg (ppm)	Al (ppm)	Si (ppm)	P (ppm)	K (ppm)	Ca (ppm)	Ti (ppm)	V (ppm)	Cr (ppm)	Mn (ppm)
A-1	-100.6	5.481	2.790	0.588	13.755	0.070	2.375	31.760	0.009	0.045	0.006	0.010
A-2	-73.0	5.787	4.765	0.666	14.310	0.076	2.816	35.184	0.009	0.055	0.007	0.020
A-3	-4.8	5.817	3.208	0.812	19.140	0.066	2.574	22.980	0.010	0.086	0.005	0.012
A-4	16.2	12.841	13.439	1.563	32.020	0.154	3.975	340.549	0.017	0.341	0.097	1.927
A-5	40.4	10.634	8.519	1.216	23.871	0.097	2.832	315.677	0.014	0.090	0.077	1.631
A-6	48.2	9.074	9.319	1.022	20.829	0.109	3.225	348.808	0.012	0.242	0.069	1.790
A-7	65.2	10.611	9.663	1.227	23.445	0.107	3.198	383.202	0.013	0.271	0.066	1.958
A-8	72.7	11.160	9.899	1.286	23.483	0.127	3.520	388.971	0.013	0.315	0.052	2.002
A-9	87.3	12.970	10.039	1.438	24.397	0.134	3.984	400.674	0.014	0.371	0.058	2.069
A-10	117.2	13.669	11.175	1.530	31.321	0.124	4.281	423.512	0.016	0.350	0.056	2.223
A-11	139.9	18.095	12.338	2.243	27.924	0.157	5.789	459.873	0.012	0.131	0.050	2.450

A-12	167.6	15.957	11.907	1.508	33.679	0.147	5.173	443.927	0.016	0.362	0.045	2.383
A-13	192.2	15.937	12.537	1.541	31.988	0.129	5.432	453.253	0.016	0.361	0.045	2.475
A-14	214.9											
A-15	264.8	10.459	14.487	0.008	39.462	0.045	6.633	291.995	0.009	0.002	0.005	0.330
A-16	338.2	8.904	15.606	0.032	42.053	0.044	7.492	544.082	0.011	0.002	0.031	3.182
A-17	375.8											
A-18	425.8											
A-19	494.8											
A-20	543.3	7.682	19.025	0.647	46.994	0.353	11.524	599.947	0.023	0.014	0.050	3.260
Sample	**Reaction time (hrs)**	**Fe (ppm)**	**Co (ppm)**	**Ni (ppm)**	**Cu (ppm)**	**Zn (ppm)**	**As (ppm)**	**Se (ppm)**	**Rb (ppm)**	**Sr (ppm)**	**Zr (ppm)**	**Mo (ppm)**
A-1	-100.6	0.022	0.000	0.038	0.004	0.028	0.000	0.000	0.006	0.126	0.010	0.463
A-2	-73.0	0.025	0.000	0.052	0.010	0.039	0.000	0.001	0.008	0.184	0.009	0.531
A-3	-4.8	0.019	0.000	0.016	0.004	0.031	0.000	0.000	0.006	0.154	0.011	0.693
A-4	16.2	0.558	0.069	5.732	0.058	0.148	0.002	0.001	0.015	0.976	0.016	0.375
A-5	40.4	0.623	0.066	4.357	0.041	0.080	0.001	0.000	0.012	0.814	0.013	0.242
A-6	48.2	0.503	0.072	4.674	0.041	0.092	0.002	0.000	0.014	0.885	0.009	0.260
A-7	65.2	0.401	0.077	5.182	0.040	0.090	0.002	0.000	0.016	0.979	0.011	0.297
A-8	72.7	0.346	0.077	5.245	0.041	0.109	0.002	0.000	0.017	0.990	0.011	0.297
A-9	87.3	0.259	0.078	5.390	0.040	0.141	0.002	0.000	0.019	1.022	0.014	0.293
A-10	117.2	0.222	0.080	5.538	0.038	0.111	0.002	0.000	0.022	1.089	0.015	0.286
A-11	139.9	0.214	0.086	5.945	0.120	0.168	0.004	0.000	0.025	1.157	0.010	0.265
A-12	167.6	0.205	0.080	5.726	0.047	0.139	0.003	0.000	0.025	1.150	0.014	0.290
A-13	192.2	0.189	0.081	5.903	0.039	0.116	0.004	0.000	0.027	1.186	0.014	0.306
A-14	214.9											
A-15	264.8	0.008	0.021	4.440	0.007	0.009	0.004	0.000	0.031	1.197	0.000	0.268
A-16	338.2	0.015	0.089	6.756	0.030	0.032	0.004	0.000	0.035	1.438	0.002	0.288
A-17	375.8											
A-18	425.8											
A-19	494.8											
A-20	543.3	0.568	0.089	7.337	0.000	-0.041	0.004	0.000	0.049	1.616	0.004	0.314
Sample	**Reaction time (hrs)**	**Ag (ppm)**	**Cd (ppm)**	**Sn (ppm)**	**Sb (ppm)**	**Cs (ppm)**	**Ba (ppm)**	**Ti (ppm)**	**Pb (ppm)**	**Bi (ppm)**	**Th (ppm)**	**U (ppm)**
A-1	-100.6	0.000	0.000	0.001	0.000	0.000	0.044	0.000	0.000	0.215	0.000	0.000
A-2	-73.0	0.000	0.000	0.001	0.000	0.001	0.120	0.000	0.000	0.254	0.000	0.000
A-3	-4.8	0.000	0.001	0.001	0.000	0.000	0.136	0.000	0.000	0.383	0.000	0.000

A-4	16.2	0.000	0.001	0.003	0.000	0.002	1.073	0.001	0.001	1.556	0.000	0.000
A-5	40.4	0.000	0.000	0.002	0.000	0.001	0.857	0.000	0.001	0.420	0.000	0.000
A-6	48.2	0.000	0.000	0.002	0.000	0.001	0.976	0.000	0.001	1.020	0.000	0.000
A-7	65.2	0.000	0.001	0.003	0.000	0.001	1.174	0.000	0.001	1.227	0.000	0.000
A-8	72.7	0.000	0.001	0.003	0.000	0.001	1.244	0.001	0.001	1.430	0.000	0.000
A-9	87.3	0.000	0.001	0.002	0.000	0.001	1.388	0.001	0.001	1.758	0.000	0.000
A-10	117.2	0.000	0.001	0.003	0.000	0.002	1.661	0.001	0.001	1.581	0.000	0.000
A-11	139.9	0.000	0.001	0.003	0.000	0.002	1.924	0.001	0.002	0.648	0.000	0.001
A-12	167.6	0.000	0.001	0.003	0.000	0.002	1.995	0.001	0.001	1.681	0.000	0.001
A-13	192.2	0.000	0.001	0.003	0.000	0.002	2.163	0.001	0.001	1.674	0.000	0.001
A-14	214.9											
A-15	264.8	0.000	0.000	0.001	0.000	0.002	2.069	0.001	0.000	0.002	0.000	0.001
A-16	338.2	0.000	0.001	0.000	0.000	0.002	2.786	0.001	0.001	0.005	0.000	0.001
A-17	375.8											
A-18	425.8											
A-19	494.8											
A-20	543.3	0.002	0.001	-0.007	0.000	0.003	3.098	0.002	-0.001	0.062	0.000	0.002

B series: CO_2 – 100°C – Miocene

Sample	Reaction time (hrs)	B (ppm)	Mg (ppm)	Al (ppm)	Si (ppm)	P (ppm)	K (ppm)	Ca (ppm)	Ti (ppm)	V (ppm)	Cr (ppm)	Mn (ppm)
B-1	-75.8	10.75	4.61	1.49	23.39	0.75	17.00	75.50	0.03	0.27	0.04	0.33
B-2	-21.9	9.43	7.16	1.36	21.05	0.84	15.23	95.63	0.03	0.34	0.01	0.40
B-3	-0.8	8.67	8.42	1.36	20.89	1.73	19.03	96.14	0.03	0.30	0.01	0.45
B-4	2.2	7.80	12.00	1.09	18.38	0.82	24.76	383.31	0.02	0.32	0.55	1.72
B-5	6.0	7.98	13.93	1.04	19.11	0.86	15.50	505.61	0.03	0.15	0.52	2.14
B-6	30.9	8.78	15.57	1.09	22.48	0.86	21.49	683.35	0.02	0.34	0.28	3.01
B-7	29.3	8.23	16.66	1.02	23.43	0.92	20.72	750.82	0.03	0.31	0.24	3.33
B-8	43.9	7.58	18.17	0.81	21.85	0.83	21.19	807.28	0.02	0.27	0.23	3.90
B-9	51.4	7.81	18.09	0.81	20.57	0.97	21.89	816.77	0.02	0.27	0.20	3.81
B-10	71.5	11.04	17.60	1.23	23.21	0.94	17.99	843.85	0.03	0.33	0.25	4.28
B-11	148.0	9.71	15.94	1.13	20.58	0.94	24.02	785.19	0.02	0.36	0.27	4.41
B-12	165.2	8.13	18.88	0.68	18.68	0.85	21.12	880.90	0.02	0.29	0.23	4.47
B-13	235.9	10.22	20.19	0.91	20.80	0.87	26.08	853.96	0.02	0.10	0.26	4.55
B-14	265.5	8.85	21.18	0.79	22.32	0.90	21.68	919.89	0.02	0.08	0.23	4.42

Sample	Reaction time (hrs)	Fe (ppm)	Co (ppm)	Ni (ppm)	Cu (ppm)	Zn (ppm)	As (ppm)	Se (ppm)	Rb (ppm)	Sr (ppm)	Zr (ppm)	Mo (ppm)

B-1	-75.8	0.14	0.00	0.13	0.41	0.15	0.003	0.00	0.05	0.55	0.02	0.56
B-2	-21.9	0.11	0.00	0.11	0.37	0.24	0.001	0.00	0.06	0.61	0.02	0.76
B-3	-0.8	0.22	0.00	0.12	0.38	0.24	-0.001	0.00	0.06	0.63	0.01	0.81
B-4	2.2	18.85	0.05	2.02	0.72	0.47	0.003	0.00	0.06	1.26	0.01	0.14
B-5	6.0	23.37	0.08	2.56	0.51	0.35	0.007	0.00	0.06	1.54	0.01	0.23
B-6	30.9	29.62	0.13	4.10	0.55	0.41	0.001	0.00	0.07	2.06	0.01	0.37
B-7	29.3	33.09	0.16	4.98	0.70	0.47	0.000	0.00	0.07	2.18	0.01	0.34
B-8	43.9	39.39	0.19	6.39	0.61	0.51	0.000	0.00	0.08	2.54	0.01	0.33
B-9	51.4	40.42	0.19	6.58	0.56	0.47	0.004	0.00	0.08	2.37	0.00	0.29
B-10	71.5	52.10	0.23	8.12	0.58	0.57	0.004	0.00	0.08	2.64	0.01	0.33
B-11	148.0	68.62	0.24	9.19	0.51	0.62	0.005	0.00	0.08	2.59	0.01	0.37
B-12	165.2	68.79	0.26	9.53	0.48	0.63	0.004	0.00	0.08	2.70	0.00	0.39
B-13	235.9	75.20	0.27	10.43	0.52	0.68	0.004	0.00	0.09	2.72	0.01	0.39
B-14	265.5	75.68	0.26	10.39	0.54	0.72	0.006	0.00	0.08	2.67	0.01	0.40

Sample	Reaction time (hrs)	Ag (ppm)	Cd (ppm)	Sn (ppm)	Sb (ppm)	Cs (ppm)	Ba (ppm)	Tl (ppm)	Pb (ppm)	Bi (ppm)	Th (ppm)	U (ppm)
B-1	-75.8	-0.04	0.00	-0.03	0.00	0.01	2.11	0.00	0.001	0.79	0.000	0.000
B-2	-21.9	-0.04	0.00	-0.03	0.00	0.01	4.08	0.00	0.001	1.09	0.000	0.000
B-3	-0.8	-0.04	0.00	-0.04	0.00	0.01	4.71	0.00	0.001	0.89	0.000	0.000
B-4	2.2	-0.04	0.00	-0.04	0.00	0.01	4.88	0.00	0.019	0.93	0.000	0.000
B-5	6.0	-0.04	0.00	-0.04	0.00	0.01	4.98	0.00	0.022	0.27	0.000	0.000
B-6	30.9	-0.04	0.00	-0.03	0.00	0.01	5.56	0.00	0.036	1.01	0.000	0.000
B-7	29.3	-0.04	0.00	-0.03	0.01	0.01	5.67	0.00	0.040	0.94	0.000	0.000
B-8	43.9	-0.04	0.00	-0.03	0.00	0.01	6.47	0.00	0.046	0.76	0.000	0.000
B-9	51.4	-0.04	0.00	-0.04	0.00	0.01	6.14	0.00	0.049	0.75	0.000	0.000
B-10	71.5	-0.04	0.00	-0.03	0.00	0.01	6.76	0.00	0.054	0.93	0.000	0.000
B-11	148.0	-0.04	0.00	-0.03	0.00	0.01	7.45	0.00	0.070	1.08	0.000	0.000
B-12	165.2	-0.04	0.00	-0.03	0.00	0.01	7.77	0.00	0.069	0.84	0.000	0.000
B-13	235.9	-0.04	0.00	-0.03	0.01	0.01	8.46	0.00	0.078	0.16	0.000	0.000
B-14	265.5	-0.04	0.00	-0.04	0.00	0.01	8.54	0.00	0.080	0.06	0.000	0.000

C series: O_2+CO_2 – 100°C – Miocene

Sample	Reaction time (hrs)	B (ppm)	Mg (ppm)	Al (ppm)	Si (ppm)	P (ppm)	K (ppm)	Ca (ppm)	Ti (ppm)	V (ppm)	Cr (ppm)	Mn (ppm)
C-1	-44.1	7.62	2.61	0.76	3.93	0.09	7.12	38.49	0.01	0.27	0.01	0.10
C-2	-27.9	7.34	8.00	0.67	4.22	0.13	10.22	106.49	0.01	0.23	0.00	0.32
C-3	-3.9	12.07	10.48	1.19	6.28	0.17	12.23	130.61	0.01	0.34	0.01	0.49

C-4	2.2	12.23	14.37	0.82	6.92	0.29	12.02	228.59	0.01	0.28	0.91	1.86
C-5	3.8	9.55	16.34	0.75	6.38	0.32	14.23	287.50	0.02	0.21	0.58	2.36
C-6	6.2	12.52	19.54	0.99	7.49	0.36	13.18	362.92	0.01	0.20	0.28	3.18
C-7	8.3	13.74	20.68	1.01	8.75	0.33	13.54	391.98	0.02	0.34	0.21	3.55
C-8	19.8	4.38	26.44	0.05	14.91	0.34	14.43	550.06	0.02	0.19	0.06	6.04
C-9	48.9	6.00	31.68	0.41	12.28	0.44	16.02	714.18	0.02	0.11	0.07	12.87
C-10	92.1	6.02	33.00	0.09	15.79	0.51	17.34	766.01	0.02	0.11	0.03	23.88
C-11	188.2	4.12	35.48	0.12	20.85	0.62	20.34	770.48	0.03	0.17	0.06	33.96
C-12	242.4	13.23	32.21	1.27	21.96	0.89	30.54	742.53	0.02	0.31	0.11	35.22
C-13	259.3	5.98	33.38	0.31	-18.60	3.22	30.06	765.64	0.07	0.00	0.01	30.19

Sample	Reaction time (hrs)	Fe (ppm)	Co (ppm)	Ni (ppm)	Cu (ppm)	Zn (ppm)	As (ppm)	Se (ppm)	Rb (ppm)	Sr (ppm)	Zr (ppm)	Mo (ppm)
C-1	-44.1	0.11	0.00	0.05	1.37	0.00	0.00	0.01	0.02	0.30	0.00	0.27
C-2	-27.9	0.05	0.00	0.07	1.65	-0.04	0.00	0.01	0.04	0.67	0.01	0.29
C-3	-3.9	0.15	0.00	0.12	1.78	0.09	0.00	0.01	0.05	0.75	0.01	0.36
C-4	2.2	8.21	0.12	5.17	2.25	0.05	0.00	0.01	0.06	1.01	0.01	0.10
C-5	3.8	7.98	0.17	6.85	2.56	0.12	0.00	0.01	0.06	1.15	0.00	0.06
C-6	6.2	3.18	0.23	10.05	2.76	0.11	0.00	0.01	0.06	1.36	0.01	0.07
C-7	8.3	1.04	0.26	11.41	2.79	0.11	0.00	0.01	0.07	1.43	0.01	0.10
C-8	19.8	0.01	0.49	22.41	3.14	0.16	0.00	0.01	0.08	1.85	0.00	0.06
C-9	48.9	0.23	1.19	56.06	4.54	0.29	0.00	0.01	0.09	2.29	0.00	0.08
C-10	92.1	0.02	2.20	107.58	6.79	0.38	0.00	0.01	0.11	2.46	0.00	0.06
C-11	188.2	8.70	3.27	178.95	11.70	0.53	0.00	0.01	0.12	2.53	0.00	0.04
C-12	242.4	18.95	3.41	212.45	9.39	0.87	0.00	0.00	0.12	2.21	0.01	0.07
C-13	259.3	0.74	2.55	179.06	1.57	-1.26	-0.01	0.01	0.14	2.37	-0.01	0.01

Sample	Reaction time (hrs)	Ag (ppm)	Cd (ppm)	Sn (ppm)	Sb (ppm)	Cs (ppm)	Ba (ppm)	Tl (ppm)	Pb (ppm)	Bi (ppm)	Th (ppm)	U (ppm)
C-1	-44.1	0.00	0.00	0.00	0.00	0.00	0.32	0.00	0.00	0.66	0.00	0.00
C-2	-27.9	0.00	0.00	0.00	0.00	0.00	1.42	0.00	0.00	0.47	0.00	0.00
C-3	-3.9	0.00	0.00	0.00	0.00	0.01	2.46	0.00	0.00	0.85	0.00	0.00
C-4	2.2	0.01	0.00	0.00	0.00	0.01	2.80	0.00	0.03	0.65	0.00	0.00
C-5	3.8	0.01	0.00	0.00	0.00	0.01	2.88	0.00	0.03	0.40	0.00	0.00
C-6	6.2	0.01	0.00	0.00	0.00	0.01	3.04	0.00	0.03	0.40	0.00	0.00
C-7	8.3	0.01	0.00	0.00	0.00	0.01	3.09	0.00	0.03	0.86	0.00	0.00
C-8	19.8	0.01	0.00	0.00	0.00	0.01	3.42	0.00	0.01	0.01	0.00	0.00
C-9	48.9	0.01	0.00	0.00	0.00	0.01	3.94	0.00	0.04	0.01	0.00	0.00

C-10	92.1	0.01	0.00	0.00	0.00	0.01	4.44	0.00	0.04	0.00	0.00	0.00
C-11	188.2	0.02	0.00	0.00	0.00	0.01	5.46	0.00	0.05	0.25	0.00	0.00
C-12	242.4	-0.03	0.00	-0.03	0.00	0.02	6.10	0.00	0.03	0.85	0.00	0.00
C-13	259.3	0.02	0.00	-0.08	-0.01	0.02	6.81	0.01	-0.01	0.00	0.00	0.00

E series: CO_2 – 100°C – 300 bars - Mi

Sample	Reaction time (hrs)	B (ppm)	Mg (ppm)	Al (ppm)	Si (ppm)	P (ppm)	K (ppm)	Ca (ppm)	Ti (ppm)	V (ppm)	Cr (ppm)	Mn (ppm)
E-1	-77.50	11.759	7.776	1.159	9.942	1.088	13.071	110.115	0.023	0.308	0.056	0.520
E-2	-5.00	15.797	9.469	1.596	15.217	1.144	14.524	114.931	0.029	0.344	0.006	0.583
E-3	-0.13	9.835	11.764	1.019	12.927	1.311	15.109	221.057	0.026	0.227	0.159	1.937
E-4	2.00	15.173	14.171	1.640	15.463	1.405	14.795	314.240	0.027	0.330	0.476	2.589
E-5	3.50	10.694	14.284	1.094	14.056	1.388	15.093	344.775	0.025	0.254	0.497	2.683
E-6	6.00	15.875	17.076	1.529	18.645	1.597	17.201	447.900	0.033	0.289	0.596	3.293
E-7	18.75	10.169	20.261	0.994	20.152	1.577	19.601	629.036	0.029	0.108	0.511	4.109
E-8	26.50	8.645	20.693	0.799	20.870	1.679	18.441	667.848	0.029	0.089	0.442	4.261
E-9	43.50	10.490	21.351	0.972	21.903	1.779	18.923	732.913	0.028	0.212	0.421	4.459
E-10	67.42	6.483	23.792	0.514	24.220	1.851	21.753	836.086	0.027	0.014	0.412	5.023
E-11	92.83	11.543	22.418	1.011	24.298	1.792	19.559	798.971	0.029	0.112	0.360	4.810
E-12	162.92	10.088	24.304	0.806	26.064	1.860	21.911	875.409	0.028	0.087	0.352	5.268
E-13	188.37	15.985	25.864	1.358	29.068	1.930	23.560	938.848	0.028	0.128	0.378	5.661

Sample	Reaction time (hrs)	Fe (ppm)	Co (ppm)	Ni (ppm)	Cu (ppm)	Zn (ppm)	As (ppm)	Se (ppm)	Rb (ppm)	Sr (ppm)	Zr (ppm)	Mo (ppm)
E-1	-77.50	0.577	0.005	0.206	0.995	0.001	0.002	0.005	0.050	0.622	0.008	3.722
E-2	-5.00	0.501	0.004	0.180	0.905	0.044	0.003	0.001	0.054	0.632	0.010	5.564
E-3	-0.13	12.613	0.099	2.044	1.050	0.093	0.003	0.003	0.054	0.919	0.007	1.836
E-4	2.00	22.196	0.165	3.669	1.238	0.173	0.009	0.003	0.059	1.167	0.007	1.065
E-5	3.50	23.567	0.173	3.979	1.248	0.158	0.005	0.003	0.058	1.222	0.006	2.075
E-6	6.00	30.745	0.222	5.362	1.559	0.241	0.004	0.004	0.069	1.552	0.010	1.838
E-7	18.75	42.278	0.282	7.454	1.704	0.291	0.012	0.003	0.081	2.093	0.008	2.322
E-8	26.50	44.595	0.294	7.785	1.716	0.303	0.007	0.003	0.083	2.184	0.006	2.185
E-9	43.50	50.483	0.315	8.562	1.659	0.359	0.010	0.001	0.087	2.360	0.007	1.987
E-10	67.42	62.854	0.353	10.112	1.782	0.436	0.012	0.001	0.096	2.677	0.002	1.982
E-11	92.83	62.802	0.334	9.806	1.590	0.441	0.014	0.001	0.091	2.539	0.008	1.720
E-12	162.92	77.414	0.364	11.332	1.624	0.578	0.010	0.002	0.099	2.772	0.006	1.628
E-13	188.37	88.230	0.394	12.565	1.768	0.625	0.019	0.004	0.105	2.984	0.008	1.698

Sample	Reaction	Ag	Cd	Sn	Sb	Cs	Ba	Ti	Pb	Bi	Th	U

	time (hrs)	(ppm)	(ppm)	(ppm)	(ppm)	(ppm)	(ppm)	(ppm)	(ppm)	(ppm)	(ppm)	(ppm)
E-1	-77.50	0.186	0.004	-0.002	0.005	0.007	1.618	0.001	0.001	1.205	0.000	0.0002
E-2	-5.00	0.125	0.006	0.000	0.003	0.008	2.803	0.001	0.001	1.374	0.000	0.0000
E-3	-0.13	0.087	0.003	-0.002	0.002	0.007	3.522	0.001	0.019	0.895	0.000	0.0001
E-4	2.00	0.066	0.002	0.000	0.002	0.009	3.944	0.001	0.043	1.284	0.000	0.0001
E-5	3.50	0.050	0.003	-0.003	0.002	0.009	3.862	0.001	0.037	1.025	0.000	0.0000
E-6	6.00	0.044	0.003	-0.003	0.002	0.010	4.524	0.002	0.051	1.195	0.000	0.0001
E-7	18.75	0.037	0.004	-0.004	0.002	0.012	5.071	0.002	0.073	0.440	0.000	0.0002
E-8	26.50	0.030	0.004	-0.005	0.002	0.012	5.196	0.002	0.079	0.365	0.000	0.0001
E-9	43.50	0.023	0.004	-0.004	0.001	0.013	5.468	0.002	0.084	0.847	0.000	0.0000
E-10	67.42	0.021	0.004	-0.005	0.001	0.014	6.338	0.002	0.101	0.061	0.000	0.0000
E-11	92.83	0.018	0.004	-0.004	0.001	0.013	6.223	0.002	0.090	0.470	0.000	0.0000
E-12	162.92	0.012	0.004	-0.004	0.001	0.013	7.449	0.002	0.102	0.377	0.000	0.0000
E-13	188.37	0.010	0.004	-0.005	0.001	0.015	8.362	0.002	0.105	0.551	0.000	0.0000

Experiments from Table 6 matrix:

D Series: CO_2 – 70°C - Miocene

Sample	Reaction time (hrs)	B (ppm)	Mg (ppm)	Al (ppm)	Si (ppm)	P (ppm)	K (ppm)	Ca (ppm)	Ti (ppm)	V (ppm)	Cr (ppm)	Mn (ppm)
D-1	-118.67	11.552	0.331	0.070	20.184	0.652	3.107	0.545	0.018	0.098	0.005	0.001
D-2	-94.42	6.347	3.873	0.594	2.832	0.737	8.768	67.233	0.018	0.108	0.008	0.316
D-3	-66.50	7.440	5.748	0.677	3.972	0.727	9.791	96.667	0.018	0.190	0.196	0.468
D-4	-1.75	7.068	7.632	0.685	4.893	0.863	10.265	126.041	0.016	0.251	0.030	0.692
D-5	2.25	9.699	11.941	0.771	4.839	0.818	11.462	348.065	0.019	0.120	0.510	2.466
D-6	4.25	5.638	13.018	0.559	3.992	0.892	11.061	414.420	0.016	0.119	0.584	2.724
D-7	6.25	9.687	14.342	0.807	5.419	0.991	11.037	481.415	0.019	0.109	0.591	3.056
D-8	8.25	8.163	15.110	0.684	5.433	0.948	11.226	522.837	0.020	0.108	0.601	3.235
D-9	25.75	8.565	18.423	0.667	6.217	1.160	11.512	732.240	0.019	0.296	0.465	4.177
D-10	32.83	7.164	18.932	0.562	6.552	1.280	12.727	781.001	0.021	0.330	0.460	4.355
D-11	49.75	9.156	19.670	0.753	7.512	1.273	12.847	840.107	0.020	0.243	0.397	4.559
D-12	100.25	14.020	21.301	1.322	10.454	1.311	13.568	957.729	0.022	0.441	0.370	5.058
D-13	166.50	11.845	22.098	1.003	11.140	1.345	13.873	1000.405	0.022	0.277	0.385	5.311
D-14	190.50	12.694	23.293	1.008	12.822	1.404	14.112	1063.990	0.021	0.340	0.376	5.655
D-15	214.25	11.131	23.191	0.583	11.060	1.483	14.437	1046.263	0.021	0.124	0.369	5.595

Sample	Reaction time (hrs)	Fe (ppm)	Co (ppm)	Ni (ppm)	Cu (ppm)	Zn (ppm)	As (ppm)	Se (ppm)	Rb (ppm)	Sr (ppm)	Zr (ppm)	Mo (ppm)
D-1	-118.67	0.014	0.000	0.050	0.905	0.017	0.000	0.003	0.002	0.009	0.000	0.010

D-2	-94.42	0.172	0.003	0.263	1.063	0.009	-0.001	0.000	0.027	0.478	0.004	0.542
D-3	-66.50	0.932	0.008	0.498	1.019	0.024	-0.001	0.000	0.032	0.552	0.005	0.989
D-4	-1.75	0.556	0.008	0.440	1.156	0.037	0.001	0.003	0.034	0.618	0.005	1.902
D-5	2.25	21.222	0.156	5.358	1.342	0.080	0.001	-0.001	0.037	1.189	0.006	0.056
D-6	4.25	25.045	0.181	6.000	1.348	0.078	0.001	-0.002	0.037	1.341	0.004	0.062
D-7	6.25	29.013	0.207	6.733	1.430	0.098	0.001	0.001	0.040	1.520	0.006	0.307
D-8	8.25	31.951	0.221	7.075	1.439	0.104	0.001	-0.001	0.041	1.638	0.005	0.180
D-9	25.75	44.647	0.290	9.822	1.544	0.153	0.006	0.001	0.047	2.261	0.005	0.472
D-10	32.83	48.274	0.300	10.174	1.592	0.188	0.004	0.000	0.048	2.400	0.005	0.415
D-11	49.75	51.806	0.313	10.776	1.571	0.181	0.004	0.003	0.051	2.543	0.006	0.558
D-12	100.25	63.634	0.352	12.263	1.597	0.249	0.005	0.001	0.056	2.860	0.007	0.747
D-13	166.50	72.899	0.367	13.273	1.587	0.233	0.006	0.003	0.057	2.971	0.005	0.851
D-14	190.50	78.643	0.395	14.331	1.660	0.248	0.002	0.003	0.061	3.163	0.005	0.909
D-15	214.25	80.032	0.394	14.302	1.614	0.229	0.007	0.001	0.060	3.080	0.001	0.954

Sample	Reaction time (hrs)	Ag (ppm)	Cd (ppm)	Sn (ppm)	Sb (ppm)	Cs (ppm)	Ba (ppm)	Tl (ppm)	Pb (ppm)	Bi (ppm)	Th (ppm)	U (ppm)
D-1	-118.67	0.001	0.000	0.000	0.001	0.001	0.007	-0.001	0.001	0.001	0.000	0.000
D-2	-94.42	0.001	0.001	0.001	0.001	0.003	0.629	0.000	0.001	0.088	0.000	0.000
D-3	-66.50	0.001	0.002	0.000	0.001	0.003	1.072	0.000	0.001	0.377	0.000	0.000
D-4	-1.75	0.001	0.003	0.001	0.001	0.003	1.615	0.000	0.001	0.587	0.000	0.000
D-5	2.25	0.001	0.001	0.000	0.001	0.004	2.214	0.000	0.007	0.109	0.000	0.000
D-6	4.25	0.001	0.001	0.000	0.004	0.004	2.191	0.000	0.008	0.121	0.000	0.000
D-7	6.25	0.001	0.002	0.000	0.001	0.004	2.309	0.000	0.015	0.070	0.000	0.000
D-8	8.25	0.001	0.002	0.000	0.001	0.004	2.360	0.000	0.014	0.064	0.000	0.000
D-9	25.75	0.002	0.002	0.000	0.001	0.005	2.734	0.000	0.024	0.718	0.000	0.000
D-10	32.83	0.002	0.002	0.001	0.004	0.005	2.817	0.001	0.026	0.871	0.000	0.000
D-11	49.75	0.002	0.002	0.001	0.001	0.005	2.964	0.000	0.033	0.548	0.000	0.001
D-12	100.25	0.002	0.003	0.003	0.001	0.006	3.469	0.000	0.035	1.345	0.000	0.001
D-13	166.50	0.001	0.003	-0.001	0.001	0.006	3.776	0.000	0.039	0.668	0.000	0.000
D-14	190.50	0.001	0.003	0.000	0.002	0.006	4.104	0.001	0.041	0.885	0.000	0.000
D-15	214.25	0.002	0.004	0.000	0.001	0.006	4.138	0.001	0.040	0.110	0.000	0.000

R Series: O_2+CO_2 – 70°C - Miocene

Sample	Reaction time (hrs)	B (ppm)	Mg (ppm)	Al (ppm)	Si (ppm)	P (ppm)	K (ppm)	Ca (ppm)	Ti (ppm)	V (ppm)	Cr (ppm)	Mn (ppm)
R-1	-66.25	8.458	2.570	0.792	9.600	2.762	11.940	64.948	0.030	0.137	1.852	0.161
R-2	-1.25	11.382	2.818	0.976	10.694	2.254	11.787	69.799	0.023	0.101	0.050	0.094
R-3	0.75	13.053	3.616	1.128	11.120	2.379	12.281	164.629	0.028	0.021	0.138	0.465
R-4	4.08	14.201	5.028	1.199	11.361	2.192	13.525	274.801	0.022	0.176	0.260	0.842
R-5	7.00	13.099	7.247	1.243	12.284	2.206	12.672	414.498	0.029	0.148	0.606	1.259
R-6	22.92	11.252	10.014	1.089	11.003	2.323	13.760	604.665	0.025	0.094	0.916	1.752
R-7	30.75	16.482	10.452	1.467	12.314	2.147	13.939	635.316	0.025	0.094	0.267	1.797

R-8	46.92	12.880	11.548	1.231	11.939	2.287	14.787	705.325	0.024	0.091	1.234	1.977
R-9	54.25	9.752	12.023	0.928	10.263	2.282	14.763	742.548	0.023	0.054	0.385	2.047
R-10	72.25	10.589	12.815	1.018	11.086	2.211	15.059	785.301	0.021	0.117	0.251	2.293
R-11	100.67	12.454	14.072	1.155	11.230	2.260	15.391	828.896	0.025	0.098	0.507	2.388
R-12	127.25	9.415	15.007	0.851	10.818	2.357	16.022	896.285	0.015	0.055	0.224	2.569
R-13	168.25	20.030	15.620	1.560	14.054	2.438	15.432	918.262	0.022	0.139	0.691	2.674
R-14	215.75	11.553	16.804	1.193	12.872	2.404	16.110	977.476	0.019	0.152	3.859	4.097
R-15	243.25	14.499	17.622	1.512	13.625	2.434	17.251	1071.189	0.020	0.124	0.605	3.140
R-16	263.75	9.519	18.309	1.109	11.858	2.386	17.745	1047.218	0.016	0.060	0.257	3.077

Sample	Reaction time (hrs)	Fe (ppm)	Co (ppm)	Ni (ppm)	Cu (ppm)	Zn (ppm)	As (ppm)	Se (ppm)	Rb (ppm)	Sr (ppm)	Zr (ppm)	Mo (ppm)
R-1	-66.25	9.083	0.017	0.727	1.087	0.149	0.019	0.004	0.050	0.913	0.007	0.299
R-2	-1.25	0.544	0.002	0.053	0.851	0.257	0.023	0.003	0.055	0.918	0.007	0.107
R-3	0.75	1.431	0.010	0.125	0.795	1.846	0.027	0.003	0.055	1.129	0.007	0.063
R-4	4.08	2.128	0.027	0.234	0.845	4.101	0.035	0.003	0.057	1.449	0.009	0.095
R-5	7.00	3.378	0.050	0.282	0.773	6.709	0.023	0.002	0.060	1.833	0.010	0.148
R-6	22.92	4.410	0.088	0.416	0.807	9.054	0.006	0.004	0.070	2.423	0.008	0.230
R-7	30.75	1.908	0.095	0.341	0.720	9.237	0.006	0.002	0.070	2.506	0.010	0.093
R-8	46.92	5.671	0.114	0.483	0.756	9.902	0.006	0.006	0.076	2.728	0.009	0.200
R-9	54.25	2.456	0.121	0.546	0.775	10.284	0.007	0.004	0.078	2.849	0.009	0.091
R-10	72.25	1.586	0.149	1.371	1.128	11.003	0.005	0.003	0.081	2.961	0.009	0.098
R-11	100.67	2.006	0.162	0.907	1.159	11.922	0.011	0.003	0.085	3.156	0.010	0.106
R-12	127.25	1.372	0.175	0.884	0.964	12.727	0.008	0.003	0.087	3.359	0.007	0.091
R-13	168.25	3.058	0.188	1.094	0.877	13.244	0.004	0.006	0.087	3.424	0.013	0.111
R-14	215.75	18.069	0.315	8.969	1.294	13.855	0.001	0.006	0.088	3.713	0.009	0.101
R-15	243.25	4.713	0.231	2.807	0.917	14.400	0.005	0.002	0.090	3.850	0.015	0.113
R-16	263.75	1.745	0.224	1.559	0.854	15.011	0.005	0.005	0.093	3.977	0.011	0.108

Sample	Reaction time (hrs)	Ag (ppm)	Cd (ppm)	Sn (ppm)	Sb (ppm)	Cs (ppm)	Ba (ppm)	Tl (ppm)	Pb (ppm)	Bi (ppm)	Th (ppm)	U (ppm)
R-1	-66.25	0.000	0.000	0.000	0.002	0.004	2.740	0.002	-0.010	0.451	-0.004	0.000
R-2	-1.25	0.000	-0.001	-0.001	0.004	0.005	3.464	0.001	-0.008	0.298	-0.003	0.000
R-3	0.75	0.001	0.000	-0.001	0.003	0.006	3.530	0.001	0.003	0.028	-0.004	0.000
R-4	4.08	0.001	0.000	0.001	0.002	0.006	3.622	0.001	0.007	0.629	-0.003	0.000
R-5	7.00	0.002	0.002	0.000	0.004	0.007	3.619	0.003	0.013	0.448	-0.003	0.002
R-6	22.92	0.001	0.001	0.001	0.002	0.007	3.743	0.002	0.080	0.154	-0.003	0.002
R-7	30.75	0.001	0.001	0.000	0.002	0.007	3.814	0.002	0.099	0.307	-0.003	0.001
R-8	46.92	0.001	0.000	0.000	0.001	0.008	3.852	0.002	0.132	0.110	-0.004	0.001
R-9	54.25	0.001	0.001	-0.002	0.001	0.008	3.848	0.002	0.143	0.163	-0.003	0.001
R-10	72.25	0.002	0.001	0.001	0.001	0.009	3.793	0.002	0.162	0.441	-0.003	0.002
R-11	100.67	0.002	0.001	0.000	0.002	0.009	3.874	0.003	0.194	0.385	-0.004	0.001
R-12	127.25	0.003	0.002	-0.002	0.002	0.011	3.930	0.003	0.218	0.180	-0.003	0.002

R-13	168.25	0.003	0.001	0.000	0.002	0.011	3.795	0.003	0.230	0.548	-0.004	0.002
R-14	215.75	0.003	0.002	-0.001	0.001	0.011	3.831	0.003	0.213	0.564	-0.003	0.002
R-15	243.25	0.003	0.002	-0.001	0.001	0.011	3.964	0.003	0.231	0.486	-0.003	0.002
R-16	263.75	0.004	0.003	-0.001	0.001	0.011	4.105	0.003	0.267	0.217	-0.004	0.002
L series: CO_2 – 100°C - Miocene												
Sample	**Reaction time (hrs)**	**B (ppm)**	**Mg (ppm)**	**Al (ppm)**	**Si (ppm)**	**P (ppm)**	**K (ppm)**	**Ca (ppm)**	**Ti (ppm)**	**V (ppm)**	**Cr (ppm)**	**Mn (ppm)**
L-1	-0.67	12.439	4.771	1.204	9.970	1.458	15.394	101.768	0.023	0.400	0.104	0.082
L-2	1.00	8.215	8.129	0.915	7.826	1.997	22.533	213.838	0.027	0.238	0.386	1.260
L-3	3.00	7.927	10.612	0.765	9.508	1.918	14.721	325.814	0.025	0.260	0.285	1.707
L-4	6.33	8.724	12.585	1.421	10.145	1.882	16.163	423.490	0.023	0.350	0.240	2.114
L-5	22.75	7.409	16.497	0.588	13.628	1.970	17.409	666.343	0.024	0.188	0.104	3.238
L-6	29.33	6.832	17.380	0.581	12.977	1.939	17.180	693.699	0.022	0.229	0.094	3.573
L-7	47.33	9.917	19.350	0.894	15.453	2.122	19.033	795.064	0.025	0.265	0.082	4.201
L-8	72.33	13.641	19.906	0.776	17.962	2.128	19.149	846.741	0.025	0.344	0.065	4.588
L-9	95.58	5.890	21.247	0.415	17.401	2.152	20.143	897.928	0.023	0.219	0.056	5.262
Sample	**Reaction time (hrs)**	**Fe (ppm)**	**Co (ppm)**	**Ni (ppm)**	**Cu (ppm)**	**Zn (ppm)**	**As (ppm)**	**Se (ppm)**	**Rb (ppm)**	**Sr (ppm)**	**Zr (ppm)**	**Mo (ppm)**
L-1	-0.67	0.170	0.001	0.121	0.822	0.061	0.004	0.001	0.085	0.716	0.007	2.710
L-2	1.00	14.889	0.062	2.828	0.686	0.198	0.004	0.001	0.085	1.030	0.003	0.773
L-3	3.00	16.475	0.075	3.029	0.738	0.185	0.005	0.003	0.092	1.310	0.003	1.012
L-4	6.33	18.571	0.092	3.410	0.755	0.251	0.010	0.002	0.096	1.563	0.003	1.140
L-5	22.75	27.465	0.153	5.163	0.815	0.331	0.007	0.002	0.106	2.153	0.002	1.048
L-6	29.33	28.802	0.172	5.704	0.808	0.366	0.007	0.000	0.110	2.301	0.003	1.018
L-7	47.33	34.432	0.218	7.218	0.836	0.421	0.009	0.003	0.119	2.628	0.004	0.959
L-8	72.33	38.148	0.252	8.765	0.830	0.453	0.007	0.001	0.120	2.754	0.004	0.892
L-9	95.58	39.144	0.299	11.025	0.873	0.484	0.005	0.000	0.124	2.932	0.002	0.778
Sample	**Reaction time (hrs)**	**Ag (ppm)**	**Cd (ppm)**	**Sn (ppm)**	**Sb (ppm)**	**Cs (ppm)**	**Ba (ppm)**	**Tl (ppm)**	**Pb (ppm)**	**Bi (ppm)**	**Th (ppm)**	**U (ppm)**
L-1	-0.67	-0.001	0.006	0.001	0.002	0.010	1.500	0.003	0.002	0.953	0.000	0.000
L-2	1.00	0.001	0.003	0.000	0.001	0.010	2.075	0.004	0.053	0.374	0.000	0.000
L-3	3.00	0.001	0.003	0.000	0.001	0.011	2.226	0.004	0.049	0.405	0.000	0.000
L-4	6.33	0.002	0.004	0.002	0.001	0.012	2.341	0.004	0.054	0.734	0.000	0.000
L-5	22.75	0.002	0.004	-0.001	0.001	0.013	2.729	0.004	0.072	0.127	0.000	0.001
L-6	29.33	0.001	0.004	-0.001	0.000	0.014	2.863	0.004	0.075	0.288	0.000	0.000
L-7	47.33	0.001	0.004	0.000	0.000	0.014	3.206	0.004	0.084	0.379	0.000	0.001
L-8	72.33	0.000	0.004	-0.001	0.000	0.015	3.400	0.004	0.085	0.667	0.000	0.001
L-9	95.58	0.002	0.004	-0.002	0.000	0.015	3.748	0.005	0.088	0.182	0.000	0.001
S series: O_2+CO_2 – 100°C - Miocene												
Sample	**Reaction time (hrs)**	**B (ppm)**	**Mg (ppm)**	**Al (ppm)**	**Si (ppm)**	**P (ppm)**	**K (ppm)**	**Ca (ppm)**	**Ti (ppm)**	**V (ppm)**	**Cr (ppm)**	**Mn (ppm)**

S-1	-1.1	8.375	7.112	0.652	11.020	2.228	17.698	126.908	0.022	0.089	0.029	0.318
S-2	1.2	9.087	8.159	0.755	10.937	2.314	17.218	196.912	0.023	0.099	0.062	0.557
S-3	2.2	13.760	8.847	1.069	12.034	2.116	16.244	222.823	0.023	0.164	0.074	0.686
S-4	4.6	8.130	10.835	0.728	11.120	2.191	17.541	294.854	0.022	0.088	0.078	0.940
S-5	22.3	14.669	17.404	1.080	14.404	2.269	17.941	546.341	0.021	0.118	0.358	1.849
S-6	29.0	8.284	19.515	0.644	13.351	2.395	18.238	610.246	0.018	0.059	0.150	2.029
S-7	45.5	17.847	21.432	1.288	16.450	2.346	18.472	678.719	0.021	0.198	0.131	2.316
S-8	71.3	12.207	24.706	1.014	16.710	2.346	19.092	768.703	0.022	0.136	0.612	2.886
S-9	94.9	13.166	26.416	1.137	17.723	2.249	19.973	824.111	0.022	0.173	0.415	3.062
S-10	123.4	11.935	29.146	1.151	19.481	2.255	21.982	899.964	0.020	0.069	0.452	3.507
S-11	168.8	12.549	32.224	1.626	20.884	2.347	23.752	951.814	0.023	0.146	0.790	4.043
S-12	243.1	19.588	34.676	2.136	22.258	2.302	22.706	969.683	0.027	0.213	0.300	4.502
Sample	**Reaction time (hrs)**	**Fe (ppm)**	**Co (ppm)**	**Ni (ppm)**	**Cu (ppm)**	**Zn (ppm)**	**As (ppm)**	**Se (ppm)**	**Rb (ppm)**	**Sr (ppm)**	**Zr (ppm)**	**Mo (ppm)**
S-1	-1.1	0.278	0.006	0.202	0.660	1.655	0.005	0.004	0.089	1.044	0.007	0.098
S-2	1.2	0.619	0.012	0.231	0.766	5.028	0.010	0.004	0.089	1.192	0.007	0.074
S-3	2.2	0.679	0.014	0.251	0.671	6.262	0.004	0.003	0.087	1.255	0.008	0.093
S-4	4.6	0.789	0.022	0.366	0.670	7.796	0.006	0.004	0.091	1.470	0.007	0.101
S-5	22.3	1.490	0.055	1.792	0.762	11.675	0.000	0.004	0.102	2.124	0.007	0.280
S-6	29.0	0.325	0.060	1.919	0.760	13.144	0.006	0.003	0.108	2.323	0.007	0.330
S-7	45.5	0.326	0.067	2.224	0.737	15.010	-0.001	0.006	0.110	2.479	0.009	0.373
S-8	71.3	2.666	0.095	3.925	0.948	17.748	-0.001	0.004	0.115	2.730	0.010	0.359
S-9	94.9	2.264	0.100	4.095	0.948	19.821	0.002	0.003	0.115	2.818	0.011	0.364
S-10	123.4	1.761	0.104	4.188	0.963	23.768	0.000	0.003	0.119	3.061	0.014	0.498
S-11	168.8	2.834	0.123	5.437	1.098	29.547	0.000	0.003	0.120	3.232	0.015	0.536
S-12	243.1	1.040	0.140	7.622	1.247	37.308	0.002	0.005	0.119	3.313	0.018	0.620
Sample	**Reaction time (hrs)**	**Ag (ppm)**	**Cd (ppm)**	**Sn (ppm)**	**Sb (ppm)**	**Cs (ppm)**	**Ba (ppm)**	**Tl (ppm)**	**Pb (ppm)**	**Bi (ppm)**	**Th (ppm)**	**U (ppm)**
S-1	-1.1	0.001	0.000	-0.002	0.001	0.010	1.535	0.003	-0.006	0.336	-0.004	0.000
S-2	1.2	0.001	0.000	0.000	0.001	0.010	1.595	0.003	0.006	0.371	-0.003	0.000
S-3	2.2	0.001	0.000	0.000	0.000	0.010	1.618	0.003	0.008	0.623	-0.004	0.000
S-4	4.6	0.001	0.001	-0.001	0.000	0.010	1.700	0.003	0.015	0.353	-0.004	0.001
S-5	22.3	0.003	0.001	0.000	0.000	0.012	1.847	0.003	0.036	0.501	-0.004	0.001
S-6	29.0	0.004	0.002	-0.002	0.003	0.012	1.923	0.004	0.044	0.238	-0.004	0.001
S-7	45.5	0.004	0.002	-0.001	0.000	0.013	1.907	0.004	0.058	0.777	-0.004	0.001
S-8	71.3	0.005	0.002	-0.002	0.000	0.015	2.040	0.004	0.055	0.544	-0.004	0.001
S-9	94.9	0.004	0.003	0.000	0.000	0.016	2.160	0.004	0.066	0.641	-0.003	0.001
S-10	123.4	0.005	0.003	-0.001	0.000	0.017	2.382	0.004	0.099	0.239	-0.004	0.001
S-11	168.8	0.005	0.004	-0.001	0.000	0.016	2.610	0.005	0.112	0.497	-0.004	0.001
S-12	243.1	0.005	0.004	0.000	0.000	0.014	2.835	0.004	0.141	0.811	-0.004	0.001

H series: CO_2 – 130°C - Miocene

Sample	Reaction time (hrs)	B (ppm)	Mg (ppm)	Al (ppm)	Si (ppm)	P (ppm)	K (ppm)	Ca (ppm)	Ti (ppm)	V (ppm)	Cr (ppm)	Mn (ppm)
H-1	-50.77	7.561		0.891	14.769	0.865			0.027	0.270	0.027	0.078
H-2	0.87	11.666		1.161	22.329	0.811			0.022	0.107	0.732	2.085
H-3	2.28	8.648		0.842	23.466	0.832			0.026	0.084	0.571	2.632
H-4	5.12	6.938		0.751	26.537	0.816			0.023	0.176	0.683	3.537
H-5	9.78	12.071		1.111	29.052	0.848			0.021	0.316	0.039	4.211
H-6	23.70	13.908		1.261	30.811	0.763			0.022	0.220	0.032	5.296
H-7	45.43	8.151		0.705	33.734	0.807			0.027	0.273	0.049	6.411
H-8	117.78	8.876		0.762	42.531	0.746			0.024	0.270	0.037	7.636
H-9	141.57	7.324		0.598	44.411	0.701			0.023	0.248	0.040	8.001
H-10	169.37	9.280		0.679	47.212	0.607			0.024	0.076	0.019	8.301
H-11	193.03	6.452		0.586	46.928	0.652			0.027	0.222	0.059	8.519
H-12	217.53	5.362		0.483	48.638	0.665			0.023	0.341	0.043	9.035
H-13	288.53	4.619		0.447	53.805	0.629			0.025	0.184	0.030	10.020

Sample	Reaction time (hrs)	Fe (ppm)	Co (ppm)	Ni (ppm)	Cu (ppm)	Zn (ppm)	As (ppm)	Se (ppm)	Rb (ppm)	Sr (ppm)	Zr (ppm)	Mo (ppm)
H-1	-50.77	0.550	-0.003	0.238	0.622	0.169	0.008	-0.001	0.082	0.539	0.005	5.651
H-2	0.87	41.558	0.129	8.280	1.444	0.212	0.020	-0.001	0.043	0.324	0.002	0.403
H-3	2.28	26.038	0.150	8.428	1.430	0.238	0.008	0.001	0.045	0.497	0.002	0.526
H-4	5.12	15.104	0.217	12.331	1.471	0.261	0.003	0.000	0.050	0.733	0.002	0.455
H-5	9.78	8.849	0.237	14.568	1.532	0.329	0.001	0.000	0.052	0.952	0.003	0.297
H-6	23.70	5.898	0.270	17.660	1.715	0.472	0.001	-0.002	0.059	1.272	0.004	0.262
H-7	45.43	4.177	0.298	19.898	1.943	0.646	0.002	0.000	0.068	1.513	0.003	0.340
H-8	117.78	3.716	0.322	19.489	1.697	0.870	0.002	0.000	0.075	1.642	0.004	0.511
H-9	141.57	3.623	0.335	20.076	1.665	0.920	0.003	-0.002	0.078	1.679	0.003	0.575
H-10	169.37	6.138	0.330	20.114	1.594	0.930	-0.001	0.002	0.081	1.696	0.005	0.722
H-11	193.03	5.295	0.364	20.123	1.539	0.951	0.004	0.001	0.079	1.683	0.004	0.637
H-12	217.53	5.215	0.393	21.039	1.647	1.054	0.005	-0.001	0.083	1.713	0.003	0.564
H-13	288.53	19.257	0.462	21.337	1.451	1.084	0.003	-0.001	0.085	1.791	0.002	0.687

Sample	Reaction time (hrs)	Ag (ppm)	Cd (ppm)	Sn (ppm)	Sb (ppm)	Cs (ppm)	Ba (ppm)	Ti (ppm)	Pb (ppm)	Bi (ppm)	Th (ppm)	U (ppm)
H-1	-50.77	-0.041	0.011	-0.034	0.003	0.013	3.279	-0.001	0.002	0.754	0.000	0.000
H-2	0.87	-0.037	0.001	-0.036	0.001	0.008	1.231	-0.002	0.083	0.178	0.000	0.000
H-3	2.28	-0.035	0.001	-0.036	0.001	0.008	1.319	-0.002	0.101	0.066	0.000	0.000
H-4	5.12	-0.035	0.001	-0.034	0.001	0.008	1.393	-0.002	0.111	0.391	0.000	0.000
H-5	9.78	-0.037	0.001	-0.035	0.000	0.009	1.436	-0.002	0.110	0.933	0.000	0.000
H-6	23.70	-0.035	0.001	-0.035	0.000	0.009	1.485	-0.002	0.107	0.606	0.000	0.000
H-7	45.43	-0.035	0.001	-0.034	0.000	0.010	1.652	-0.002	0.115	0.744	0.000	0.000
H-8	117.78	-0.038	0.002	-0.036	0.000	0.010	1.827	-0.002	0.126	0.718	0.000	0.000
H-9	141.57	-0.038	0.002	-0.034	0.001	0.011	1.910	-0.002	0.129	0.653	0.000	0.000

H-10	169.37	-0.037	0.003	-0.036	0.011	0.012	1.935	0.000	0.124	0.013	0.000	0.000
H-11	193.03	-0.038	0.003	-0.036	0.003	0.011	1.935	-0.001	0.136	0.550	0.000	0.000
H-12	217.53	-0.035	0.003	-0.031	0.001	0.011	1.999	-0.001	0.135	0.983	0.000	0.000
H-13	288.53	-0.037	0.003	-0.034	0.001	0.012	2.132	-0.001	0.147	0.377	0.000	0.000

Cardium sand series

Major ions (IC):

Sample	Reaction time (hrs)	Li (ppm)	Na (ppm)	NH4 (ppm)	K (ppm)	Mg (ppm)	Ca (ppm)	F (ppm)	Cl (ppm)	NO2 (ppm)	Br (ppm)	PO4 (ppm)	SO4 (ppm)	Alk. (ppm)
K series: CO_2 – 70°C - Cardium														
K-1	-1.50	0.0	***43200***	0.0	5.9	2.5	7.6	0.0	***66600***	0.0	83.8	0.0	11.9	48.2
K-2	1.17	0.0	***43200***	0.0	5.9	2.8	7.2	0.0	***66600***	0.0	87.3	0.0	12.4	113.7
K-3	6.17	0.0	***43200***	0.0	6.9	3.2	8.6	0.0	***66600***	0.0	80.7	0.0	11.6	157.6
K-4	23.50	0.0	***43200***	0.0	7.5	3.7	9.5	0.0	***66600***	0.0	80.2	0.0	13.4	210.6
K-5	97.50	0.0	***43200***	0.0	9.5	7.7	10.8	0.0	***66600***	0.0	83.5	0.0	16.0	311.7
K-6	142.50	0.0	***43200***	0.0	9.8	8.2	10.6	0.0	***66600***	0.0	82.0	0.0	16.3	326.0
K-7	191.00	0.1	***43200***	0.0	10.1	10.2	11.1	0.4	***66600***	0.0	78.5	0.0	12.7	446.5
K-8	242.50	0.0	***43200***	0.0	10.5	9.2	10.9	0.2	***66600***	0.0	81.0	0.0	14.8	467.5
K-9	287.00	0.0	***43200***	0.0	10.7	9.4	11.1	0.5	***66600***	0.0	82.8	0.0	16.0	492.8
K-10	335.25	0.0	***43200***	0.0	10.9	9.6	11.1	0.4	***66600***	0.0	84.7	0.0	13.7	513.9
K-11	383.00	0.1	***43200***	0.0	12.0	9.8	11.4	0.2	***66600***	0.0	83.0	0.0	23.0	556.0
N series: O_2+CO_2 – 70°C - Cardium														
N-1	-1.50	0.1	***43200***	0.0	15.1	5.9	47.7	0.0	***66600***	0.0	73.2	0.0	25.7	
N-2	0.17	0.1	***43200***	0.0	15.6	6.3	31.2	0.0	***66600***	0.0	71.3	0.0	19.2	
N-3	2.50	0.1	***43200***	0.0	16.3	6.9	32.6	0.0	***66600***	0.0	73.6	0.0	20.0	
N-4	7.00	0.1	***43200***	0.0	22.8	8.1	36.2	0.0	***66600***	0.0	71.2	0.0	24.8	
N-5	23.00	0.1	***43200***	0.0	21.2	11.3	41.3	0.0	***66600***	0.0	74.6	0.0	38.5	200.3
N-6	30.50	0.1	***43200***	0.0	21.7	12.4	51.0	0.0	***66600***	0.0	74.9	0.0	45.1	
N-7	48.25	0.1	***43200***	0.0	23.4	15.2	45.6	0.0	***66600***	0.0	74.1	0.0	58.0	261.9
N-8	72.17	0.1	***43200***	0.0	24.9	18.7	49.0	0.0	***66600***	0.0	73.3	0.0	77.5	200.3
N-9	99.17	0.1	***43200***	0.0	26.5	22.4	59.1	0.0	***66600***	0.0	78.8	0.0	88.2	261.9
J series: CO_2 – 100°C - Cardium														
J-1	-0.6	0.04	**42559**	0.0	7.2	4.0	8.2	0.0	**70343**	0.0	91.5	0.0	10.2	

Sample	Reaction time (hrs)	Li (ppm)	Na (ppm)	NH4 (ppm)	K (ppm)	Mg (ppm)	Ca (ppm)	F (ppm)	Cl (ppm)	NO2 (ppm)	Br (ppm)	PO4 (ppm)	SO4 (ppm)	Alk. (ppm)
J-2	0.6	0.03	**42519**	0.0	7.1	4.0	8.5	0.0	**70465**	0.0	89.8	0.0	14.2	151.6
J-3	1.7	0.03	**43868**	0.0	7.8	4.5	7.5	0.0	**72442**	0.0	94.8	0.0	11.1	168.5
J-4	3.9	0.03	**43408**	0.0	8.2	4.9	8.4	0.0	**73280**	0.0	94.5	0.0	10.7	
J-5	5.7	0.03	**41677**	0.0	8.3	5.2	8.7	0.0	**70090**	0.0	87.3	0.0	10.7	214.8
J-6	24.0	0.05	**43976**	0.0	10.7	7.5	12.5	0.0	**73288**	0.0	92.9	0.0	12.9	315.9
J-7	29.7	0.06	**45494**	0.0	11.3	8.3	13.8	0.0	**75158**	0.0	95.2	0.0	11.8	
J-8	46.7	0.05	**45916**	0.0	12.3	9.2	14.7	0.0	**76793**	0.0	100.0	0.0	13.5	341.2
J-9	97.5	0.07	**46419**	0.0	13.6	10.6	17.3	0.0	**78028**	0.0	100.2	0.0	13.4	446.8
J-10	169.9	0.08	**47710**	0.0	14.6	11.4	18.3	0.0	**80379**	0.0	105.3	0.0	14.4	522.3
J-11	196.6	0.08	**47285**	0.0	15.3	11.6	18.3	0.0	**80770**	0.0	103.9	0.0	13.4	530.7
J-12	241.6	0.24	**47142**	0.0	15.7	13.1	22.9	0.0		0.0	104.2	0.0	13.9	556.0
J-13	335.4	0.09	**47954**	0.0	15.4	12.9	20.7	0.0		0.0	108.3	0.0	16.1	564.4

Major and Trace elements (ICP-MS):

K Series: CO_2 – 70°C - Cardium

Sample	Reaction time (hrs)	B (ppm)	Mg (ppm)	Al (ppm)	Si (ppm)	P (ppm)	K (ppm)	Ca (ppm)	Ti (ppm)	V (ppm)	Cr (ppm)	Mn (ppm)
K-1	-1.50	6.927	3.159	0.690	7.618	2.136	9.877	7.894	0.022	0.234	0.010	0.382
K-2	1.17	8.559	3.830	1.440	6.366	2.795	9.571	9.989	0.023	0.356	0.215	0.588
K-3	6.17	7.080	4.805	1.627	6.782	2.681	12.142	11.713	0.025	0.332	0.528	0.697
K-4	23.50	9.262	6.570	2.101	8.623	2.688	11.600	13.943	0.023	0.171	0.767	1.045
K-5	97.50	7.120	9.647	1.934	11.479	2.556	14.030	17.711	0.022	0.268	0.773	1.831
K-6	142.50	8.502	10.185	2.036	13.097	2.395	17.444	18.590	0.026	0.173	1.049	2.099
K-7	191.00	6.402	12.425	1.968	12.035	3.596	14.926	19.013	0.025	0.228	0.701	2.821
K-8	242.50	8.313	11.242	1.932	13.987	2.494	15.144	19.943	0.024	0.354	0.638	2.691
K-9	287.00	12.604	11.331	2.175	15.634	2.598	15.199	20.468	0.025	0.489	0.587	2.828
K-10	335.25	6.737	12.668	1.739	14.386	2.920	15.933	21.362	0.024	0.346	0.587	3.306
K-11	383.00	7.373	12.497	1.782	16.682	2.701	17.414	25.029	0.026	0.420	0.566	3.351

Sample	Reaction time (hrs)	Fe (ppm)	Co (ppm)	Ni (ppm)	Cu (ppm)	Zn (ppm)	As (ppm)	Se (ppm)	Rb (ppm)	Sr (ppm)	Zr (ppm)	Mo (ppm)
K-1	-1.50	1.461	0.016	0.741	0.689	0.041	-0.001	0.000	0.044	0.392	0.002	0.882
K-2	1.17	17.713	0.063	2.483	0.793	0.203	0.003	0.000	0.049	0.434	0.002	0.073

K-3	6.17	38.349	0.085	3.053	0.830	0.216	0.004	0.001	0.058	0.437	0.001	0.080
K-4	23.50	70.688	0.143	5.818	1.100	0.272	0.003	0.001	0.074	0.467	0.001	0.094
K-5	97.50	120.338	0.253	10.487	0.829	0.462	0.008	0.001	0.101	0.509	0.002	0.125
K-6	142.50	133.558	0.294	12.652	0.792	0.522	0.013	0.001	0.105	0.521	0.002	0.103
K-7	191.00	148.268	0.372	16.426	0.899	0.657	0.008	0.001	0.126	0.593	0.002	0.123
K-8	242.50	162.841	0.357	16.008	0.791	0.628	0.012	0.001	0.113	0.531	0.002	0.137
K-9	287.00	171.365	0.379	17.160	0.758	0.687	0.004	0.000	0.113	0.540	0.003	0.152
K-10	335.25	185.299	0.434	19.869	0.825	0.750	0.012	0.000	0.124	0.590	0.001	0.139
K-11	383.00	217.282	0.448	20.583	0.934	0.848	0.009	0.001	0.123	0.584	0.003	0.142

Sample	Reaction time (hrs)	Ag (ppm)	Cd (ppm)	Sn (ppm)	Sb (ppm)	Cs (ppm)	Ba (ppm)	Tl (ppm)	Pb (ppm)	Bi (ppm)	Th (ppm)	U (ppm)
K-1	-1.50	-0.002	0.002	-0.001	0.001	0.005	2.573	0.002	0.006	0.362	0.000	0.000
K-2	1.17	-0.002	0.000	-0.001	0.001	0.006	2.998	0.002	0.069	0.790	0.000	0.001
K-3	6.17	-0.001	0.000	-0.002	0.001	0.006	3.076	0.002	0.081	0.661	0.000	0.000
K-4	23.50	-0.002	0.000	-0.002	0.000	0.008	3.310	0.002	0.112	0.093	0.000	0.000
K-5	97.50	-0.001	0.001	-0.001	0.001	0.010	3.829	0.003	0.144	0.442	0.000	0.000
K-6	142.50	-0.001	0.001	-0.001	0.000	0.010	3.890	0.003	0.144	0.105	0.000	0.000
K-7	191.00	-0.001	0.001	-0.001	0.001	0.013	4.706	0.003	0.170	0.214	0.000	0.000
K-8	242.50	-0.002	0.001	-0.001	0.001	0.011	4.121	0.003	0.149	0.743	0.000	0.000
K-9	287.00	-0.002	0.001	0.000	0.000	0.012	4.183	0.003	0.146	1.247	0.000	0.000
K-10	335.25	-0.001	0.001	-0.001	0.001	0.012	4.705	0.003	0.162	0.646	0.000	0.000
K-11	383.00	-0.002	0.001	0.000	0.001	0.012	4.656	0.003	0.155	0.943	0.000	0.000

N series: O_2+CO_2 – 70°C - Cardium

Sample	Reaction time (hrs)	B (ppm)	Mg (ppm)	Al (ppm)	Si (ppm)	P (ppm)	K (ppm)	Ca (ppm)	Ti (ppm)	V (ppm)	Cr (ppm)	Mn (ppm)
N-1	-1.50	15.571	5.682	1.320	25.803	1.581	17.144	46.531	0.085	0.206	0.081	0.127
N-2	0.17	18.104	7.176	1.337	24.762	1.407	20.418	50.243	0.118	0.215	0.668	0.279
N-3	2.50	16.741	8.246	1.461	20.921	1.549	22.110	53.349	0.149	0.133	0.343	0.311
N-4	7.00	15.750	9.253	1.758	22.371	1.622	22.980	55.427	0.177	0.173	0.549	0.418
N-5	23.00	16.474	12.213	2.093	22.202	1.346	26.078	56.629	0.172	0.168	0.126	0.472
N-6	30.50	14.604	13.333	2.102	22.994	1.178	26.874	59.322	0.182	0.191	0.140	0.653
N-7	48.25	16.566	15.899	2.056	23.738	1.555	28.670	61.387	0.193	0.204	0.154	0.680
N-8	72.17	22.259	18.474	2.436	28.533	1.417	28.909	64.730	0.182	0.283	0.069	0.875
N-9	99.17	15.164	22.293	1.835	23.819	1.256	31.914	70.750	0.160	0.163	0.074	1.039

Sample	Reaction time (hrs)	Fe (ppm)	Co (ppm)	Ni (ppm)	Cu (ppm)	Zn (ppm)	As (ppm)	Se (ppm)	Rb (ppm)	Sr (ppm)	Zr (ppm)	Mo (ppm)
N-1	-1.50	0.314	0.002	0.144	0.666	1.277	0.006	0.005	0.072	1.353	0.008	0.160
N-2	0.17	3.364	0.013	0.636	1.035	3.279	0.002	0.003	0.088	1.667	0.002	0.173
N-3	2.50	6.031	0.045	0.819	1.143	7.036	0.007	0.003	0.099	1.742	0.002	0.103
N-4	7.00	10.844	0.090	1.409	1.280	10.033	0.006	0.005	0.110	1.725	0.002	0.137
N-5	23.00	12.429	0.164	1.321	1.264	12.940	0.011	0.006	0.145	1.743	0.002	0.099

N-6	30.50	13.169	0.211	2.281	1.608	13.597	0.007	0.006	0.158	1.756	0.002	0.091
N-7	48.25	10.220	0.246	1.704	1.792	14.472	0.007	0.007	0.180	1.773	0.002	0.043
N-8	72.17	3.873	0.290	2.230	2.031	15.343	0.001	0.008	0.202	1.760	0.004	0.052
N-9	99.17	1.648	0.327	2.129	2.348	16.701	0.004	0.010	0.229	1.834	0.004	0.033

Sample	Reaction time (hrs)	Ag (ppm)	Cd (ppm)	Sn (ppm)	Sb (ppm)	Cs (ppm)	Ba (ppm)	Tl (ppm)	Pb (ppm)	Bi (ppm)	Th (ppm)	U (ppm)
N-1	-1.50	0.004	-0.003	-0.001	0.000	0.006	9.630	-0.008	-0.001	0.809	-0.002	-0.002
N-2	0.17	0.005	-0.002	0.001	-0.001	0.008	12.241	-0.008	0.017	0.783	-0.002	-0.002
N-3	2.50	0.004	-0.002	-0.002	-0.001	0.010	12.875	-0.008	0.020	0.489	-0.002	-0.001
N-4	7.00	0.004	-0.002	-0.002	-0.001	0.011	12.651	-0.008	0.035	0.651	-0.002	-0.001
N-5	23.00	0.006	-0.001	-0.002	-0.001	0.015	12.502	-0.007	0.113	0.618	-0.002	-0.001
N-6	30.50	0.007	0.000	-0.002	-0.001	0.016	12.426	-0.007	0.138	0.720	-0.002	-0.001
N-7	48.25	0.009	0.001	-0.002	-0.002	0.019	12.121	-0.007	0.185	0.779	-0.002	-0.001
N-8	72.17	0.011	0.002	-0.001	-0.002	0.021	11.355	-0.007	0.227	1.092	-0.002	-0.001
N-9	99.17	0.013	0.003	0.000	-0.002	0.024	11.184	-0.007	0.269	0.659	-0.002	0.000

J series: CO_2 – 100°C - Cardium

Sample	Reaction time (hrs)	B (ppm)	Mg (ppm)	Al (ppm)	Si (ppm)	P (ppm)	K (ppm)	Ca (ppm)	Ti (ppm)	V (ppm)	Cr (ppm)	Mn (ppm)
J-1	-0.6	11.04	5.23	1.07	11.36	1.89	11.17	9.84	0.0243	0.3232	0.0078	1.01
J-2	0.6	15.81	4.82	1.86	20.76	2.04	10.44	9.98	0.0310	0.5110	0.4212	1.65
J-3	1.7	10.72	5.85	1.17	12.58	2.03	12.74	12.04	0.0243	0.2085	0.5339	1.61
J-4	3.9	14.64	6.31	1.58	15.60	2.03	12.71	13.23	0.0254	0.4258	0.5322	1.66
J-5	5.7	11.66	7.06	1.18	14.10	2.35	13.05	14.39	0.0254	0.1773	0.4685	1.79
J-6	24.0	15.73	9.24	1.62	19.01	2.23	15.34	18.90	0.0251	0.2408	0.2550	2.09
J-7	29.7	11.04	10.11	1.16	21.28	2.38	16.23	20.52	0.0305	0.2255	0.2160	2.26
J-8	46.7	11.67	11.12	1.27	21.96	2.48	17.03	22.09	0.0296	0.1917	0.1761	2.39
J-9	97.5	9.54	12.86	1.24	25.94	2.46	18.81	26.77	0.0321	0.3092	0.1268	2.72
J-10	169.9	7.01	13.83	0.85	26.38	2.69	19.80	29.39	0.0281	0.2359	0.1032	3.01
J-11	196.6	13.27	13.91	1.28	30.56	2.81	20.72	29.17	0.0340	0.3106	0.1003	3.09
J-12	241.6	5.06	14.62	0.66	27.35	2.93	19.50	31.01	0.0290	0.1950	0.1029	3.80
J-13	335.4	9.76	14.98	1.06	29.68	2.92	20.72	32.89	0.0323	0.3425	0.0996	4.64

Sample	Reaction time (hrs)	Fe (ppm)	Co (ppm)	Ni (ppm)	Cu (ppm)	Zn (ppm)	As (ppm)	Se (ppm)	Rb (ppm)	Sr (ppm)	Zr (ppm)	Mo (ppm)
J-1	-0.6	4.71	0.0247	0.61	0.606	0.098	0.001	0.000	0.071	0.346	0.003	1.107
J-2	0.6	36.22	0.1664	5.96	0.826	0.358	0.004	0.001	0.069	0.335	0.009	0.081
J-3	1.7	47.82	0.1544	5.15	0.876	0.224	0.009	0.000	0.083	0.373	0.001	0.047
J-4	3.9	58.27	0.1609	5.59	0.887	0.265	0.007	-0.001	0.089	0.381	0.002	0.076
J-5	5.7	69.70	0.1780	6.52	0.939	0.263	0.009	0.000	0.101	0.403	0.001	0.045
J-6	24.0	109.65	0.2164	9.09	1.045	0.475	0.012	0.001	0.127	0.420	0.002	0.074
J-7	29.7	122.29	0.2312	9.80	0.921	0.436	0.017	0.000	0.139	0.439	0.002	0.060
J-8	46.7	136.21	0.2457	10.96	0.897	0.517	0.015	-0.001	0.151	0.455	0.003	0.066

J-9	97.5	167.06	0.2868	13.86	0.891	0.746	0.023	0.000	0.173	0.499	0.003	0.078
J-10	169.9	191.82	0.3208	16.33	0.912	0.907	0.022	0.000	0.185	0.521	0.002	0.093
J-11	196.6	195.36	0.3254	16.77	0.958	0.900	0.023	0.000	0.181	0.516	0.003	0.092
J-12	241.6	214.21	0.3527	18.43	0.981	0.927	0.028	-0.001	0.189	0.543	0.001	0.085
J-13	335.4	235.25	0.3792	20.02	1.448	1.022	0.031	0.000	0.187	0.546	0.002	0.110

Sample	Reaction time (hrs)	Ag (ppm)	Cd (ppm)	Sn (ppm)	Sb (ppm)	Cs (ppm)	Ba (ppm)	Ti (ppm)	Pb (ppm)	Bi (ppm)	Th (ppm)	U (ppm)
J-1	-0.6	-0.002	0.002	0.000	0.000	0.011	3.00	0.002	0.029	0.678	0.000	0.000
J-2	0.6	-0.002	0.000	0.006	0.000	0.011	3.14	0.002	0.131	1.470	0.000	0.000
J-3	1.7	-0.001	0.000	0.000	0.000	0.011	3.42	0.002	0.107	0.261	0.000	0.000
J-4	3.9	0.000	0.000	0.002	0.000	0.013	3.46	0.002	0.112	1.040	0.000	0.000
J-5	5.7	-0.001	0.000	-0.001	0.000	0.015	3.63	0.002	0.136	0.131	0.000	0.000
J-6	24.0	-0.001	0.000	0.004	0.000	0.018	3.68	0.002	0.172	0.421	0.000	0.000
J-7	29.7	0.000	0.000	0.000	0.000	0.019	3.85	0.003	0.182	0.312	0.000	0.000
J-8	46.7	0.000	0.000	-0.002	0.000	0.021	3.89	0.002	0.187	0.218	0.000	0.000
J-9	97.5	-0.001	0.001	0.002	0.000	0.024	4.35	0.003	0.212	0.631	0.000	0.000
J-10	169.9	-0.001	0.001	0.001	0.000	0.025	4.32	0.003	0.214	0.330	0.000	0.000
J-11	196.6	-0.001	0.001	-0.002	0.000	0.025	4.29	0.003	0.204	0.565	0.000	0.000
J-12	241.6	-0.001	0.001	-0.001	0.000	0.025	4.42	0.003	0.209	0.190	0.000	0.000
J-13	335.4	-0.001	0.002	0.001	0.000	0.026	4.39	0.003	0.200	0.706	0.000	0.000

Cranfield series

Major ions (IC):

Sample	Reaction time (hrs)	Li (ppm)	Na (ppm)	NH4 (ppm)	K (ppm)	Mg (ppm)	Ca (ppm)	F (ppm)	Cl (ppm)	NO2 (ppm)	Br (ppm)	PO4 (ppm)	SO4 (ppm)	Alk. (ppm)
P series: CO_2 – 70°C - Cranfield														
P-1	-0.5	0.0	***43200***	0.0	5.8	10.0	125.0	0.0	***66600***	0.0	78.7	0.0	21.8	61
P-2	3.4	0.0	***43200***	0.0	6.1	11.0	129.8	0.0	***66600***	0.0	80.6	0.0	23.7	113.7
P-3	5.3	0.0	***43200***	0.0	6.3	11.8	133.8	0.0	***66600***	0.0	79.6	0.0	20.8	124.3
P-4	23.1	0.0	***43200***	0.0	7.2	15.8	154.6	0.0	***66600***	0.0	75.4	0.0	25.5	174.4
P-5	29.3	0.0	***43200***	0.0	7.5	16.7	156.4	0.0	***66600***	0.0	80.1	0.0	23.6	214.8
P-6	50.6	0.0	***43200***	0.0	8.1	18.7	159.0	0.0	***66600***	0.0	77.1	0.0	26.3	275.5
P-7	118.8	0.1	***43200***	0.0	9.8	21.2	178.4	0.0	***66600***	0.0	76.8	0.0	28.5	235
P-8	143.8	0.1	***43200***	0.0	10.6	22.5	173.6	0.0	***66600***	0.0	81.8	0.0	34.0	362.2
P-9	167.1	0.0	***43200***	0.0	2.0	3.0	57.3	0.0	***66600***	0.0	91.6	0.0	23.8	379.1

Sample	Reaction time (hrs)	Li (ppm)	Na (ppm)	NH4 (ppm)	K (ppm)	Mg (ppm)	Ca (ppm)	F (ppm)	Cl (ppm)	NO2 (ppm)	Br (ppm)	PO4 (ppm)	SO4 (ppm)	Alk. (ppm)
P-10	197.1	0.0	***43200***	0.0	11.3	24.1	167.6	0.0	***66600***	0.0	83.1	0.0	27.4	412.8
P-11	214.1	0.0	***43200***	0.0	11.7	26.8	178.6	0.0	***66600***	0.0	86.5	0.0	29.9	391.7
O series: O_2+CO_2 – 70°C - Cranfield														
O-1	-1.6	0.0	***43200***	0.0	5.2	9.2	104.7		***66600***	0.0	75.7	0.0	21.5	61
O-2	1.3	0.0	***43200***	0.0	6.1	7.7	100.0		***66600***	0.0	67.7	0.0	18.3	83.4
O-3	4.9	0.0	***43200***	0.0	6.0	8.9	113.6		***66600***	0.0	73.0	0.0	20.7	83.4
O-4	24.8	0.0	***43200***	0.0	6.2	12.2	134.1		***66600***	0.0	73.7	0.0	24.1	214.8
O-5	46.5	0.0	***43200***	0.0	6.5	14.8	147.8		***66600***	0.0	73.6	0.0	27.5	193.8
O-6	120.2	0.0	***43200***	0.0	6.8	20.6	158.5		***66600***	0.0	72.5	0.0	34.9	240.1
O-7	142.3	0.1	***43200***	0.0	6.6	21.9	162.7		***66600***	0.0	74.4	0.0	44.9	227.4
O-8	171.8	0.0	***43200***	0.0	7.0	22.7	163.0		***66600***	0.0	77.3	0.0	43.2	278
O-9	194.5	0.0	***43200***	0.0	6.9	24.0	163.8		***66600***	0.0	77.8	0.0	42.9	265.4
O-10	215.8	0.0	***43200***	0.0	7.0	27.3	163.4		***66600***	0.0	77.1	0.0	45.1	261.1
O-11	265.3	0.0	***43200***	0.0	7.0	27.7	167.0		***66600***	0.0	79.7	0.0	47.4	261.1

Major and Trace elements (ICP-MS):

P Series: CO_2 – 70°C - Cranfield

Sample	Reaction time (hrs)	B (ppm)	Mg (ppm)	Al (ppm)	Si (ppm)	P (ppm)	K (ppm)	Ca (ppm)	Ti (ppm)	V (ppm)	Cr (ppm)	Mn (ppm)
P-1	-0.5	12.459	11.223	0.978	19.704	2.129	8.571	123.595	0.036	0.136	0.317	0.329
P-2	3.4	12.637	12.140	1.565	20.169	1.975	9.000	130.412	0.032	0.133	0.142	0.661
P-3	5.3	11.760	12.983	1.923	20.422	2.004	9.652	137.573	0.027	0.149	0.130	0.810
P-4	23.1	15.817	17.428	3.858	23.252	2.230	10.180	152.936	0.031	0.175	0.129	1.645
P-5	29.3	12.657	18.509	3.824	23.049	2.017	10.860	157.082	0.033	0.120	0.223	1.811
P-6	50.6	16.467	20.308	3.873	24.914	2.099	11.572	161.857	0.034	0.121	0.290	2.084
P-7	118.8	18.980	22.853	3.420	26.137	2.239	13.526	168.326	0.032	0.157	0.191	2.306
P-8	143.8	28.416	22.757	3.967	28.062	2.338	13.929	165.210	0.039	0.307	0.322	2.267
P-9	167.1	14.279	24.721	2.912	25.316	2.251	15.226	178.213	0.033	0.158	0.122	2.411
P-10	197.1	18.364	25.999	3.466	26.356	2.445	15.272	181.892	0.033	0.186	0.151	2.481
P-11	214.1	13.552	25.558	2.296	23.702	2.349	16.006	178.520	0.028	0.163	0.106	2.372

Sample	Reaction time (hrs)	Fe (ppm)	Co (ppm)	Ni (ppm)	Cu (ppm)	Zn (ppm)	As (ppm)	Se (ppm)	Rb (ppm)	Sr (ppm)	Zr (ppm)	Mo (ppm)
P-1	-0.5	1.437	0.004	0.167	0.948	1.675	0.000	0.000	0.050	5.780	0.002	0.095
P-2	3.4	5.333	0.016	0.478	1.076	10.427	0.002	0.001	0.053	5.864	0.002	0.048

P-3	5.3	8.700	0.015	0.369	1.014	13.030	0.001	0.003	0.055	6.045	0.001	0.046
P-4	23.1	30.374	0.029	0.610	0.974	18.398	-0.001	0.002	0.061	5.932	0.001	0.055
P-5	29.3	35.208	0.031	0.742	1.046	19.034	0.002	0.002	0.061	5.953	0.002	0.077
P-6	50.6	45.146	0.035	0.807	1.058	20.023	-0.002	0.000	0.064	5.976	0.002	0.082
P-7	118.8	57.556	0.042	0.843	1.064	21.931	0.002	0.002	0.064	5.926	0.002	0.105
P-8	143.8	58.017	0.043	0.945	0.992	21.967	-0.001	0.002	0.063	5.795	0.003	0.121
P-9	167.1	61.197	0.044	0.924	1.128	23.914	0.001	0.001	0.068	6.202	0.002	0.081
P-10	197.1	62.067	0.046	0.994	1.121	24.906	-0.001	0.002	0.069	6.411	0.002	0.109
P-11	214.1	59.590	0.046	0.967	1.120	23.817	0.003	0.000	0.067	6.114	0.002	0.103

Sample	Reaction time (hrs)	Ag (ppm)	Cd (ppm)	Sn (ppm)	Sb (ppm)	Cs (ppm)	Ba (ppm)	Tl (ppm)	Pb (ppm)	Bi (ppm)	Th (ppm)	U (ppm)
P-1	-0.5	0.002	-0.001	0.000	0.000	0.005	1.440	0.000	-0.008	0.526	-0.002	0.000
P-2	3.4	0.004	0.000	-0.001	0.001	0.006	1.588	0.001	-0.002	0.510	-0.002	0.000
P-3	5.3	0.001	-0.001	0.001	0.000	0.006	1.657	0.000	-0.003	0.578	-0.004	0.000
P-4	23.1	0.002	0.000	-0.002	0.000	0.007	1.813	0.001	0.013	0.651	-0.002	0.000
P-5	29.3	0.002	0.000	0.000	0.000	0.007	1.968	0.000	0.018	0.427	-0.003	0.000
P-6	50.6	0.002	0.000	-0.001	0.000	0.008	2.166	0.001	0.031	0.410	-0.003	0.000
P-7	118.8	0.002	0.000	0.000	0.000	0.008	2.570	0.000	0.044	0.585	-0.003	0.000
P-8	143.8	0.002	-0.001	0.000	0.000	0.009	2.584	0.000	0.044	1.249	-0.003	0.000
P-9	167.1	0.001	0.000	0.000	0.000	0.009	2.804	0.000	0.050	0.637	-0.003	0.000
P-10	197.1	0.001	0.000	0.001	0.000	0.009	2.864	0.001	0.053	0.731	-0.003	0.000
P-11	214.1	0.002	0.000	0.001	0.004	0.008	2.776	0.001	0.053	0.669	-0.003	0.000

O series: O_2+CO_2 – 70°C - Cranfield

Sample	Reaction time (hrs)	B (ppm)	Mg (ppm)	Al (ppm)	Si (ppm)	P (ppm)	K (ppm)	Ca (ppm)	Ti (ppm)	V (ppm)	Cr (ppm)	Mn (ppm)
O-1	-1.6	10.088	9.095	0.894	19.213	1.132	8.720	117.913	0.163	0.006	0.080	0.192
O-2	1.3	10.463	9.357	1.211	19.137	1.368	10.196	122.487	0.193	0.054	0.138	0.294
O-3	4.9	9.368	10.271	1.524	19.197	1.335	9.860	128.680	0.212	0.101	0.072	0.571
O-4	24.8	8.857	14.069	3.260	21.323	1.383	10.377	151.416	0.251	0.056	0.092	1.649
O-5	46.5	11.343	16.068	3.225	22.725	1.350	10.073	158.049	0.262	0.102	0.050	2.200
O-6	120.2	9.565	21.704	2.408	23.666	1.218	10.731	169.090	0.252	0.059	0.054	2.731
O-7	142.3	28.718	21.487	3.406	26.395	1.244	10.463	161.406	0.195	0.208	0.076	2.626
O-8	171.8	14.216	23.653	2.506	24.051	1.152	10.569	168.246	0.076	0.101	0.069	2.754
O-9	194.5	12.016	24.474	2.291	24.142	1.127	10.271	169.289	0.078	0.080	0.046	2.765
O-10	215.8	13.242	25.599	2.304	24.925	1.153	10.866	170.121	0.085	0.068	0.059	2.799
O-11	265.3	9.894	28.821	2.015	24.824	1.206	11.609	177.355	0.089	0.035	0.102	2.920

Sample	Reaction time (hrs)	Fe (ppm)	Co (ppm)	Ni (ppm)	Cu (ppm)	Zn (ppm)	As (ppm)	Se (ppm)	Rb (ppm)	Sr (ppm)	Zr (ppm)	Mo (ppm)
O-1	-1.6	0.679	0.012	0.138	1.764	2.278	0.001	0.000	0.037	5.142	0.003	0.125
O-2	1.3	2.380	0.006	0.499	2.053	4.280	-0.001	0.000	0.036	5.025	0.002	0.175
O-3	4.9	5.107	0.013	0.880	2.315	7.489	0.003	0.000	0.039	5.165	0.002	0.150

O-4	24.8	14.685	0.029	1.591	2.748	10.112	0.006	0.001	0.044	5.253	0.001	0.112
O-5	46.5	12.601	0.035	1.782	3.002	10.497	0.002	0.001	0.046	5.194	0.002	0.052
O-6	120.2	0.527	0.050	2.412	3.171	11.942	0.000	0.001	0.050	5.278	0.002	0.014
O-7	142.3	0.799	0.050	2.598	2.797	11.600	0.001	0.004	0.047	5.090	0.003	0.040
O-8	171.8	0.617	0.055	2.665	1.635	12.242	0.004	0.002	0.048	5.290	0.002	0.021
O-9	194.5	0.433	0.057	2.779	1.775	12.449	0.001	0.002	0.049	5.336	0.003	0.019
O-10	215.8	0.519	0.060	2.934	1.905	12.708	0.001	0.001	0.050	5.383	0.003	0.016
O-11	265.3	0.694	0.066	3.342	2.169	13.508	0.000	0.000	0.052	5.565	0.003	0.013
Sample	**Reaction time (hrs)**	**Ag (ppm)**	**Cd (ppm)**	**Sn (ppm)**	**Sb (ppm)**	**Cs (ppm)**	**Ba (ppm)**	**Tl (ppm)**	**Pb (ppm)**	**Bi (ppm)**	**Th (ppm)**	**U (ppm)**
O-1	-1.6	0.000	-0.002	-0.003	-0.001	0.003	1.056	-0.009	-0.002	0.001	-0.002	-0.002
O-2	1.3	0.000	-0.002	-0.003	-0.002	0.003	1.119	-0.009	0.008	0.180	-0.002	-0.002
O-3	4.9	0.000	-0.002	-0.001	-0.001	0.003	1.214	-0.009	0.006	0.371	-0.002	-0.002
O-4	24.8	0.000	-0.003	-0.003	-0.002	0.004	1.482	-0.009	0.020	0.179	-0.002	-0.002
O-5	46.5	0.000	-0.003	-0.003	-0.002	0.004	1.649	-0.009	0.027	0.374	-0.002	-0.002
O-6	120.2	0.000	-0.003	-0.002	-0.002	0.004	2.117	-0.009	0.038	0.216	-0.002	-0.002
O-7	142.3	0.000	-0.002	0.000	-0.002	0.005	2.109	-0.009	0.038	0.814	-0.002	-0.002
O-8	171.8	0.000	-0.002	-0.004	-0.002	0.005	2.350	-0.009	0.042	0.387	-0.002	-0.002
O-9	194.5	0.000	-0.002	-0.003	-0.002	0.005	2.475	-0.008	0.042	0.314	-0.002	-0.002
O-10	215.8	-0.001	-0.002	-0.003	-0.002	0.005	2.599	-0.009	0.043	0.261	-0.002	-0.002
O-11	265.3	-0.001	-0.002	-0.004	0.002	0.005	3.057	-0.009	0.046	0.140	-0.002	-0.002

XI-2. Release Rate Results

Offshore Miocene series

Sample	Reaction time (hours)	K (mmol/L*hr)/g	Mg (mmol/L*hr)/g	Ca (mmol/L*hr)/g	SO4 (mmol/L*hr)/g
D series: CO_2 – 70°C - Miocene					
D-1	-94.42				
D-2	-94.42				
D-3	-66.50				
D-4	-1.75				
D-5	2.25	0.00148	0.01531	0.42164	0.00217
D-6	4.25	0.00095	0.01029	0.29547	0.00155
D-7	6.25	0.00064	0.00756	0.22579	0.00055
D-8	8.25	0.00058	0.00636	0.19606	0.00051
D-9	25.75	0.00025	0.00259	0.09017	0.00034
D-10	32.83	0.00020	0.00208	0.07513	0.00033
D-11	49.75	0.00011	0.00139	0.05208	0.00027
D-12	100.25	0.00009	0.00083	0.03073	0.00011
D-13	166.50	0.00007	0.00055	0.02050	0.00011
R series: O_2+CO_2 – 70°C - Miocene					
R-1	-66.25				
R-2	-1.25	0.00412	0.00721	0.40846	0.00522
R-3	0.75	0.00100	0.00290	0.16567	0.00134
R-4	4.08	0.00071	0.00288	0.16177	0.00122
R-5	7.00	0.00030	0.00146	0.07239	0.00063
R-6	22.92	0.00025	0.00120	0.05870	0.00070
R-7	30.75	0.00019	0.00093	0.04298	0.00049
R-8	46.92	0.00017	0.00082	0.03824	0.00040
R-9	54.25	0.00012	0.00065	0.02953	0.00034
R-10	72.25	0.00010	0.00053	0.02324	0.00040
R-11	100.67	0.00009	0.00046	0.01977	0.00038
R-12	127.25	0.00008	0.00039	0.01630	0.00035
R-13	168.25	0.00007	0.00034	0.01344	0.00030
R-14	215.75	0.00006	0.00031	0.01199	0.00028
R-15	243.25	0.00006	0.00030	0.01137	0.00027
R-16	263.75				
L series: CO_2 – 100°C - Miocene					
L-1	-0.67				
L-2	1.00	-0.00073	0.01638	0.40660	0.00016
L-3	3.00	-0.00026	0.00941	0.25296	-0.00256
L-4	6.33	0.00009	0.00574	0.17257	-0.00042
L-5	22.75	0.00018	0.00245	0.08016	0.00013

Sample	Reaction time (hours)	K (mmol/L*hr)/g	Mg (mmol/L*hr)/g	Ca (mmol/L*hr)/g	SO4 (mmol/L*hr)/g
L-6	29.33	0.00019	0.00214	0.06896	0.00011
L-7	47.33	0.00019	0.00151	0.04968	0.00002
L-8	72.33	0.00013	0.00104	0.03495	0.00014
S series: O_2+CO_2 – 100°C - Miocene					
S-1	-1.1				
S-2	1.2	0.00023	0.00397	0.14766	-0.00211
S-3	2.2	0.00030	0.00428	0.13531	0.00063
S-4	4.6	0.00028	0.00366	0.10388	0.00100
S-5	22.3	0.00020	0.00234	0.05646	0.00102
S-6	29.0	0.00018	0.00204	0.04868	0.00080
S-7	45.5	0.00010	0.00154	0.03621	0.00074
S-8	71.3	0.00010	0.00123	0.02574	0.00064
S-9	94.9	0.00010	0.00108	0.02255	0.00061
S-10	123.4	0.00009	0.00093	0.01833	0.00052
S-11	168.8	0.00007	0.00077	0.01466	0.00049
S-12	243.1	0.00007	0.00061	0.01090	0.00017
H series: CO_2 – 130°C - Miocene					

Cardium Sand series

Sample	Reaction time (hours)	K (mmol/L*hr)/g	Mg (mmol/L*hr)/g	Ca (mmol/L*hr)/g	SO4 (mmol/L*hr)/g
K series: CO_2 – 70°C - Cardium					
K-1	-1.5				
K-2	1.2	0.00018	0.00122	-0.00098	0.00056
K-3	6.2	0.00053	0.00062	0.00050	-0.00007
K-4	23.5	0.00022	0.00026	0.00025	0.00008
K-5	97.5	0.00012	0.00027	0.00010	0.00005
K-6	142.5	0.00009	0.00021	0.00007	0.00004
K-7	191.0	0.00007	0.00021	0.00006	0.00001
K-8	242.5	0.00006	0.00014	0.00004	0.00002
K-9	287.0	0.00005	0.00012	0.00004	0.00002
K-10	335.3	0.00005	0.00011	0.00003	0.00001
K-11	383.0	0.00005	0.00010	0.00003	0.00004
N series: O_2+CO_2 – 70°C - Cardium					
N1	-1.5				
N2	0.2	0.00738	0.00937	0.00000	0.00000
N3	2.5	0.00124	0.00157	0.00136	0.00033
N4	7.0	0.00272	0.00124	0.00171	0.00080
N5	23.0	0.00066	0.00093	0.00106	0.00084

Sample	Reaction time (hours)	K (mmol/L*hr)/g	Mg (mmol/L*hr)/g	Ca (mmol/L*hr)/g	SO4 (mmol/L*hr)/g
N6	30.5	0.00053	0.00084	0.00156	0.00085
N7	48.2	0.00043	0.00076	0.00072	0.00081
N8	72.2	0.00033	0.00070	0.00059	0.00081
N9	99.2	0.00028	0.00066	0.00068	0.00070
J series: CO_2 – 100°C - Cardium					

Cranfield series

Sample	Reaction time (hours)	K (mmol/L*hr)/g	Mg (mmol/L*hr)/g	Ca (mmol/L*hr)/g	SO4 (mmol/L*hr)/g
P series: CO_2 – 70°C - Cranfield					
P-2	3.4	0.00027	0.00147	0.00412	0.00066
P-3	5.3	0.00026	0.00168	0.00489	-0.00024
P-4	23.1	0.00018	0.00122	0.00379	0.00020
P-5	29.3	0.00017	0.00112	0.00317	0.00007
P-6	50.6	0.00014	0.00084	0.00199	0.00011
P-7	118.8	0.00010	0.00046	0.00133	0.00007
P-8	143.8	0.00010	0.00043	0.00100	0.00010
P-9	167.1	-0.00007	-0.00020	-0.00120	0.00001
P-10	197.1	0.00008	0.00035	0.00064	0.00003
P-11	214.1	0.00008	0.00038	0.00074	0.00005
O series: O_2+CO_2 – 70°C - Cranfield					
O-1	-1.6				
O-2	1.3	0.00227	-0.00630	-0.01163	-0.00324
O-3	4.9	0.00052	-0.00032	0.00559	-0.00021
O-4	24.8	0.00012	0.00062	0.00365	0.00014
O-5	46.5	0.00009	0.00062	0.00285	0.00017
O-6	120.2	0.00004	0.00048	0.00138	0.00014
O-7	142.3	0.00003	0.00045	0.00125	0.00021
O-8	171.8	0.00003	0.00040	0.00105	0.00016
O-9	194.5	0.00003	0.00039	0.00093	0.00014
O-10	215.8	0.00003	0.00043	0.00084	0.00014
O-11	265.3	0.00002	0.00035	0.00072	0.00013

XII. Appendix G: Batch Modeling PHREEQC Input file

by Changbing Yang

XII-1. A series

A series describes a Miocene sample exposed to DI water and pure CO_2 at 100°C and 200 bars

```
PHASES
Calcite
        Mg0.035Ca0.965CO3 = CO3-2 + 0.965Ca+2 + 0.035Mg+2
        log_k           -8.480
        delta_h -2.297 kcal
        -analytic       -171.9065     -0.077993      2839.319      71.595

SOLUTION 1
   temp      100
   pH       6.92
   pe       4
   redox     pe
   units     ppm
   density   1.11
   K        6.583e-5  Mol/kgs
   Mg        1.32e-4 Mol/kgs
   Ca       5.734e-4 Mol/kgs
   Cl        0.001 Mol/kgs  charge
   Na       1.058e-3 Mol/kgs
   Al      3.008e-5 Mol/kgs
   Si       6.815e-4 Mol/kgs
   -water    0.15 # kg

GAS_PHASE 1
   -fixed_pressure
   -pressure 120.36
   -volume 1
   -temperature 100
   CO2(g)    120.36

KINETICS 1
-cvode
Quartz
      -parms 1.023e-14
      -m0 0.0579      # moles in rocks
      -m  0.0579
     -steps   1966000 in 5000 steps       # in seconds
Kaolinite
      -parms 6.918e-14 4.898e-12  8.913e-18
      -m0 0.00192
      -m  0.00192
Calcit
      -parms 1.549e-6 5.012e-1
      -m0 0.009432
      -m  0.009432
Illite
      -parms 1.660e-13 1.047e-11 3.020e-17
      -m0 0.00104
      -m  0.00104
Albite
      -parms 1.445e-12 2.138e-10
      -m0 0.005613448
      -m  0.005613448
K-feldspar
      -parms 3.89e-13 8.71e-11 6.31e-22
      -m0 0.004369
      -m  0.004369
Magnesite
```

```
        -parms 4.571e-10 4.169e-7
        -m0 0.0
        -m  0.0
Ankerite
        -parms 1.26e-9 1.59e-4
        -m0 0.0
        -m  0.0
Dawsonite
        -parms 1.26e-9 1.59e-4
        -m0 0.0
        -m  0.0
Ca-smectite
        -parms 1.66e-13 1.047e-11 3.020e-17
        -m0 0.0
        -m  0.0
Siderite
        -parms 1.26e-9 1.59e-4
        -m0 0.0
        -m  0.0

INCREMENTAL_REACTIONS   true

RATES
Quartz
-start
  40  SR_Qu = SR("Quartz")
  45  if (M <= 0 and SR_Qu < 1) then goto 200
  50  k1 = exp(-87.7e3/8.314472*(1/TK - 1/298.15))
  52  SA = 100.0
  55  rate = SA*PARM(1) * (M/M0)^0.67 * (1 - SR_Qu)
  60  moles=rate*TIME
  70  PUT(rate,1)
  200 SAVE moles
-end
Kaolinite
 -start
  40  SR_kao = SR("Kaolinite")
  45  if (M <= 0 and SR_kao < 1) then goto 200
  50  ek1 = exp(-87.7e3/8.314472*(1/TK - 1/298.15))
  52  ek2 = exp(-65.9e3/8.314472*(1/TK - 1/298.15))
  54  ek3 = exp(-17.9e3/8.314472*(1/TK - 1/298.15))
  56  SA = 0.1
  60  r1=ek1*PARM(1)
  65  r2=ek2*PARM(2)*act("H+")^.777
  67  r3=ek3*PARM(3)*act("H+")^-.472
  70  rate = SA*(M/M0)^0.67 *(1 - SR_kao)*(r1+r2+r3)
  80  moles=rate*TIME
  90  PUT(rate,2)
  200 SAVE moles
 -end
Calcit
 -start
  40  SR_ca = SR("Calcit")
  45  if (M <= 0 and SR_ca < 1) then goto 200
  50  ek1 = exp(-23.5e3/8.314472*(1/TK - 1/298.15))
  52  ek2 = exp(-14.4e3/8.314472*(1/TK - 1/298.15))
  56  SA = 0.00004
  60  r1=ek1*PARM(1)
  65  r2=ek2*PARM(2)*act("H+")
  70  rate = SA*(M/M0)^0.67 *(1 - SR_ca)*(r1+r2)
  80  moles=rate*TIME
  90  PUT(rate,3)
  200 SAVE moles
 -end
Illite
 -start
  40  SR_Il = SR("Illite")
  45  if (M <= 0 and SR_Il < 1) then goto 200
  50  ek1 = exp(-35e3/8.314472*(1/TK - 1/298.15))
  52  ek2 = exp(-23.6e3/8.314472*(1/TK - 1/298.15))
```

```
  54  ek3 = exp(-58.9e3/8.314472*(1/TK - 1/298.15))
  56  SA = 0.1
  60  r1=ek1*PARM(1)
  65  r2=ek2*PARM(2)*act("H+")^.34
  67  r3=ek3*PARM(3)*act("H+")^-.4
  70  rate = SA*(M/M0)^0.67 *(1 - SR_Il)*(r1+r2+r3)
  80  moles=rate*TIME
  90  PUT(rate,4)
  200 SAVE moles
 -end
Albite
 -start
  40  SR_og = SR("Albite")
  45  if (M <= 0 and SR_og < 1) then goto 200
  50  ek1 = exp(-69.8e3/8.314472*(1/TK - 1/298.15))
  52  ek2 = exp(-65.0e3/8.314472*(1/TK - 1/298.15))
 # 54  ek3 = exp(-58.9e3/8.314472*(1/TK - 1/298.15))
  56  SA = 0.17
  60  r1=ek1*PARM(1)
  65  r2=ek2*PARM(2)*act("H+")^.457
#  67  r3=ek3*PARM(3)*act("H+")^-.4
  70  rate = SA*(M/M0)^0.67 *(1 - SR_og)*(r1+r2)
  80  moles=rate*TIME
  90  PUT(rate,4)
  200 SAVE moles
 -end
 K-feldspar
 -start
  40  SR_Kf = SR("K-feldspar")
  45  if (M <= 0 and SR_Kf < 1) then goto 200
  50  ek1 = exp(-38.0e3/8.314472*(1/TK - 1/298.15))
  52  ek2 = exp(-51.7e3/8.314472*(1/TK - 1/298.15))
  54  ek3 = exp(-94.1e3/8.314472*(1/TK - 1/298.15))
  56  SA = 0.35
  60  r1=ek1*PARM(1)
  65  r2=ek2*PARM(2)*act("H+")^.5
  67  r3=ek3*PARM(3)*act("H+")^-.4
  70  rate = SA*(M/M0)^0.67 *(1 - SR_Kf)*(r1+r2+r3)
  80  moles=rate*TIME
  90  PUT(rate,6)
  200 SAVE moles
 -end

Magnesite
 -start
  40  SR_Ma = SR("Magnesite")
 # 45  if (M <= 0 and SR_Ma < 1) then goto 200
  50  ek1 = exp(-23.5e3/8.314472*(1/TK - 1/298.15))
  52  ek2 = exp(-14.4e3/8.314472*(1/TK - 1/298.15))
  56  SA = 0.01
  60  r1=ek1*PARM(1)
  65  r2=ek2*PARM(2)*act("H+")
  70  rate = SA*(1 - SR_Ma)*(r1+r2)
  80  moles=rate*TIME
  90  PUT(rate,7)
  200 SAVE moles
 -end

Dawsonite
 -start
  40  SR_da= SR("Dawsonite")
 # 45  if (M <= 0 and SR_da < 1) then goto 200
  50  ek1 = exp(-62.76e3/8.314472*(1/TK - 1/298.15))
  52  ek2 = exp(-45.0e3/8.314472*(1/TK - 1/298.15))
  56  SA = 0.01
  60  r1=ek1*PARM(1)
  65  r2=ek2*PARM(2)*act("H+")^0.9
  70  rate = SA*(1 - SR_da)*(r1+r2)
  80  moles=rate*TIME
  90  PUT(rate,9)
```

```
 200 SAVE moles
-end

Ca-smectite
-start
 40  SR_smv= SR("Ca-smectite")
# 45  if (M <= 0 and SR_smv < 1) then goto 200
 50  ek1 = exp(-35e3/8.314472*(1/TK - 1/298.15))
 52  ek2 = exp(-23.6e3/8.314472*(1/TK - 1/298.15))
 54  ek3 = exp(-58.9e3/8.314472*(1/TK - 1/298.15))
 56  SA = 0.01
 60  r1=ek1*PARM(1)
 65  r2=ek2*PARM(2)*act("H+")^.34
 67  r3=ek3*PARM(3)*act("H+")^-.4
 70  rate = SA*(1 - SR_smv)*(r1+r2+r3)
 80  moles=rate*TIME
 90  PUT(rate,12)
 200 SAVE moles
-end

Siderite
-start
 40  SR_si = SR("Siderite")
#  45  if (M <= 0 and SR_si < 1) then goto 200
 50  ek1 = exp(-62.76e3/8.314472*(1/TK - 1/298.15))
 52  ek2 = exp(-45.0e3/8.314472*(1/TK - 1/298.15))
 56  SA = 0.01
 60  r1=ek1*PARM(1)
 65  r2=ek2*PARM(2)*act("H+")^0.9
 70  rate = SA*(1 - SR_si)*(r1+r2)
 80  moles=rate*TIME
 90  PUT(rate,9)
 200 SAVE moles
-end

Ankerite
-start
 40  SR_an= SR("Ankerite")
# 45  if (M <= 0 and SR_an < 1) then goto 200
 50  ek1 = exp(-62.76e3/8.314472*(1/TK - 1/298.15))
 52  ek2 = exp(-45.0e3/8.314472*(1/TK - 1/298.15))
 56  SA = 0.01
 60  r1=ek1*PARM(1)
 65  r2=ek2*PARM(2)*act("H+")^0.9
 70  rate = SA*(1 - SR_an)*(r1+r2)
 80  moles=rate*TIME
 90  PUT(rate,10)
 200 SAVE moles
-end

SELECTED_OUTPUT
       -file  a_run1.sel
       -pe            false
       -totals         Ca Mg Na K Si C(4) Al
       -si             Quartz Kaolinite calcit Illite K-Feldspar Magnesite Dawsonite Ankerite
              -kinetic_reactants  Quartz Kaolinite calcit Illite K-Feldspar Magnesite  Dawsonite  Ankerite
#PRINT
#       -reset false
USER_PUNCH
 -head pH  HCO3T CO32T CO2 CO2mas SICO2
 10 HCO3T = mol("HCO3-") + mol("CaHCO3+") + mol("FeHCO3+") + mol("MgHCO3+") + mol("NaHCO3")
 20 CO3T = mol("CO3-2") + mol("CaCO3") + + mol("MgCO3")
 100 PUNCH  -la("H+"), HCO3T, CO3T, mol("CO2"), GAS("CO2(g)"), SI("CO2(g)")
END
```

XII-2. N series

N series describes a Cardium sample exposed to brine and a O_2-CO_2 mixture at 70°C and 200 bars

```
DATABASE     llnl.dat
SOLUTION 1
   temp      70
   pH        6
   pe        -4
   redox     pe
   units     ppm
   density   1
   Na        49688.6
   K         15.1
   Mg        5.9
   Ca        31.2
   Br        73.2
   S(6)      25.7
   Alkalinity 48.2  # used  from K experiment
   -water    0.11 # kg

EQUILIBRIUM_PHASES 1
   Fe(OH)3   0 0

GAS_PHASE 1
   -fixed_pressure
   -pressure 104.243
   -volume 10
   CO2(g)    94.178
   O2(g)     10.065

KINETICS 1
#-cvode
Quartz
       -parms 1.023e-14 0.1336
       -m0 0.1256      # moles in rocks
       -m  0.1256
       -steps   1440000 in 500 steps
Kaolinite
       -parms 6.918e-14 4.898e-12  8.913e-18 0.01912
       -m0 0.004186
       -m  0.004186
Illite
       -parms 1.660e-13 1.047e-11 3.020e-17 0.001139
       -m0 0.001759
       -m  0.001759
Albite
       -parms 2.75423e-13 6.9183e-11 2.5119e-16 0.4406
       -m0  0.000991
       -m    0.000991
K-feldspar
       -parms 3.89e-13 8.71e-11 6.31e-22 2.67783
       -m0 0.001568
       -m  0.001568
Siderite
       -parms 1.26e-9 1.59e-4 0.001095
       -m0 0.000807
       -m  0.000807
Pyrite
        -parms   2.81838e-5  3.01995e-8  0.000001962     # neutral and acid
 #       -parms 6.45654E-09     # 2.81838e-5
        -m0 0.0000866
        -m  0.0000866
Calcite
        -parms   1.54882e-6 0.501187234  0.000331131 0.000000001078    # neutral and acid
        -m0 0.0001103
        -m  0.0001103
Magnesite
```

```
        -parms   4.57e-10 4.17e-7 6.03e-6 0.000000015978    # neutral and acid
        -m0 0.0002003
        -m  0.0002003
Dawsonite
        -parms 1.26e-9 1.59e-4   0.1
        -m0 0.0
        -m  0.0
Dolomite
        -parms 2.951e-8 6.457e-4 7.76247E-06 0.1
        -m0 0.0
        -m  0.0

INCREMENTAL_REACTIONS      true

RATES
Quartz
-start
  40  SR_Qu = SR("Quartz")
  45  if (M <= 0 and SR_Qu < 1) then goto 200
  50  k1 = exp(-87.7e3/8.314472*(1/TK - 1/298.15))
  52  SA = PARM(2)
  55  rate = SA*PARM(1) * (M/M0)^0.67 * (1 - SR_Qu)
  60  moles=rate*TIME
  70  PUT(rate,1)
  200 SAVE moles
-end

Kaolinite
 -start
  40  SR_kao = SR("Kaolinite")
  45  if (M <= 0 and SR_kao < 1) then goto 200
  50  ek1 = exp(-87.7e3/8.314472*(1/TK - 1/298.15))
  52  ek2 = exp(-65.9e3/8.314472*(1/TK - 1/298.15))
  54  ek3 = exp(-17.9e3/8.314472*(1/TK - 1/298.15))
  56  SA = PARM(4)
  60  r1=ek1*PARM(1)
  65  r2=ek2*PARM(2)*act("H+")^.777
  67  r3=ek3*PARM(3)*act("H+")^-.472
  70  rate = SA *(M/M0)^(2/3)*(1 - SR_kao)*(r1+r2+r3)
  80  moles=rate*TIME
  90  PUT(rate,2)
  200 SAVE moles
 -end

Illite
 -start
  40  SR_Il = SR("Illite")
  45  if (M <= 0 and SR_Il < 1) then goto 200
  50  ek1 = exp(-35e3/8.314472*(1/TK - 1/298.15))
  52  ek2 = exp(-23.6e3/8.314472*(1/TK - 1/298.15))
  54  ek3 = exp(-58.9e3/8.314472*(1/TK - 1/298.15))
  56  SA = PARM(4)
  60  r1=ek1*PARM(1)
  65  r2=ek2*PARM(2)*act("H+")^.34
  67  r3=ek3*PARM(3)*act("H+")^-.4
  70  rate = SA *(M/M0)^(2/3)*(1 - SR_Il)*(r1+r2+r3)
  80  moles=rate*TIME
  90  PUT(rate,3)
  200 SAVE moles
 -end

Albite
 -start
  40  SR_og = SR("Albite")
  45  if (M <= 0 and SR_og < 1) then goto 200
  50  ek1 = exp(-69.8e3/8.314472*(1/TK - 1/298.15))
  52  ek2 = exp(-65.0e3/8.314472*(1/TK - 1/298.15))
  54  ek3 = exp(-71.0e3/8.314472*(1/TK - 1/298.15))
  56  SA = PARM(4)
  60  r1=ek1*PARM(1)
```

```
  65  r2=ek2*PARM(2)*act("H+")^.457
  67  r3=ek3*PARM(3)*act("H+")^-.572
  70  rate = SA*(M/M0)^0.67 *(1 - SR_og)*(r1+r2+r3)
  80  moles=rate*TIME
  90  PUT(rate,4)
  200 SAVE moles
 -end

K-feldspar
 -start
  40  SR_Kf = SR("K-feldspar")
  45  if (M <= 0 and SR_Kf < 1) then goto 200
  50  ek1 = exp(-38.0e3/8.314472*(1/TK - 1/298.15))
  52  ek2 = exp(-51.7e3/8.314472*(1/TK - 1/298.15))
  54  ek3 = exp(-94.1e3/8.314472*(1/TK - 1/298.15))
  56  SA = PARM(4)
  60  r1=ek1*PARM(1)
  65  r2=ek2*PARM(2)*act("H+")^.5
  67  r3=ek3*PARM(3)*act("H+")^-.4
  70  rate = SA*(M/M0)^0.67 *(1 - SR_Kf)*(r1+r2+r3)
  80  moles=rate*TIME
  90  PUT(rate,5)
  200 SAVE moles
 -end

Siderite
 -start
  40  SR_si = SR("Siderite")
#  45  if (M <= 0 and SR_si < 1) then goto 200
  50  ek1 = exp(-62.76e3/8.314472*(1/TK - 1/298.15))
  52  ek2 = exp(-45.0e3/8.314472*(1/TK - 1/298.15))
  56  SA = PARM(3)
  60  r1=ek1*PARM(1)
  65  r2=ek2*PARM(2)*act("H+")^0.9
  70  rate = SA*(1 - SR_si)*(r1+r2)
  80  moles=rate*TIME
  90  PUT(rate,6)
  200 SAVE moles
 -end

Pyrite    # Pandera and Kharaka
  -start
  40  SR_py= SR("Pyrite")
  45  if (M <= 0 and SR_py < 1) then goto 200
  50  ek1 = exp(-56.9e3/8.314472*(1/TK - 1/298.15))
  52  ek2 = exp(-56.9e3/8.314472*(1/TK - 1/298.15))
  56  SA = PARM(3)
  60  r1=ek1*PARM(1)*act("O2")^.5
  65  r2=ek2*PARM(2)*act("H+")^-0.5*act("Fe+3")^0.5
  70  rate = SA*(1 - SR_py)*(r1+r2)
  80  moles=rate*TIME
  90  PUT(rate,7)
  200 SAVE moles
  -end

Dawsonite
 -start
  40  SR_da= SR("Dawsonite")
 # 45  if (M <= 0 and SR_da < 1) then goto 200
  50  ek1 = exp(-62.76e3/8.314472*(1/TK - 1/298.15))
  52  ek2 = exp(-45.0e3/8.314472*(1/TK - 1/298.15))
  56  SA = PARM(3)
  60  r1=ek1*PARM(1)
  65  r2=ek2*PARM(2)*act("H+")^0.9
  70  rate = SA*(1 - SR_da)*(r1+r2)
  80  moles=rate*TIME
  90  PUT(rate,8)
  200 SAVE moles
 -end
```

```
Magnesite
 -start
  40  SR_Ma = SR("Magnesite")
  45  if (M <= 0 and SR_Ma < 1) then goto 200
  50  ek1 = exp(-23.5e3/8.314472*(1/TK - 1/298.15))
  52  ek2 = exp(-14.4e3/8.314472*(1/TK - 1/298.15))
  54  ek3 = exp(-62.8e3/8.314472*(1/TK - 1/298.15))
  56  SA = PARM(4)
  60  r1=ek1*PARM(1)
  65  r2=ek2*PARM(2)*act("H+")
  68  r3=ek3*PARM(3)*(10^SI("CO2(g)"))
  70  rate = SA*(M/M0)^(2/3)*(1 - SR_Ma)*(r1+r2+r3)
  80  moles=rate*TIME
  90  PUT(rate,9)
  200 SAVE moles
 -end

Dolomite
 -start
  40  SR_do = SR("Dolomite")
  45  if (M <= 0 and SR_do < 1) then goto 200
  50  ek1 = exp(-52.2e3/8.314472*(1/TK - 1/298.15))
  52  ek2 = exp(-36.1e3/8.314472*(1/TK - 1/298.15))
  54  ek3=  exp(-34.8e3/8.314472*(1/TK - 1/298.15))
  56  SA = PARM(4)
  60  r1=ek1*PARM(1)
  65  r2=ek2*PARM(2)*act("H+")^0.5
  68  r3=ek3*PARM(3)*(10^SI("CO2(g)"))^0.5
  70  rate = SA*(1 - SR_do)*(r1+r2+r3)
  80  moles=rate*TIME
  90  PUT(rate,10)
  200 SAVE moles
 -end

Calcite
 -start
  40  SR_Cal = SR("Calcite")
  45  if (M <= 0 and SR_Cal < 1) then goto 200
  50  ek1 = exp(-23.5e3/8.314472*(1/TK - 1/298.15))
  52  ek2 = exp(-14.4e3/8.314472*(1/TK - 1/298.15))
  54  ek3 = exp(-35.4e3/8.314472*(1/TK - 1/298.15))
  56  SA = PARM(4)
  60  r1=ek1*PARM(1)
  65  r2=ek2*PARM(2)*act("H+")
  68  r3=ek3*PARM(3)*(10^SI("CO2(g)"))
  70  rate = SA*(M/M0)^(2/3)*(1 - SR_Cal)*(r1+r2+r3)
  80  moles=rate*TIME
  90  PUT(rate,11)
  200 SAVE moles
 -end


SELECTED_OUTPUT
       -file  N_run1-spt.sel
       -pe             true
       -totals         Br Ca Mg Na K Si C(4) Al Fe O(0) Fe(3)  Fe(2) S(6)
       -si             Fe(oh)3 O2(g) CO2(g) Quartz Kaolinite Illite Albite K-Feldspar siderite pyrite Dawsonite Magnesite Calcite Dolomite
              -kinetic_reactants  Quartz Kaolinite Illite Albite K-Feldspar siderite pyrite Ankerite Dawsonite  Magnesite Calcite Dolomite
 #PRINT
 #       -reset false
USER_PUNCH
  -head     molo2      actFe+3
 100 PUNCH  mol("O2")  act("Fe+3")
```